STUDIES OF LOW LATITUDE IONOSPHERIC PHENOMENA

Ph.D thesis submitted to
Saurashtra University, Rajkot
by
Banerjee Swarup Bhabataran

Department of Physics
SAURASHTRA UNIVERSITY
RAJKOT, GUJARAT, INDIA
November, 2011

STUDIES OF LOW LATITUDE IONOSPHERIC PHENOMENA

Submitted by

Banerjee Swarup Bhabataran

REGISTRATION NO. : 3502

DATE OF REGISTRATION: 31-07-2006

Submitted to

SAURASHTRA UNIVERSITY, RAJKOT

Faculty: Science, Subject: Physics

November, 2011

Under the guidance of

PROF. K. N. IYER,

Department of Physics, SAURASHTRA UNIVERSITY,

RAJKOT, GUJARAT, INDIA

Statement under O.Ph.D 7 of Saurashtra University

The work presented in this thesis is my own work carried out under the supervision of Prof. K.N.Iyer and leads to some important contributions in Physics supported by necessary references.

Date:17/11/2011

Place: Rajkot Banerjee S.B.

CERTIFICATE

This is to certify that the present work submitted for the award of Ph. D. degree of Saurashtra University, Rajkot by Mr. Banerjee Swarup Bhabataran has been the result of about 5 years of work under my supervision and is a valuable contribution in the field of IONOSPHERIC PHYSICS.

Prof. K. N. Iyer

Research Guide,
Department of Physics,
Saurashtra University,
Rajkot – 360 005, INDIA

Author

(Swarup B. Banerjee)

Dedicated to my

Mother

&

fond memory of my

Late Father

Acknowledgement

It is impossible to thank individually all the people – teachers, friends and colleagues – who have moulded my understanding of the subject over the years. I am deeply conscious of their contribution, and warmly thank all those, who, through books, lectures, discussions and other indirect ways, have influenced this work.

I shall always remain indebted to Professor K. N. Iyer for consenting to supervise the study towards this thesis. I have great pleasure in thanking him for his invaluable guidance throughout my Ph.D. work. I am very grateful to him for useful discussions we had which helped me in understanding the various phenomena in the earth's atmosphere. His knowledge and his organizing capacities have benefited me a lot.

I would also like to thank Prof. H. Chandra for going through my thesis in spite of his busy schedule and for giving useful suggestions.

I am extremely grateful to Dr. Somkumar Sharma and Dr. P. K. Rajesh for encouraging me to carry out the thesis work, and helping me to keep my moral up. Without their encouragement it would not have finished in time.

I thank all members of Atmospheric Science group which includes M. B. Dadhania, N. Dutta, P. K. Rajesh and others with whom I have spent sleepless night taking observations at dark remote areas.

I thank Prof. H.H.Joshi, Head, Dept. of Physics of Saurashtra University, other Faculty members and staff of the Physics Dept. for their support to carry out this work.

I thank to Prof. H. S. S. Sinha for initiating the fabrication of the all sky imager at PRL used in this study and the authorities at Kavalur for facilitation the observations from there.

I thank Mrs. Nistha Anilkumar and staff members for the library services. I am thankful to all the computer section staff members for their co-operation. I must thank all my friends in PRL who have helped unfailingly in keeping more and spirit high.

It is impossible to state the innumerable ways in which my family members have contributed to this venture. My daughter Upasana (Tuktuk) has given the initial inspiration and support for the work. My wife Shubhra has provided continued encouragement, and support on a day to day basis. Special thanks go to my son Siddhant (bhai) also provided positive encouragement in many ways.

Finally, I thank PRL director for allowing me to carry out the work in this laboratory.

Banerjee S.B.

Preface

The atmospheric region of our interest is the upper mesospheric and lower thermosphere region, where electrons and ions exist in sufficient number to affect the radio wave propagation and is termed as ionosphere. In the nighttimes, if we look the variation of electron density with altitude, sometimes we can see lot of fluctuations in it. These are generally called ionospheric irregularities and we want to study them. The irregularities present in the equatorial F-region of ionosphere are also known as Equatorial Spread-F (ESF).

Equatorial Spread-F or ESF is a night-time phenomenon. The irregularities associated with ESF are generated in the steep gradients of electron density present in the nighttime bottomside ionosphere when the background conditions are favorable. ESF is associated with irregularities of a wide range of scale sizes, varying from more than a thousand kilometer, down to less than a meter. They are classified in to different groups and there is different generation mechanism for each group. We study the large-scale structures associated with ESF. They are known as plasma depletions.

Plasma depletions are the large-scale structures associated with ESF. Large scale means, few tens of kilometer to more than a thousand kilometers. These are regions of large-scale reduction in electron density. These structures often exhibit 2-3 orders of magnitude reduction in electron density. These are generated in the bottom side of F-region (200 km). They move eastwards as well as upwards. They evolve non-linearly to the topside, which is otherwise a stable region. At times these are found to attain very high altitudes over equator. Sometimes they reach altitudes beyond 2500 km. As they move upwards, they drift down along the field lines, which are highly conductive, to low latitudes. Thus, they appear as field aligned structures of large-scale reduction in electron density. To study such large-scale dynamic feature, one needs to have an instrument that can cover a wide area of sky. All sky imaging systems, which have a large FOV are used effectively to study plasma depletions.

All sky imaging system takes snap shots of night sky in selected nightglow wavelengths. Such instruments normally have 180^o FOV and cover a large area of the sky. The intensity of the nightglow emission line selected should be a known function of electron density. Also, we can see the structures of plasma depletions in the all sky images only when the structures are present at the altitude of bulk emission of these lines. The first version of such a system was developed by Mende and Eather (1976) of Air Force Geophysics Laboratory to carry out airborne studies of airglow emissions at 630 nm. The all sky imaging system developed at PRL is similar to the one described by Mendilo and Baumgardner (1982). The front-end fish eye lens covers a circular area of diameter more than 3600 km. The signals from the fish-eye pass through narrow band interference filters, where emission lines are isolated. This signal is intensified and the images are taken using a CCD camera. The camera is capable of operating in very low light level conditions and long period exposures can be taken with it. The results from such observations are the basic of our current understanding of plasma depletions.

This dissertation focuses on the study of ionospheric irregularities using selected airglow emissions whose intensity is related to plasma density. The experiments were conducted from Kavalur (12.5˚N, 78.8˚E; 4.6˚N geomagnetic), and Mt. Abu (24.5^{o}N, 72.7^{o}E, 18.5^{o}N geomagnetic), India. The 630.0, 557.7, and 777.4 nm emissions are used for studying the different features of the plasma depletions. The ionosonde data is used to monitor the base height of the F-layer as well as the presence or absence of Spread-F at the time of the appearance of depletions in all sky images.

Several new features of plasma depletions are observed in this study such as the new type of ‘joined’ pair of depletions where the northern (and later the southern) ends join together, producing an inverted ‘V’ shape bifurcation, which later merge together, sequences of depletions developing in the field of view of the all sky imager in the post-midnight period.

Content Page No.

Acknowledgement i

Preface ii

List of tables vii

1. Introduction

1.1 Structure of Neutral Atmosphere 1

1.2 Structure of the ionosphere 4

1.3 Formation of the ionosphere 5

1.4 Airglow and Ionosphere 8

1.5 Ionospheric Irregularities 9

1.6 Study of Plasma Depletions 11

1.7 Current Understanding 12

1.8 Focus of the Current Study 15

2. Airglow Imaging of Plasma Depletions

2.1 Airglow Emissions 16

2.2 Airglow and Ionospheric Irregularities 18

2.3 Airglow Chemistry 20

2.3.1 Dissociative Recombination: 630.0 and 557.7 nm Emission 21

2.3.2 Radiative recombination: 777.4 and 135.6 nm Emission 24

2.3.3 Barth mechanism: Emission of 557.7 nm 25

2.4 All Sky Imaging 26

2.4.1 PRL All Sky Imager 29

2.4.2 Optical design details of the All sky Imager 30

2.5 Image Geometry 31

2.6 Image Analysis 35

3. Observation and Image Analysis

3.1 Observations at Mt. Abu 37

3.2 Observations from Kavalur 39

3.3 Apex mapping 46

4. **Characteristics of Plasma Depletion over Indian Region**

4.1 All sky observations over India 50
4.2 East-west extension 55
4.3 Drift velocity of depletions 62
4.4 Depletions and wave disturbances 68
4.5 Bubble rise velocity 73
4.6 Depletions at equatorial and off-equatorial latitudes 77

5. **Some New Features of Plasma Depletions**

5.1 Depletions in 557.7 nm 79
5.2 Appearance in 630.0 nm 102
5.3 Bifurcation and joining 122
5.4 Post-midnight depletions 130

6. **Conclusions** 142

References 145

List of publications 153

List of Tables **Page No.**

Table 2.1 Reaction coefficients for dissociative recombination process 22

Table 2.2 Reaction coefficients for radiative recombination process. 23

Table 2.3 The spatial coverage of the all sky imager for 100, 250, and 350 km altitudes. 35

Table 3.1 Details of observations from Kavalur during February-April 2002. 41

Table 4.1 The east-west extension of selected plasma depletion in the 630.0, 557.7, and 777.4 nm airglow images taken in the pre-midnight period of 11 March 2002 over Kavalur, India. 60

Table 4.2 East-west extensions of two plasma depletions in the 630.0 and 557.7 nm airglow images taken in the post-midnight period of 11 March 2002 over Kavalur, India. 61

Table 5.1 Number of nights with plasma depletions observed during February-April 2002. 91

Chapter1. **Introduction**

*This thesis is a compilation of the airglow observations conducted from Kavalur (12.5 ° N, 78.8 ° E, 4.6 ° N Magnetic) and Mt. Abu (*24.5° N, 72.7° E; 18.5° N *Magnetic) in the high solar activity period of 1999-2002. The observations are carried out using the all sky imaging system developed at Physical Research Laboratory, Ahmedabad, India. The objective of the study is to understand the characteristics of plasma depletions over the Indian region during solar maximum. Kavalur, being an equatorial station, could give features of plasma depletions in the early stages of their evolution, once the scale sizes are sufficient to be detected by the imager. From the low latitude station Mt. Abu, it is expected to study features of well developed plasma depletions. In this chapter, an attempt is made to introduce the ionospheric physics, starting with a brief description of the structure of the atmosphere and the details of the structure and formation of ionosphere. The characteristics of equatorial ionosphere and various ionospheric processes such as Equatorial Spread-F are then explained, which leads to the main topic, "plasma depletions". The background material given below is mainly based on the works of Rishbeth and Garriott (1969), and Hargreaves (1992).*

1.1 Structure of Neutral Atmosphere

The earth's atmosphere is divided mainly into four regions viz. troposphere, stratosphere, mesosphere and thermosphere, based on the vertical distribution of temperature. Troposphere, meaning *turning* or *changing* sphere, ranges from ground to about 17 km near tropics. It accounts for more than 80% of the mass and virtually all of the water vapor, clouds and precipitation in the atmosphere. All the weather systems are within the troposphere. It is characterised by very strong vertical mixing. The surface of the earth acts as a black body that absorbs the solar radiation, which is rich in short waves, and re-radiates longer wavelengths. The atmospheric molecules such as water vapour, carbon dioxide, ozone etc. absorb and emit these infrared radiations, thus providing an efficient heat transfer in the troposphere. As we go up in the troposphere, the temperature initially decreases due to adiabatic cooling, until above a certain altitude where it remains uniform (about 17-20 km in the tropics), which is known as tropopause.

The temperature starts to increase with altitude above tropopause, and this region is known as stratosphere, which extends from 20 km to about 50 km. It is highly stratified or layered region. Unlike in the troposphere, there is very small vertical mixing in stratosphere and is characterized by the presence of ozone layer. The ozone absorbs most of the harmful ultraviolet rays from the Sun, and thus acts as heat source. This explains the observed temperature variation in the stratosphere. The region above stratosphere is termed as stratopause, where the temperature ceases to increase with altitude. The pressure at stratopause level is about 1 mb, whereas at ground it is 1000 mb. About 99.9% of the atmospheric mass resides within troposphere and stratosphere.

Mesosphere, the middle sphere, ranges from 55 km to about 85 km. In mesosphere also temperature decreases with altitude. Vertical air motions are present in mesosphere. During summer season, thin layers of clouds are produced in this region. During twilight, when lower atmosphere is in the earth's shadow, these clouds will be visible from ground as noctilucent clouds. The upper region of mesosphere, known as mesopause, falls among the coldest regions in the atmosphere. The mesospheric temperature minimum is due to the radiative cooling of that region by airglow emissions both in IR and visible range.

The region above 90 km is called thermosphere and it extends to several hundred kilometers. In thermosphere, temperature increases first steeply and then slowly with height. The temperature in these regions varies from 500 K to 2000 K. The heating is caused by the absorption of solar EUV and X-rays by the atmospheric constituents. In this process these constituents get ionised and result in the formation of *ionosphere*. At higher heights, the density is extremely low and heat conductivity is very high, resulting in almost uniform temperature distribution. Figure 1.1 illustrates the vertical temperature distribution in detail.

The region of atmosphere below 100 km is generally called homosphere, which is marked by turbulent mixing of the gas molecules. As a result, various atmospheric species are well mixed and are distributed according to their mean mass. In the region above 100 km there is no turbulent mixing. Above this height diffusive separation controls the distribution of gases. This region is called heterosphere. The height region where turbulent mixing becomes less important than diffusive separation is called turbopause. Heavier elements are prominent in the lower parts and as we go up lighter elements become the important species. In the region above 600 km, where the mean free path exceeds scale height, is called exosphere. In exosphere, collisions are negligible and molecules move under the influence of gravity. If the velocity of molecules is greater than the escape velocity, they escape from the gravitational field of the earth.

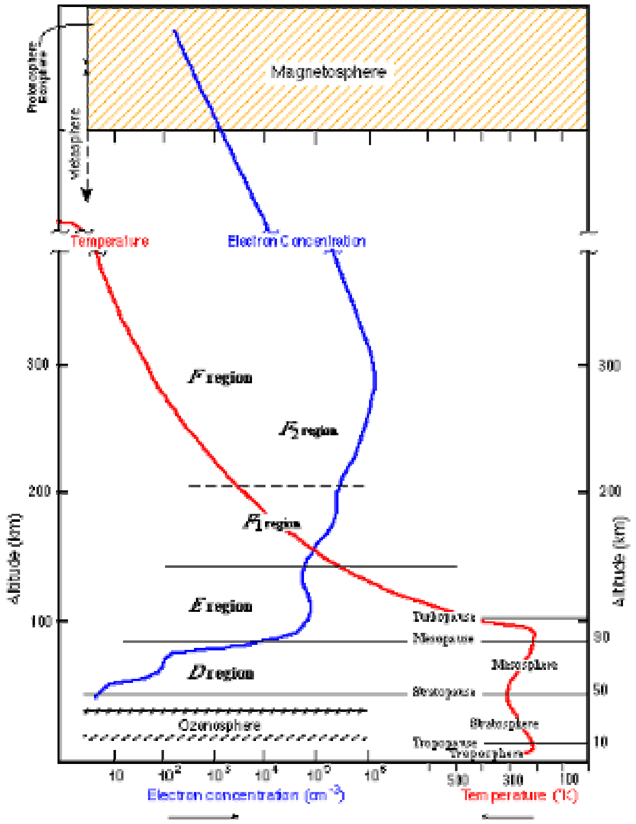

Figure 1.1 *Vertical structure of the ionosphere showing the different layers marked as D, E, F (F_1 and F_2) etc. This nomenclature is due to the fact that when an electrically conducting layer was first proposed to exist around 100 km, it was termed as E region. Following the convention, later when other layers were discovered to exist below and above the E region, they were respectively called D and F regions. The F_1 and F_2 regions are the sub divisions of the F region, which is found to split into two layers during day time, owing to the differences in the photochemistry at different altitudes. Also shown is the vertical distribution of temperature, based on which the atmosphere is divided into different regions as indicated. [Source: http://ion.le.ac.uk]*

1.1 Structure of the ionosphere

The solar X-ray and UV radiation entering the upper atmosphere ionise the elements present at those altitudes and results in the formation of ionised layers in the upper mesospheric and lower thermospheric regions. This region is known as ionosphere. Ionosphere is defined as that region of the earth's atmosphere, where free electrons exist in sufficient numbers to affect the radio wave propagation. Ionosphere starts from about 50 km and extends up to more than 1000 km. The presence of a conducting layer in the upper atmosphere was suggested long back in eighteenth century from the study of the geomagnetic field variations. The ionospheric studies gathered momentum in 1901, after the success of the Trans Atlantic radio propagation by Marconi. This revealed the importance of ionospheric studies in the field of radio wave communication. Various techniques were employed to study the ionosphere. They involve ground-based instruments such as conventional radar, ionosonde etc. and in-situ techniques such as Langmuir probes, double probes, etc. carried using rockets or satellites.

Ionosphere is described as a laboratory, where different verities of chemical and physical processes take place. The major source of ionisation is the solar X-ray and EUV radiation. At high latitudes the solar wind particle precipitation plays an important role in ionisation. Depending on the vertical distribution of the electron density, ionosphere is divided into different regions. They are known as D region, E region and F region etc. D region starts from about 50 km and extends to about 90 km. The important chemical species in this region are O_2, N_2 and NO. Radiation having absorption cross section less than 10^{-19} cm^2 causes ionisation in this region [Banks and Kockarts, 1973]. The hard X-rays (0.1- 1 nm) ionise all elements. The Ly α (121.6 nm) line ionise NO and solar UV rays (102.7-111.8 nm) ionise O_2 (^1D). Cosmic rays are also responsible for ionisation in this region. The typical electron density in this layer is about 10^3 electrons per cc. The dynamics of this region is mainly determined by the dynamics of neutral elements.

The region extending from 90 km to about 140 km is called E region. The important ionising radiations in this layer are the soft X-rays (1-20 nm), which ionises all and the EUV radiation 91.1-102.7 nm that ionises O_2. Absorption cross section of radiation in this region is less than 10^{-18} cm^2 [Banks and Kockarts, 1973]. The prominent ions are NO^+ and O_2^+. In this region, electron density is of the order of 10^5 cm^{-3}. The region above 140 km is called F region. The most important species in this layer is atomic oxygen. The ionising radiation is the EUV rays in the range 20-91.1 nm that ionises N_2, O_2 and O, and the absorption cross-section is less than 10^{-17} cm^2. F region is usually split into two layers F1 and F2 during daytime in certain seasons. The region below 50 km, where ionisation negligible compared to neutrals, is called C region. The main source of ionisation in this region is the cosmic rays that ionise all elements. In this region electron density is very small. The electron distribution with altitude is given in Figure 1.1.

1.2 Formation of the ionosphere

While the high energy radiation entering the upper atmosphere ionise the neutral atoms and molecules, the ions and electron thus produced undergo recombination reactions. Under quiescent conditions, the balance between production and loss of ions maintains the stable ionosphere. The layered structure of the ionosphere is as a result of the relative variation of the intensity of the ionising radiation and neutral distribution with altitude. Maximum ionisation occurs at the level where, the increase in the attenuation of the radiation and the gas density balances, as we go down from the top of the atmosphere. O_2, N_2 and O are the important chemical elements in the ionospheric region. These elements are ionised by the solar EUV and X-rays through photo dissociation, photo ionisation etc. and form ionised regions in the upper atmosphere. Photons with energies greater than 12 eV can ionise one or more atmospheric constituents. The processes involved in the production and loss of ions are described in detail by Chapman in 1931. The simple production function given by Chapman for a horizontally stratified atmosphere having a single component with constant scale height is,

$$q(z) / q_{m0} = \exp\{1 - z - e^{-z} \sec\chi\} \qquad (1.1)$$

where, the optical depth z is given by,

$$z = \frac{h - h_{m0}}{H} \qquad (1.2)$$

Here q is the rate of production at a given height h when the solar zenith angle is χ, q_{m0} is the maximum rate of production when the sun is overhead and h_{m0} is the corresponding height of maximum production. H is the scale height. At heights above the height of maximum production h_{m0}, z is positive and for large values of z,

$$q \approx q_{m0}\, e^{-z} \qquad (1.3)$$

At heights well below h_{m0}, z is negative and

$$q \approx q_{m0} \exp\{- e^{-z} \sec\chi\} \qquad (1.4)$$

In the above equation, the height of unit optical depth and the height of maximum ionisation coincide, since scale height is assumed to be independent of height.

The process of ionisation is complete only if the loss mechanisms are also considered. In D region the photo-ions produced are lost through dissociative recombination with electrons or neutralisation with negative ions. The rate coefficient for the above two processes is approximately 10^{-6} cm^3 sec^{-1}. A three-body reaction involving attachment of electrons with neutrals is suggested for the production of negative ions. Photo-detachment, associative detachment and collisional detachment are the important loss mechanisms of negative ions. The coefficient of photo detachment for O_2^- is ~ 0.4 sec^{-1} and coefficient of associative attachment is of the order of 10^{-10} cm^3 sec^{-1}.

In E and lower F regions, the important loss process is dissociative recombination. This is a two-stage process involving a charge transfer reaction followed by dissociative recombination. The direct or radiative recombination of atomic ions and electrons is an extremely slow process in this region. Hence the atomic ions undergo charge transfer reactions with neutrals as given below.

$$A^+ + X_2 \rightarrow XA^+ + X \qquad (1.5)$$

Here A^+ is the atomic ions and X_2 denotes any neutral molecule. The rate coefficient (γ) of this reaction is of the order of 10^{-10} cm^3 sec^{-1}. The molecular ion (XA^+) thus formed undergo dissociative recombination with electrons as given by,

$$XA^+ + e \rightarrow X + A \qquad (1.6)$$

The rate coefficient (α), for the above reaction is of the order of 10^{-7} cm^3 sec^{-1}.

At lower altitudes neutral density is more and hence equation 1.5 is faster and hence the overall rate is controlled by rate of equation 1.6, which is given as αN^2, where N is the electron density. The layer thus formed is called α-Chapman layer. At higher heights, reactions given in equation 1.5 become slow and overall reaction depends on the production rate of molecular ions. Here the rate of reaction is given as γNN^+ or βN where $\gamma Nn=\beta$ and Nn is the number density of neutrals. This layer is called β-Chapman layer. As we go high from lower altitudes, gradual transition occurs from α-type to β-type process. At intermediate heights where α and β type reactions are important, the production rate is given by

$$\frac{1}{q} = \frac{1}{\beta N} + \frac{1}{\alpha N^2} \qquad (1.7)$$

The ionosphere is sometimes called a laboratory, where variety of such chemical reactions takes place, involving neutrals as well as ionized species. Some of the products of these processes may be in higher energy (excited) sates, and, the subsequent de-excitation results in photon emissions, characteristic of the particular interaction. These transitions could occur in the ultraviolet, visible or infrared regions of the electromagnetic spectrum, and are termed as *airglow*. Anders Angstrom was the first to note the weak radiations and discovered green line in the night sky in 1868. The detailed investigations of the spectral emission were done in 1920's with the efforts of Lord Rayleigh. John McLennon and G. M. Shrum, in 1923, identified the green line to be originated from atomic oxygen. In the beginning of 1930's, Sydney Chapman proposed chemical recombination as the mechanism for these lines. In 1950, the term airglow was coined to describe the emissions.

1.3 Airglow and Ionosphere

The airglow is generated through the photochemistry in the upper atmosphere, and the intensity of the emission depends on the strength of the reactants and the corresponding cross-sections. If the excitation process involves ionospheric plasma, then the airglow intensity can be represented as a function of the plasma (electron) density. Thus, the variations in the plasma distribution would reflect as intensity fluctuations of such emissions. This very fact is used or is made use of to determine ionospheric parameters from airglow measurements. It is known that 630.0 nm intensity is proportional to Ne and depends on height while 777.4 nm intensity is proportional to Ne^2 .

Earlier works associating airglow with the ionosphere are from the observations of 630.0 nm enhancements, which were interpreted in terms of the descent of F-region. [Greenspan, 1966; Nelson and Cogger, 1971]. Higher F-layer altitude slowdown the dissociative recombination and results in less thermospheric emission [Bittencourt and Sahai, 1979]. Sharp gradients in 630.0 nm intensity results when F-layer height is modified by meridional circulation [Herrero and Meriwether, 1980]. Such studies point towards the relationship between the airglow emissions and the height of ionosphere, and show how these measurements give information about ionospheric and atmospheric dynamics. Coordinated experiments have been carried out to investigate thermospheric-ionospheric coupling by means of airglow, neutral winds, and ionospheric observations. For example, the study of brightness waves in airglow images and their relation to the mid-night temperature maximum (MTM) [Colerico et al., 1996; Mendillo et al., 1997; Otsuka et al., 2003]. The association of MTM with atmospheric tides [Fesen et al., 1986; Fesen, 1996] throws light on the role of lower atmospheric process in controlling ionospheric behavior. Recent studies have shown the signatures of non-migrating tides in the global airglow distribution, thus revealing direct coupling between troposphere and ionosphere [Immel et al., 2006].

The interaction between neutral atmosphere and ionosphere sometimes also appear as periodic modulations of airglow, often associated large scale wave propagations known as traveling ionospheric disturbances (TID) [Garcia et al., 2000; Shiokawa et al., 2003]. TID's are the perturbation of ionospheric plasma by acoustic gravity waves (AGW) [Hines, 1960]. The large scale AGWs or traveling atmospheric disturbances (TADs) are generated during geomagnetic storms, when the heating and subsequent rapid expansion of the high latitude results in pressure gradients and modify the thermospheric composition as well as circulation. These composition changes are transported to middle and low latitudes as TADs or AGWs [Roble et al., 1978; Prolss, 1987; Rishbeth, 1987]. Another common source of AGWs is in the lower atmosphere, often associated with weather fronts or land topography, which propagate upwards and sometimes perturb the ionosphere.

In addition to the modulations caused by external agencies, ionospheric plasma in the equatorial region is often re-structured by instabilities that operate when suitable conditions exist. These irregularities in plasma density appear as corresponding airglow patterns, and can be studied by measuring these intensity variations.

1.4 Ionospheric Irregularities

The nighttime equatorial ionosphere is characterized by irregularities of a wide range of scale sizes. After sunset, loss process in the ionosphere becomes predominant and sharp density gradients are generated. Also, the F layer is lifted up to very high altitudes due to the pre-reversal enhancement of zonal electric field. Under such conditions, instability processes can operate and render the plasma unstable. Any small initial perturbations can grow in amplitude and will appear as ionospheric irregularities. These irregularities are collectively known as Equatorial Spread-F or ESF.

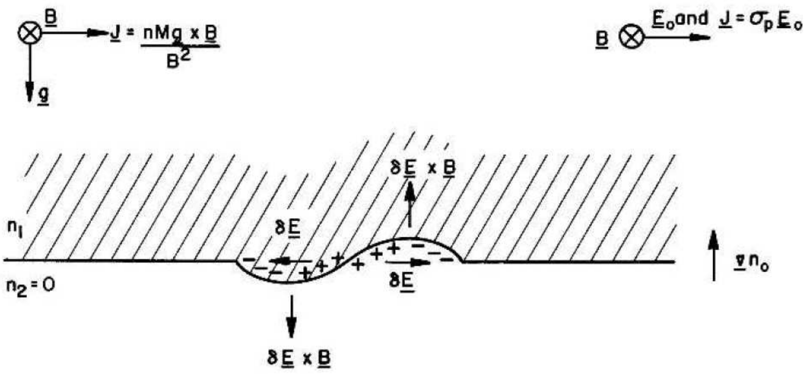

Figure 1.2 *Rayleigh-Taylor instability in the equatorial plane [Kelley, 1989]*

Rayleigh-Taylor instability is thought to be the mechanism responsible for ESF [*Kelley*, 1989]. The instability process could be understood with the help of Figure 1.2, which illustrates a simplified model of the post-sunset equatorial ionosphere, where the directions of density gradient, gravitational force and the magnetic field are indicated. This is a situation where the heavy plasma, on which gravity acts downward, is supported by the light magnetic field. The **g**×**B** force acting on the plasma results in an eastward current that depends on plasma density. Assuming sinusoidal initial density perturbation as given in Figure 1.2, the current will be more in the high density trough and less in the low density crest, causing the charge particles to be piled up at the walls of the perturbation. The polarization electric field thus generated will drive the low density plasma to higher altitudes and high density plasma to lower regions.

The irregularities are first detected from the spreading of ionogram traces [*Booker and Wells*, 1938], which explains the name ESF. This phenomenon occurs after sunset when F layer drifts upward to reach higher altitudes [*Farely et al*., 1970], and, manifest as ‘bite-outs’ in satellite density measurements [*Hanson and Sanatani*, 1973], plumes in radar RTI maps [*Woodman and LaHoz*, 1976], and cause scintillations of radio signals [*Basu et al*, 1978]. These irregularities convect upwards with large velocities through the F layer peak to the topside by flux tube interchange and can reach very high altitudes [*Woodman and LaHoz,* 1976; *McClure et al.*, 1977; *Burke et al.*, 1979]. *Tsunoda* [1980] showed that the irregularities are field aligned and extend to hundreds of kilometers.

The ESF is associated with irregularities ranging a wide variety of scale sizes. The scale sizes vary from few centimeters to about a thousand kilometer. The irregularities are aligned along the magnetic field lines. They move upwards with velocities ranging from tens of ms^{-1} to hundreds of ms^{-1}. Also they move eastward with velocity about 100 to 200 ms^{-1}. The small-scale irregularities associated with ESF cause scintillation in VHF signals. The large-scale structures are called *plasma depletions*. They represent a large-scale reduction in plasma density. Two to three orders of magnitude reduction in density are observed. They have vertical scale sizes of several hundreds to thousand kilometers. Their east-west scale size varies from tens of kilometers to hundred kilometers. They move upwards and eastwards.

1.5 Study of Plasma Depletions

Since the first observation by Booker and Wells in 1938, many investigators have looked into the phenomenon of ESF using various techniques. But, the mechanism responsible for the generation of irregularities over such a wide scale is still not completely understood. The occurrence of ESF is highly unpredictable. ESF occurs only on certain nights. The appearance of plasma depletions is even more unpredictable. Plasma depletions are not observed on all spread-F nights. This makes their study very important and interesting.

Ionosonde, scintillation receivers, radars, rocket and satellite borne probes etc. can be used to study the ionospheric irregularities. Ionosonde can be used to detect the onset of spread-F. But, once spread-F has set in, it cannot provide much information. Strong scintillations will be recorded in the scintillation receivers when the signals received traverse through these irregularities. The movement of irregularities can be studied using spatially separated receivers. But, this gives information about the smaller scale irregularities that give rise to scintillations. The plasma bubbles appear as plumes in the RTI maps obtained using VHF radars. Here also, the backscatter signals are due to small-scale irregularities. Since the small-scale irregularities are found at the edges of large-scale structures, one can use the RTI maps to derive information about plasma depletions under certain assumptions. But field of view (FOV) is limited. Rocket and satellite borne probes are also used to study these phenomena. But they cannot give any information along perpendicular directions to their trajectory.

To get a complete picture about the formation of the depletions and their growth and movement an instrument that can cover a very large area of the sky is required. Optical imaging of the upper atmosphere is a powerful technique that can be used to understand this phenomenon completely. The technique is to take images of the night sky using the airglow emissions using an *all sky imaging* system. The imaging system employs a large field-of-view, front-end optics and hence is capable of covering thousands of kilometers of the sky and can be used to study the dynamics of plasma depletions.

1.6 Current Understanding

The signatures of ESF irregularities, which are the structures in plasma density distribution, should manifest as corresponding airglow intensity variations. Thus, ground based measurements of airglow intensity can be used to study these irregularities. Wide angle optical instruments were employed to image the auroral arcs at high latitudes [*Mende and Eather*, 1976], using television cameras. Similar technique was applied in the study of equatorial F-region using the 630.0 nm line. The observations revealed North-South aligned reduced airglow intensity, which are now called plasma depletions [*Weber et al*, 1978]. Further studies were conducted to understand the drift, strength (degree) and scale size of the depletions [*Weber et al.*, 1980]. The depletions are considered as footprints of depleted flux tubes at the airglow emitting region. The reverse of this concept, the so-called ‘apex mapping’, was used to trace the poleward ends of depletions along the magnetic field lines to determine the corresponding altitude attained by the irregularities at the magnetic equator. This information was then used to determine the vertical rise velocity of depletions. The

777.4 nm emission was also incorporated in the measurements for detailed investigations [*Moore and Weber*, 1981].

Ground based intensified all sky imagers were introduced in early 80's [*Mendillo and Baumgardner,* 1982]. These observations revealed several features of depletions. The pronounced occurrence of depletions was observed between 2030 LT-2330 LT. The poleward end of depletion was found to have a westward tilt. Branching or bifurcation of depletions was also observed. Numerical simulations had shown that rising bubbles start bifurcating when contribution of E-region Pedersen conductivity to F-region conductivity is included in the calculations, and the bifurcations occur when the ratio of conductivities inside and outside the bubble becomes less than 10 [*McDonald*, 1981; *Zalesak*, 1982]. Detailed analysis showed that the conductivity ratio inside and outside the bifurcated depletion met the requirement, but the appearance of linear and bifurcated depletions side-by-side remained unexplained [*Anderson and Mendillo*, 1983]. The westward tilt of depletion was explained based on the latitudinal variation in zonal wind [*Mendillo and Taylor*, 1983]. Coordinated all sky imaging and scintillation observations showed that the irregularities producing scintillations are located on the walls of the bubbles [*Weber*, 1982].

With the establishing of ground based all sky imager, many investigators followed such observations, which revealed several characteristics such as sharp eastern walls [*Rohrbaugh et al*., 1989], day-to-day variability, high altitude (~ 2500 km) bubbles, post-midnight depletions associated with magnetic storms [*Sahai et al*. 1994], supersonic (2.8 km/s) vertical velocity, and absence of simultaneous 777.4 depletions with that in 630.0 nm [*Weber et al* 1996], etc. The association between spread-F in ionograms and irregularities in the walls of the depletions were demonstrated using ray tracing methods [*Sales et al*, 1996].

The trans-equatorial, meridional wind at the sunset terminator is believed to play an important role in the growth or suppression of the R-T instability [*Maruyama*, 1988]. When there is a strong N-S component, the ionospheric height decreases in the downwind side, hence the Pederson conductivity increases (more O_2^+, NO^+ ions), in comparison to the conductivity at the upwind side (O^+ ions). This, results in an E-region type of load at one end of the flux tube, and lowers the growth rate. The attempts to study the role of meridional wind in generating or inhibiting spread-F by simultaneous wind and depletion measurements did not show any conclusive evidence [*Mendillo et al*., 1992, *Bittencourt et al*., 1997]. It was found that during spread-F season, depletions were generated when large fluctuations were present in the meridional wind. During non-spread-F season, no depletion was seen when there were fluctuations in meridional wind. But, depletions were produced when magnetic storms were present; showing that when there is s strong seed present (magnetic storm) meridional wind also doesn't suppress ESF. Several all sky observations have studied the occurrence of depletions and geomagnetic activity [*Sahai et al*. 1988; *Aarons et al*. 1999; *Sinha et al*., 2000, 2001].

The all sky measurements generally show eastward drifting depletions, but there are reports of deviation from this pattern when depletions reversed direction to westward for a period of about 1 hour [*Taylor et al*., 1997]. There are also reports of stationary depletions that do not show any movement for very long time period [*Fagundes et al*., 1999; *Sinha et al*. 2001]. The anomalies in the eastward drift are believed to be due to the modification of F-region dynamo by the changes in neutral circulation caused by magnetic activity. *Sinha* et al. [2003] reported splitting and joining of depletions, indicating strong shear in plasma drift. The zonal drift measurements are used to understand the latitudinal difference in plasma drift [*Martinis et al*., 2003; *Pimenta et al*., 2003a, 2003b]. The depletions were found drift at higher velocities near the equator compared to off-equatorial latitudes. The plasma drift measurements deduced from simultaneous 630.0 and 777.4 nm images showed slightly higher velocities near the F-peak altitude [*Ablade et al*., 2004].

The seasonal and solar cycle variations in the occurrence of depletions are only available from the Brazilian sector, owing to the extended data set recorded over that region.. It is shown that the probability of occurrence of plasma depletions increases significantly during the periods of high solar activity [*Sobral et al*., 2002; *Sahai et al*., 2000].

1.7 Focus of the Current Study

The present work is aimed to study the various parameters of plasma depletions and to understand the role of various atmospheric and ionospheric conditions that result in the generation of these large-scale irregularities. The study is carried out using the all sky imaging system developed at the Physical Research Laboratory (PRL), Ahmedabad, India. The all sky imaging system of PRL was operated from Mt. Abu (24.5° N, 72.7° E; 18.5° N Magnetic) as well as Kavalur (12.5 N, 78.8 E, M.L. 4.6 N Magentic), India. The observations were carried out during the increasing phase of solar activity in 1999-2002. The images obtained from this campaign were analysed to determine various parameters of plasma depletions such as degree of depletion, width of depletion, inter depletion distance and eastward drift velocity. Mt. Abu is an off-equatorial station where as Kavalur is very close to the equator. Thus, the results give an opportunity to investigate the characteristics of depletions near the equatorial region as well as at off-equatorial latitudes. Over the equator, one could study the developing depletions or the initial stages of developed depletions. At off-equatorial location, the depletion would be already well developed.

The organization of the thesis is as follows. The mechanism of airglow emissions and all the technique of sky imaging are given in Chapter 2. The details of the PRL's all sky imager is given in Chapter 3, which also gives an overview of the imaging observations used in the current study. Chapter 4 gives the characteristics of the plasma depletions from the observations conducted for this work, and Chapter 5 highlights some of the new observations and information revealed from these investigations. A summary of the results are given in Chapter 6.

Chapter 2. **Airglow Imaging of Plasma Depletions**

This chapter describes the methodology followed in the study. First an introduction is given to the ionospheric processes those results in major airglow lines. While there are several airglow lines, only certain emission could be used for ionospheric research. Thus, it is important that the intensities of the selected airglow lines are related to the plasma density. The detailed emission mechanisms of the important spectral emissions that are used in the current study are provided, elaborating how the observed intensities are related with electron density. Next, the concept of all sky optical imaging is introduced, and the details of the imaging system are described. A brief description of the all sky imager developed at the Physical Research Laboratory, Ahmedabad, INDIA, which is used to collect the data used in the current study is provided, followed by some of the procedures used for image analysis.

2.1 Airglow Emissions

The earth's ionosphere is sometimes called a chemical laboratory, where a number of chemical reactions take place. These reactions involve neutrals as well as ionised species. Some of the products of these reactions may be in the excited sates and as they transfer to lower energy state, spectral lines are emitted. The emissions may be in the ultraviolet, visible or infrared regions of the electromagnetic spectrum, depending up on the particular reaction responsible for it, and are generally termed as airglow. It is continuous throughout the globe. The main source of airglow emissions is the photochemical reactions involving solar radiation and various atmospheric species. At higher latitudes, the energetic particles from the solar wind give rise to the fascinating phenomenon called aurora. The main emission mechanism is the excitation of atmospheric species into higher states. The excited species returns to ground state in one or more steps, emitting radiation characteristic of that species. The excitation mechanisms involve (a) fluorescence and resonance scattering, (b) excitation by energetic particles, (c) chemical excitation and (d) energy transfer through collisions.

The important airglow emissions that are used in optical aeronomy, are the emission lines of atomic oxygen, atomic sodium and hydroxyl radicals. These emissions are present at all altitudes, but bulk of the emission comes from a certain altitude range where the constituents responsible for the emission have a maximum concentration. The altitude profile of the important species in the upper atmosphere is given in F**igure 2.1**. Nitrogen (N_2), and Oxygen (O_2) molecules are the dominant neutral species in the lower heights, while above about 220 km, atomic oxygen becomes important. As a result of the small mean free path at the low altitudes (F-region bottom side), N_2, and O_2 plays an important role in loss processes. At higher heights the neutrals do not have any significant role in the interactions.

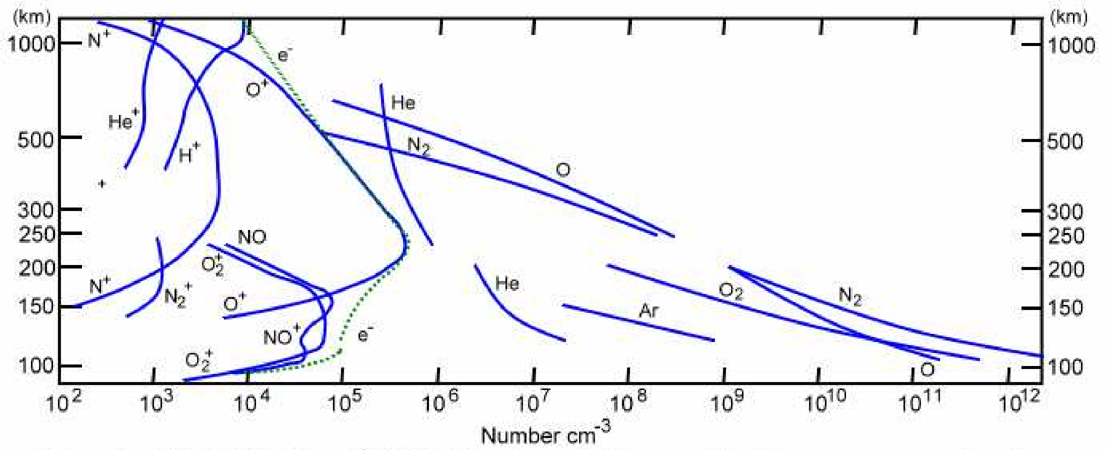

International Quiet Solar Year (IQSY) daytime atmospheric composition, base on mass spectrometer measurements above White Sands, New MexXico (32 N, 106 W). The helium distribution is from a nighttime measrrement. Distributions above 250 km are from the Elektron II satellite results of Istomin (1966) and Explorer XVII results or Reber and Nicolet (1965). [C.Y. Johnson, U.S. Navel Research Laboratory, Washington, D.C. Reprinted form John (1969) by permission of the MIT Press, Cambridge, Massachusets. Copyright 1969 by MIT.]

Figure 2.1 *The distribution of neutral particles above 100 km. Also shown are the distributions of charged particles.*

The important emission lines of atomic oxygen are 630.0 nm, 777.4 nm and 557.7 nm (**Figure 2.2**). The bulk emission of 630.0 nm line comes from an altitude region centered at about 250 km. This height region corresponds to the bottom side of the F region. The 7774. nm bulk emission is from the F-peak, which is at about 350 km. The 557.7 nm OI green line has two emission peaks, one is at about 100 km altitude region (mesospheric contribution) and the second peak it at about 250 km (F region contribution). So this emission can be used to study different altitude regions, depending on which altitude region contributes more to the total emission. The sodium doublet is originating from an altitude region of 90 km to 95 km. The source of this metallic ion at these altitude regions is attributed to the meteoritic activity. Another important emission is the IR emission of OH radical at 839.4 nm. It comes from about 90 km. This emission is responsible for the cooling of this atmospheric region.

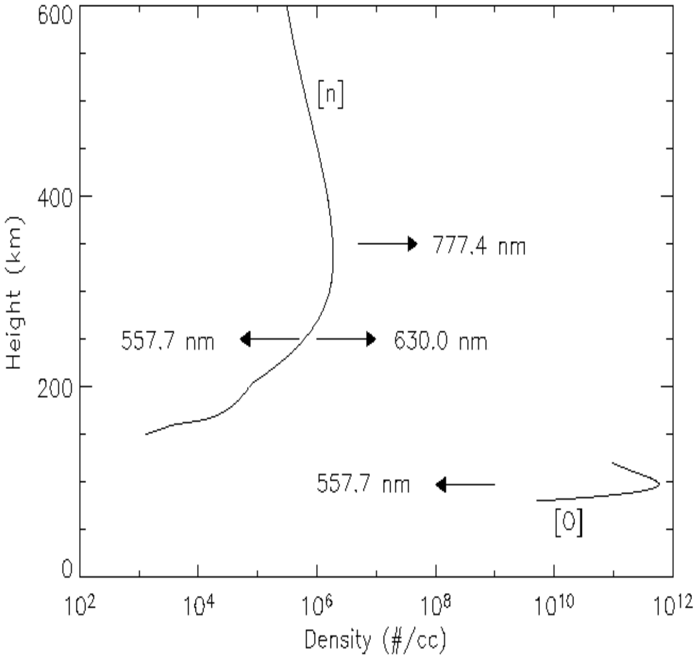

Figure 2.2 *Altitudes of the important spectral emissions from atomic oxygen (777.4 nm, 630.0 nm, and 557.7 nm) used in the current study. The electron density profile from the IRI model and atomic oxygen density from MSISE model for 2002 March are also shown.*

2.2 Airglow and Ionospheric Irregularities

The recombination processes in the coupled ionospheric-thermospheric system results in the excitation of neutral particles, especially the atomic oxygen, and the subsequent transition to the ground state results in airglow emissions in the ultraviolet (UV), visible, and near infrared (IR) regions. The intensity of these emissions is a function of the plasma density. Thus, by monitoring the airglow using a ground based instrument, one can study the plasma density at the altitude of their bulk emission. A time series of such observations can be used to investigate the plasma density variations. Though there are numerous spectral emissions from the upper atmosphere, but only those lines produced as a result of recombination processes, and, whose intensity is a function of the plasma density can be used for ionospheric research. The emissions from the excited states of atomic oxygen such as 630.0, 557.7, and 777.4 nm are related to the plasma density, and are used as tracers of ionospheric properties in ground based observations.

The study of airglow intensities gives important information regarding the source of the emission. From the measured intensity of the emitted lines and knowing the excitation cross-section, the column density of the emitting species can be calculated. The line of sight velocities and temperatures can be calculated from the Doppler profiles and line shifts of radiation. The airglow intensity gets modulated as a result of interaction between neutrals and plasma. Hence, by studying the airglow intensity variations, dynamics of the neutrals and plasma can be understood. Also, this enables the study of coupling mechanism of different atmospheric regions. If the intensity of the airglow emission is some known function of the electron density, then from the variations in the intensity of that particular emission one can study the electron density variation at the altitude of bulk emission. The irregularities in the electron density distribution will appear as airglow intensity variations.

Plasma depletions are regions of large-scale reduction in electron density. When they are generated at the equator in the ionosphere, the low density regions distribute along the magnetic field lines to reach low-latitudes. Thus, along a very large area, the plasma density drops by orders of magnitudes. Such, irregularities move with velocities of the order of 100-150 m/s, which gradually decreases with time. Thus, over such regions, the intensity of any airglow emission that is related to electron density will also be less. The intensity of airglow emission depends on the intensity of the source of emission and the corresponding excitation cross-sections. If one could monitor the time variation of the airglow intensity over the area, it is possible to study the ionospheric irregularities producing the intensity variations. So, any variation in the observed intensity can be attributed to a corresponding variation in the density of the emitting source, under normal conditions.

The present study is conducted using the All Sky Imaging System developed at P.R.L., Ahmedabad. The atomic oxygen emissions at 630.0, 557.7 and 777.4 nm are used to image the plasma depletions. These airglow lines are chosen since their intensity is a known function of electron density at the altitude where they are produced. In the case of 630.0 and 557.7 nm line, intensity is proportional to the electron density where as in the case of 777.4 nm line; intensity is proportional to square of the electron density. Hence, any variation in the electron density at the corresponding altitudes can be inferred from the intensity variation of the airglow lines. Hence the depletion images obtained using these two emission lines can be used to study the formation, growth and propagation of ionospheric irregularities. The important mechanisms involved in the emission of these lines are described below.

2.3 Airglow Chemistry

Atomic oxygen is the source of major airglow emissions in the ionosphere. As a result of the various photochemical reactions involving neutral and charged particles, the oxygen atoms are populated in higher energy states. Figure 2.3 gives the energy level diagram of atomic oxygen. The oxygen in the excited states transfers to the lower energy states, emitting the difference in the energy as radiation. Figure 2.3 also gives the wavelength of the possible emissions from atomic oxygen. Though, there are several such emission lines, as described above, the 630.0, 557.7, and 777.4 nm wavelengths are used here.

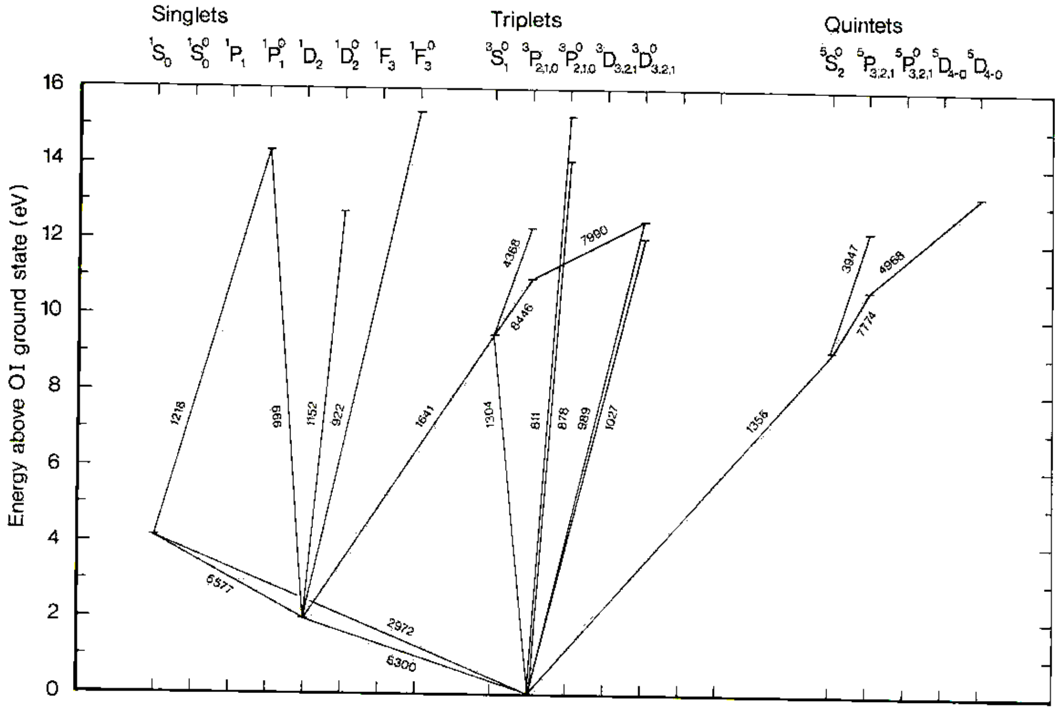

Figure 2.3 *The energy level diagram of atomic oxygen, showing the various spectral transitions (Rees, M. H., Cambridge Uni. Press, 1989).*

2.3.1 Dissociative Recombination: 630.0 and 557.7 nm Emission

The 630.0 nm, known as the ‘red line’, is the most extensively observed airglow emission of the night sky. In a review, *Chakrabarti* [1998] describes the first observation of 630.0 nm by Garrigue as early as in 1936. The 557.7 nm green line is known several years before, and its association with atomic oxygen was suggested in 1923. The green emission comprises of two components, a weaker emission from the lower thermosphere, and a much stronger emission from the upper mesosphere. The main source of the 630.0 nm, as well as the thermospheric component of the 557.7 nm, is the dissociative recombination of O_2^+ [*Peterson et al.*, 1966; *Peterson and VanZandt*, 1969; *Link and Cogger*, 1988; *Sheeshan and St.-Maurice*, 2004, *Vlasov et al.*, 2005].

The transitions from the metastable states $O(^1D)$, and, $O(^1S)$, of the atomic oxygen to the ground state $O(^3P)$, result in the red and green emissions, respectively. The main source of these metastable states in the nighttime thermosphere is the dissociative recombination of O_2^+ given by the reaction,

$$O_2^+ + e \xrightarrow{\alpha_1} 2O(^3P,^1D,^1S) \qquad (2.1)$$

where, α_1 (cm^3/s) is the rate coefficient, which depends on electron temperature (see Table 2.1). The fraction of the atomic oxygen resulting in either of the $O(^1D)$ or $O(^1S)$ states as a result of equation (2.1) is given by the quantum yields (μ_D and μ_S, respectively) of these states. The production rates of $O(^1D)$ and $O(^1S)$ states can be written as,

$$\mu_{1D}\alpha_1[O_2^+][e], \text{ and} \qquad (2.2a)$$

$$\mu_{1S}\alpha_1[O_2^+][e] \qquad (2.2b)$$

The O_2^+ ions are produced through the charge exchange reaction,

Table 2.1 Reaction coefficients for dissociative recombination process

Reaction	Coefficient	Value (cm^3s^{-1}, s^{-1})
$O(^1D)+N_2 \rightarrow O+N_2$	k_1	$2\times10^{-11}\exp(107.8/T_n)$
$O(^1D)+O_2 \rightarrow O+O_2$	k_2	$2.9\times10^{-11}\exp(67.5/T_n)$
$O(^1D)+O \rightarrow O+O$	k_3	$(3.730+1.1965\times10^{-1}T_n^{0.5}-6.5898\times10^{-1}T_n)\times10^{-12}$
$O(^1D)+O \rightarrow h\nu(630.0nm)$	A_{1D}	7.1×10^{-3}
$O(^1D)+O \rightarrow h\nu(636.4nm)$	A_{2D}	2.2×10^{-3}
$O(^1S)+O \rightarrow h\nu(557.7nm)$	A_{1S}	1.215
$O(^1S)+O \rightarrow h\nu(297.2nm)$	A_{2S}	0.076
	γ_1	$1.95\times10^{-7}(T_e/300)^{-0.7}$
	μ_D	1.1
	μ_S	0.08

$$O_2 + O^+ \xrightarrow{\gamma_1} O_2^+ + O \tag{2.3}$$

where, γ_1 is the rate of the charge exchange process. The main loss process of O_2^+ thus formed is the dissociative recombination given by equation (2.1). Combining the equations (2.1) and (2.3), the O_2^+ concentration can be written as,

$$[O_2^+] = \frac{\gamma_1[O_2][O^+]}{\alpha_1[e]} \tag{2.4}$$

Using equation (2.4) in (2.2) gives the production rates of $O(^1D)$ and $O(^1S)$ as,

$$\mu_{1D}\alpha_1[O_2][O^+], \text{ and} \tag{2.5a}$$

$$\mu_{1S}\alpha_1[O_2][O^+] \tag{2.5b}$$

There is another contribution to the $O(^1D)$ state due to the dissociative recombination of NO^+, but the quantum yield of the production is very small [*Link*, 1992], and have been shown to minor compared to the above reactions [*Sobral et al.*, 1993]. The $O(^1D)$ state can be deactivated through collisions with neutrals as well as electrons, in addition to the emission of 630.0 nm photon, where as the O(^{1}S) deactivation by collisions with neutral constituents is negligible. The collisional quenching of O(^{1}D) state are given by,

$$O(^1D) + N_2 \xrightarrow{k_1} O(^3P) + N_2 \tag{2.6}$$

$$O(^1D) + O_2 \xrightarrow{k_2} O(^3P) + O_2 \tag{2.7}$$

$$O(^1D) + O \xrightarrow{k_3} O(^3P) + O \tag{2.8}$$

The radiative deactivation of O(^{1}D) state can be realized either by the emission of a 630.0 nm photon or by the emission of a 636.4 nm photon, as illustrated in Figure 2.3. The transition probability (Einstein coefficient) of the 630.0 nm is represented by A_{1D}, while that of the 636.4 nm is A_{2D} (Table 2.1). It can be seen from Figure 2.3 that the

Table 2.2 Reaction coefficients for radiative recombination process

Reaction	Coefficient	Value (cm^{3}s^{-1}, s^{-1})
$O^+ + e \rightarrow O^* + N_2$	α_1	7.8×10^{-13}
$O + e \rightarrow O^- + O_2$	k_1	1.3×10^{-15}
$O^- + O^+ \rightarrow O^* + O^*$	k_2	1.5×10^{-7}
$O^- + O \rightarrow O_2 + e$	k_3	1.4×10^{-10}
	$\beta_{777.4}$	0.42
	$\beta_{135.6}$	0.54

O(^{1}S) state too has two transition probabilities, A_{1S} for the emission of 557.7 nm photon, and A_{2S} for the transition to the ground state O(^{3}P) emitting a 297.2 nm photon.

Combining the production and loss processes and the reaction probabilities, and since $[O^+]\approx[e]$ in the F2 region, the volume emission rate for the 630.0 nm can be written as,

$$V_{630.0} = \frac{A_{1D}\mu_D\gamma_1[O_2][e]}{k_1[N_2]+k_2[O_2]+k_3[O]+A_{1D}+A_{2D}} \tag{2.9}$$

and, that for the 557.7 nm,

$$V_{557.7} = \frac{A_{1S}\mu_S\gamma_1[O_2][e]}{A_{1S}+A_{2S}} \tag{2.10}$$

It can be seen from equations (2.9), and, (2.10), that the volume emission rate is directly proportional to the electron density. Also, when the F-layer altitude decreases, the numerator in the equations decreases more rapidly than the denominator (the quenching efficiency is very low), and hence the emission intensity decreases.

2.3.2 Radiative recombination: 777.4 and 135.6 nm Emission

The 777.4 nm and 135.6 nm lines are also used for ionospheric studies, where the latter is a favorite choice in satellite experiments [Ogo 4, IMAGE/FUV, TIMED/GUVI, COSMIC/TIP]. The earlier measurements of 135.6 nm are done from Ogo 4 [*Hicks and Chubb*, 1970; *Barth and Schaffner*, 1970], while ground based instruments are used to observe the 777.4 nm [*Tinsley*, 1966; 1972]. These allowed transitions of atomic oxygen are due to the radiative recombination of O$^+$ [*Hanson*, 1969; *Tinsley et al.*, 1973]. The reaction can be written as,

$$O^+ + e \xrightarrow{\alpha_1} O^* + h\nu \tag{2.11}$$

where α_1 is the rate of the radiative recombination (see Table 2.2). The excited oxygen atom (O*) gives rice to a 135.6 nm or 777.4 nm photon, depending on its particular energy level and the level to which the transition occurs. As illustrated in Figure 2.3, the 777.4 nm emission would occur if the excited oxygen is in the O(^{5}P) state and undergoes transition to the O(^{5}S) state, and the 135.6 nm is emitted when the oxygen atom transfers from O(^{5}S) state to the ground (O(^{3}P)) state.

In addition to the radiative recombination process, the ion-ion recombination between O$^+$ and O$^-$ is also found to excite oxygen atom to the corresponding energy levels [*Knudsen*, 1970; *Tinsley*, 1973]. The O$^-$ ions are produced through radiative attachment. The reactions are,

$$O + e \xrightarrow{k_1} O^- + h\nu \tag{2.12}$$

$$O^- + O^+ \xrightarrow{k_2} O^* + O^* \tag{2.13}$$

The loss of O$^-$ ions are given by,

$$O^- + O \xrightarrow{k_3} O_2 + e \qquad (2.14)$$

The volume emission rate for the 777.4 nm can be written as,

$$V_{777.4} = \alpha_1[O^+][e] + \frac{\beta_{777.4} k_1 k_2 [O][O^+][e]}{k_2[O^+] + k_3[O]}, \text{ and,} \qquad (2.15)$$

the volume emission rate for 135.6 nm,

$$V_{135.6} = \alpha_1[O^+][e] + \frac{\beta_{135.6} k_1 k_2 [O][O^+][e]}{k_2[O^+] + k_3[O]}, \qquad (2.16)$$

where, $\beta_{777.4}$, and $\beta_{135.6}$ are the fractions of the ion-ion recombination that result in the emissions of 777.4, and 135.6 nm, respectively.

It can be seen from equations (2.15) and (2.16), that the 777.4 and 135.6 nm lines also depend on the electron density. The contribution through ion-ion recombination in the nighttime is smaller compared to the radiative recombination [*Hanson*, 1970; *DeMajistre et al.*, 2004]. Since $[O^+]\approx[e]$ in the F2 region, the emission has a quadratic relationship with the electron density. Also, the radiative recombination process is independent of height, and hence the intensities do not vary significantly with the F-layer movements.

2.3.3 Barth mechanism: Emission of 557.7 nm

In the case of 557.7 nm, in addition to the dissociative recombination, there is an additional process of emission described as Barth mechanism (*Barth*, 1961, 1964). This process is responsible for the mesospheric component of this emission. In this method, two oxygen atoms, in presence of other neutral species, combine together to form an oxygen molecule, which undergoes collisions with other oxygen atoms to dissociate back to oxygen atoms. These oxygen atoms, if in the ^{1}S state, will result in 557.7 nm photons upon transition to the ground state. The reactions are given below.

$$O + O + M \xrightarrow{k_1} O_2(c^1\Sigma_u^-, b^1\Sigma_g^+) + M \qquad (2.17)$$

$$O_2(c^1\Sigma_u^-) + O \longrightarrow O_2(\mathrm{X}^3\Sigma_g^-) + O(^1S) \qquad (2.18)$$

$$O(^1S) \longrightarrow O(^1D) + 557.7nm \qquad (2.19)$$

where M represents a neutral species, and could be N_2, O_2, or atomic oxygen. In these reactions, the exact precursor state responsible for the production of O(^{1}S) is not known. Laboratory studies have shown that there are about six possible precursor states [*Bates*, 1988], and hence there is an uncertainty in the estimation of volume emission rate.

McDade et al. [1986], using simultaneous measurements of atomic oxygen density and the airglow intensity, derived a set of empirical parameters that can be used to describe the emission, without having any prior knowledge of the precursor state. The volume emission rate according to *McDade et al.* [1986] is given by,

$$V_{557.7} = \frac{A_5 k_1 [O]^3 ([N_2] + [O_2])}{(A_6 + k_5 [O_2])(C'^{O_2} [O_2] + C'^{O} [O])}, \qquad (2.20)$$

where, A_5 is the 557.7 nm line (O^1D-O^1S) transition probability, k_1 is the rate coefficient for the three body recombination of atomic oxygen, A_6 is the inverse radiative life time of O^1S state, k_5 is the quenching coefficient of O^1S state by O_2. C'^{O2} and C'^{O} are the empirical parameters provided by *McDade et al.* [1986].

It can be seen from equation (2.20) that the mesospheric 557.7 nm, unlike the other emission, is independent of electron density, and hence cannot be used for ionospheric studies. This emission, much stronger compared to the thermospheric component, contaminates the ground based measurements of the latter, and thus makes the 557.7 nm not very useful for ionospheric research. Nevertheless, this line is widely used to the dynamics and wave activities in the mesospheric region.

2.4 All Sky Imaging

The ESF irregularities are considered to be generated in the bottom side F region at the geomagnetic equator in the post-sunset period, and the regions of depleted plasma density grow non-linearly to the stable topside [Scannapieco and Ossakow, 1976]. In this process, the low-density plasma diffuses down along the geomagnetic field lines to low and mid-latitude regions, affecting the recombination reactions, and hence the airglow. The locations where the foot prints of these depleted flux tubes encounter the airglow emitting regions corresponds to a drastic reduction in the intensity, provided the emission is a function of the plasma density. The basic principle of all sky imaging is to take snapshots of the night sky using selected airglow lines that are related to ionospheric plasma density. When large scale irregularities associated with ESF are generated, the regions of reduced airglow would appear in these images as dark bands extending along the geomagnetic N-S direction. The name *plasma depletion* is related to this manifestation as dark bands of depleted airglow intensity.

Mende and Eather [1976] came up with a wide-angle instrument to study auroral emissions. *Weber et al.*, [1978, 1980] developed a similar system to study the equatorial airglow emissions. They conducted observations carrying the instrument on an aircraft, and reported depletion bands at 630.0 nm. *Mendillo and Baumgardner* [1982] described a ground base photographic method to image the airglow depletions. They used a 180° field of view (FOV) lens to achieve large spatial coverage required for the plasma depletion studies. The work reported here is carried out using an imaging system, which is developed based on the system described by *Mendillo and Baumgardner* [1982], at Physical Research Laboratory (PRL), Ahmedabad, India [*Raizada*, 1998; *Sinha and Raizada*, 2000; *Sinha et al.*, 2001].

The basic setup of an all sky imager consists of 180° FOV front end lens, a collimating arrangement, interference filters of desired wavelengths to isolate the emission from background, and an imaging optics to focus the beam to a detector, which is normally a CCD camera. The 180° FOV provides a large spatial coverage that helps the study of evolution and dynamics of large scale irregularities. At an altitude of about 250 km, this FOV is estimated to cover a hemispherical area of about 1800 km radius. The mapping of such a wide area into a circular image results in large compression at the edges of the images. Thus, any attempt to determine depletion parameters from such regions in the image could result in large errors. To avoid such situations, for all practical calculations, the imager FOV is restricted to 150°.

Narrow band interference filters are used to select the airglow emissions. Interference filter works on the principle of interference of light. The filter, a multi-layer thin-film device, consists of a set of thin films of high and low refractive indices with spacers or absentee layers between these sets. When the light beam is incident on the film, reflection and transmission occurs and the transmitted beam undergoes multiple reflections, and, interferes in the region between the film boundaries. The thickness of the film ($\lambda/4$) and the spacing between them ($\lambda/2$) are fixed such that only the wavelength λ satisfies the condition for constructive interference given by,

$$2\mu t \cos\theta = n\lambda , \tag{2.21}$$

where λ is the refractive index of the spacer, t is the thickness of spacer and n is the order of interference fringe. From equation (2.21), it can be seen that the wavelength transmitted by the filter will change with a change in the angle θ. The collimating lens is to make sure that the light collected by the system is parallel to the optical axis, so that near normal incidence with the surface of the filter is possible. Note that λ and t depends on temperature. Hence, in the environments where large fluctuations in temperature are expected, it is desired to use some mechanism to maintain uniform filter temperature.

The airglow emissions to be imaged are very weak, and hence the choice of the CCD camera is very important. The camera should have high quantum efficiency in the spectral region of interest, and should be capable for integrating the signal for a longer period of time. Thus the thermal noise of the CCD should be as low as possible, and the dynamic range should be high.

All sky imagers can be developed with relatively lower costs than that required for setting up radar, ionosonde, or lidar facilities, or conducting a rocket or satellite experiment. The imager offers a wide spatial coverage and provides two dimensional information about the evolution and dynamics of large scale irregularities that no other technique is capable of doing. Moreover, an imager system can be easily transported from one location to other location. One of the major drawbacks of the method is that uninterrupted monitoring of the ionosphere is not possible, and the observations are limited to dark, clear sky nights (free of moon, clouds, and any other light pollution) only.

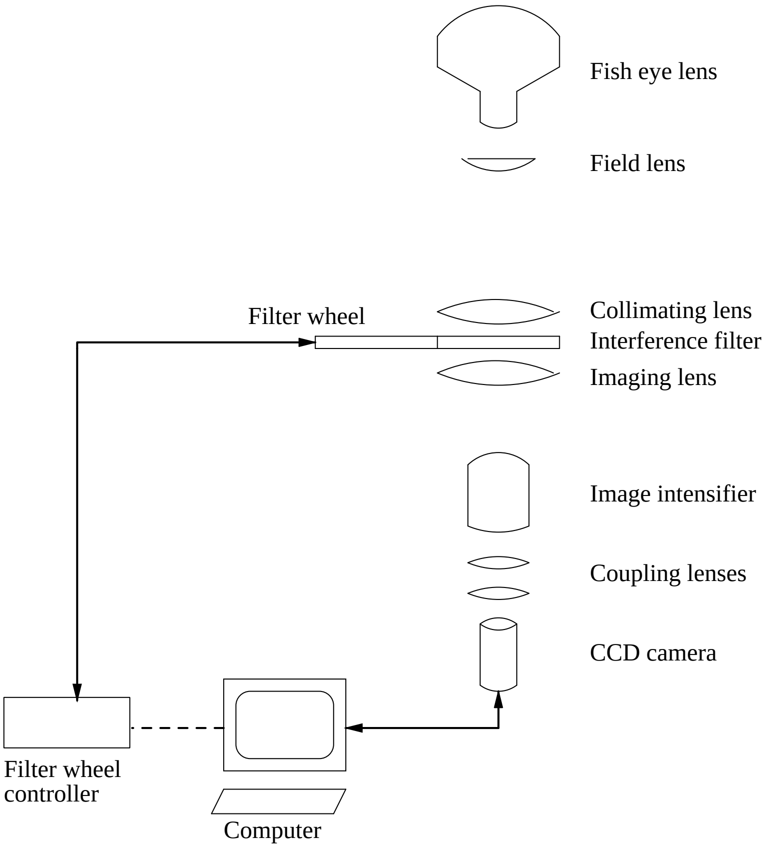

Figure 2.4 *The optical arrangement of the PRL all sky imaging system*

2.4.1 PRL All Sky Imager

The optical arrangement of PRL all sky imager is shown in Figure 2.4. A Nikkor 8mm, f/2.8, 180° FOV, fish eye lens is used to collect the airglow photons. The fish eye lens creates a circular image of 23 mm diameter at the film plane. The light beam from the fish eye is diverging in nature. A field lens is used to reduce the divergence of the beam so that all the rays pass through the interference filter. A 50 mm, f/1.2 plano-convex lens is used as field lens. The collimating lens is a 280 mm, f/2.8 lens of 100 mm diameter. The interference filters used are of 100 mm in diameter, and have a bandwidth of 1 nm. A filter wheel that can accommodate four filters is used to select the desired emissions. The 630.0, 557.7, and 777.4 nm wavelengths are used for the present study.

Since the emissions are very weak, the imager system uses an image intensifier to amplify the signal. An imaging lens, identical to the collimating lens, is used to focus the parallel beam from the filter to the input photocathode window of the intensifier, which converts the incident photons to electrons, forming an electrical image corresponding to the optical signal. These electrons are accelerated through a micro channel plate (MCP), wherein each electron gets multiplied several times by the production of secondary electrons at the walls of the MCP channels. The micro channel plate is in the form of a small disc of 0.48 mm in thickness and 25 mm in diameter, formed by fused glass fibers numbering in millions, each of which having a diameter of about 12 μm. The end surface of the intensifier is a phosphor screen, which re-converts the amplified electrical image to optical image. The intensifier output is transferred to the CCD camera using a combination of Nikkor 105 mm, f/1.2, and 24 mm, f/1.2 lenses. A 16 bit CCD camera from Starlight Express, which employs a thermo electric cooling, is used for recording the images.

2.4.2 Optical design details of the All sky Imager

The front end of All sky imager is a commercially available fish-eye lens (f/2.8, 8mm), used to image the sky, which makes an image of 23mm diameter at the image plane.

Four interference filters are used to select different emissions. Filter requires that the beam is parallel to the optical axis. Hence we need a collimating lens. In order to get best results, the maximum incident angle should be less than 3 degrees.

$(\Delta \lambda_{max} = \lambda \theta^{2}_{max} / 2 \mu^{2}$; for $\theta = 3^{o}$ $\Delta \lambda_{max} = 3 A^{o}$)

This requires that we must use a collimating lens of a large focal length to minimize the angle

[**tan(angle) = (23 mm) / (2*focal length)**]

If we consider angle to be 3 degrees, then the focal length of collimating lens should be at least 220 mm (or more for angle less than 3 degrees). Since we need to keep the angle well below 3 degrees, 280 mm is used. For f/2.8 optics, the diameter should be 100 mm. Hence we need to use 100 mm filters.

The 180 degree FOV of the fish-eye lens produces an image with beams of large divergence. Some of the diverging beams from the image plane of the fish eye lens could miss the collimating lens kept at about 280 mm. To minimize this, a field lens is used. A field lens reduces the divergence of the beam from the focus without losing flux.

The field lens should have the **f-number** as that of fish-eye lens, and its diameter should be at least as that of the image size produced by the fish-eye. Now, we use an **f/2.8** optics and the image size by the fish-eye is 23 mm. Thus, if we consider 23 mm as the diameter of the field lens, then its focal length should be,

f = 2.8*23 = 64.4 mm.

The field lens is kept at the image plane of the fish eye. Since the focal length of field lens is about 64 mm, and the collimating lens is kept at about 280 mm from it, the image magnification is about a factor of ~4 (280/64), which also comes to about 100 mm (for an image size of 23 mm). The angle of the rays after field lens is calculated using the diameter and focal length of field lens as:

Tan(angle) = (diameter of field lens (23 mm)) / (2*focal length (64 mm)).

Therefore the reduced divergence with Field lense = 10^{o}

Thus, the field lens reduces the 180 FOV of the fish-eye lens to a maximum divergence angle from the above calculation.

2.5 Image Geometry

It is often required to calculate the widths as well as velocity of plasma depletions from airglow images. For such calculations it is necessary to convert the pixel locations of depletions into distances in standard units from a reference point in the sky at the corresponding altitude of the emission. This can be done with the help of Figure 2.5, which shows the response curve of the fisheye lens provided by the manufacturer. The curve gives the relationship of the distance (y) in millimeters of any point in the image from the center, with the zenith angle (θ) of that point. Figures 2.6a and 2.6b illustrates the definitions of y and θ. The task at hand now is to determine y of any given pixel in the image, and then convert the corresponding θ from Figure 2.5 into distance in km or any other convenient unit. The first part (determining y), is straightforward and can be easily done knowing the physical size of an individual pixel, and, that the fisheye lens produces a circular image of 23 mm diameter.

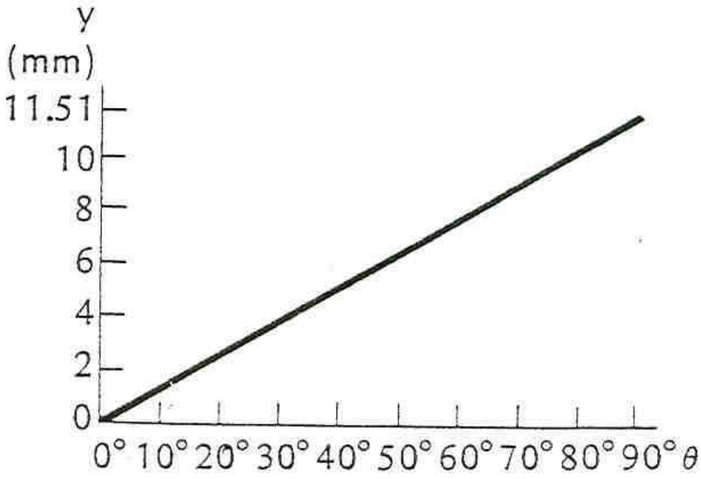

Figure 2.5 *The response curve of the fisheye lens, provided by the manufacturer showing the relationship between distance from the center of the image and zenith angle.*

The second part, i.e. of converting θ into distance can be done by considering the geometry shown in Figure 2.7. *I* is the location of the imager, *D* is the depletion, *O* is the center of the earth, and *d* is the distance to be determined. From the geometry, it can be seen that the arc length *d* can be calculated if the angle ϕ is known. Applying the law of sine's to ΔOID,

$$\frac{R_E + h}{\sin(180 - \theta)} = \frac{R_E}{\sin(\theta - \phi)} \tag{2.22}$$

The equation (2.22) can be used to calculate ϕ, and hence the distance d. The only assumption required in this calculation is the value of *h*, which is the mean altitude of the emission layer.

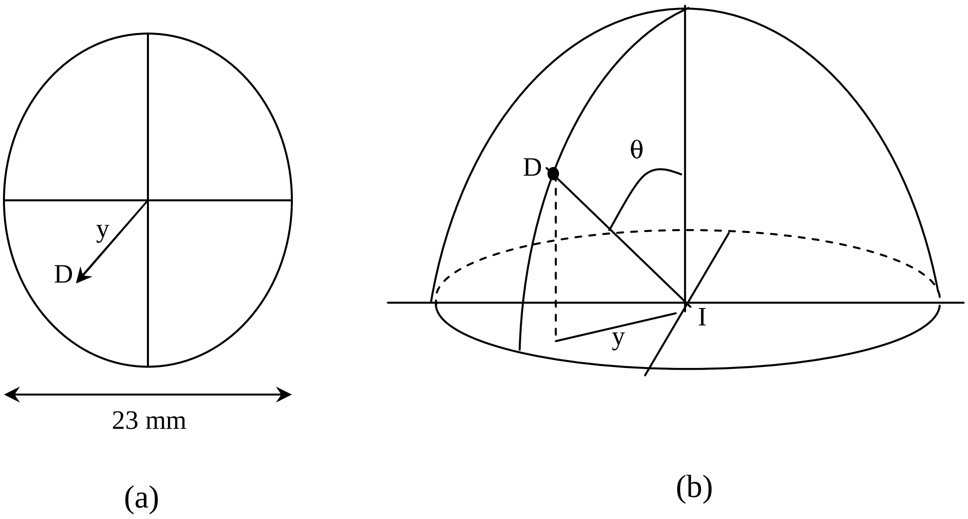

Figure 2.6 (a) Distance of a point from the image center. (b) The corresponding zenith angle.

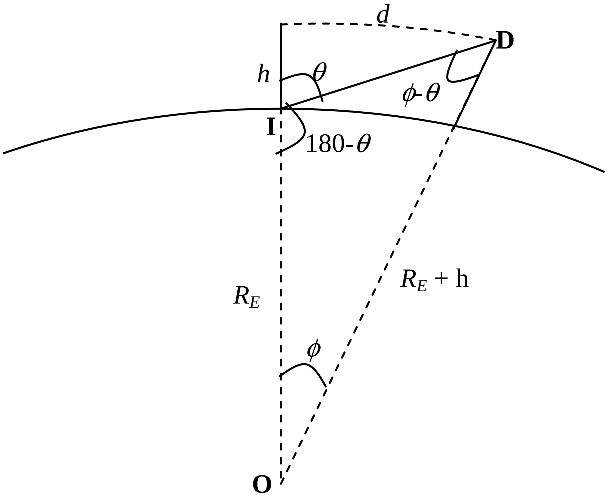

Figure 2.7. converting θ into distance can be done by considering the above geometry shown

As mentioned above, the all sky imager uses three airglow emissions, 630.0, 557.7, and 777.4 nm, to take the images of the night sky. However, these emissions are not from the same altitude region. While 630.0 nm has its peak altitude around 250 km altitude, the 777.4 nm is mainly from the F-peak altitude of about 350 km. The spatial coverage of the instrument at the two altitudes regions is thus slightly different. Figure 2.8 gives a sketch of the observing geometry of the all sky imager for the 630.0 nm airglow. The geometry is drawn for the observation site at Kavalur. The 180° degree FOV covers approximates 17° S to 28° N latitudes for the 630.0 nm layer centered at 250 km altitude. The figure also gives the magnetic field-lines over the observing site, showing their corresponding apex altitudes. It can be seen from the figure that the low density flux tubes that produce depletions at the north most edge of the image corresponds to an altitude of about 1800 km over the magnetic equator. Note that the wide FOV of the fish eye lens results in large compression at the edges of the images. Hence in the calculations, the usable FOV is restricted to only 150°. The spatial coverage of the imager at 100, 250, and 350 km altitudes are given in Table 2.3.

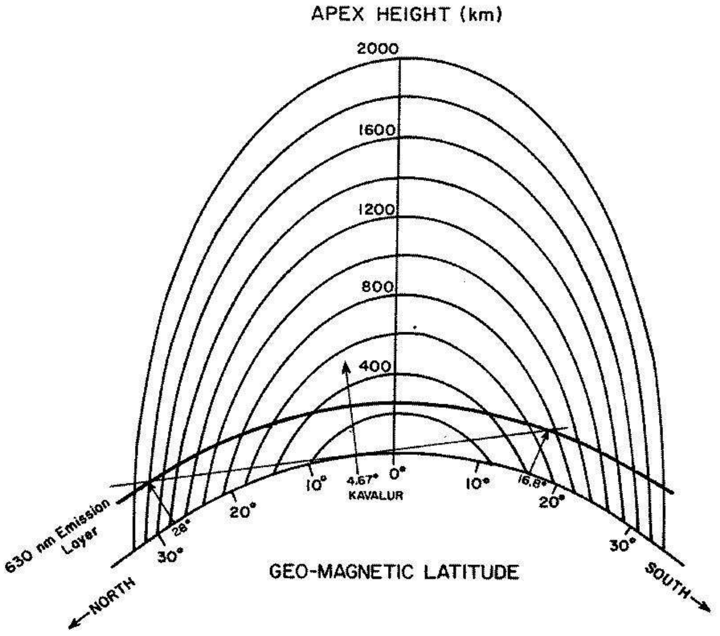

***Figure 2.8** Viewing geometry of the all sky imager at Kavalur. The vertical arrows denote the center, as well as the north and south edges of the FOV, for a 180° observing geometry. The thick dark curve is the 630.0 nm airglow layer centered at 250 km and the thin curves are the magnetic field lines.*

Table 2.3 The spatial coverage of the all sky imager for 100, 250, and 350 km altitudes.

Emission lines	*Altitude of bulk emission*	*Spatial extent of the instrument*
557.7 nm	100 km	2275 km
630.0 nm	250 km	3640 km
777.4 nm	350 km	4340 km

Based on the observation geometry explained above, the spatial resolutions of the imager at the center as well as for a zenith angle of 75° are calculated. For an airglow layer at 250 km altitude, one pixel of the CCD camera used for the observations in 2002 can resolve structures with horizontal scale of about 2 km or less at the center of the image and about 10-12 km at 75°. At an altitude of 350 km, the corresponding resolutions are about 2 km and 16 km, respectively.

2.6 Image Analysis

The data analysis is mainly done using the softwares Image Reduction and Analysis Facility, IRAF developed by Smithsonian Astrophysical Observatory (SAO) and also using Interactive Data Language (IDL) by Visual Information Solutions. In a CCD, the response of different pixels for a uniform light is not similar. That is, there will be always a pixel to pixel variation in the value of the signal recorded for a uniform input. This arises due to the inherent error associated with each pixel. Hence flat fielding was done to correct this pixel defect. For this, a frame was generated, by exposing the CCD using a uniform light. An image having same pixel value throughout was divided by this image, and a flat fielding frame was thus generated. This value was selected by taking the average of the maximum and minimum pixel values in the frame generated using the uniform input. All images were multiplied using this flat fielding frame.

These images were then corrected for the image intensifier noise and dark current of the CCD. For this a frame with same exposure time as the data frame was taken, keeping the fish eye lens covered, which is with cover on. This frame was subtracted form each data frame to remove the system noise. The next step was to remove the constant background noise. This was done by averaging all data frames and subtracting each frame from this averaged frame. By this process, constant features in the image such as building lights etc. gets subsided, thus enhancing the depletions. This also compensates for the Van Rhijn and vignetting effects. (Ref. Mendillo and Baumgardner, JGR, 1982,87, 7641-7652).

The 16 bit digitiser is capable of detecting an intensity variation of about 0.02%. To utilise the full intensity levels provided by the digitiser, the frames were subjected to histogram equalisation. The geographical N-S and E-W of these images were disoriented by about 20^o from the perpendicular axes that pass through the center of the image. Hence, to rectify this, the images were rotated by 20^o. These images were then further analysed to calculate various parameters, such as degree of depletion, drift velocity, orientation and tilt of depletions, their E-W and N-S extent, width of depletions and spacing between depletions etc.

The ESF irregularities are generated over magnetic equator and grow vertically upward by non-linearly to reach very high altitudes. In this processes, the low density flux tubes are distributed along magnetic field lines to low latitudes. Thus, imaging observations in the post-sunset period conducted over a station near the equator gives the details of the depletions at or immediately after their generation. On the other hand, observations from off-equatorial stations are useful to study the features of well developed depletions. In the present analysis, images taken at two different locations, one over a low-latitude station Mt. Abu, and other one over the equatorial station Kavalur are used. This chapter gives the details of the observations at both the stations and the steps used to analyze the images.

3.1 Observations at Mt. Abu

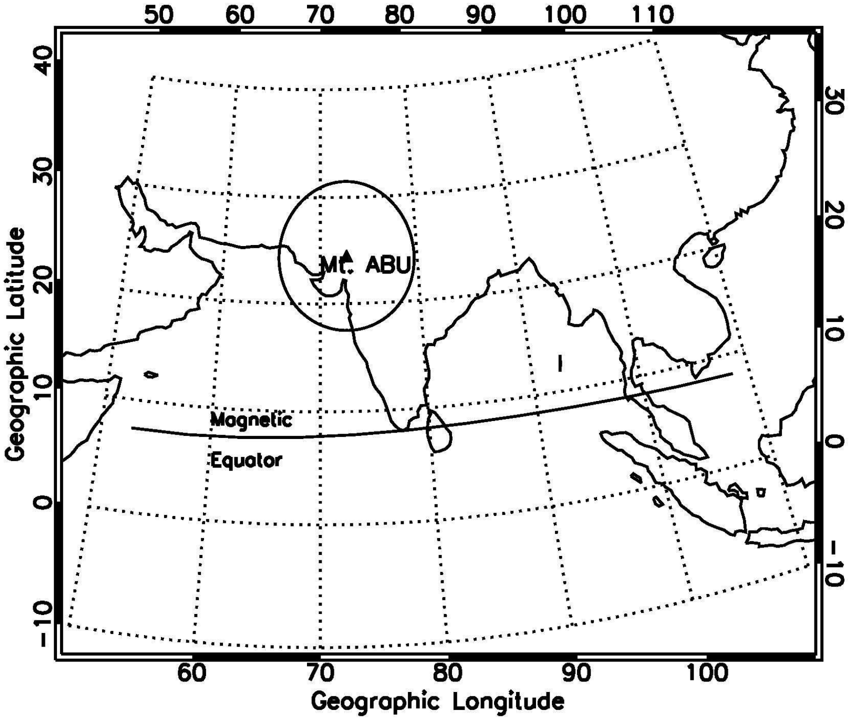

Figure 3.1 *The coverage of the all sky imager and observation geometry at Mt. Abu for the observations in 1999. The circle gives the approximate FOV assuming an emission altitude of 250 km, for a zenith angle of 75°. The dark line denotes the geomagnetic equator.*

The PRL's all sky optical imaging system was operated from Mt. Abu (24.5°N, 72.7°E, 18.5°N Magnetic) during 12-18 April 1999. The images were taken using 630 nm emission line. Observations start after the local sunset and continue till local moonrise, depending on the sky conditions. Normally observations are taken with 15 minutes interval between consecutive exposures. An exposure time of 30 seconds was used in the present experiment. From a low latitude station like Mt. Abu, it is possible to study the movement of the northern end of the plasma depletions. In principle the all sky imaging system is capable of covering 180° field of view (FOV). But in calculations, the actual FOV was restricted to ±75° from zenith to minimize the possible errors at the edges of the FOV. Figure 3.1 gives the observation geometry and the coverage of the all sky imager centered at Mt. Abu.

In general, the observations start around 1930-2200 LT, immediately after the local sunset. During the observations at Mt. Abu, the CCD camera was not available, and hence an SLR camera with photographic film was used to take the images. Thus, each frame was taken manually, and after each exposure, the film is advanced to take the next frame. The observations were continued until about 0000-0100 LT, depending on the moonrise time. Though imaging was carried out during 12-18 of April 1999, out of the 5 nights, plasma depletions were observed on two nights, 14th and 15th April 1999. The days were geo-magnetically quiet.

Since the images at Mt. Abu are taken using an SLR camera, the image analysis is very sophisticated. First, the photographic films are carefully washed. The developed negatives are then digitized to convert the data to electronic format. This process was done using the digitizer at the Udaipur Solar Observatory. Note that, as described in section 2.6, while taking the observations, cover images are taken at specific intervals to remove the system noise. The digitized images are then processed to remove such system noise as well as background contamination. Here, one major disadvantage is that the locations of the center of the image in individual images do not coincide. This is because, while digitizing, the photographic film is manually advanced frame by frame. In this process the individual frames do not necessarily align with the light source in the same as the previous or next frame, and there will be a slight offset in the location of the center pixels.

Thus, to carry out further image analysis of the Mt. Abu images, each image has to be checked manually, and the center pixels of the circular image caused by the airglow is determined. This is done in IRAF. First, a circle is drawn so that it coincides with the image, and its center locations and radius are noted. This is repeated for each frame taken in a given night. Once the process is completed, a reference center location is determined and each frame is processed so that it center is now the reference center. This makes sure that the center of all the images taken in one night is now aligned, and that further image analysis such as averaging, subtraction, etc. could be carried out. The entire process is repeated for all the 5 nights. Later, these images are analyzed to derive information of the images such as the scale-size, velocity, etc. A detail description of the observation, digitization, and image analysis for an imaging system using photographic film is given in the Ph.D. thesis of Shikha, 1999.

3.2 Observations from Kavalur

Though in the initial stages the all sky observations were take using photographic films, the PRL's imaging system was subsequently modified and updated using CCD camera. With the inclusion of the CCD camera, the observation as well as image analysis became much simple. The software that controls the CCD camera is used to run the all sky camera in a semi-automated mode. And, since the images are directly stored in electronic format, the center locations are identical for all the images, as long as the position of the imaging system is not disturbed. This simplifies the operation as well as analysis in a great way. Though a CCD camera was incorporated with the PRL all sky imager in 1998, unfortunately it failed during one of the observation campaigns in 1999. A replacement camera could be purchased only by the end of the year 2001. With the arrival of the new camera, the all sky imager optics was modified to suit the new camera and the system was made ready to conduct observations in early 2002. Further improvements were made in the optical alignment and image quality. Meanwhile, a computer controlled filter wheel mechanism was also introduced, which made it easier to employ multiple filters with minimum manual operation. This time, it was decided to carryout observations from Kavalur (12.5° N, 78.8° E, 4.6° N Magnetic), which is an equatorial station from where the depletions at their formative stages could be imaged.

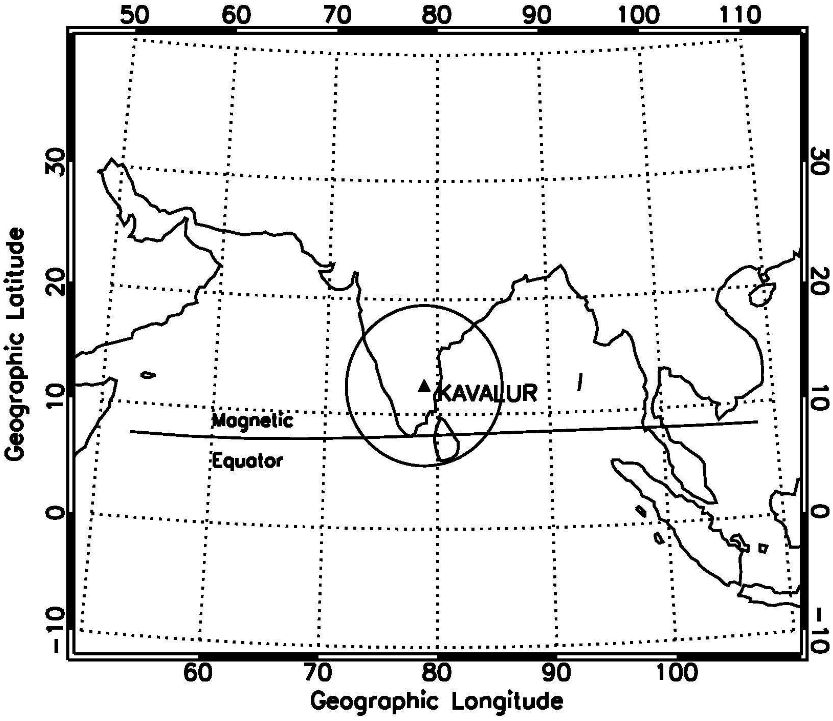

Figure 3.2 *The coverage of the all sky imager and observation geometry at Kavalur for the observations in 2002. The circle gives the approximate FOV assuming an emission altitude of 250 km, for a zenith angle of 75°. The dark line denotes the geomagnetic equator.*

Figure 3.2 gives the geometry and the FOV for the observations from Kavalur. It can be seen that the southern end of the imager covers the locations just to the south of the magnetic equator. Thus, it is possible to observe depletions, whenever they develop to the sensitive range of the spatial and intensity scales of the imaging camera. The images were taken using 630.0, 557.7, and 777.4 nm emissions, with exposure times of 60, 30, and 120 seconds, respectively. Interference filters of 1 nm bandwidth were used to isolate the emissions from the background. Each filter is repeated approximately in every 10-15 minutes, and observations are taken in each night depending on the sunset and moonrise times. Since the probability of ESF irregularities as well clear weather conditions are suitable in the February-April period, observations are conducted during this interval.

Table 3.1 *Details of observations from Kavalur during February-April 2002*

Month	Nights of observations	Depletions in 630.0 nm	777.4 mm	557.7 nm
February	10	4	4	3
March	12	12	10	8
April	11	11	11	8
Total (%)	33 (100 %)	27 (81%)	25 (75%)	19 (57%)

The all sky imager of PRL was operated from Kavalur during the months of Februry-April, in the year 2002. In this period, the imager was operated for 33 nights, with 10 days of observations in February (6-16), and 12 days in March (4-17), and 11 days in April (5-15). Out of this, depletions were observed in the 630.0 nm images in 27 (~80%) nights and in the 777.4 nm about 25 (~75%) nights. Also, about 19 (~57%) nights there were depletions in the 557.7 images also. The details of the imaging observations from Kavalur in 2002 are summarized in Table 3.1. It is rather unusual that depletions were observed in 630.0 nm in 11 consecutive nights of March (4-14), and April (5-15). About 70% (19/27) of the nights with depletions in 630.0 nm also had depletions in 557.7 nm images. The bright mesospheric 557.7 nm emission generally makes it difficult to observe the F-region signatures in ground based observations.

The observations in 2002 from Kavalur were remarkable in that there were several nights with intense depletions. Moreover, depletions appeared in all the three wavelengths in some of the nights. The generation of irregularities could be more during geomagnetic disturbances. Also, in the solar maximum year of 2002, magnetic disturbances could be frequent. In order to check the magnetic conditions during the period of observations in 2002, the Kp and Dst indices during Februay-April in 2002 are plotted in **Figure 3.3**. It can be seen from the figure that there is no significant geomagnetic activity during the observation period. The only magnetic disturbance in this period occurs after the observation in March is over, and the activity becomes normal well before the observation in April begins.

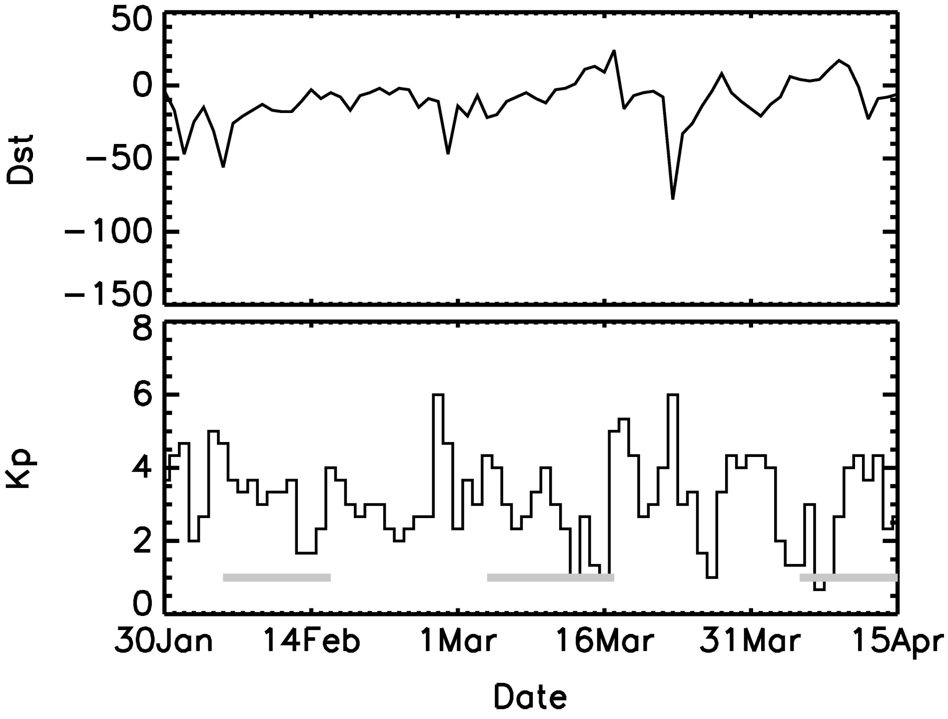

***Figure 3.3** The Dst (top panel) and Kp (bottom panel) indices during February-April, 2002. The Dst plotted here are the daily average values, and the Kp values are the maximum value recorded in a 24 hour period. The values are taken from the national geomagnetic data center (NGDC). The shaded horizontal bar in the bottom panel represent the duration of imaging observations in each month in this interval. Note that there are disturbed conditions immediately before or during the experiment.*

The images were taken at every 10-15 minutes interval using the 630.0, 557.7 and 777.4 nm airglow lines, with exposure times of 60, 30, and 120 seconds, respectively, when clear sky conditions were available between sunset and moonrise. Though several hours of the night are imaged in different days, depletions do not appear over entire period. Their occurrence varies from night to night. Also, it is different for each wavelength used. To give an idea of the period of observations in each night, as well as the duration for which depletions appear, the summary plots of observations and depletions are generated for each wavelength, whenever depletions appear. **Figure 3.4** gives the details of the depletions observed in 630.0 nm. Three different shades of gray are used to denote depletions (light gray), no observation (medium gray), and no depletions (dark gray). The Y-axis is the days when depletions are observed. The X-axis is the time of observations with an offset of 18 hours. Thus, 0 on X-axis corresponds to 1800 LT, and 12 correspond to 0600 LT on the next morning.

Kavalur

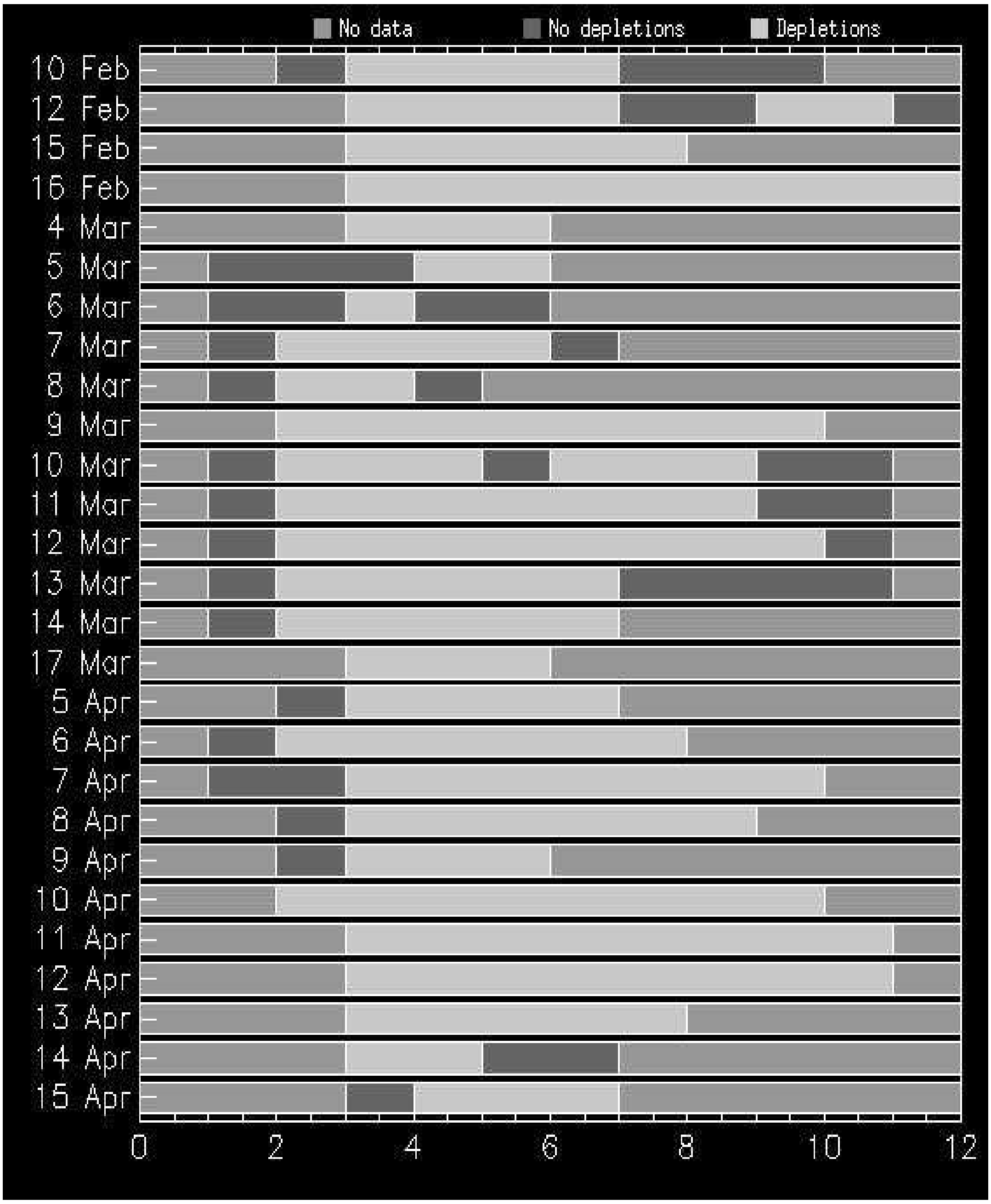

Figure 3.4 *The details of the hours of night for which depletions are observed in 630.0 nm during February-April, 2002. Three different shades of gray are used. The light gray shade denotes the period for which depletions appear in the images. The medium shade of gray corresponds to the period of no observation. The dark gray shade represents the period when imaging was conducted, but no depletion appeared in the images. The Y-axis is the days when depletions are observed in 630.0 nm. The X-axis is the time of observations with an offset of 18 hours. Thus, 0 on the X-axis corresponds to 1800 LT on the corresponding day and 12 correspond to 0600 LT on the next morning.*

Kavalur

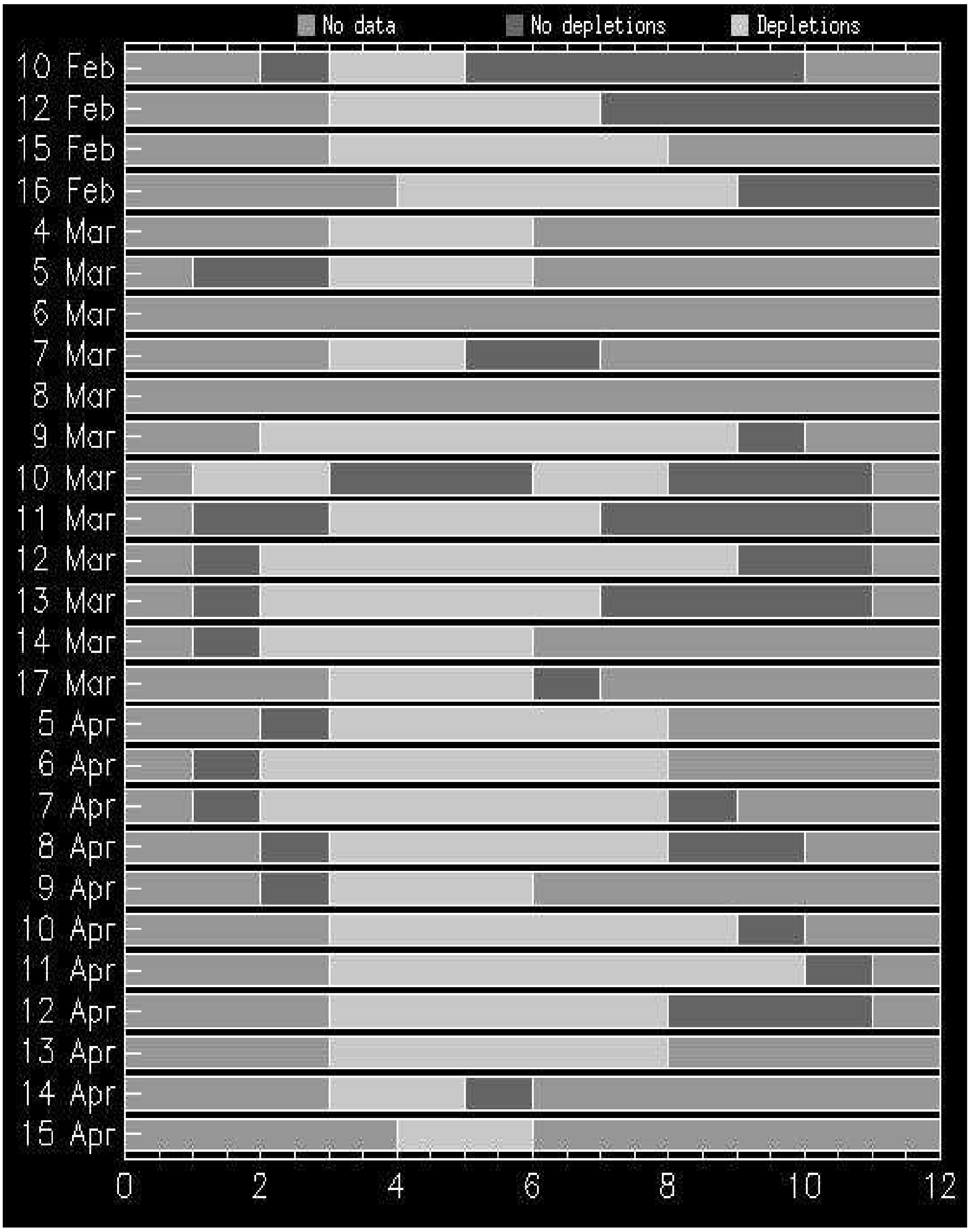

Figure 3.5 *The details of the hours of night for which depletions are observed in 777.4 nm during February-April, 2002. Three different shades of gray are used. The light gray shade denotes the period for which depletions appear in the images. The medium shade of gray corresponds to the period of no observation. The dark gray shade represents the period when imaging was conducted, but no depletion appeared in the images. The Y-axis is the days when depletions are observed in 630.0 nm. The X-axis is the time of observations with an offset of 18 hours. Thus, 0 on the X-axis corresponds to 1800 LT on the corresponding day and 12 correspond to 0600 LT on the next morning.*

Kavalur

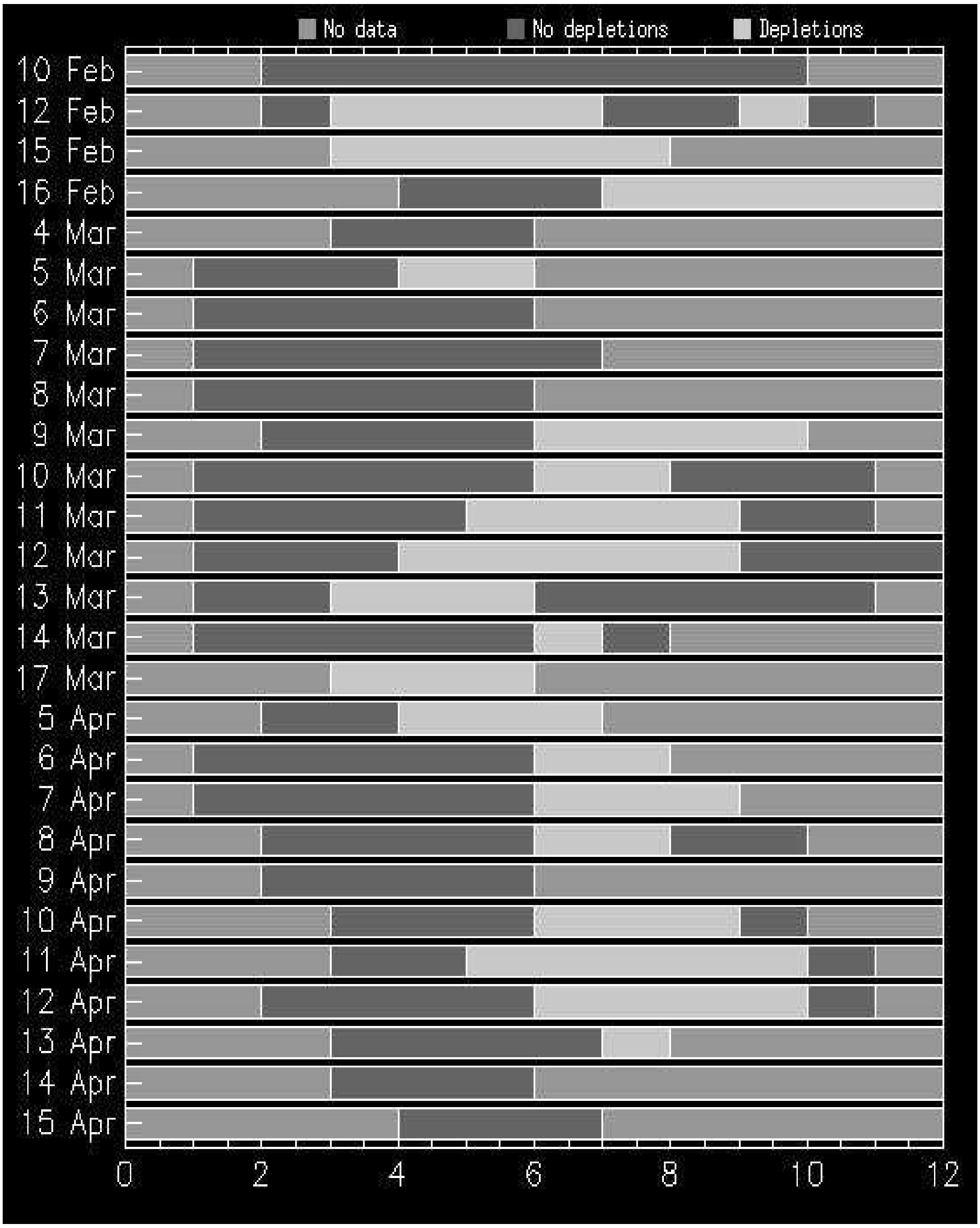

Figure 3.6 *The details of the hours of night for which depletions are observed in 555.7 nm during February-April, 2002. Three different shades of gray are used. The light gray shade denotes the period for which depletions appear in the images. The medium shade of gray corresponds to the period of no observation. The dark gray shade represents the period when imaging was conducted, but no depletion appeared in the images. The Y-axis is the days when depletions are observed in 630.0 nm. The X-axis is the time of observations with an offset of 18 hours. Thus, 0 on the X-axis corresponds to 1800 LT on the corresponding day and 12 correspond to 0600 LT on the next morning.*

Similarly, Figure 3.4 gives the hourly details of the depletions in 777.4 nm images and Figure 3.5 gives that of the depletions in 557.7 nm. It can be seen that the depletions in 630.0 nm appear around 2000 LT in most of the nights. Further, in several nights the depletions are seen well beyond the post-midnight period. Note that in the night of 16 February 2002, depletions are imaged till sunrise hours. In the case of 777.4 nm also, the depletions appear around 2000 LT or earlier. However, there are only very less number of nights when they persist till post-midnight period. In most of the cases, depletions are not imaged beyond midnight. The appearance of depletions in 557.7 nm is slightly different from the other two emissions. In this case, the depletions start appearing only around 2300 LT or later. However, similar to the 630.0 nm, they persist well into the post-midnight hours.

The analysis of the CCD based Kavalur images are less sophisticated than the images at Mt. Abu. However, the nights with depletions are much more in this case. The raw images were first corrected for the system noise. For this, cover images were taken by keeping the fisheye lens covered with the same exposure times used for different filters. The cover image was subtracted from each image to remove system noise. The background noise was removed by subtracting the average of the images taken in about 1 hour period from each of the corresponding images. In the average images, stationary features such as background noise, station light, etc. are retained, while non-stationary features such as the intensity variation due to depletions are smoothened out. Thus, subtracting the average image removes the background noise from the images, and enhancing the depletions. After the noise subtraction, the images are displayed so as to have the best possible contrast.

3.3 Apex mapping

Equatorial Spread-F (ESF) irregularities in the nighttime ionosphere manifest as dark bands of reduced intensity in all sky airglow images, known as plasma depletions [Weber et al., 1978]. It is generally understood that the depletions elongate to low- and mid-latitudes depending on the upward (vertical) movement of the irregularities at the equator [Weber et al., 1978; Mendillo et al., 2005]. The less density plasma associated with the irregularities when transported along the geomagnetic field lines to off-equatorial latitudes modifies the airglow intensities, and result in North-South (N-S) aligned depletions. Thus, as the irregularities rise above the equator to higher altitudes, the flux tubes extending to lower altitudes and low latitudes will have less plasma density. At the locations of these low density flux tubes, the photochemistry also will be affected, resulting in less airglow emission, and produce plasma depletions in all sky images.

Thus, when the irregularities are driven to more and more altitudes at the equator, the latitude extension of the depletion also increases. The latitude extent of the depletion depends on the maximum altitude of the bubble above the equator [Mendillo et al., 2005]. In other words, a time sequence of images depicting the poleward extension of the edge of plasma depletion actually represents the vertical upward movement of the irregularities above the equator. This poleward extension of depletions in all sky images can hence be used to understand the vertical movement of the irregularities above the equator. This is done by mapping the latitude of the poleward end of depletion along the field line back to the corresponding altitude at the magnetic equator. This process of finding the altitude of the bubble above the equator is known as apex mapping. For apex mapping, observations conducted from a low latitude station such as Mt. Abu are more suitable. The northern limit of the plasma depletions can be mapped back to the corresponding altitude attained by the depletions at the equator with the help of the International Geomagnetic Reference Field (I.G.R.F.) Model. Detailed illustration of apex mapping is given below.

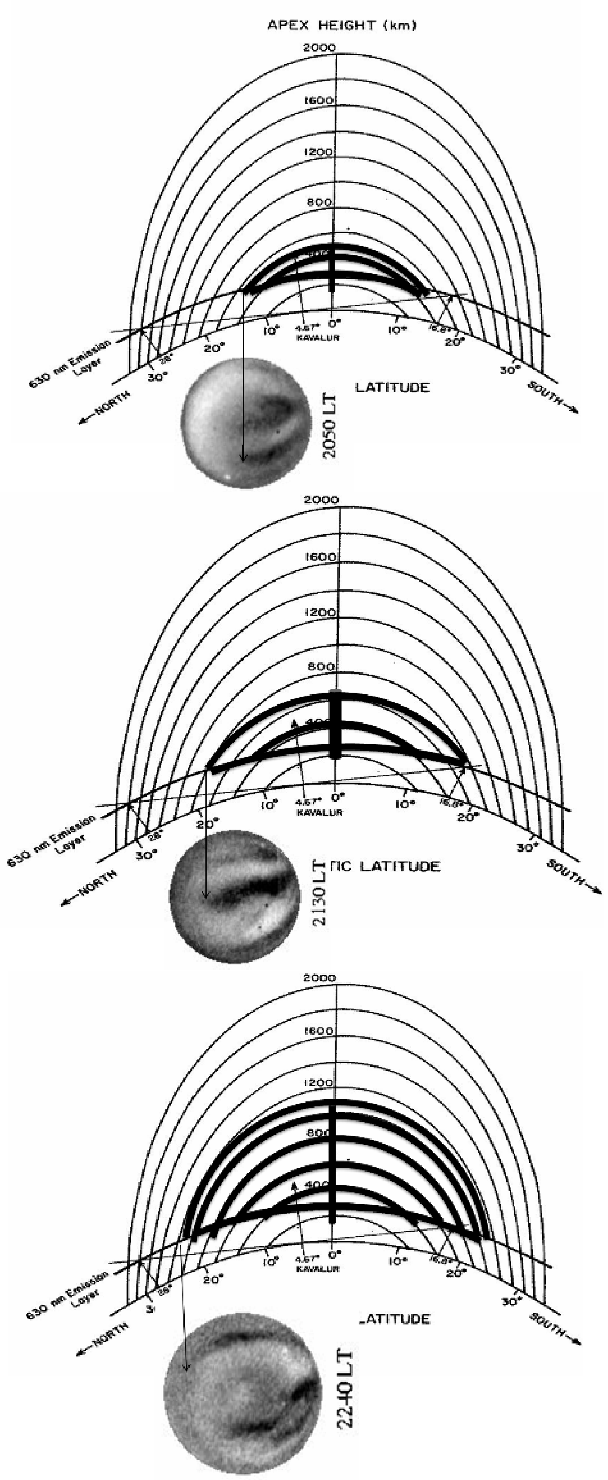

__Figure 3.7__ Illustration of apex mapping. Sketch of magnetic field geometry is used. The depletion is at different stages of vertical motion in the selected images. The thick dark lines over the field line geometry denotes the vertical motion of the bubble, and the associated latitudinal extension. When the bubble reaches higher altitude, depletion grows to more northern latitudes.

In Figure 3.7, the top panel represents the case after sunset when the bubble the bubble develops. The low density plasma regions grow to the topside non-linearly by the action of polarization electric field. The plasma bubble is denoted by the thick dark vertical line over the equator. As the bubble move upward, the low density plasma regions are distributed to lower latitudes along the field line as indicated by the thick black curves plotted over the field lines. In the top panel, an example for the image taken at 2050 on 14 Aril 1999 from Mt. Abu is shown. The depletion is seen almost above the center of the image here. In the second panel, the image taken at 2130 LT is shown. Here the bubble already moved to much higher altitude above the equator. Consequently, the dark regions of low plasma density also extends polewards, causing the depletion in the image to be seen extending Northward. Similarly, in the third panel at 2240 LT, the bubble rises to much higher altitudes over the equator. In this case it reaches about 950 km, and the corresponding latitudinal limit is about 23.1 N.

Thus, by noting the poleward latitudinal limit of depletion in a sequence of images, it is possible to map back the corresponding field line and estimate the maximum altitude the bubble might have reached at the equator for each of the image taken. Using this time series data of the altitude above the equator, the vertical velocity of the bubble above the equator is calculated.

Chapter 4. Characteristics of Plasma Depletion over Indian Region

Plasma depletions appear as dark bands of reduced intensity in all sky airglow images. They usually align along magnetic field lines, and drift eastwards with velocities of about 100-150 m/s in the evening hours. The depletions often show 50-60% reduction in intensity, and could be about a few 100 km wide along East-West direction. Along the North-South direction, the structures could elongate over 1000 km, where the poleward limit depends on the maximum altitude attained over the equator. In this chapter, the general characteristics of plasma depletions observed over Indian region are discussed. The observations carried over equatorial as well as off-equatorial stations are used to demonstrate different features of depletions with their evolution.

4.1 All sky observations over India

The first results of all sky airglow imaging of plasma depletions over Indian region was reported by Sinha *et al.,* 1996. The observations were carried out using the all sky imager developed at Physical Research Laboratory, Ahmedabad, India, from Shriharikota rocket range (SHAR) (14° N, 80° E, 5.5° dip latitude), and depletions were observed in the images taken using the 630.0 and 777.4 nm emissions. They showed that the depletions in airglow images are accompanied by intense spread-F in ionograms, as well as strong VHF scintillations. Further detailed analysis of the observations is reported by Sinha and Raizada [2000], giving morphology of the depletions, relation with magnetic activity, and occurrence of brightness patterns. The depletions showed eastward drift in the range 40-190 m/s, and their east-west dimension varied from about 100 km to over 800 km. They noted that shallower depletions have smaller width compared to steeper ones. Another early, but independent, observational campaign was carried out by Mukherjee *et al.,* 1998, using 630.0 nm images from the low latitude station Kolhapur (16.8° N, 74.2° E; 10.6° N dip latitude). Their results in general agreed with that described above.

Using multi-wavelength all sky observations from low latitude station Kavalur (12.5° N, 78.8° E, Mag. Lat 4.6° N), Sinha *et al.* [2001] discussed several important features of plasma depletions. They showed that, starting with different initial as well as background conditions, depletions tend to take about 2 hours 40 minutes to come to a fully developed state after the onset of ESF in ionograms. Further, they classified depletions into three distinct types based on the east-west extent and inter-depletion distance, and pointed out that the existence of different types indicate the involvement of different seeding agencies in the development of the instability process. In their work, they reported the first observation of depletions in 557.7 nm images over the Indian region on a magnetically disturbed night. They noted that on that particular night, depletions were first seen around 2130 LT in the 777.4 nm images. In the 630.0 nm images, depletions were visible about 1 hour later and after about another 45 minutes the depletions appeared in the 557.7 nm. They attributed the time difference in the appearance of depletions to prompt penetration as well as disturbed dynamo effects associated with the magnetic disturbance. Another important feature reported in their work was the occurrence of brightness patterns in all the three emissions. In a separate study Mukherjee *et al.* [2002] showed the observation of depletions during the periods of reversal of EIA.

The results reported here are carried out using the PRL's all sky imaging system. The observations were conducted in April 1999 from Mt. Abu (24.5^{o}N, 72.7^{o}E, 18.5^{o}N Magnetic) using 630.0 nm as well as those carried from Kavalur (12.5° N, 78.8° E, 4.6° N Magnetic) during February-April in 2002 using 557.7, 630.0, and 777.4 nm emissions. The individual images in each night are first processed to remove system noise. Then further processing is carried out to remove the background noise. The images are later subjected to contrast enhancement, cropping of outer areas, and then rotation by a suitable angle so that the depletions align along North-South direction. The effects of system noise removal, background subtraction, as well as the contrast enhancement and orientation on a raw image are illustrated in Figure 4.1. It can be seen that the raw image appear more intense, but the features of depletion is not clearly distinguishable. Here it must be noted that though the depleted region is easily visible in the raw image in Figure 4.1, in many other cases depletions are barely identifiable from the raw images. After system noise removal, the overall intensity reduces, but the depletion can be better recognized. The background removal process causes the image intensity to reduce further. However, the depletion is well defined in this image, and multiple depletions can be identified in this image. The next step is to enhance the contrast of the image so that each of the depletions could be analyzed to extract required information from them. In the example given in Figure 4.1, the contrast is enhanced so that the borders of the depletion at the center of the image are well defined. Note that in this step, the portions that lie outside the circular image formed by the fisheye lens are also cropped.

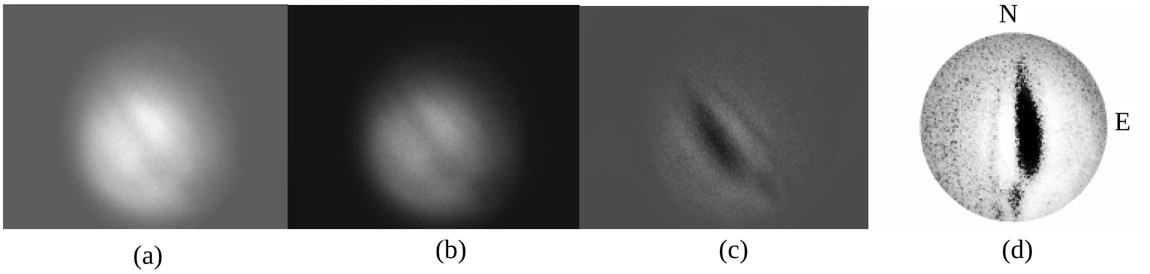

Figure 4.1 *The effect of different stages of image processing; (a) raw image at 630.0 nm taken in the night of 16 February 2002 at 0326 LT, (b) the image after system noise correction, (c) after background removal, and (d) the final image with proper orientation, after contrast enhancement and cropping the portions outside the circular image formed by the fisheye lens. Here North is upward and East is to the right.*

After a series of such complicated processing steps, the images in each night are organized as a time sequence for further analysis to extract different features of plasma depletions. Figure 4.2 gives an example of the series of 777.4 nm images taken in the night of 12 February 2002. In this night the observations could be started only after 2130 LT since the Moon set was after a couple of hours of the Sun set. The 777.4 nm images show multiple depletions in the images, extending the entire FOV. The depletions could be seen till midnight in this night, and it disappears thereafter. Figure 4.3 displays the sequence of 630.0 nm images taken almost simultaneously in the same night. The images also show depletions similar to that in the 777.4 nm images. It can be seen that the depletions in the 777.4 nm images appear more narrow compared to that in the 630.0 nm. The sequence of 557.7 nm images taken in the same night is shown in Figure 4.4. Note that in these images, depletion is clearly seen only after 2300 LT.

The examples given here demonstrate the irregularity process occurred in this night, resulting in the generation of depletions in all the three emissions. It should be noted that the depletions in this night were not very intense compared to many other

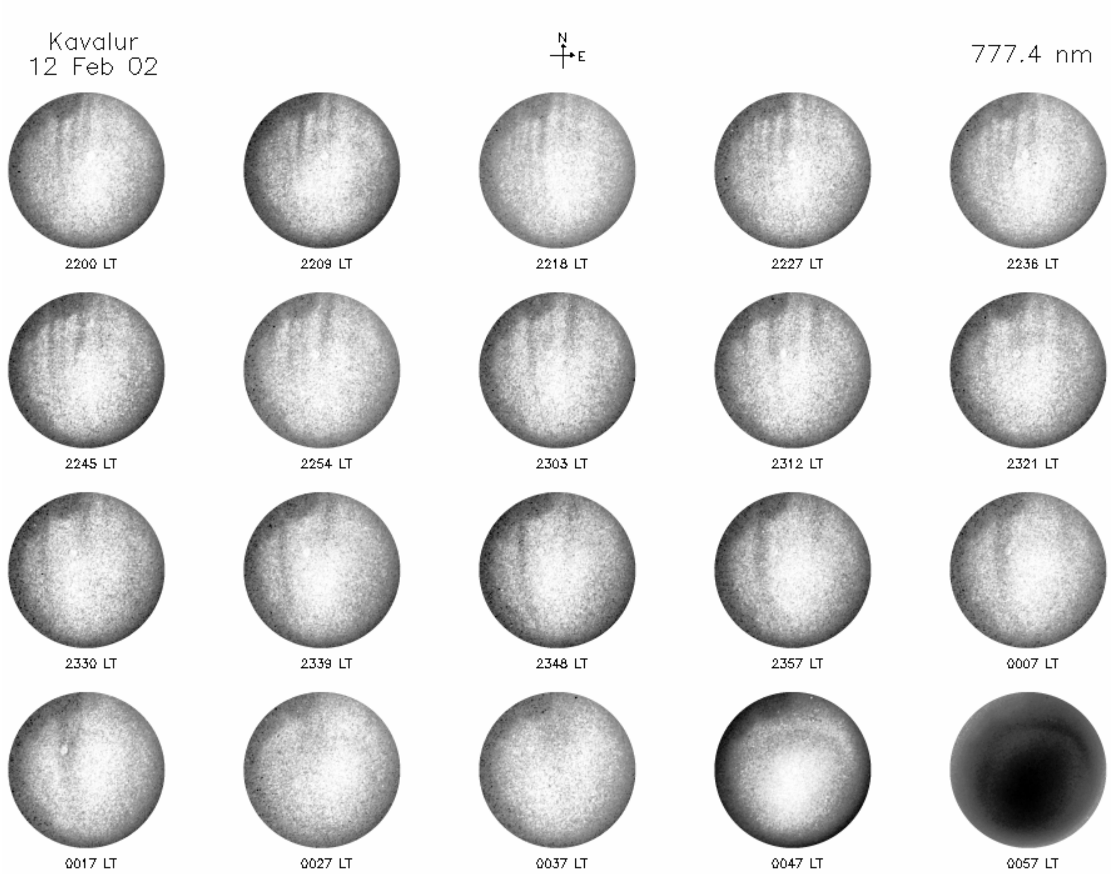

Figure 4.2 *A sequence of 777.4 nm images taken in the night of 12 February 2002*

cases observed in this period. Further, the depletions in this night weakened after midnight, and disappeared thereafter. However, it is worth to note that the depletions continued to occur in 630.0 and 557.7 nm images for several minutes even after their disappearance in the 777.4 nm images. Thus, one major different among the three wavelengths are that, the depletions first appear very distinct in the 777.4 nm images. However, towards the midnight or in the later part of the night, they are weaker in the 777.4 nm, but still continue to appear strongly in the 630.0 and 557.7 nm images. The major reason for this difference could come from the intrinsic nature of the emissions itself. The 777.4 nm comes from F-peak altitude, and its intensity is mostly independent of the F-layer height variations. Whereas the 630.0 nm and the thermospheric 557.7 nm emissions come from about 250-300 km region, and the dissociative recombination

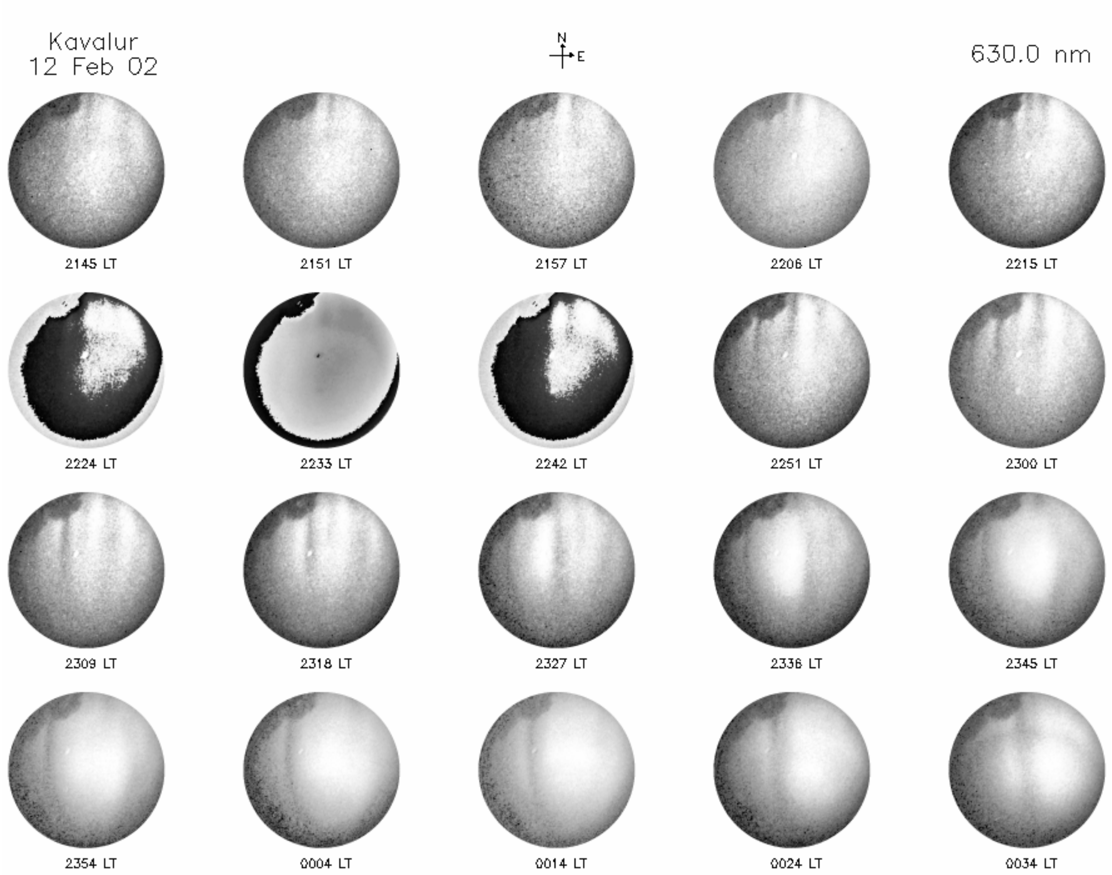

Figure 4.3 *A sequence of 630.0 nm images taken in the night of 12 February 2002. Some of the images were contaminated by station light during the observation.*

responsible for the emission depends on the neutral particle density as well. Hence, the chemistry depends on the altitude and the intensity changes with F-layer height variations. Now, in the early evening hours, the F-layer moves to very high altitudes due to pre-reversal enhancement. This results in the reduction of the 630.0 as well as 557.7 nm intensities, and hence the depletions are not well defined in those emissions. However, the 777.4 nm intensity, which comes from the F-peak height do not change much and depletions will be well distinguishable in those images. Later in the night, when the F-layer moves to lower altitudes, the 630.0 and 557.7 nm emission could be strong enough, but the decrease in plasma density with night result in the 777.4 nm intensity to fall faster. As a result, towards midnight the depletions could still be seen in

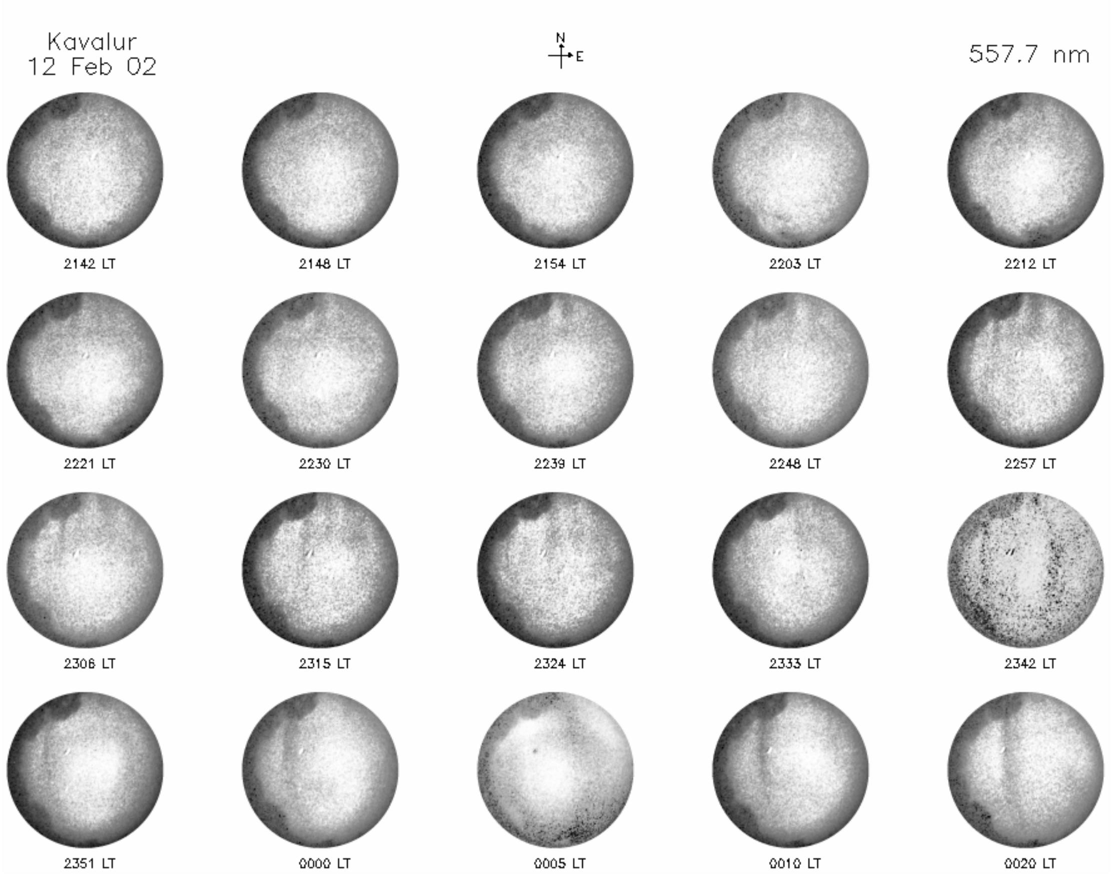

Figure 4.4 *A sequence of 557.7 nm images taken in the night of 12 February 2002*

630.0 and 557.7 nm images, but becomes weaker or disappears in the 777.4 nm. Another factor affecting the nature of depletions in these images could be the life-time of the meta stable states that give rise to the respective emissions. The 777.4 nm emission is prompt, and similarly the 557.7 nm emission also a quick process. However, the life-time of the O(^{1}D) state giving the 630.0 nm emission is about 110 seconds. As a result of this large life-time, the depletions in this emission appear more smeared, while in the 777.4 nm the features appear more distinct.

Several other nights during the observations from Kavalur in February-April 2002 showed the presence of very strong depletions, and in many such nights, the depletions were seen in all the three emissions. These observations are thus analyzed in detail to understand morphological characteristics of plasma depletions in different airglow images.

4.2 East-west extension

Plasma depletions are regions of very large scale fluctuations in the plasma density, often having east-west extent or width ranging from a few tens of kilometers to a few hundred kilometers. The east-west extents of depletions are indicative of the scale size of the seeding agencies involved in the instability operation. Most of the previous studies have reported the width of depletions mainly based on the observations at 630.0 nm, and in some cases using 777.4 nm images. The large data set collected as part of this study enables a detailed comparison of the scale size of same depletion in all the three wavelengths simultaneously. Further, the results also give opportunity to examine how the widths of the depletions behave in the post-midnight and per-midnight observations.

Figures 4.5 to 4.7 display the images taken in the night of 11 March 2002 using 630.0, 557.7, and 777.4 nm emissions, respectively. The observations in this night started immediately after the Sun set, and continued almost till Sun rise. In the examples the images taken only up to about 0230 LT are given. A visual comparison of the images reveals that the depletions are much stronger in the 630.0 nm images, and they are seen from around 2100 LT. In the 630.0 nm images, the depletions could be seen in this night even after 0400 LT (not shown in Figure 4.5). In the 557.7 nm, the depletions are seen only after 2300 LT, and though weak, they look almost identical to the ones in the 630.0 nm images. In this case, after about 0230 LT, the depletions were very weak to be identified. The depletions are seen in the 777.7 nm images starting from around 2100 LT. However, they are very weak and after about 0130 LT, the depletions almost disappear in the images.

The observations shown in the Figures 4.5 – 4.7 are used to examine the east-west extent of depletions in different images in the pre-midnight and post-midnight periods. To make a meaningful comparison, the same depletion was identified in all the three emissions. Note that the depletions in 557.7 nm appear only after 2300 LT, and in 777.4 nm they are not visible after 0130 LT. Hence the results from only those images taken after 2300 LT are used for the study here. Further, the 777.4 nm images could be analyzed only for the pre-midnight case. Note that in the calculations made here, the uncertainty that could arise in the estimation of depletion parameters is about 10% for the 630.0 nm images [Sinha et al., 2001].

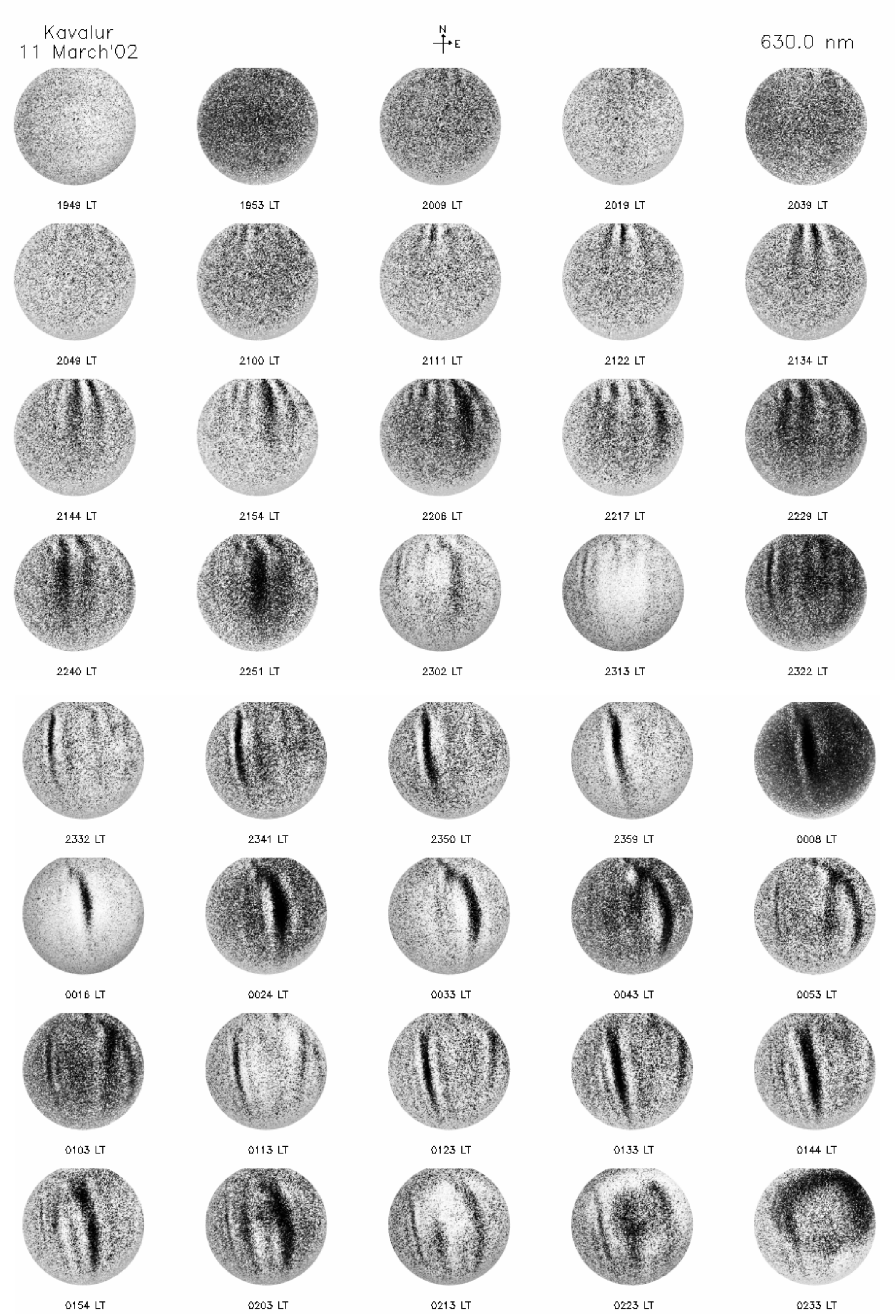

Figure 4.5 *Sequence of all sky images taken in the night of 11 March 2002 using 630.0 nm emission.*

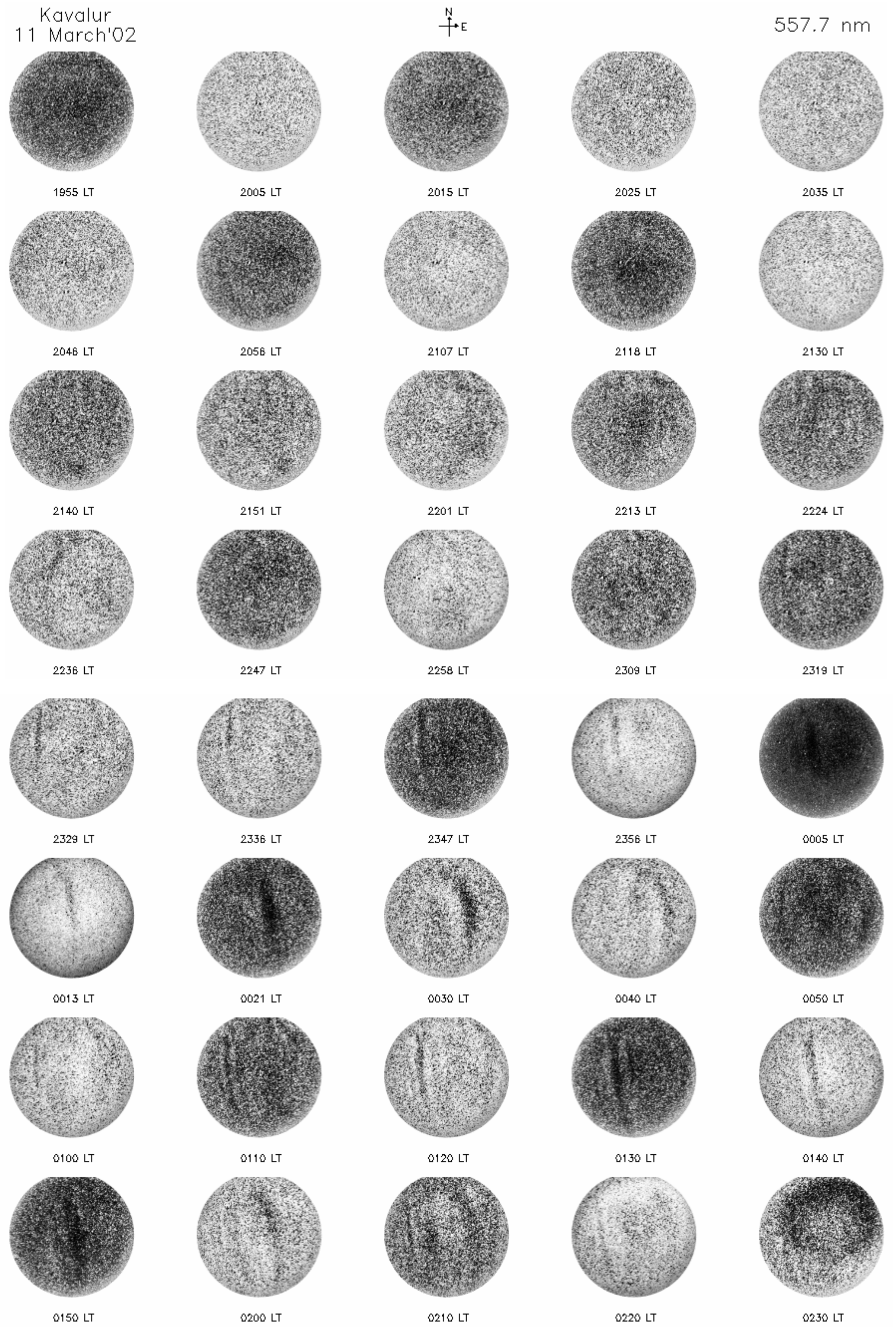

Figure 4.6 *Sequence of all sky images taken in the night of 11 March 2002 using 557.7 nm emission.*

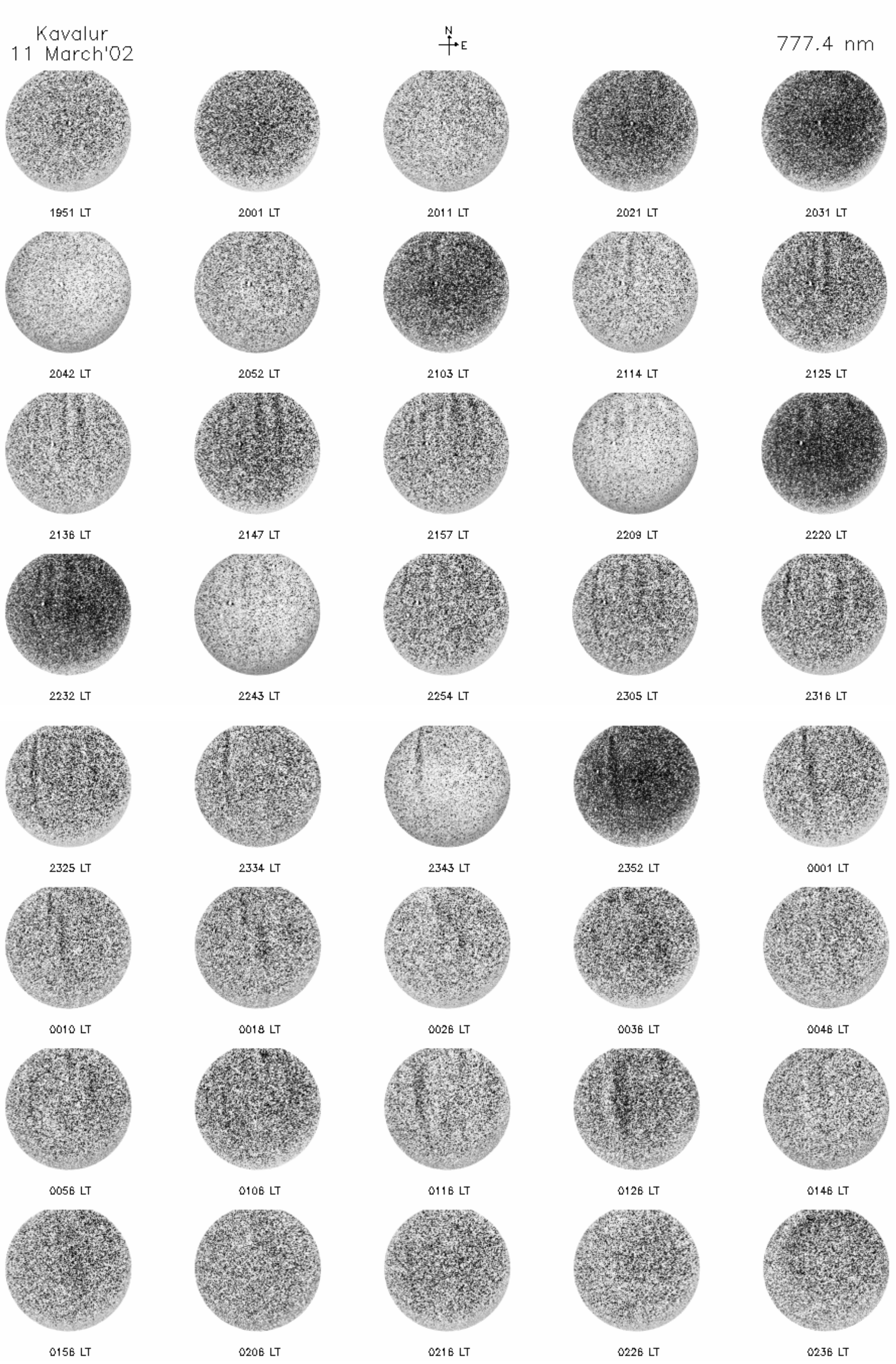

Figure 4.7 *Sequence of all sky images taken in the night of 11 March 2002 using 777.4 nm emission.*

Table 4.1 *The east-west extension of selected plasma depletion in the 630.0, 557.7, and 777.4 nm airglow images taken in the pre-midnight period of 11 March 2002 over Kavalur, India.*

Local Time (hours)	East-West extension (km)		
	630.0 nm	557.7 nm	777.4 nm
2302	265		
2305			345
2313	243		
2316			288
2319		207	
2322	214		
2325			256
2329		191	
2332	176		
2334			236
2336		153	
2341	150		
2343			198
2347		118	
2350	110		
2352			115
2356		90	

It can be seen from Table 4.1 that the east-west extension of the depletion is about 100-300 km, and is very similar in the 630.0 and 557.7 nm, but appears to be a bit wider in the corresponding 777.4 nm. It should be noted that the spatial resolution for the 777.4 nm image is slightly coarser than the other two images. Thus, though the values appear slightly more, they agree well within the expected uncertainty in the calculation. The depletion that was tracked in the three emissions to construct Table 1 started appearing in the 630.0 nm image at 2251 LT near the western edge of the FOV, and can be seen as a weak depletion at the eastern edge of the FOV at 0113 LT. Thus, the particular depletion remained over the FOV of the 630.0 nm image for about 2 hours and 22 minutes. The width of the depletion decreases with time in all the three cases, and the overall rate of decrease is about 3.2-3.6 km per minute, which however need not to be linear with time. The observations thus suggest the effective rate at which diffusion comes into play, weakening the density gradient associated with the depletion.

Table 4.2 *East-west extensions of two plasma depletions in the 630.0 and 557.7 nm airglow images taken in the post-midnight period of 11 March 2002 over Kavalur, India.*

Local Time (hours)	East-West extension (km)	
	630.0 nm	557.7 nm
0050		223
0053	219	
0100		189
0103	191	
0110		162
0113	158	
0120		129
0123	118	
0130		98
0133	79	
0144	267	
0154	253	
0203	214	
0210		199
0213	195	
0220		176
0223	169	

Table 4.2 gives the east-west size of two different depletions that could be traced as a function of time in the 630.0 and 557.7 nm images in the post-midnight period. The first depletion is between 0050-0133 LT and the second depletion is between 0149-0223 LT.

The results indicate that the east-west extension of the post-midnight depletions is more-or-less of the same range as that of the pre-midnight depletions. It can be seen from Figure 4.5 that the depletions, when they first appear in the image around 2000 LT, are seen almost over the longitude that crosses the center of the image. This implies that it is most likely that the depletions are generated overhead, and not drifting into the FOV from western longitudes. However, it is not possible to conclude of all other depletions imaged later in the night is generated within the FOV, or at other longitudes. However, from the similar ranges of the east-west extension of the observed depletions in the pre-midnight and post-midnight cases, it appears that they might be at similar stages of their evolution when appeared over the imager FOV.

The post-midnight depletion used for the analysis in Table 4.2 remains visible in the FOV of the 630.0 nm images for about 1 hour and 30 minutes. The post-midnight depletions also show that the east-west extension gradually decreases with time. For the case of the first depletion that appears in the image first around 0043 LT in the 630.0 nm, the width decreases at an overall rate of about 3.1-3.5 km/minute. This is similar to that of the pre-midnight case. However, for the second depletion in the post-midnight period, which is first seen around 0133 LT in the 630.0 nm image, the rate of decrease is about 2.3-2.5 km/minute. The density gradient associated with the depletions that are seen in the post-midnight period could be different from that in the earlier hours, and hence their rate of decay also could be different.

Though in the cases discussed here, the pre-midnight and post-midnight depletion are of similar width, in general the depletions seen in the earlier part of the night tend to be slightly wider than those appear later in the night. However, it should be noted that in some of the nights during the observations, there were cases when depletions seemed to develop overhead in the post-midnight period. Such developing depletions could have smaller widths and could have influenced the observed results. In general, the east-west extensions of the observed depletions were in the range of 50-350 km, which agrees with the values reported elsewhere.

4.3 Drift velocity of depletions

All sky imaging is regarded as a relatively cheaper, but most useful diagnostic tool to investigate the large-scale structures associated with ESF, called plasma depletions. This is particularly significant, considering the fact that it is not possible to monitor the evolution and dynamics of such large-scale features, and collect spatial and temporal information with any other technique as simple as this method. One major advantage of all sky images is that by collecting images throughout the night at specific intervals, one could estimate the drift velocity of the depletions. By measuring the drift speed of the depletions, one could relate it with the zonal plasma drift because the depletions at their developed stage drift at the same speed as that of the ambient plasma. However, this could be different if one were to image depletions at their early stages of development. In that case the depletions could drift at a much faster rate [Martinis *et al.,* 2003; Lin *et al.,* 2005].

The previous studies using all sky images have reported zonal drift speeds between 100-200 m/s around 2000-2300 LT, which gradually decreases with time to below about 50 m/s in the post-midnight period [Mendillo and Baumgardner, 1982; Sinha and Raizada, 2000; Sinha *et al*., 2001]. The drift velocities reported in these analyses agree well with that based on incoherent radar observations [Fejer *et al.,* 1991]. Some of discrepancies of the estimated drifts using different all sky imager observations across the globe could be attributed to the assumption of the height of the emission layer in the calculations. Pimenta *et al.* [2003] showed that an increase of about 50 km in the assumption of the layer height could cause about 20% increase in the derived velocities.

Note that in the analysis used for this study, an altitude of 250 km is assumed for the 630.0 and 557.7 nm emissions, and the 777.4 nm emission is assumed to arise from about 350 km altitude. Figure 4.8 gives the drift velocities of all depletions observed during February-April in 2002 in 630.0 nm images as a function of time. Multiple depletions were observed on several nights and each of the depletions is considered separately in calculating the drift velocity. The result shown here includes all such depletions imaged within the observation period.

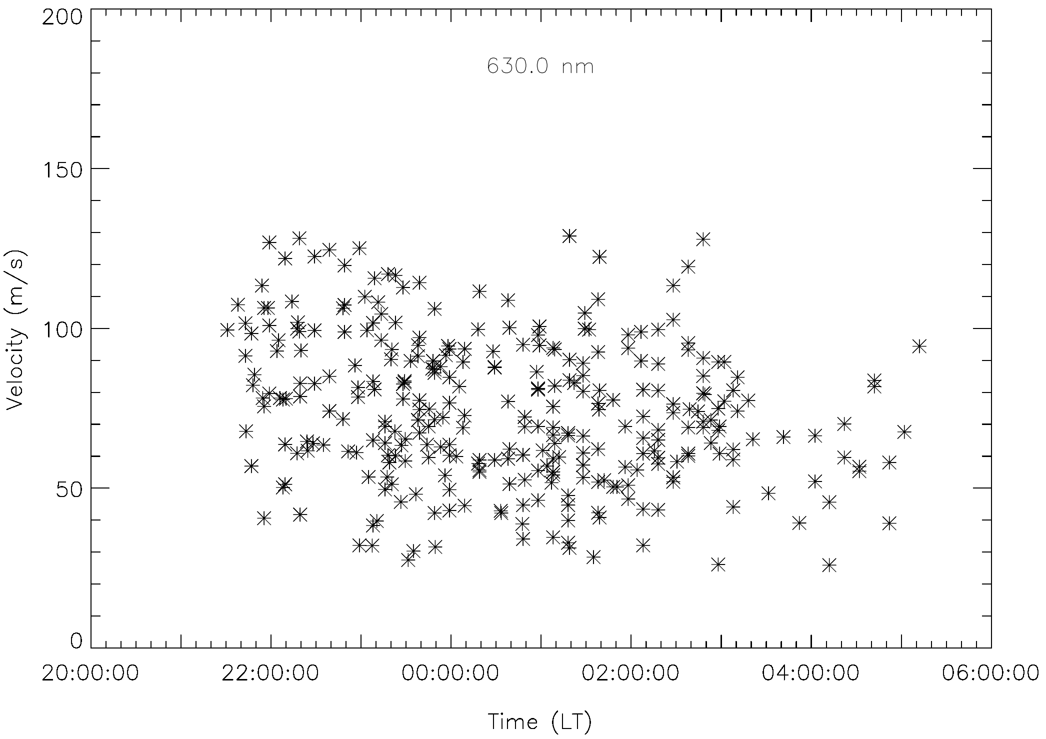

Figure 4.8 *Zonal drift velocity calculated using all the depletions observed in 630.0 nm images observed during February-April, 2002.*

The overall trend of the observed zonal drift of depletions in 630.0 nm is similar to that have been reported in the past. The median values who about 100-120 m/s in the evening period, which gradually decreases with time in the night. Note that there is a lot of scatter in the data points. Considering the large data set used to derive the velocity, the scatter in the values could partly indicate the day-to-day variations in the F-region characteristics. Such variations could account for about 25% of the deviation. It should also be mentioned that, while following multiple depletions in a sequence of images, any slight error in estimating the location of the depletions could add to the scatter in the values. The spatial resolution of the images is different at the center region as well as at the edges. So, when depletion is near the edge of the image, even a slight change in the pixel location could contribute to a large change in the calculation of its spatial location. For the results reported here, the process of estimation of drift velocities was repeated several times to make sure that the results are consistent.

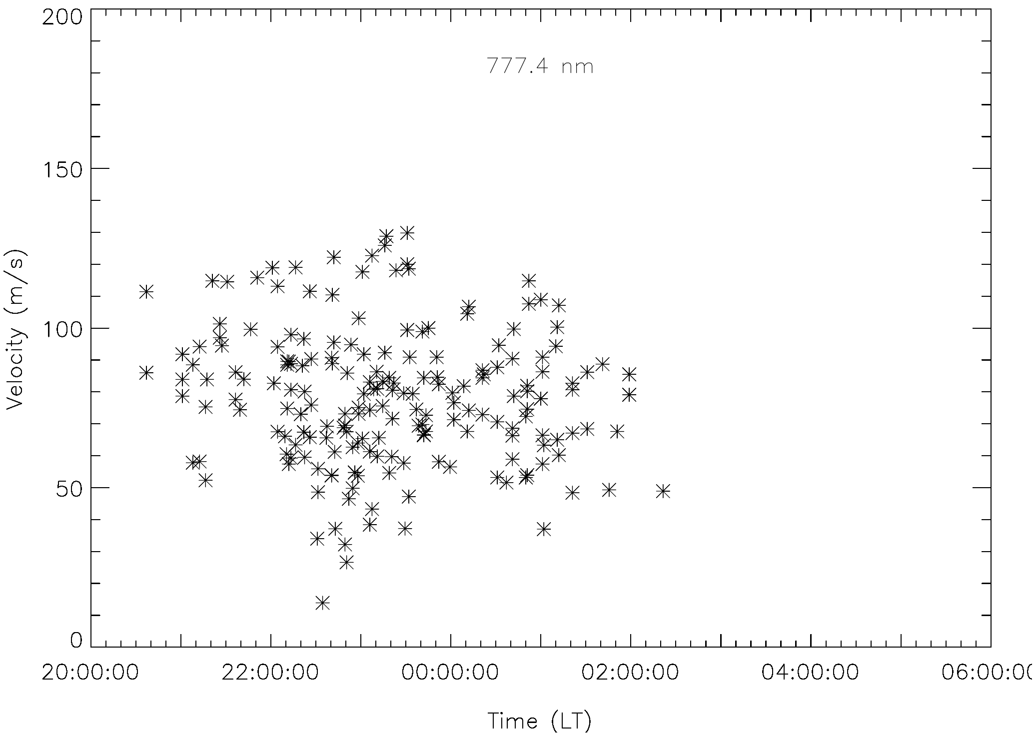

Figure 4.9 *Zonal drift velocity calculated using all the depletions observed in 777.4 nm images observed during February-April, 2002.*

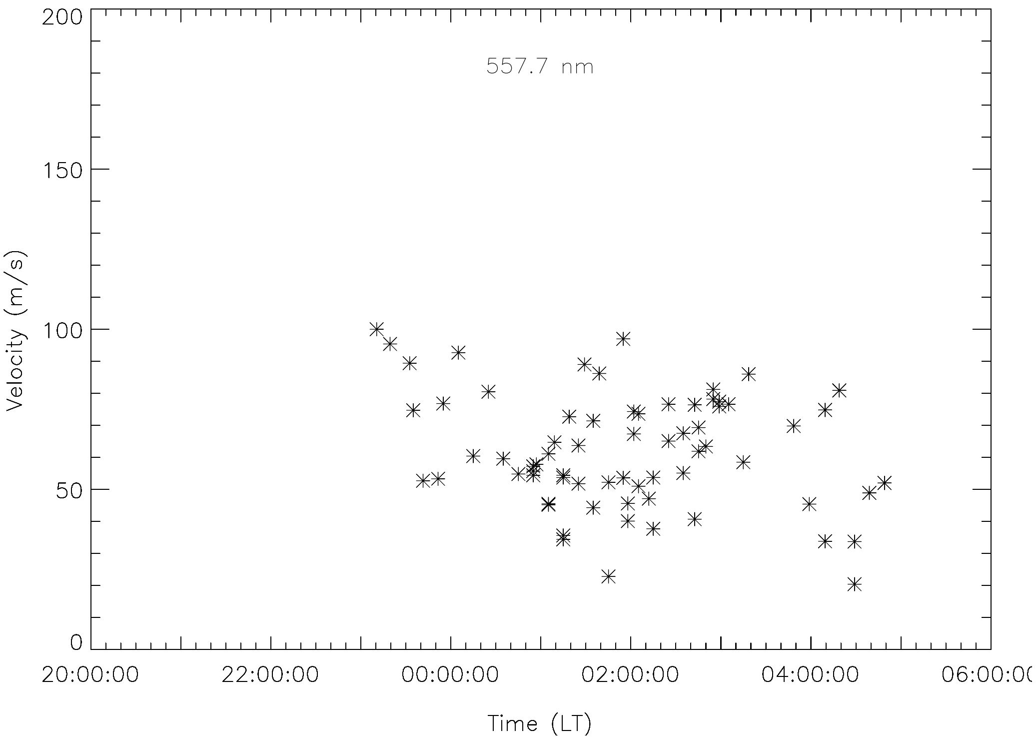

Figure 4.10 *Zonal drift velocity calculated using all the depletions observed in 557.7 nm images observed during February-April, 2002.*

The zonal drift velocities determined using all the depletions in the 777.4 nm images in this period are shown in Figure 4.9. The general trend is very similar to that seen in the corresponding 630.0 nm values. However, there is a large scatter of the values around 2300 LT. Further, there are only very less data points in this case after midnight. One of the reasons for this could be the fact that depletions in the 777.4 nm images becomes weak by 2300 LT, and mostly disappears by midnight. Thus, the process of estimation of the velocities around 2300 LT might result in large computational error, giving rise to the observed scatter. Since most of the depletions disappear around this time, there are very less data points after midnight.

Most of the previous all sky imager observations have reported the drift velocities of depletions using either 630.0 nm or 777.4 nm images. In some cases both the emissions are used. In this study, for the first time the drift velocity of the depletions are estimated using 557.7 nm. In Figure 4.10, the zonal velocities of all the depletions observed in 557.7 nm images in the observation period are plotted. The general trend appears to be similar to that in Figure 4.9. However, there are no data points before 2300 LT, and most of the values are in the post-midnight period. This is due to the fact that in 557.7 nm, depletions mainly appeared only around the mid-night period.

In order to have a better comparison the observed drift velocities in all the three emissions, all the values are plotted together in Figure 4.11. The velocities in all the three emissions do reveal a very similar average behavior. The median values suggest that the 777.4 velocities are slightly less than that of the 630.0 nm values in the evening period. However, in the post-midnight period, the 777.4 nm velocities are a bit larger. Further, there is a slight difference in the drift velocities of 557.7 nm and 630.0 nm in the 0000-0230 LT interval. In this period, the 557.7 nm velocities are less than that of the 630.0 nm values. However, after this interval, both the velocities tend to show very similar magnitude. One of the reasons for the different average behaviors of the zonal drift velocities in could be the difference in the data points used. Especially for the 557.7 nm depletions, there are much less data points in the 2300-0100 LT periods as seen from Figure 4.10. This could influence the observed velocities in the two emissions. Note that in the later part of the night, both 557.7 and 630.0 nm have more-or-less similar data points, and the estimated drift velocities during this period show very good agreement with each other.

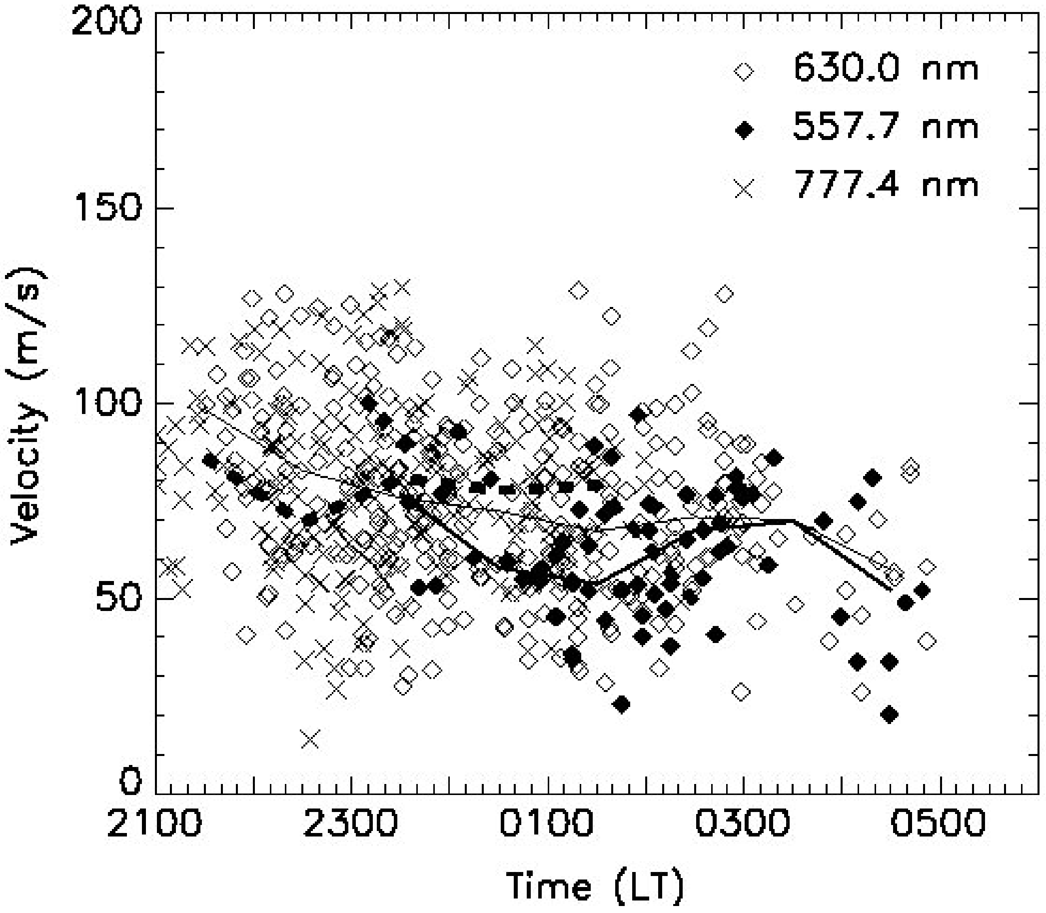

Figure 4.11 *The zonal drift velocities estimated using 557.7, 630.0, and 777.4 nm images during the observation period. The dashed line is the median value of all the 777.4 nm velocities, this dark line is the median velocity for the 630.0 nm depletions, and the thick dark line stands for that of the 557.7 nm velocities.*

The 630.0 and 777.4 nm velocities are estimated for different altitudes, and the observed difference in their values could thus indicate altitude difference in the zonal plasma drift. Further, both the 557.7 and 630.0 nm velocities reveal an increasing trend during the 0100-0300 LT time intervals. Such an increasing trend is not reported in the past studies. Since the same trend is seen in both the 557.7 as well as 630.0 nm velocities, this variation seems to come from the actual zonal drift values in that period. However, the 777.4 nm velocities do not give any such indication. One possibility is that, in this observation period several nights showed developing depletions within the FOV in the post-midnight period. At the time of such post-midnight generation, the depletions were seen only in 630.0 and 557.7 nm, and the 777.4 nm emission was too weak to image such depletions. Now, the zonal drift of depletions in their generative stage is reported to be larger than that of the ambient plasma drift. Thus, the increasing trend in the 557.7 and 630.0 nm velocities in the post-midnight period could be influenced by such newly developing depletions.

4.4 Depletions and wave disturbances

Most of the previous all sky imager observations report depletions using 630.0 nm and/or 777.4 nm emissions. There are only a few occasions when plasma depletions are reported in all the three wavelengths. The observations conducted from Kavalur during February-April 2002 were remarkable in that several nights depletions were imaged in all the 630.0, 777.4, as well as 557.7 nm observations. Such observations prompted a detailed investigation of the conditions when depletions could be imaged in 557.7 nm emission. However, there are several observations of wave disturbances being imaged using 557.7 nm emission [Mukherjee, 2003, Brown *et al.,* 2004]. The perturbations modulate the airglow in the upper mesospheric region. The 557.7 nm emission has two components, one from the mesospheric region, from about 97 km altitude and then the thermospheric component. Thus, if there are any wave disturbances in the mesospheric region affecting the airglow intensity, it will appear as band like intensity enhancement and depletion patterns in all sky images.

Figure 4.12 is a sequence of 630.0 nm images taken in the night of 12 April 2002. In this night depletion could be seen from the first image taken at 2103 LT, and intense depletion activity continues almost throughout the night. In the early evening period, two well separated depletions bands are seen, which appear wider. However, later in the night several multiple depletions bands are seen, which are narrower. The sequence of 777.4 nm images taken in the same night is given in Figure 4.13. These images also show the presence of plasma depletions in the images taken from the beginning, and are visible till about 0200 LT. Later in the night, the emission becomes very weak to show any depletion features.

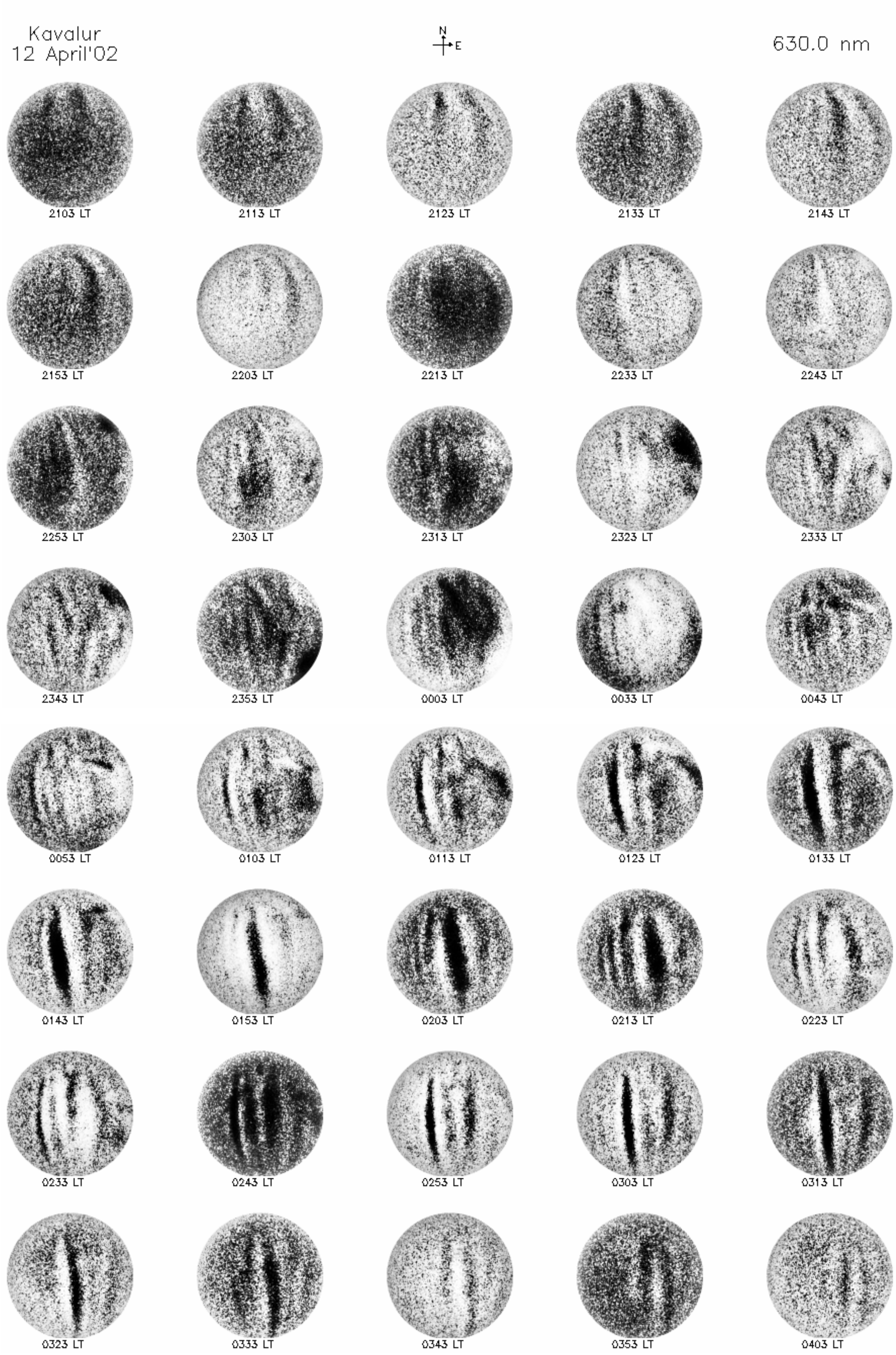

Figure 4.12 *A sequence of all sky images taken in the night of 12 April 2002 using 630.0 nm emission showing plasma depletions.*

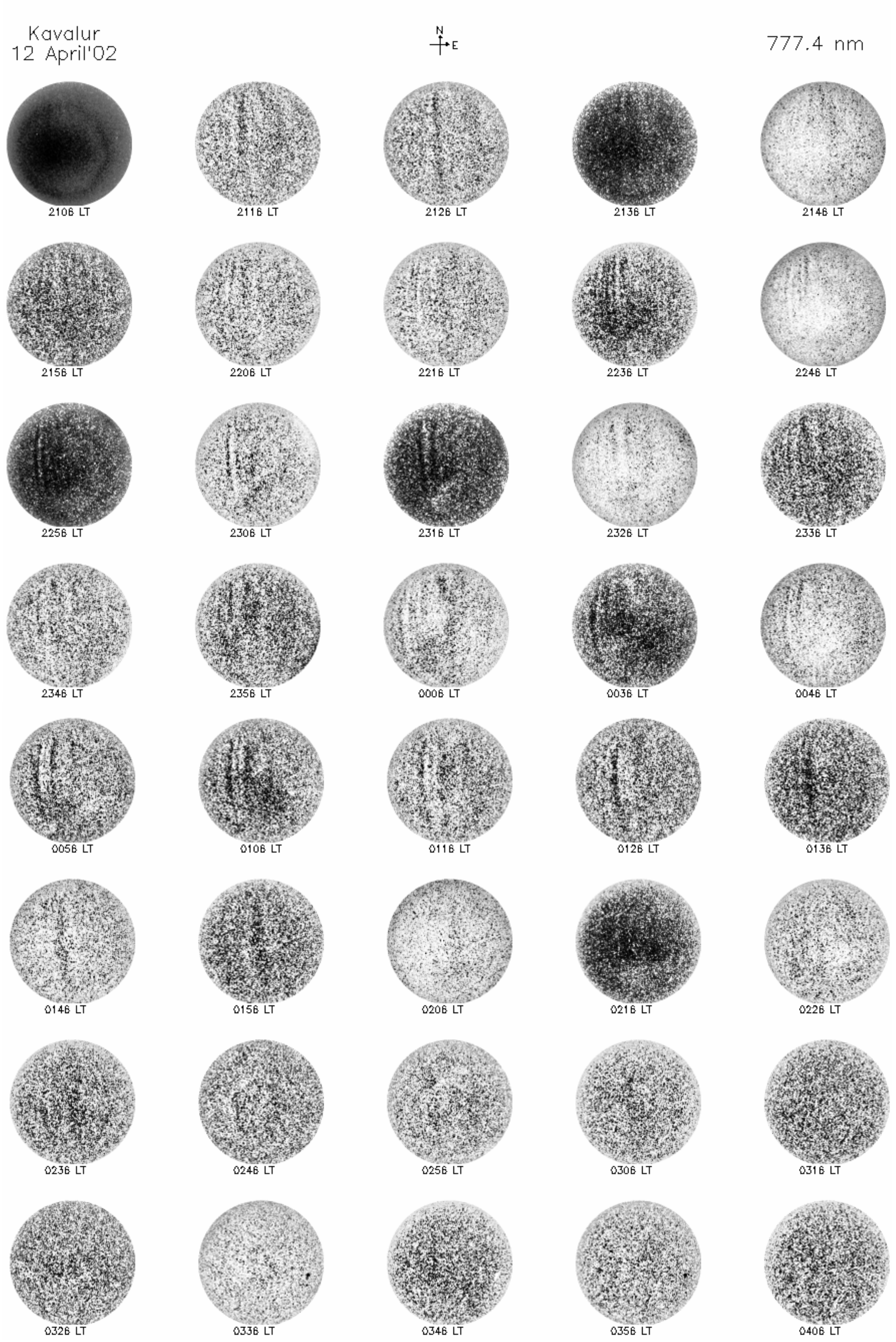

Figure 4.13 *A sequence of all sky images taken in the night of 12 April 2002 using 630.0 nm emission showing plasma depletions.*

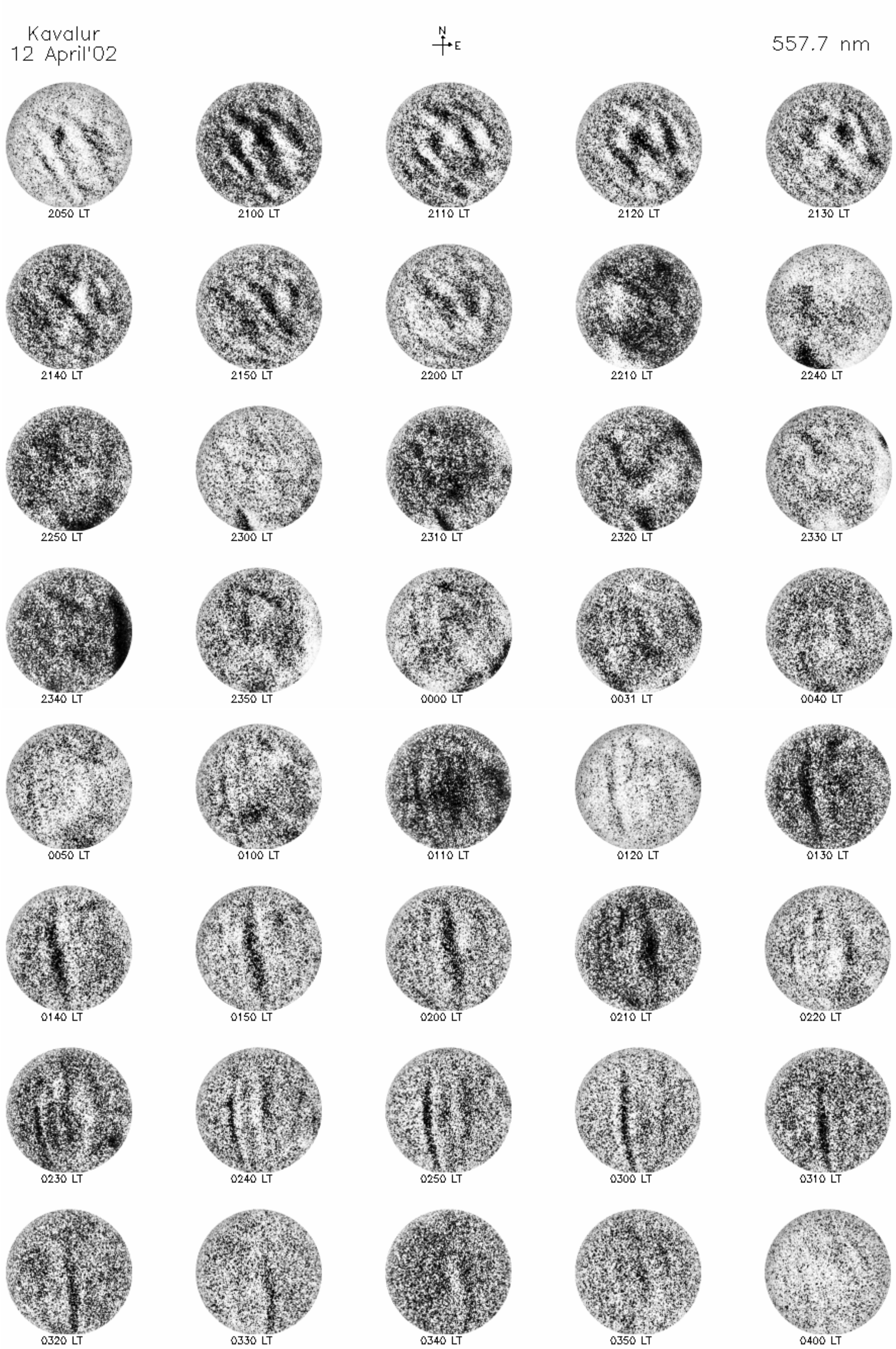

Figure 4.14 *A sequence of all sky images taken in the night of 12 April 2002 using 630.0 nm emission showing wave features in the pre-midnight period and plasma depletions in the post-midnight period.*

The sequence of 557.7 nm images taken in this night is displayed in Figure 12.14. In these images plasma depletions are not seen in the initial images. Even in the earlier examples, plasma depletions are not seen in the 557.7 nm images in the evening period, but they appear towards the midnight. However, in the example in Figure 12.14, the images taken from 2050 LT show the presence of some wave disturbance, which gradually decay after 2210 LT and disappear completely by midnight. Though several all sky imaging observations have shown similar wave patterns produced by gravity waves in the all sky airglow images, this is the first time such observations are imaged over the Indian region. The finger like band structures appears to be oriented in the Northwest-Southeast direction, and propagate in the Northeast direction.

In complete contrast to the wave pattern that appeared earlier in the night, the images from about 0050 LT displays North-South aligned plasma depletions. In fact, a careful examination reveals that weak depletions features can be seen in the images from midnight. Later in the night, the depletions become very intense, and the activity continues almost till 0400 LT. The observations in Figure 4.14 reveal remarkable airglow characteristics. In the early evening hours, the images characterize the dynamical processes in the mesospheric region. Towards midnight, the integrated images display the intensity modulations in the thermospheric altitudes. However, the almost simultaneously taken 630.0 and 777.4 nm images show that plasma depletions exist in this night from the period when the observations began.

The observations indicate that the 557.7 nm intensity shows mesospheric features in the pre-midnight period, and thermospheric features are seen in the post-midnight period. The fact that plasma depletions appear in the 557.7 nm images only around midnight has already been demonstrated in the earlier example figures as well as the zonal drift velocities estimated from the depletions. This feature has been revealed for the first time in the observations used for this study. The fact that no depletions are seen in the evening period in 557.7 nm images when the other two emissions show intense depletions prove that in the evening period the mesospheric component of the 557.7 nm emission could be stronger. It is possible that either the mesospheric component becomes weaker or the thermospheric component becomes stronger by midnight. As a result, plasma depletions appear in the 557.7 nm images around 2300 LT or later only.

4.5 Bubble rise velocity

In addition to the all sky observations at the equatorial station Kavalur described above, observations were also conducted from the off-equatorial latitude station at Mt. Abu (24.55°N, 72.71°E, 18.48°N Geomagnetic Lat.) during during 8-12 April 1999. Out of the 5 nights of observation, plasma depletions were observed on two nights, 14th and 15th April 1999. This was geo-magnetically quiet period. Figure 4.15 gives the sequence of images showing depletions that appeared on 14th April 1999. In this night observations could be started at 2050 LT and the very first image itself showed the presence of plasma depletions. Two clear bands of depletion are seen in the image. The depletion bands can be seen extending from the southern end of the image and reach up to the middle of the image FOV. In the subsequent images, the depletions further extend within the FOV, with their poleward end moving northwards, and at the same time the depletions drifting eastwards. Similarly, Figure 4.16 shows the sequence of depletions imaged in the night of 15 April 1999, showing the northward as well as eastward propagation of the depletion.

From a low latitude station like Mt. Abu, it is possible to study the movement of the northern end of the plasma depletions. The northward latitude extent of the plasma depletions is mapped back to the corresponding altitude attained by the depletions at the equator with the help of the International Geomagnetic Reference Field (I.G.R.F.) Model. The calculations showed that the plasma depletions observed on 14th April 1999 attained a maximum northward extended of about 23.1°N geomagnetic latitude. This when mapped back in terms of the maximum altitude attained by the plasma depletions at the equator corresponds to about 950 km. The poleward movement of the northern end of plasma depletion was traced in a few images, till it reached the maximum northern limit. This information was used to calculate the vertical velocity of the rising plasma bubbles at the equator. The calculations showed that the average vertical drift velocity of plasma bubbles was about 56.89 ms^{-1} during the period 2050 LT and 2225 LT. In the night of 15 April 1999, the depletions appeared weaker and were limited within the southern half of the image, with a maximum northward extent of about 17.9°N. This corresponds to an altitude of about 590 km at the equator. The average vertical bubble rise velocity for the period 2045 LT to 2115 LT on this night was about 53.03 ms^{-1}.

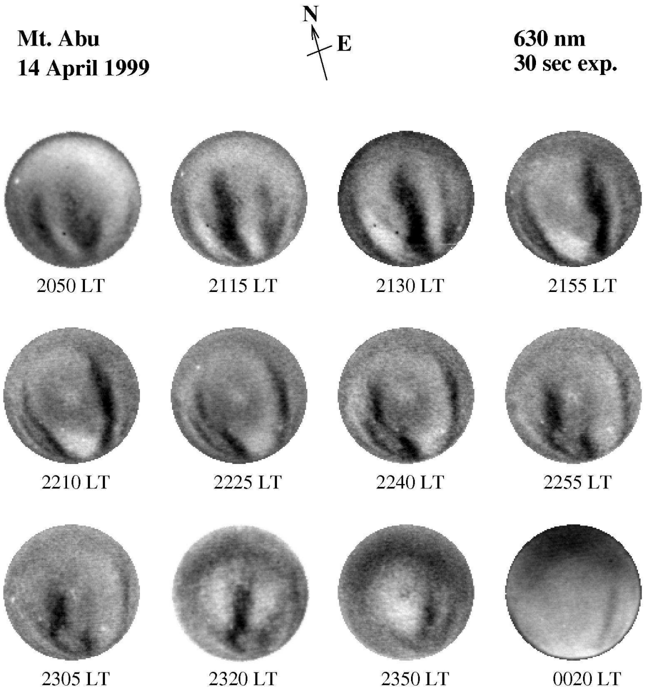

Figure 4.15 *A sequence of all sky images taken in the night of 14 April 1999 using 630.0 nm emission from the low latitude station Mt. Abu.*

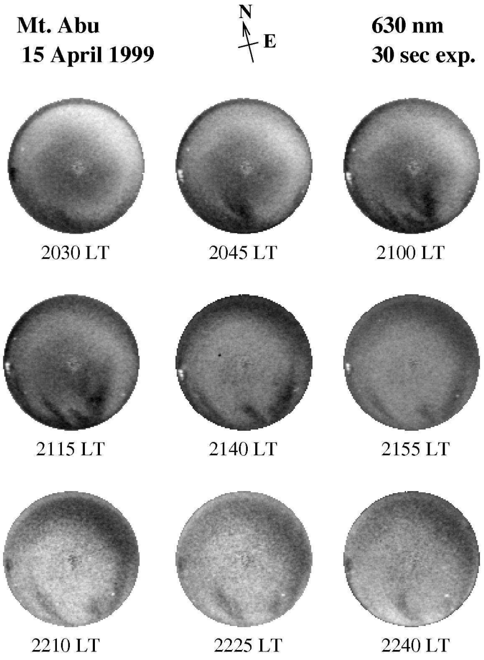

Figure 4.16 *Same as in Figure 4.15, but taken on 15 April 1999.*

It is interesting to note that even though the average vertical rise velocities were almost similar on both the nights, the bubble could rise to much higher altitude on 14th April 1999 compared to the altitude achieved on 15th April 1999. Plasma bubbles/depletions are generated in the sharp density gradients that exist in the post sunset equatorial bottomside ionosphere when the background conditions such as neutral winds, electric field, collision frequency etc. are suitable for instability mechanism to act. The instability makes the plasma unstable so that any initial perturbation present can grow in amplitude and give rise to a spectrum of irregularities. It is generally accepted that plasma depletions are generated in the bottom side of the F region through the Generalized Rayleigh-Taylor instability mechanism, and gravity waves are identified as the source for producing the initial density perturbation. These plasma depletions once generated move upwards as well as eastwards. The depletions drift eastward with velocities almost similar to the ambient plasma drift velocity whereas the vertical rise velocity depends on the percentage perturbation from the mean plasma density, geometrical shape of the bubble, electric field etc.

The appearance of plasma depletions observed on 14th April 1999 and 15th April 1999 were different. The depletions observed on 14th April 1999 cover almost the entire FOV, while the depletions observed on 15th April 1999 are limited to the southern half of the image. This can happen if the vertical rise velocity of the depletions observed on 15th April 1999 is much lower than those observed on 14th April 1999. However, the average vertical velocity of depletion calculated for both the nights are approximately equal. But this velocity was calculated after the images start appearing in the FOV. On 14th April 1999, the first image taken at 2050 LT showed well-developed bands of depletions covering almost half of the FOV in the north-south (NS) direction. On 15th April 1999 no depletion could be seen up to 2030 LT. After 2030 LT, depletions started appearing near the southern end of the image.

The vertical motion of plasma depletions depends on the local ionospheric conditions. Fagundes *et al.* [1997] observed in their images that when some depletion showed vertical motion, some depletion observed on the same night did not show vertical motion. In the present case, since in the developed stage plasma depletions on both the nights rose up with almost equal velocity, the initial ionospheric conditions on 15th April 1999 might not have been favoring the rise of bubbles. Ossakow and Chaturvedi [1978] simulated the effect of background conditions such as electric field, collision frequency etc. on the vertical rise velocity of the bubbles at different altitudes. The effect of electric field is more at lower altitudes and at higher altitudes its effect is negligible even if it reverses direction. The ambient electric filed can also affect the vertical motion of the bubbles. An eastward electric field can increase the bubble rise velocity, while a westward electric field can slow down the bubble rise velocity or even lead to its downward movement.

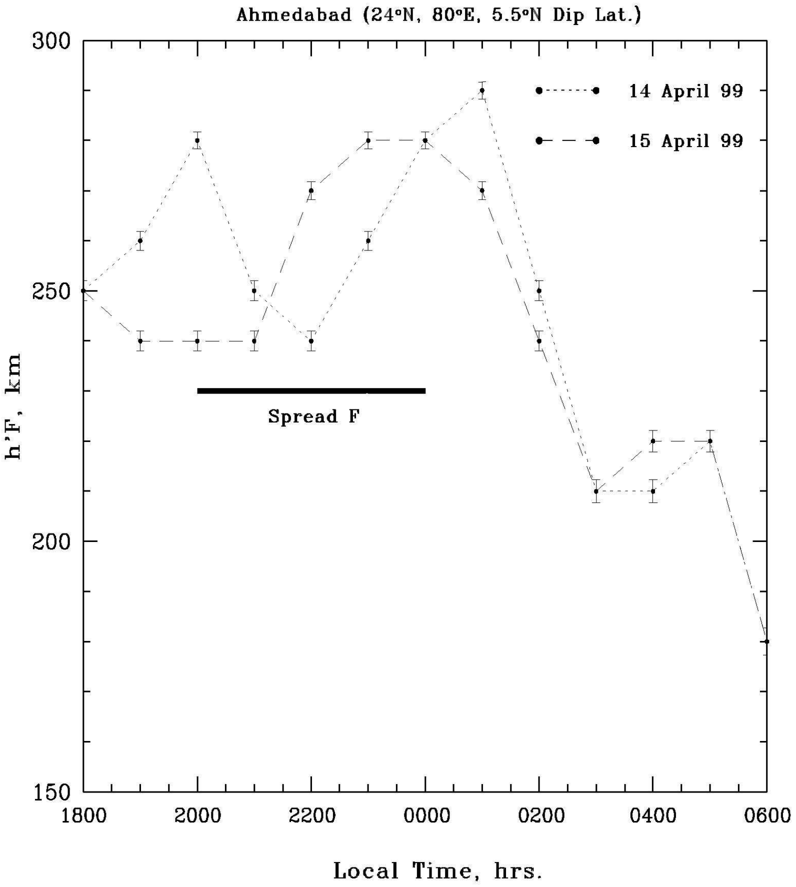

Figure 4.17 Variation of h'F over Ahmedabad on 14th April 1999 and 15th April 1999. The horizontal bar shows the duration of spread F.

Figure 4.17 shows the movement of the bottom of the F region (h'F) on both the nights. On 14th April, F layer was moving upward at the onset time of ESF. That means the electric field was eastward. On 15th April 1999, the F layer first showed a downward motion and then remained at a lower altitude in the early evening hours, indicating a westward electric field at that time. The Figure 4.17 is based on the ionograms taken at Ahmedabad (23°N, 72.4°E, 16.8°N Geomagnetic Lat.) and cannot be in principle used to infer the ionospheric conditions near the equator at the onset time of the irregularities. At the equator it is mainly the electric field that controls the plasma dynamics. At latitudes away from equator, in addition to the electric field, neutral winds also play an important role in the local plasma dynamics. The behaviour of plasma depletions on 14th April 1999 and 15th April 1999 suggests that the electric field conditions at the equatorial region in these two nights might have been similar to that shown in Figure 4.17. The electric field reversal later occurred on both the nights did not affect the bubble rise velocity because as shown by Ossakow and Chaturvedi (1978) by that time the bubbles had reached sufficiently higher altitudes where the influence of electric field is negligible.

4.6 Depletions at equatorial and off-equatorial latitudes

In this study the all sky imaging observations taken at two different locations are analyzed, one from the equatorial station Kavalur, and the other one at the off-equatorial station Mt. Abu. A set of selected examples from both the observations are given below.

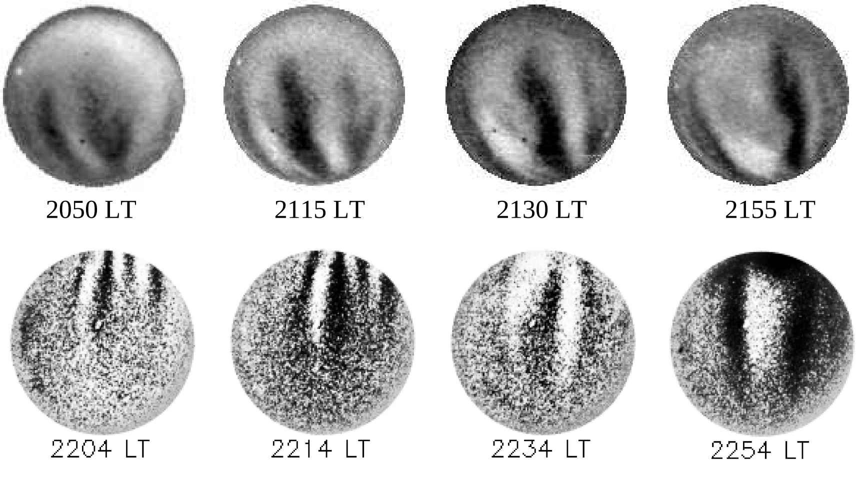

2050 LT 2115 LT 2130 LT 2155 LT

2204 LT 2214 LT 2234 LT 2254 LT

Figure 4.18 *A set of selected examples from the images taken at the off-equatorial station Mt. Abu (top panel) and the equatorial station Kavalur (bottom panel).*

It can be seen that the northern end of the second depletion taken from Mt. Abu appears to be bifurcated. Also, note that the northern end of first depletion also begins to bifurcate by 2155 LT. Another characteristic feature seen in the depletions from Mt. Abu is their significant westward tilt. Such bifurcation and tilt can be seen clearly in the images displayed in the Figures 4.15 and 4.16. Further, in the images in Figure 4.15, the middle one out of the three existing depletions in the images between 2210-2240 LT can be seen to split into two parts after 2240 LT, and its upper part appears to have joined with the preceding depletion in the next image at 2255 LT. Such spitting and joining of depletions indicate the complex turbulent nature of the irregularities. Strong shear in the vertical plasma motion could result in such structures and westward tilt.

When comparing with such bifurcation, westward tilt, and other complex patterns, the depletions taken from the equatorial station appear very simple linear bands. A comparison of the images in the top and bottom panels in Figure 4.18 reveals the difference. The westward tilt and bifurcation of depletion are more frequent when imaged from off-equatorial stations such as Mt. Abu, while at the locations such as Kavalur, which is more close to the equator, depletions tend to appear as dark bands with minimum structuring. This indicates that bifurcation occurs as the bubble rise over certain altitude, and it is not necessarily produced when the irregularity is generated. Further simultaneous observations using two different all sky imagers with overlapping FOV, one at an equatorial station and the other one at an off-equatorial station could reveal the details of the time evolution of depletions and the generation of complex patterns such as bifurcation, and westward tilt and also about splitting and joining of depletions.

Chapter 5 **Some New Features of Plasma Depletions**

This chapter describes some of the new and interesting features of plasma depletions observed in the all sky observations over Kavalur, India, during the solar maximum period of February-April, 2002. In this period, depletions were imaged in 630.0, 777.4, and 557.7 nm in several nights. There are only very limited reports of depletions in 557.7 nm in the past. A detailed analysis of their occurrence is carried out here. Also, in most of the days, the depletions tend to appear as a dark patch in the northern end of the image FOV in the post-sunset hours, and gradually expand the entire North-South around mid-night. Plasma depletions originate at the magnetic equator, and expand pole-ward. The equatorward propagation observed here is investigated in detail. In the observations carried out in the solar maximum year of 2002, there were several cases of post-midnight generation of depletions, and their evolution within the imager FOV. In addition, an example for a strange type of bifurcation of the depletion is also described.

5.1 Depletions in 557.7 nm

Plasma depletion is the name given to the irregularities corresponding to the outer scale of the irregularity spectrum associated with Equatorial Spread-F (ESF) based on their manifestation in the all sky nightglow images. The phenomenon of ESF was first reported by Booker and Wells [1934] from the spreading of the traces in the ionograms. Ever since it has become a major topic of research, the main reason being the poor understanding of the complete mechanism responsible for the generation of irregularities in a wide range of scale sizes. There has been a general agreement that the large-scale structures such as plasma depletions are generated due to the Generalised Rayleigh-Taylor Instability (GRTI) mechanism. But, the exact role of seeding agencies in the generation of the initial perturbation is not clearly understood. The background ionospheric conditions necessary for the growth of irregularities is also not properly known. The all sky imaging technique for the study of large-scale structures present in the airglow emissions was first developed by Mende and Ether [1976] and later modified by Mendillo and Baumgardner [1981]. Similar instruments were developed at different parts of the globe and many observational campaigns were conducted. Most of the observations have reported the occurrence of plasma depletions in the OI 630 and 777.4 nm nightglow emissions. 630 nm emission comes from an altitude region centered around 250 km and 777.4 nm emission is originating from the peak of F-region, centered around 350 km. Both are emissions of atomic oxygen. Dissociative recombination is the main process responsible for the emission of 630 nm, while the 777.4 nm emissions is due to the direct (radiative) recombination of atomic oxygen.

The characteristics of large-scale ionospheric plasma depletions have been studied extensively using all sky imagers for more than two decades. Many experiments were carried out using the 630.0 nm emission [Makela *et al*., 2004, and references therein]. In contrast, there are rather limited reports using 557.7 nm [Mendillo *et al*., 1997; Sinha *et al.,* 2001; Takahashi *et al.,* 2001; Kelley *et al.,* 2002; Mukherjee *et al.,* 2003]. The 557.7 nm emission has two main source regions, one in the thermosphere, located at about 250 km altitude and, the other one in the upper mesosphere, at about 97 km altitude. The thermospheric component is virtually non-existent except at equatorial latitudes [Shepherd *et al.,* 1997], and in presence of strong mesospheric emission it is difficult to observe the F-region structures in the 557.7 nm all sky images [Mendillo *et al.,* 1997; Takahashi *et al.,* 2001].

The all sky observations from Kavalur used for this study showed the field aligned depletions in 557.7 nm images in several nights, which were similar in appearance and characteristics to those in the simultaneous 630.0 nm images. Out of the total 39 nights of observations, plasma depletions were present on 27 nights in the 630.0 nm images. Note that, in any night if depletions appear in all sky images, the 630.0 nm always detected them, irrespective of their occurrence in the other emission. In these 27 nights, on 18 nights plasma depletions were observed simultaneously in 630, 557.7 and 777.4 nm images. On one night plasma depletions were seen in 630 and 557.7 nm images and were not present in 777.4 nm images. Thus in total, plasma depletions were observed on 19 nights in 557.7 nm images. Such frequent occurrence of depletions in 557.7 nm images is different from the previous experiences of observations in this emission. A detailed investigation to the conditions in which depletions could be imaged in the 557.7 nm is carried out.

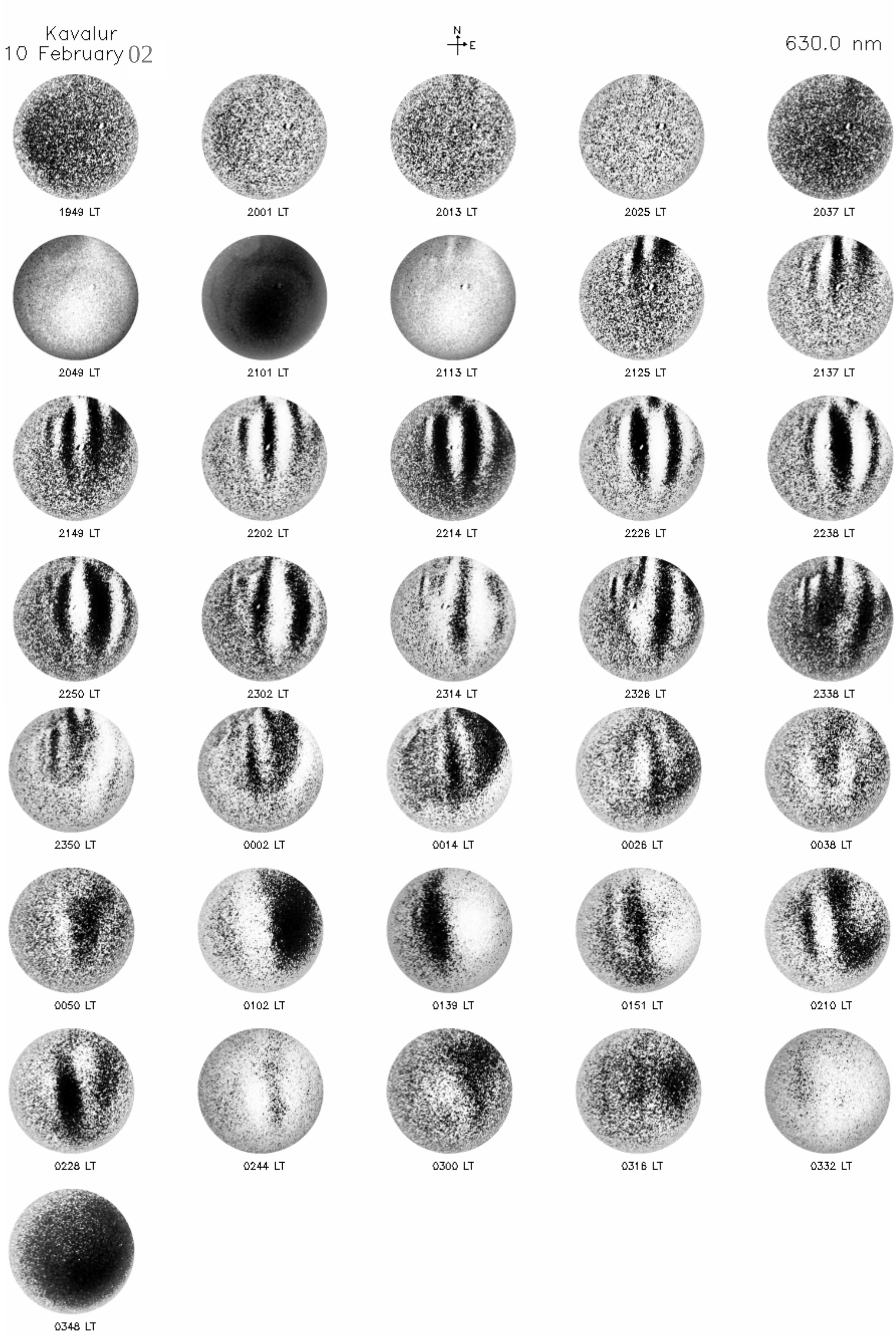

Figure 5.1 *A sequence of all sky images taken in the night of 10 February 2002 using 630.0 nm. Intense bands of plasma depletions can be seen in the images till midnight.*

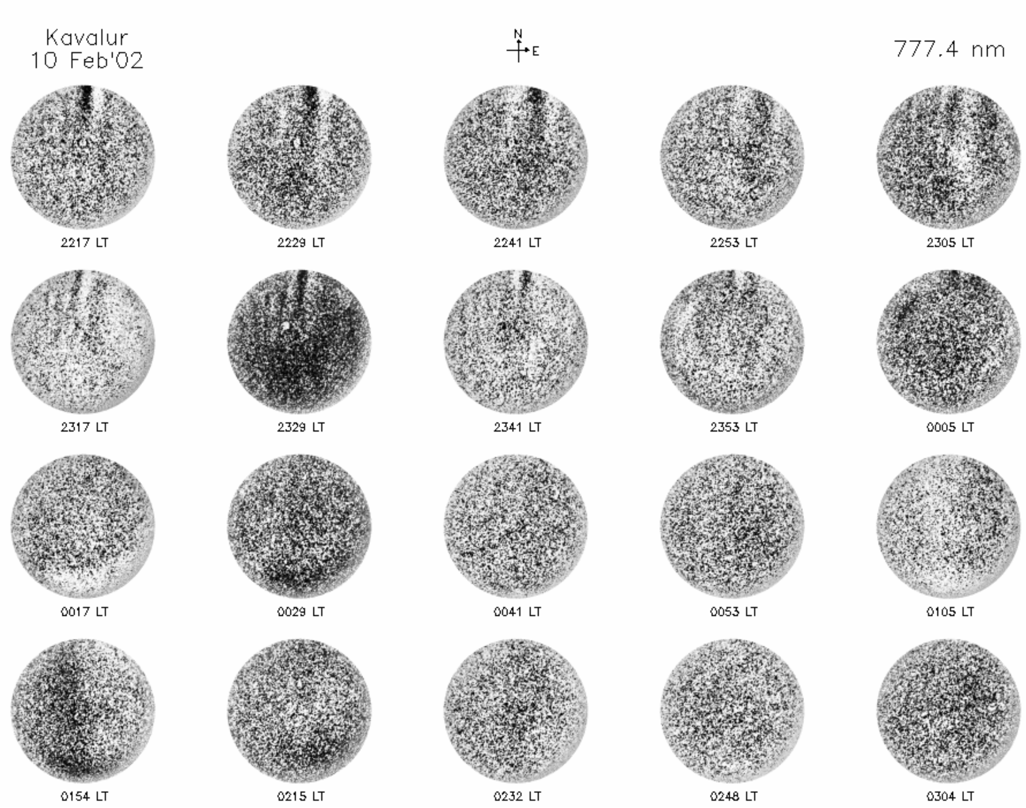

Figure 5.2 *A sequence of all sky images taken in the night of 10 February 2002 using 777.4 nm. The emission is weak in this case, showing some faint depletions in the pre-midnight period.*

A sequence of the all sky images taken in the night of 10 February 2002 using 630.0 nm emission is given in Figure 5.1. In this night the observations started around 1945 LT. Some dark patches can be seen in the northern part of the FOV in the image at 2013 LT, and intense depletion bands are seen from 2125 LT. Multiple bands of intense depletions occur in this night, and the bands could be seen till 0030 LT. Though some dark bands or patches could be seen in the images later in the night, no clear depletions could be identified. The sky was partially cloudy in the post-midnight period, making it impossible to image clear depletions. Figure 5.2 gives selected 777.4 nm images taken in the same night. It can be seem that the emission is very weak in this night. Though, some very faint depletion could be seen in the top two panels, the depletions are not visible in the images taken after the midnight.

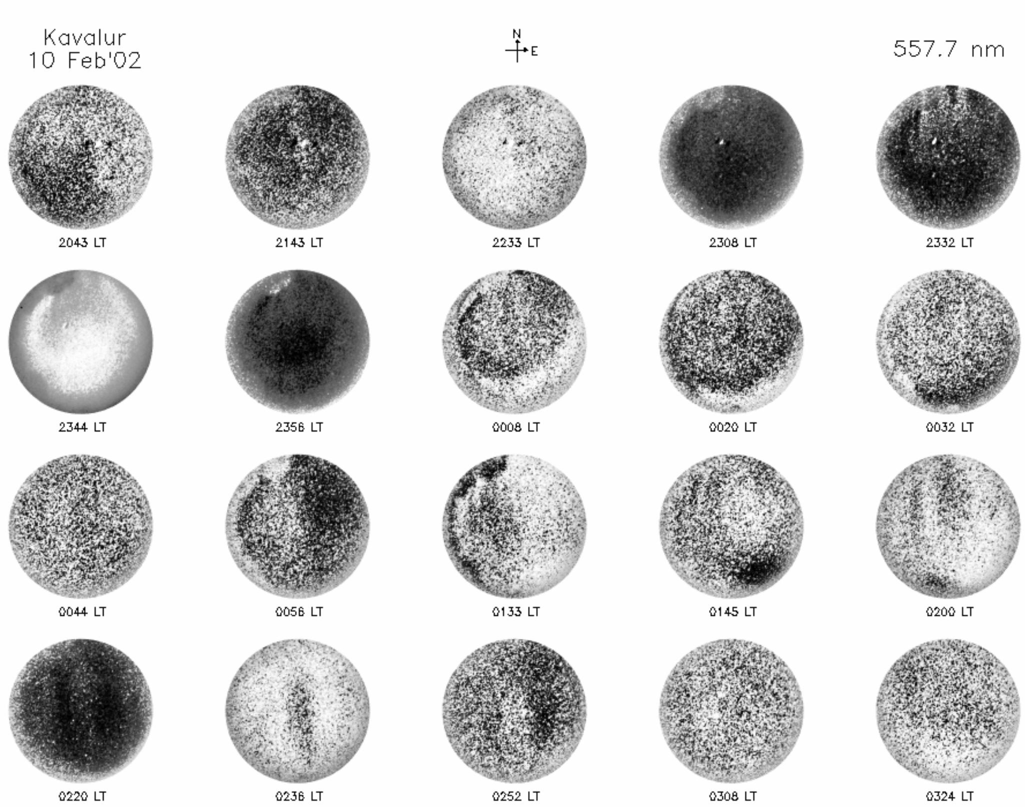

Figure 5.3 *A sequence of all sky images taken in the night of 10 February 2002 using 557.7 nm. Compared to the 630.0 nm depletions in Figure 5.1, the images here do not reveal any distinct plasma depletions.*

A set of selected 557.7 nm images recorded in this night is displayed in Figure 5.3. When compared to the intense multiple depletions in Figure 5.1, it is not possible to identify clear depletions in these images, though some dark bands could be seen in some of the frames. From the point of view of a time sequence of images, which can be analyzed to extract various details of plasma depletions, the observations in the night of 10 February 2002 mainly show depletions only in the 630.0 nm. Most of the earlier multi-wavelength observations also provided such type of results. However, conditions were not the same in all the nights of the observations in this study. Very intense depletions appeared in the 557.7 nm images also, in many of the nights, in complete contrast to most of the previous observations. Some of the examples of such observations are given below.

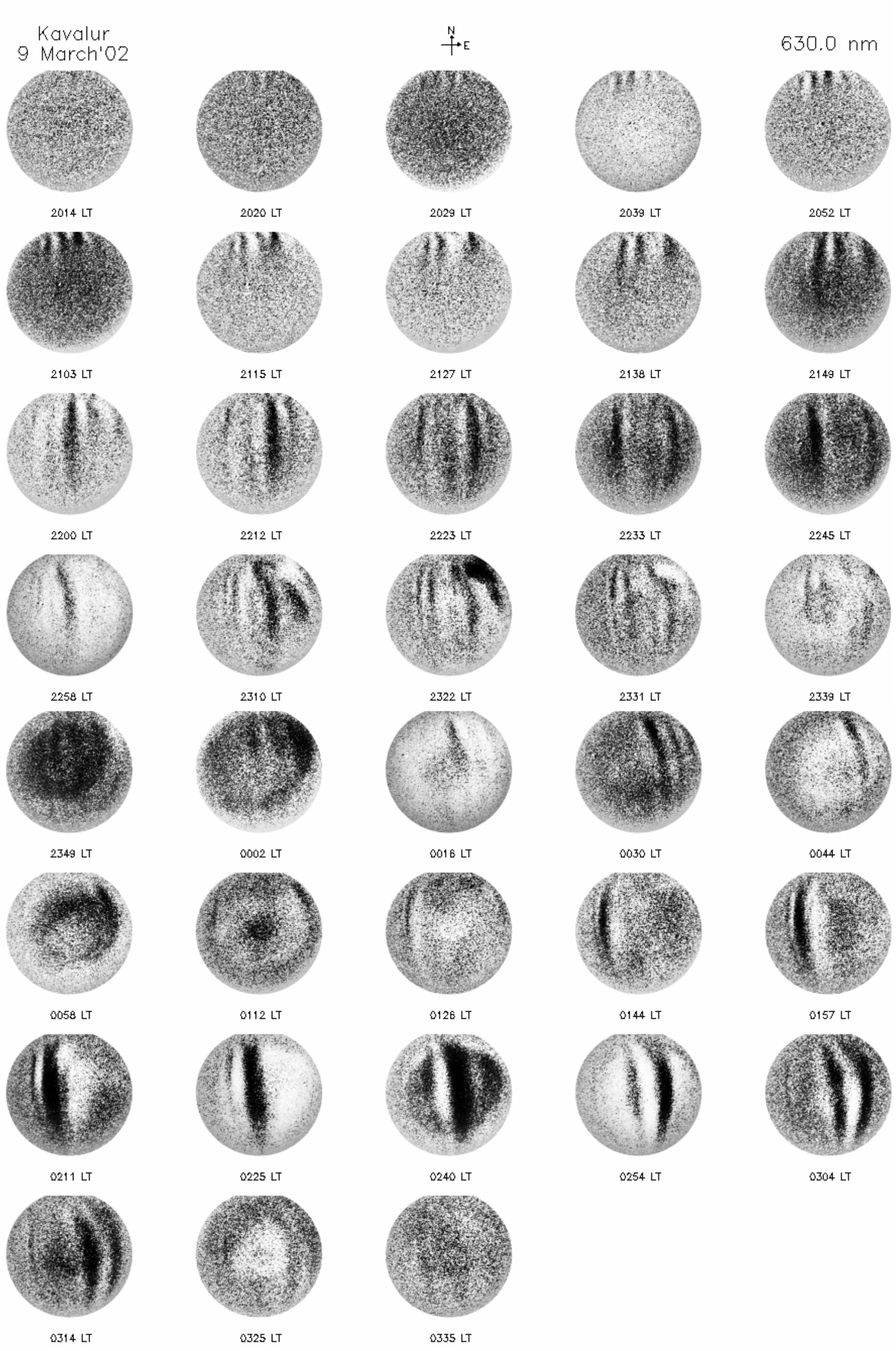

Figure 5.4 *A sequence of all sky images taken in the night of 9 March 2002 using 630.0 nm. Intense bands of plasma depletions can be seen in the images throughout the night.*

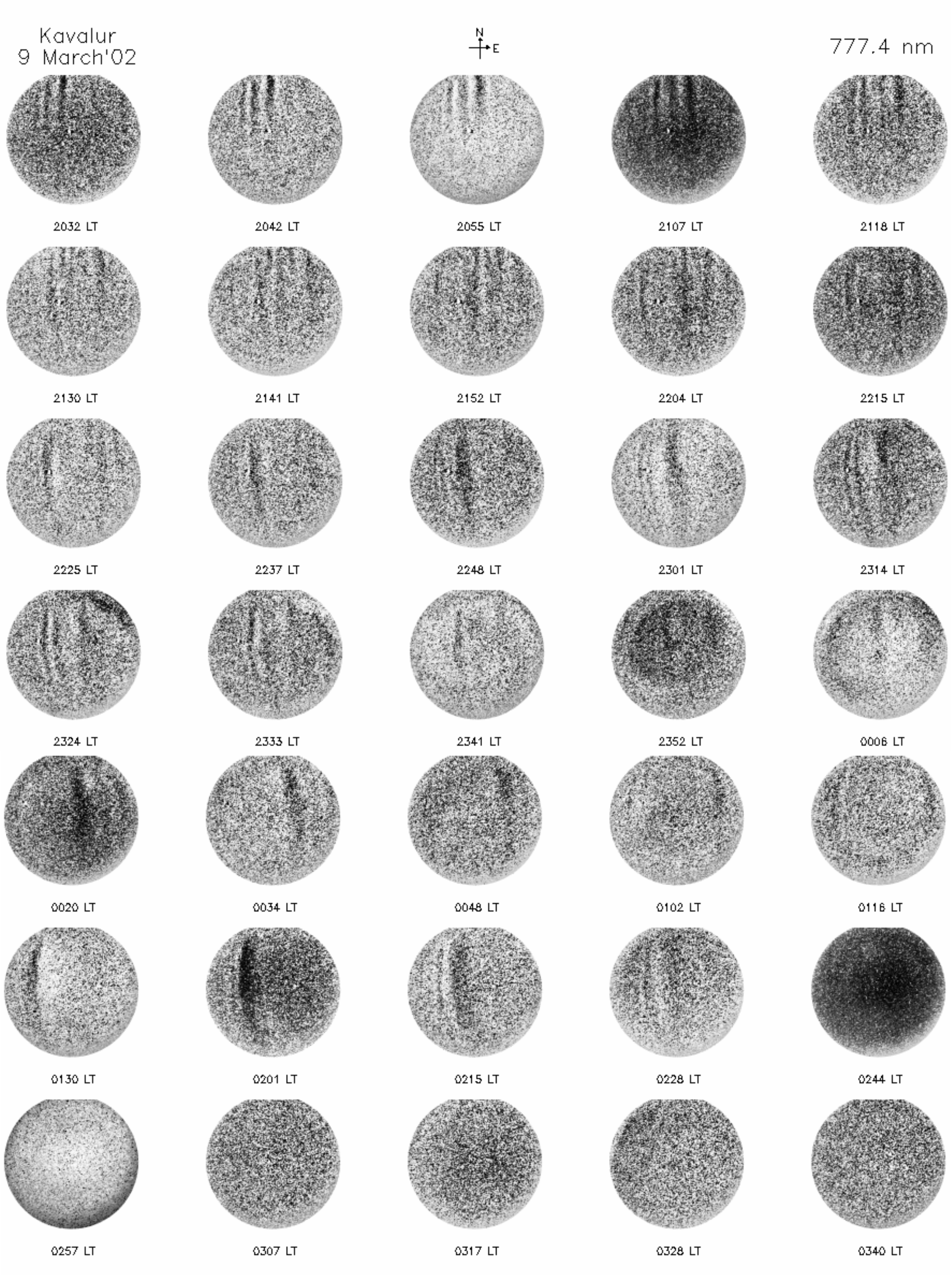

Figure 5.5 *A sequence of all sky images taken in the night of 9 March 2002 using 777.4 nm. Dark bands of plasma depletions can be seen in the images from the evening period till about 0230 LT.*

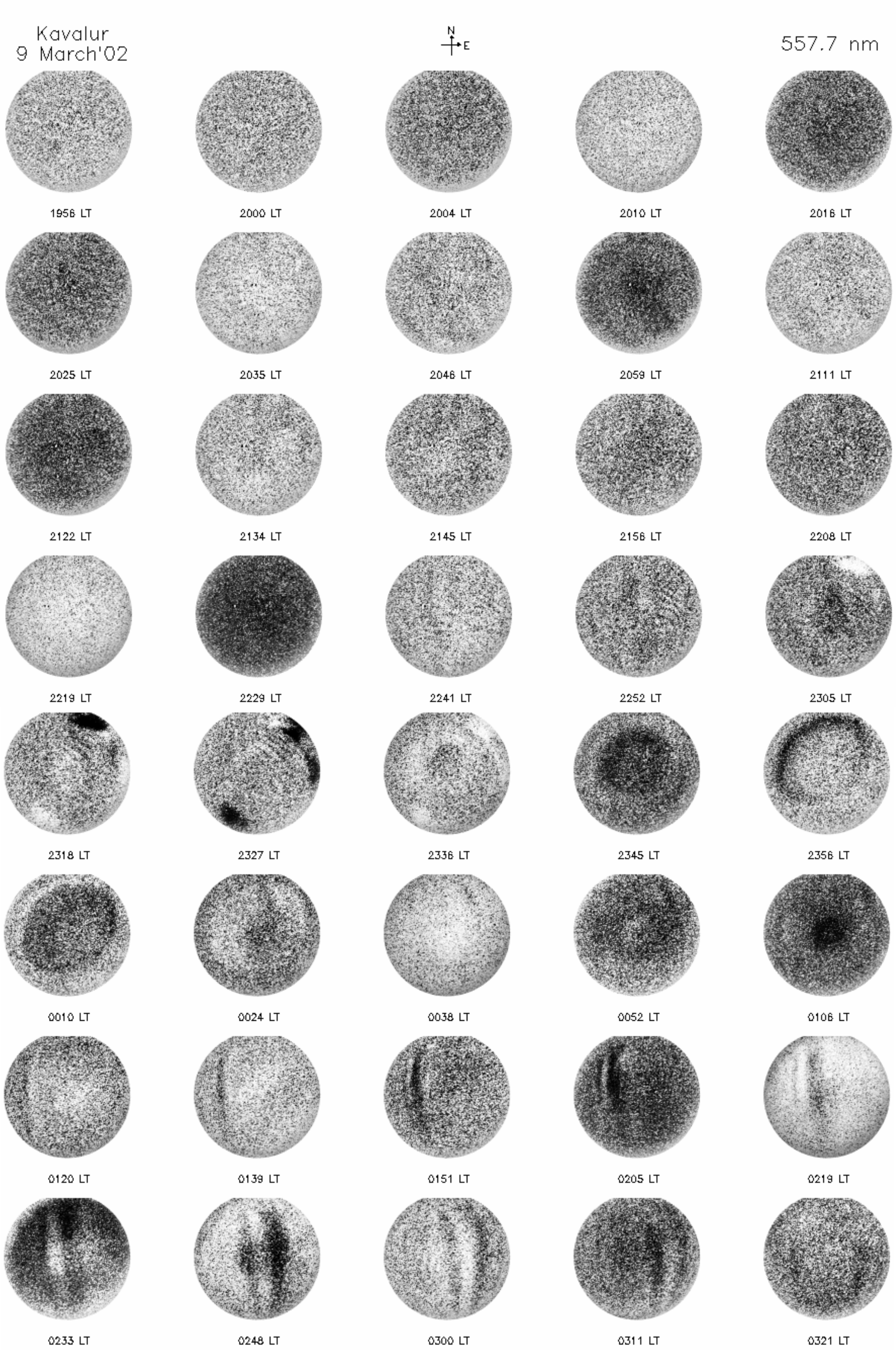

Figure 5.6 *A sequence of all sky images taken in the night of 9 March 2002 using 557.7 nm. Dark bands of plasma depletions can be seen in consecutive images during 0120-0311 LT. However, no clear depletion could be identified in the earlier images.*

Figures 5.4-5.5 give examples for the all sky images taken in the night of 9 March 2002 using the 630.0, and 777.4 nm emissions, respectively. Observations in this night could be conducted from the early evening period, till almost the Sunrise hours. Some dark patches can be seen in the northern edge of the image FOV in the 630.0 nm starting from 2020 LT. The corresponding 777.4 nm images, however show North-South aligned depletions bands. By around 2200 LT, the North-South aligned depletion bands that extend the entire FOV is seen in the 630.0 nm images also. The depletion activity in the 630.0 nm continue till about 0330 LT, and very intense depletions are seen during the 0130-0315 LT interval. The depletions in 777.4 nm also continue till about 0230 LT in this night, with most intense depletion appearing at about 0200 LT. Though, in principle, the 630.0 and 777.4 nm images in this night show depletions similar to the example illustrated in Figures 5.1-5.2, they differ in that the activity here is seen in the post-midnight period also, with very strong depletions bands in some of the images.

The sequence of 557.7 nm images taken in the night of 9 March 2002 is given in Figure 5.6. No clear depletion can be seen in the images in the pre-midnight period in this case. Note that the corresponding 630.0 and 777.4 nm images show clear depletions in the period 2200-2330 LT. However, except for some very faint dark features in some of the images, no similar depletions appear in the 557.7 nm in this period. In complete contrast, in the post-midnight period between 0120-0311 LT, the images show plasma depletions identical to that seen in the corresponding 630.0 nm images. One major difference between Figure 5.3 and Figure 5.6 is that, in the former there are not much observations after midnight, whereas in the latter case the images are available for the entire night.

The airglow intensity, which is basically a function of the plasma density, is supposed to decrease as the night progresses. Though the dissociative recombination producing 630.0 nm and the thermospheric 557.7 nm depends on the neutral density also, the overall intensity falls with the drop in the plasma density in the nighttime. However, it appears to be very unusual that the 557.7 nm do not reveal depletions in the evening period when it is supposed to be stronger, but do show them in the post-midnight period of weaker intensity. One possibility in the above example could be that the depletions in this case were very intense in the 0130-0330 LT period.

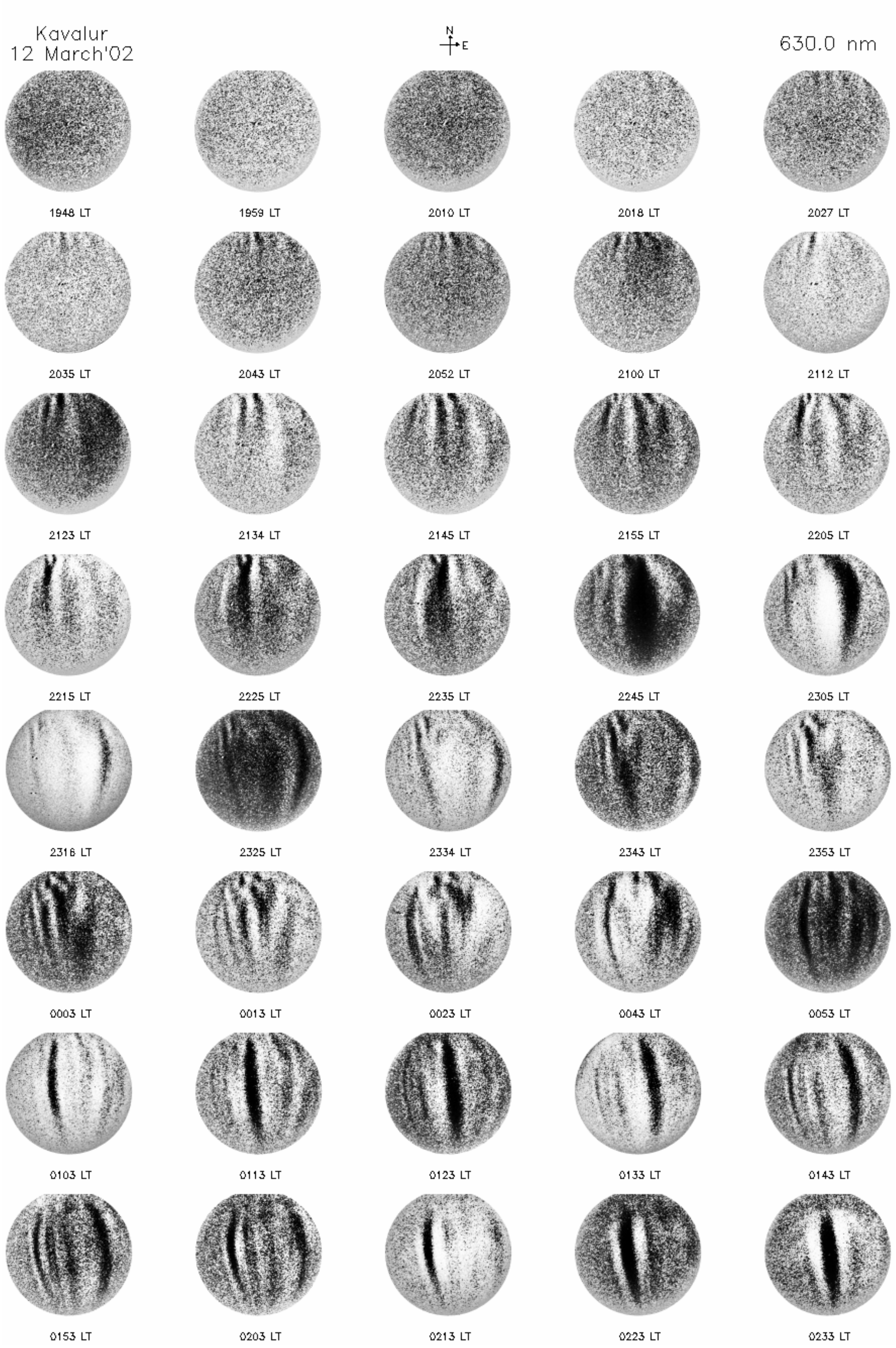

Figure 5.7 *A sequence of all sky images taken in the night of 12 March 2002 using 630.0 nm. Intense bands of plasma depletions appeared in the images throughout the night.*

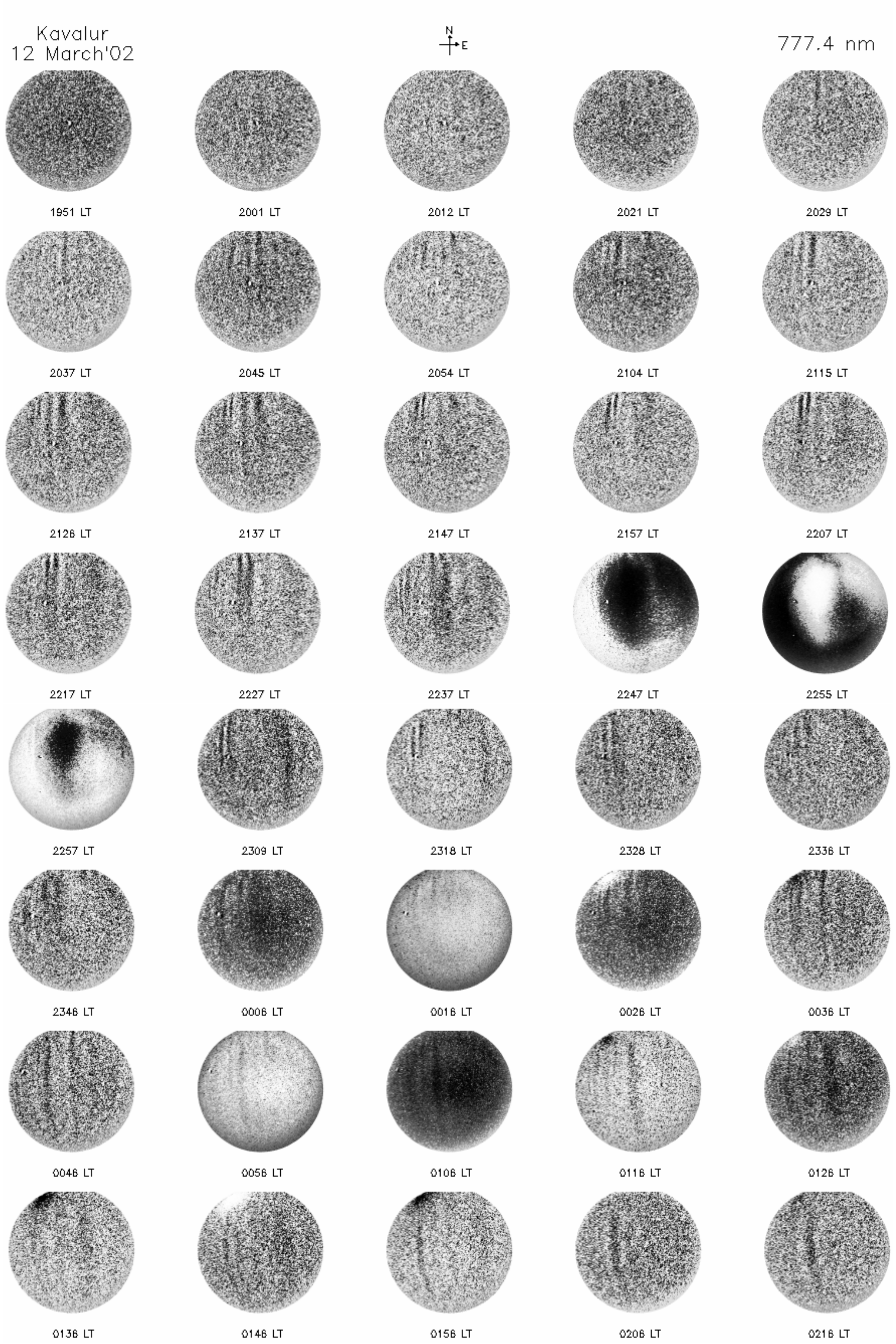

Figure 5.8 *A sequence of all sky images taken in the night of 12 March 2002 using 777.4 nm. Dark bands of plasma depletions could be seen in the images from the evening period till about 0230 LT.*

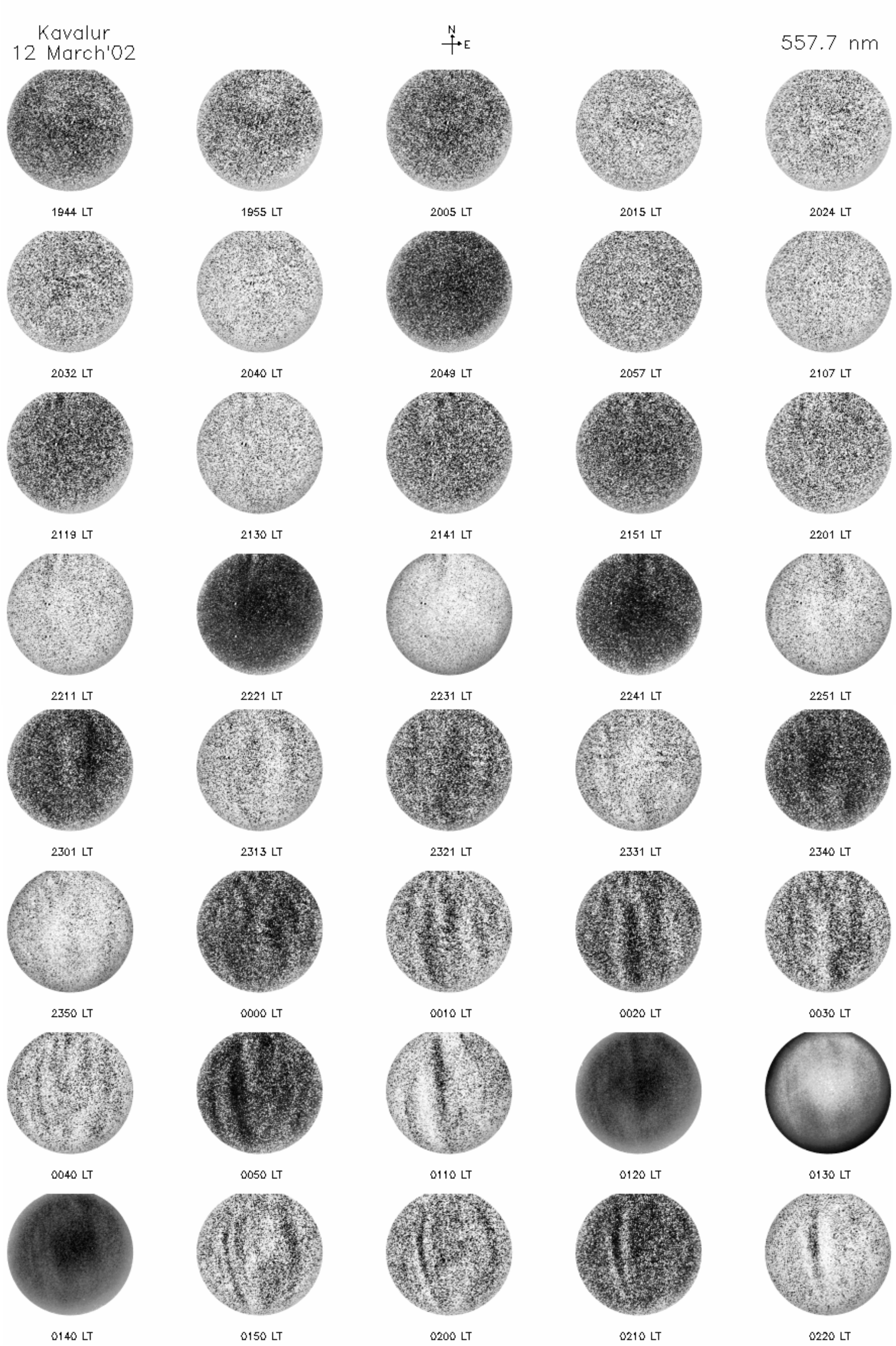

Figure 5.9 *A sequence of all sky images taken in the night of 12 March 2002 using 557.7 nm. Dark bands of plasma depletions can be seen in the images in the post-midnight period.*

Another set of examples are given in the Figures 5.7-5.9. Plasma depletions are seen in the 630.0 and 777.4 nm images from the Sunset period and the activity continues throughout the night. However, in the corresponding 557.7 nm images, the depletions are seen only after midnight. The images in the post-midnight period reveal depletions that resemble those seen in the corresponding 630.0 nm images. Further, it can be seen from Figure 5.7 that the 630.0 nm depletion at 0123 and 0223 LT are stronger than that at 0023 LT. However, all the three corresponding 557.7 nm images in Figure 5.9 do show depletions at these times. Thus, it is not just the strength of the depletion that makes it appear in the 557.7 nm images.

In order to understand more about the appearance of depletions in the 557.7 nm, all the observations in this period are analyzed in detail. It was found that similar depletion features were also observed in several other nights such as 12 and 15 February; 5, 9-14, and 17 March; 5-8, and 10-13 April. Table 5.1 summarizes the number of nights with depletions in 557.7 nm, compared to that in 630.0 nm. About 70% (19/27) of the nights with depletions in 630.0 nm are accompanied by remarkable depletions in 557.7 nm images. Note that this is the longest period and the most pronounced depletions in 557.7 nm ever observed at Kavalur, and also reported from elsewhere.

Table 5.1 *Number of nights with plasma depletions observed during February-April 2002.*

Month	Total Nights of Observations	Depletions in 557.7 (630.0) nm
February	10	3 (4)
March	12	8 (12)
April	11	8 (11)

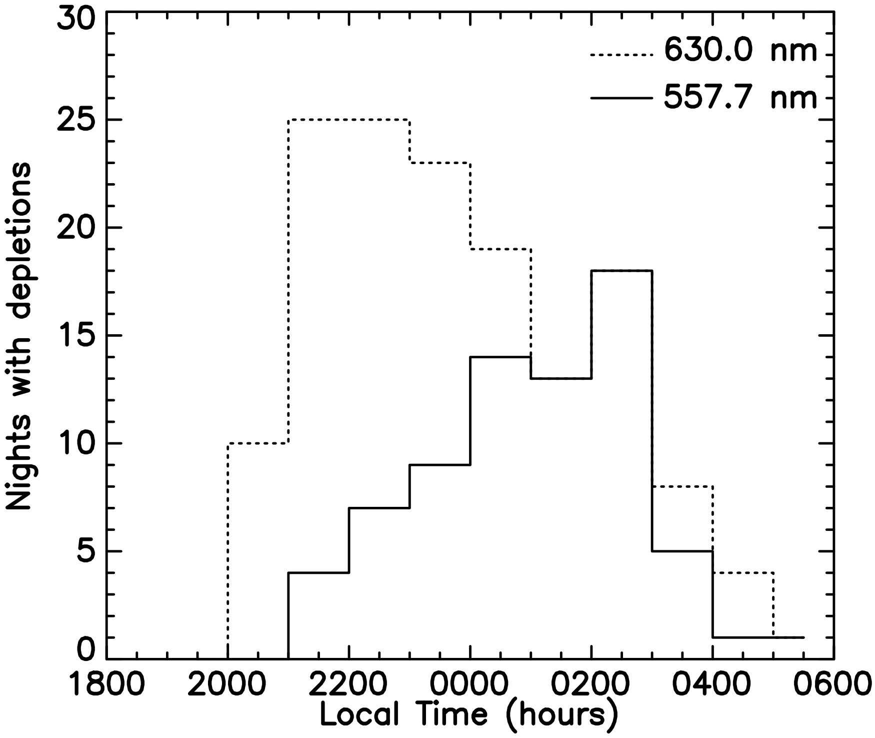

Figure 5.10 *Occurrence of depletions at each hour of the night in 630.0, and 557.7 images during February-April in 2002.*

To further investigate the appearance of depletions in the 557.7 nm images in several nights, the occurrence of plasma depletions at every hour in the night during the observations in February-April in 2002 are plotted in Figure 5.10. Here, the occurrence in 557.7 nm is compared with that in the corresponding 630.0 nm images. The 630.0 nm depletions show a clear maximum in their occurrence during 2130-2330 LT time intervals. In contrast, the occurrence of depletions in that period is very less in the 557.7 nm images, but it gradually shows an increase towards the midnight. During 0100-0300 LT period, both the 630.0 and 557.7 nm depletions show very similar occurrence. The statistics given in Figure 5.10 reveals that plasma depletions are seen in 557.7 nm images mostly in the post-midnight period, though the 630.0 nm emissions do show the occurrence of depletions even in the earlier hours of the same nights. This suggests that the 557.7 nm images are suitable to study plasma depletions in the post-midnight period.

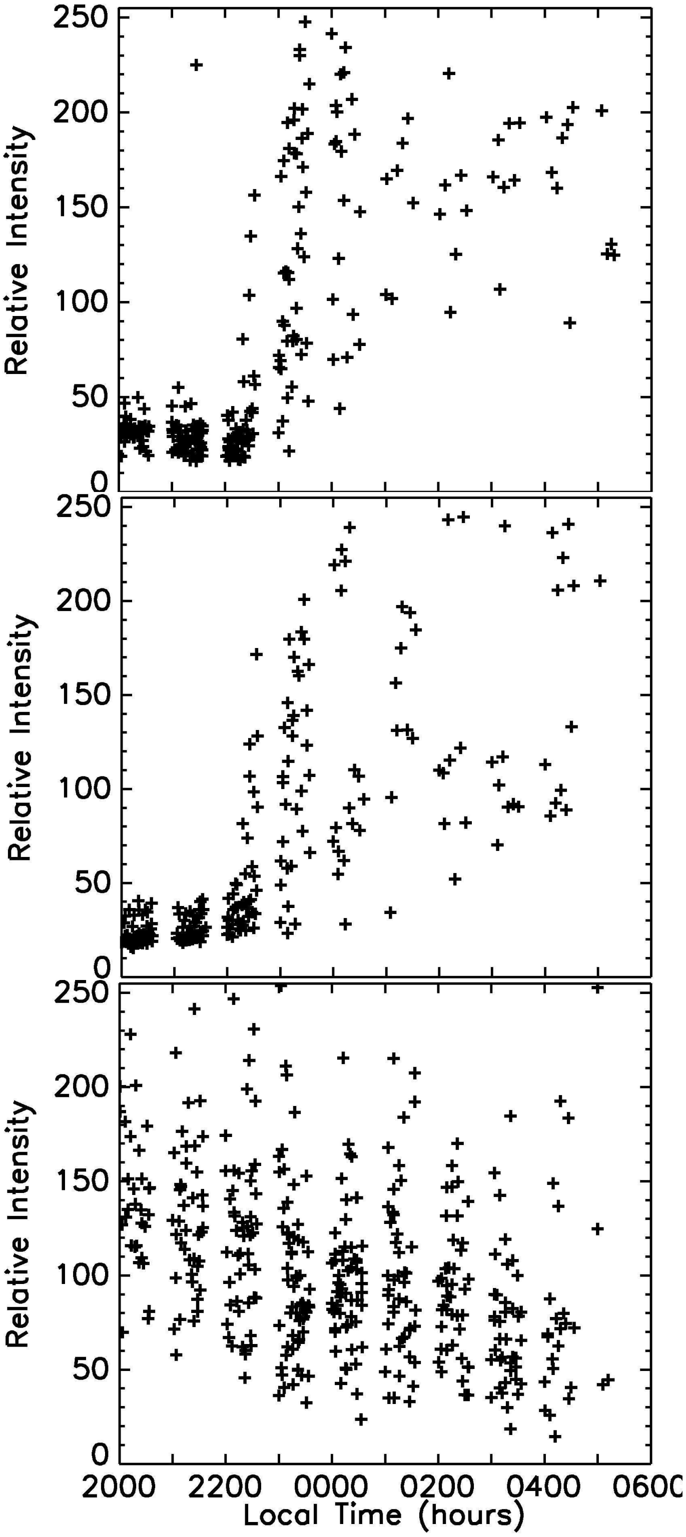

Figure 5.11 *The nocturnal variation of the total 630.0 (top), 557.7 nm (middle) and 777.4 nm (bottom) intensities (in relative units of 8-bit scale), measured near the center of the images.*

One possibility for the depletions to appear in the 557.7 nm images only in the post-midnight period could be that the intensity of the emission is much less in the pre-midnight period, and improves in the post-midnight hours. In this case, if the emission is weak, it might not be able to identify depletions in the pre-midnight period. In order to confirm such a possibility, the relative intensities of all the three emission are displayed in Figure 5.11. The relative intensities plotted in the figures are the average intensities in a rectangular area of 10x10 pixels near the center of each image. It can be seen from Figure 5.11 that the nocturnal variation of the 557.7 and 630.0 nm intensities are very identical, both in the pre-midnight as well as the post-midnight cases. The intensities are less in the period 1900-2200 LT, but rapidly increase after 2200 LT for both the emissions. However, the occurrences of the depletions observed in these emissions (Figure 5.10) are very different, that the depletions in 630.0 nm become pronounced during 2000-0000 LT while the maximum in 557.7 nm lies between 0200 and 0300 LT. For a comparison, the nocturnal variation of the 777.4 nm intensity is also given in Figure 5.11. The intensity in this case is more in the evening hours, and reveals a gradual decreasing tendency with time, and becoming very weak by 0200 LT. This explains the appearance of depletions in 777.4 nm from the post-sunset hours till about 0200 LT in most of the nights.

In 630.0 nm, depletions can be observed in the evening hours, even when the emission is weak, with the maximum occurrence in the pre-midnight period. By contrast, the depletions in 557.7 nm starts appearing only after the sudden increase in intensity at around 2200 LT, and the occurrence of depletions reach its peak in the post-midnight hours. This behavior clearly suggests that, when the 557.7 nm intensity in the evening hours from the thermosphere is weak, the integrated images taken from the ground cannot reveal the features in the ionosphere. This indicates that the less intense thermospheric component of 557.7 nm in the evening period is masked by its mesospheric component. Note that the thermospheric component of 557.7 nm intensity is usually very weak [Shepherd *et al.*, 1997], and could be masked by the strong mesospheric component making the intensity variations caused by the F-region plasma depletions difficult to detect from ground [Mendillo *et al.*, 1997; Takahashi *et al.*, 2001].

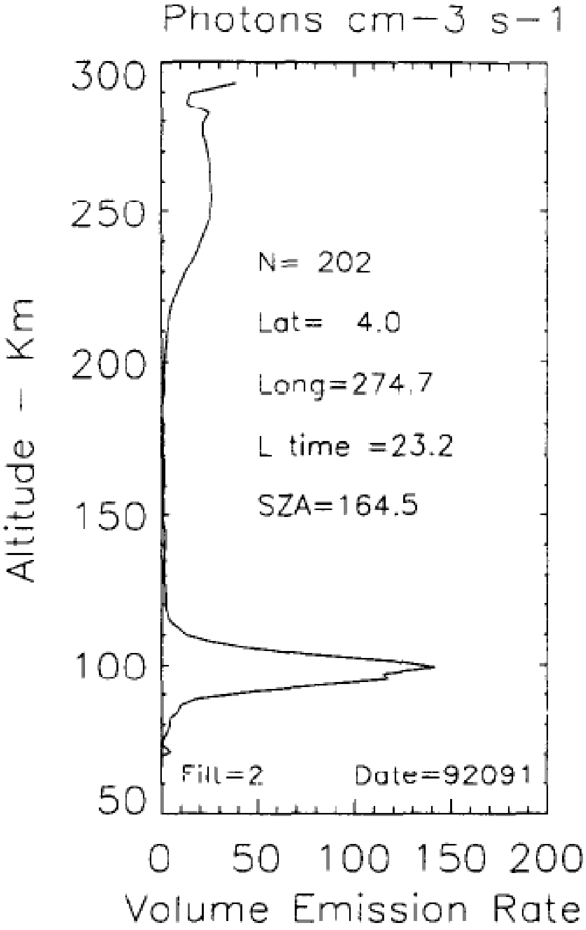

Figure 5.12 *Vertical profile of 557.7 nm intensity measured by WINDII. The figure is taken from Shepherd et al. [1997]. The measurements show peak around 100 km altitude and a very weak secondary maximum around 250 km region.*

The 557.7 nm vertical profile measured by WIND Imaging Interferometer (WINDII) onboard the Upper Atmospheric Research Satellite (UARS), which recently fell on Earth, is shown in Figure 5.12. The result is taken from the work of Shepherd *et al.,* [1997]. It can be seen that the main peak of the emission is around 100 km, and in comparison, the secondary thermospheric peak around 250 km is almost insignificant. Thus, from this result, it is reasonable to conclude that the thermospheric component will be masked by the stronger mesospheric component. If this is the case, then it should not be possible to observe any thermospheric features in the ground based 557.7 nm images.

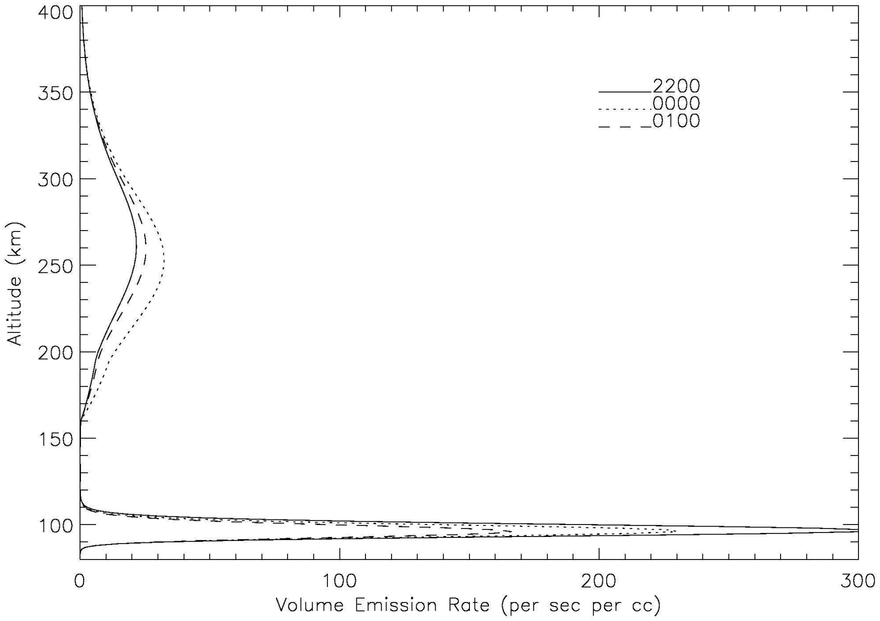

Figure 5.13 *Vertical profile of 557.7 nm volume emission rate simulated using IRI and MSISE models for equinox conditions in 2002 for 2200, 0000, and 0100 LT periods.*

However, Figure 5.10 shows that the masking effect is not present throughout the night, or at least in the post-midnight period of some nights during February-April in 2002. The observations reported by Shepherd *et al.*, [1997] are taken around 2300 LT. In order to check how the intensities might behave at different local times in the night in the equinox period of 2002, the volume emission profile is simulated for different local times in the night. The volume emission rate for the mesospheric component of 557.7 nm emission (V_M) arises through Barth mechanism [McDade *et al.*, 1986] given by,

$$V_M = \frac{A_5 k_1 [O]^3 ([N_2] + [O_2])}{(A_6 + k_5 [O_2])(C'^{O_2} [O_2] + C'^{O} [O])} \tag{5.1}$$

where, A_5 is the 557.7 nm line (O^1D-O^1S) transition probability, k_1 is the rate coefficient for the three body recombination of atomic oxygen, A_6 is the inverse radiative life time of O^1S state, k_5 is the quenching coefficient of O^1S state by O_2. C'^{O2} and C'^{O} are the empirical parameters provided by McDade *et al.*, [1986].

The thermospheric 557.7 nm emission arises through the dissociative recombination of O_2^+ [Peterson *et al.*, 1966], which is produced through the charge exchange reaction between O^+ and neutrals, mainly O_2. The volume emission rate of the thermospheric 557.7 nm is given as,

$$V_T = \left\{1 + \frac{A_{2S}}{A_{1S}}\right\}^{-1} \mu_S \gamma [O_2][e] \tag{5.2}$$

where A_{1S} and A_{2S} are the transition probabilities corresponding to the 557.7 nm and 297.2 nm emissions, γ is the rate of the charge exchange process, μ_S is the quantum yield of the O^1S state responsible for the 557.7 nm emission, and $[O_2]$ and [e] stands for the oxygen and electron densities, respectively. The laboratory experiments have shown O^1S quantum yields of 3-4% for electron temperatures (T_e) in the range of 600-1100 K [Peverall *et al.*, 2000], but are much less than the values inferred from rocket measurements [Sobral *et al.*, 1992]. In view of this large discrepancy, a quantum yield of 8% [Sobral *et al.*, 1992] is used in the simulations for both solar maximum and solar minimum, which is justified considering the complexity involved in the laboratory experiments. The charge exchange rate is given by St.-Maurice and Torr [1978] and the transition probabilities are taken from Baluja and Zeippen [1988] (For detail see papers listed in Singh *et al.* [1995]; Vlasov *et al.* [2005]). The O_2 density and neutral temperature are computed using the Mass Spectrometer Incoherent Scatter (MSISE-90) model [Hedin, 1991], while the electron density and electron temperature are derived from the International Reference Ionosphere (IRI-01) model [Bilitza, 2001].

The simulated emission profiles are given in Figure 5.13. It can be seen that the mesospheric peak is still much stronger than the corresponding thermospheric peak at all local times. However, the maximum of the mesospheric emission decreases with local time in the night, where as the thermospheric peak tend to increase at the midnight. This could be very significant considering that the ground based instruments are sensitive to the integrated signal. Note that the half width of the mesospheric component is much narrower compared to that of the thermospheric component, and hence it will reflect in the integrated intensity.

To further understand the appearance of depletions in 557.7 nm observed in 2002, the mesospheric and the thermospheric components are simulated and the ratio of their integrated intensities is calculated. It can be seen from Equation (5.1) that the mesospheric intensity is sensitive to the atomic oxygen density. Equation (5.2) reveals that the dissociative recombination depends on electron density as well as the neutral density. The integrated intensities for the mesospheric (80-120 km altitude) and the thermospheric (200-600 km altitude) components under quiet geomagnetic conditions during the equinox of 2002 (near solar maximum) and 1996 (solar minimum) are simulated.

The simulation results are illustrated in Figure 5.14. The total 557.7 nm intensity exhibits lower values in the 1900-2200 LT, increasing thereafter, and attains peak value in the post-midnight period around 0100 LT (Figure 5.14a). This nocturnal variation agrees with that of the observed intensity in Figure 5.11 middle panel. The mesospheric 557.7 nm intensity at solar maximum is greater than that in the solar minimum by a factor of about 2. By contrast, the thermospheric intensity at solar minimum is very small, but during solar maximum is much greater and drastically enhances after 2300 LT. Note in the solar minimum, the thermospheric component of 557.7 nm emission is much weaker than the mesospheric component throughout the night. Therefore, it is unlikely to observe the thermospheric emissions during solar minimum. Moreover, during the pre-midnight period 2000-2300 LT, the mesospheric intensity is constantly stronger than thermospheric intensity either in solar maximum or solar minimum, and therefore it is also difficult to observe the thermospheric emission. In contrast, the thermospheric component becomes stronger in the post midnight hours in the solar maximum and the ratio of the thermospheric to mesospheric intensities reaches a maximum at 0200 LT. The mesospheric region is very dynamic and photo chemically active, but least explored, and hence the atomic oxygen density derived from the models may have limitations. In order to verify how well the simulation reproduces the mesospheric emission, the simulated results are compared with the intensities extracted from the WINDII measurements in the same latitude region for the equinox period of 1992 [Zhang and Shepherd, 1999*; Zhang et al.,* 2001]. Figure 5.14a confirms that the simulated results are consistent with the WINDII measurements.

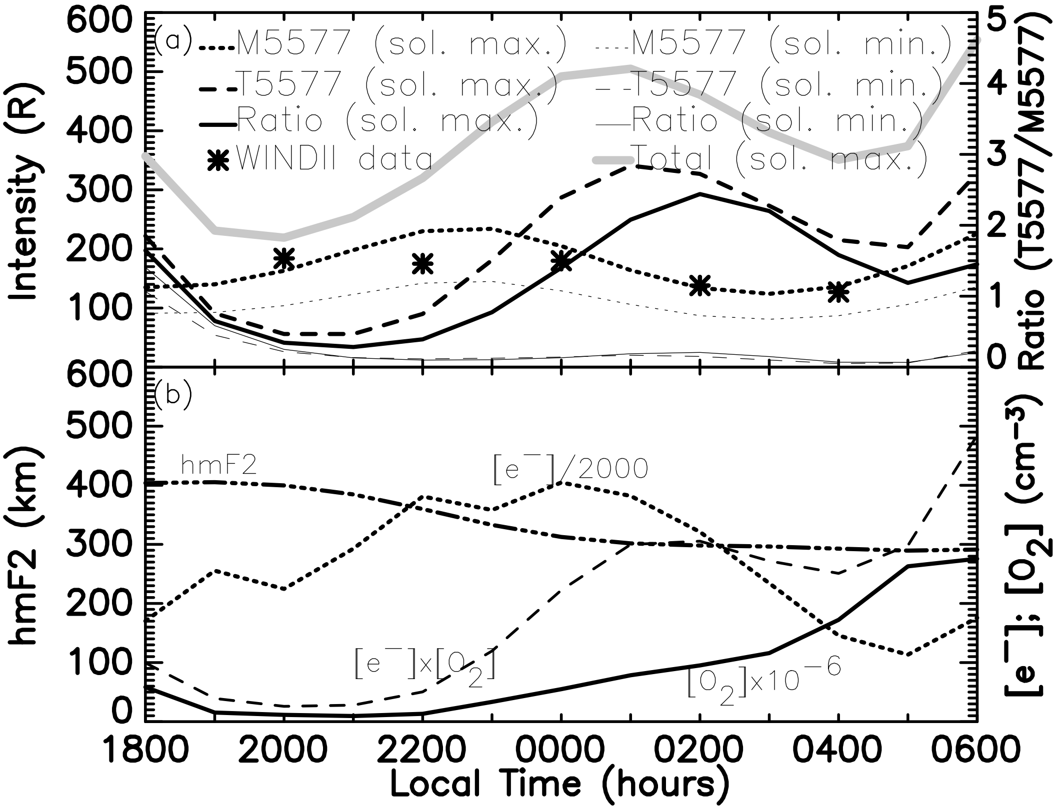

Figure 5.14 *The simulations of 557.7 nm emission using the IRI-01 and MSIS-90 models under equinoctial conditions. (a) The dashed, dotted and solid lines stand for the 557.7 nm emission from the thermosphere, from the mesosphere and the ratio of the thermospheric to the mesospheric components, respectively. The heavy and the thin curves denote the years of solar maximum in 2002 and solar minimum in 1996. The asterisks represent the 557.7 nm intensity extracted from the WINDII measurements for the latitude corresponding to that of Kavalur, made in the equinox period in 1992. The thick, light curve gives the total 557.7 nm intensity for the year 2002. (b) The hmF2 as well as the electron density, O_2 density, and their product at the altitude of the emission peak in the nights of 2002. The quantities to the right of $[e^-]$ and $[O_2]$ are the scaling factors used to fit the values within the range of the Y-axis used, and applies to the product $[e^-]x[O_2]$ as well. The concentration is in the c.g.s unit.*

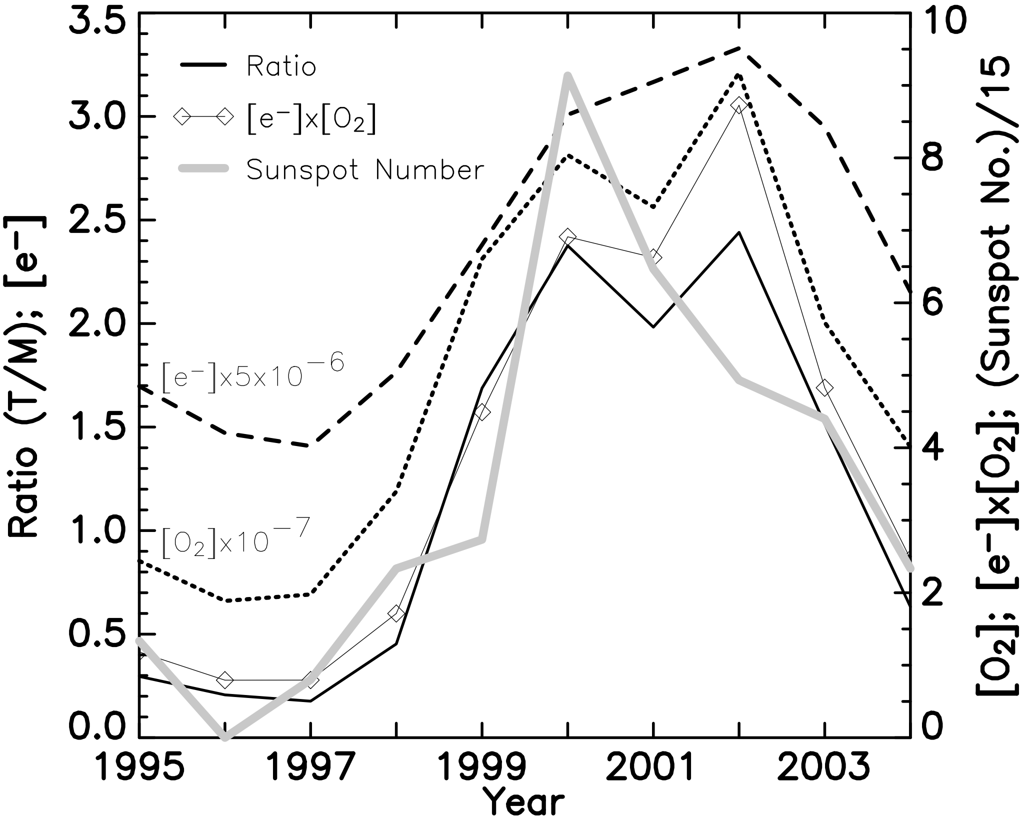

Figure 5.15 *The ratio of thermospheric to the mesospheric 557.7 nm intensities as well as the electron density, O_2 density, and their product in the equinox period from 1995 to 2004. The quantities to the right of $[e^-]$ and $[O_2]$ are the scaling factors used to fit the values within the range of the Y-axis used, and applies to the product $[e^-]x[O_2]$ as well. The concentration is in the c.g.s unit.*

In Figure 5.14b, the nocturnal variation of the electron $[e^-]$ and oxygen $[O_2]$ densities corresponding to the altitude of peak thermospheric 557.7 nm emission for the solar maximum of the year 2002, their product, as well as the altitude of the peak electron density (hmF2) are displayed. The electron density has higher values in the period 2200-0200 LT, and the nocturnal variation of the product of $[e^-]$ and $[O_2]$ is identical to that of the thermospheric component of 557.7 nm emission (Figure 5.14a). The hmF2 shows a gradual decrease with time, with a reduction of about 100 km from the sunset to 0100 LT.

To understand the solar activity variation, we further calculated the ratio at 0200 LT in the equinox period from 1995 to 2004. Figure 5.15 illustrates that the ratio is less than one in the solar minimum, and rapidly increases near the solar maximum years, reaching values about two. Similarly, the electron and oxygen densities at the peak altitude of the thermospheric emission at 0200 LT vary accordingly with the solar activity.

The results show that the observed occurrence of depletions in 557.7 nm and the ratio of the simulated thermospheric to mesospheric emissions concurrently reach their maximum at about 0200 LT. The higher value of the ratio implies the masking of the thermospheric component to be insignificant in the post-midnight period of 2002. Figure 5.15 further demonstrates that during post-midnight period the masking is efficient in the solar minimum years, but not in the solar maximum. The simulations during solar maximum reveal that the integrated 557.7 nm emission is dominated by the mesospheric component in the pre-midnight hours, while the thermospheric component become significant in the post-midnight period. It can be seen that the thermospheric intensity is weaker than the mesospheric intensity in the evening hours (2000-2330 LT). Bittencourt and Sahai [1979] find that the higher F layer altitude slows down the dissociative recombination and results in less thermospheric emission. Figure 5.14b illustrates that the F2 peak height (hmF2) descends by about 100 km from 2000 LT to 0100 LT in the equinoctial period of 2002. The F2 layer at a higher altitude results in the weak thermospheric 557.7 nm intensity between 2000 LT and 2330 LT. However, the F2 layer descent increases the O_2 density and in turn enhances the thermospheric emission, which becomes stronger than the mesospheric emission after 2330 LT. Meanwhile, it can be seen that the electron density also increases towards midnight, which adds to the greater thermospheric emission in the post-midnight period and reaches the peak emission around 0100 LT. Moreover, the airglow intensity increases after the midnight could be also caused by equator ward movement of the electron density crest associated with the equatorial anomaly by westward electric fields. The mesospheric intensity becomes very weak around midnight due to diurnal tide [Shepherd *et al.,* 1995], causing the ratio to be much higher.

Similar tendencies in solar activity variations of the electron, oxygen densities and their product as well as the ratio of the thermospheric to the mesospheric intensities of the 557.7 nm suggest that the plasma depletions in 557.7 nm emission most likely occur in the post-midnight period in the solar maximum (Figure 5.15). While the mesospheric contamination can mask out the depletions in the thermospheric 557.7 nm, there is no such secondary source for the 630.0 nm emission. Thus, in 630.0 nm, one would expect to observe the depletions even if the intensity is low. This is evident from the higher occurrence during 2000-0000 LT (Figure 5.10) even though the emission is less intense during 2100-2200 LT (Figure 5.11 middle panel), and also explains the difference in the observed occurrence of depletions in 557.7 and 630.0 nm (Figure 5.10). Note that the masking effect significantly affects the chances of observing the 557.7 nm depletions. Meanwhile, the much stronger 630.0 nm emission intensity might result in the associated depletion having a better chance to be observed. The two facts might be the reason for the depletions of 630.0 nm appearing more frequent than that of the 557.7 nm during the observation period.

In conclusion, due to enhancement of the thermospheric component of the 557.7 nm emission and/or the less efficient masking effect, the occurrence of depletions becomes pronounced in the post-midnight period of the solar maximum. By contrast, the significant mask results in the 557.7 nm depletions of the thermosphere being unlikely observed during years of the solar minimum. The simulation further shows that the recombination process related to the ionospheric height as well as the electron and oxygen densities play important roles.

5.2 Appearance in 630.0 nm

In all sky images, plasma depletions are expected to appear as intensity depleted bands forming near geomagnetic equator and extending almost symmetrically in the magnetic N-S direction, if imaged from an equatorial or near equatorial station. But this is not the case always. The all sky observations conducted from Kavalur (12.5˚N, 78.8˚E, 4.6˚N, geomagnetic), INDIA, have shown that in the post sunset hours when the observations begin, the depletions in 630.0 nm airglow images appear as dark patches of low intensity regions entering the field of view (FOV) from the northern end. These patches later grow equator ward, and after a couple of hours appear as fully N-S aligned plasma depletion. Thus, one could argue that these are the irregularities generated at low or mid latitudes and mapped to the equatorial regions along the geomagnetic field lines.

Equatorial Spread-F (ESF) irregularities in the nighttime ionosphere manifest as dark bands of reduced intensity in all sky airglow images, known as plasma depletions [Weber *et al.,* 1978]. It is generally understood that the depletions elongate to low- and mid-latitudes depending on the upward (vertical) movement of the irregularities at the equator [Weber *et al.,* 1978; Mendillo *et al.,* 2005]. The less density plasma associated with the irregularities when transported along the geomagnetic field lines to off-equatorial latitudes modifies the airglow intensities, and result in North-South (N-S) aligned depletions. This implies that the irregularities develop at the equatorial region and reach to off-equatorial latitudes with their vertical evolution. The larger field-of-view (FOV) of an all sky imager makes it an ideal tool to monitor such field-aligned depletions that extend hundreds of kilometers along the N-S, and confirm the origin and development from sequence of images.

Several all sky camera experiments have been conducted using 630.0, 777.4, and/or 557.7 nm airglow emissions [Rohrbaugh *et al*., 1989; Sales *et al*., 1996; Weber *et al*, 1996; Fagundes *et al*., 1997; Kelley *et al*., 2000; Sahai *et al*., 2000; Abalde *et al*., 2001; Otsuka *et al*., 2002; Sinha *et al*., 2003; Shiokawa *et al*., 2004; Mendillo *et al*., 1997]. These studies invariably report that the depletions extend from equatorial regions to low- and mid-latitudes (poleward extension). This work, on the other hand, presents the observations of depletions in 630.0 nm airglow images that appear at the northern edge in the post-sunset hours, and are seen extending towards the equator in the later hours. The all sky observations from Kavalur, during the equinox period in the solar maximum of 2002 provided a large data set, enabling the study of the characteristics of depletions in different wavelengths, and their day-to-day variations. Several nights in this observation period showed depletions in the post-sunset as well as post-midnight period, but there were differences in their appearance in different filters, as well at different hours of the night. In the post-sunset hours (prior to 2200 LT), the 630.0 nm depletions appeared in the FOV from northern latitudes as dark patches, which subsequently grew equator ward.

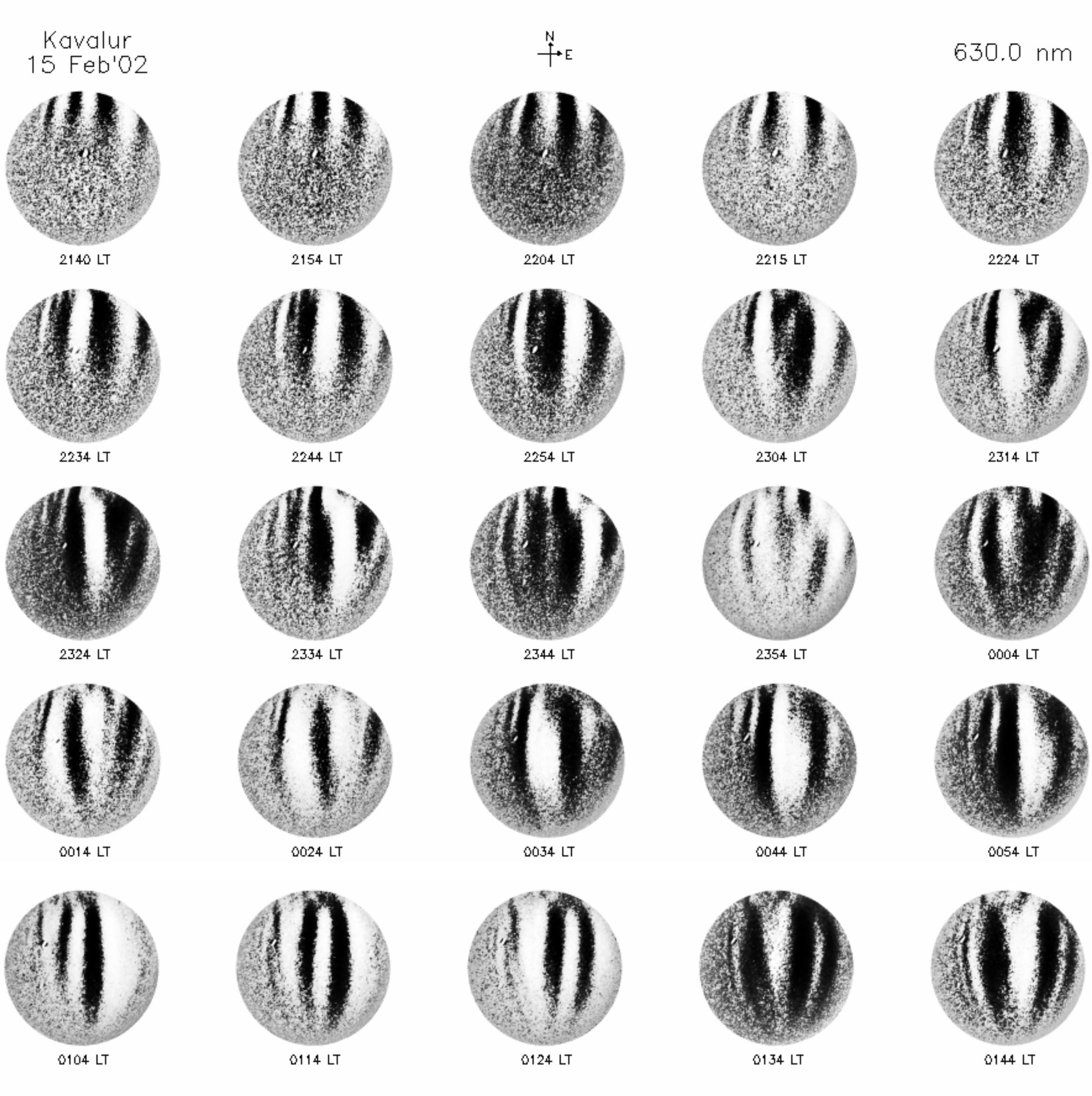

Figure 5.16 *A series from the 630.0 nm images taken in the night of 15 February 2002, illustrating the dark patches that enter the FOV from north, which grow subsequently to extend the whole FOV in the N-S direction by midnight.*

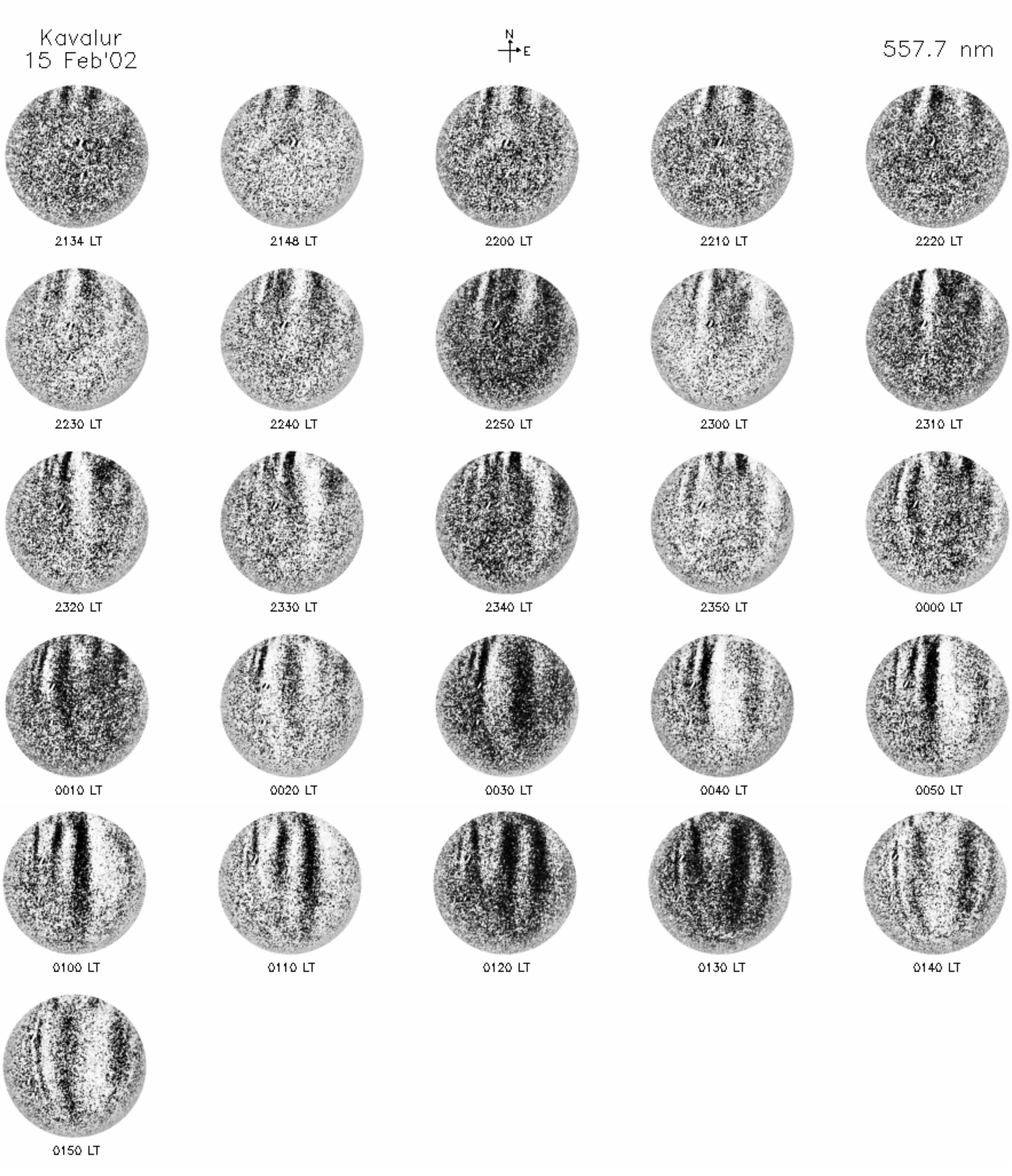

Figure 5.17 *A series from the 557.7 nm images taken in the night of 15 February 2002, illustrating the dark patches that enter the FOV from north, which grow subsequently to extend the whole FOV in the N-S direction by midnight. Note that this is one of the rare cases when depletion patches were seen as early as 2130 LT.*

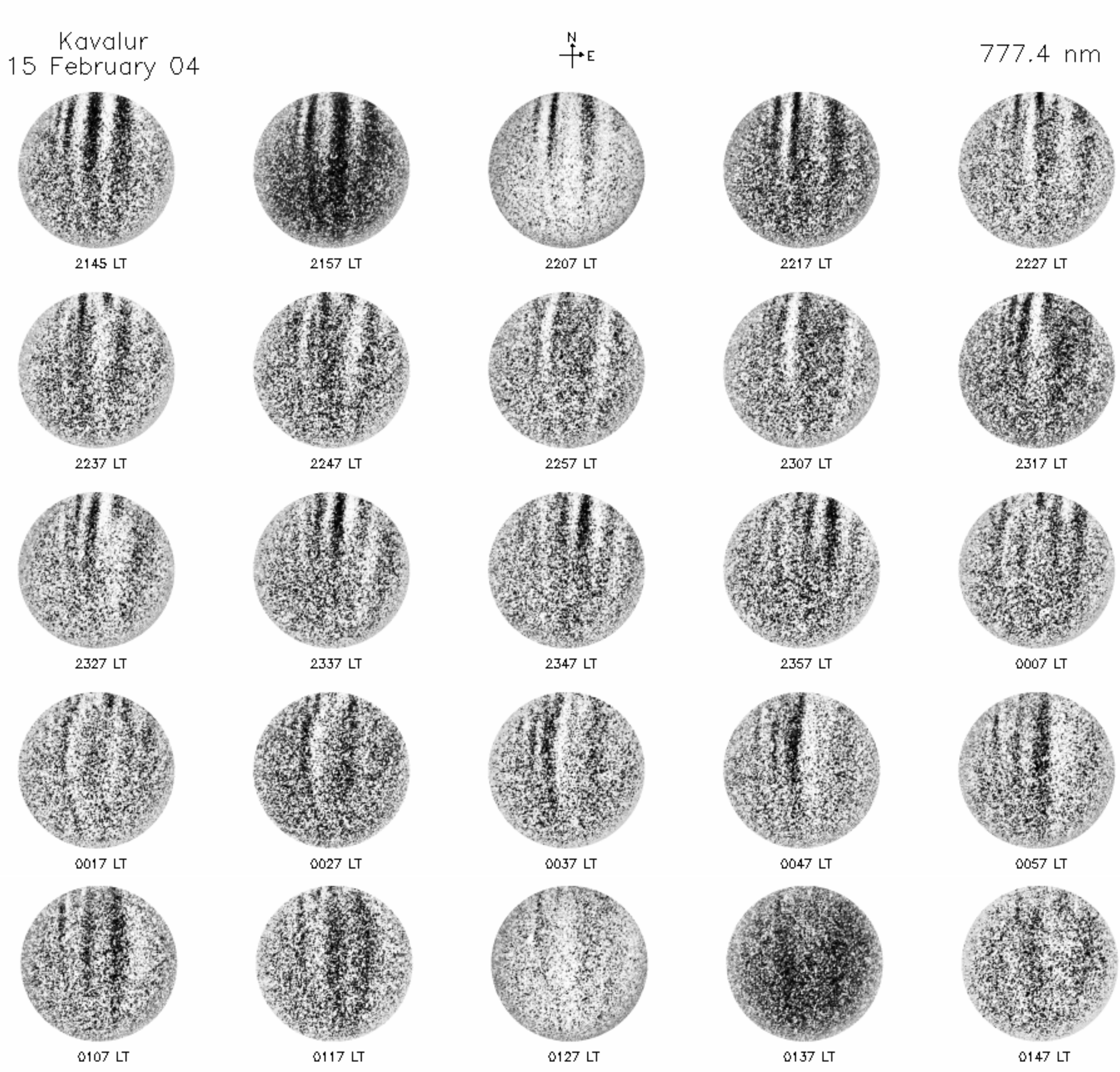

Figure 5.18 *A series from the 777.4 nm images taken in the night of 15 February 2002. The images show dark bands of intensity depletions extending along the entire North-South of the image FOV appearing from the very first image and continue to occur until the depletions disappear.*

Figures 5.16-5.18 show the all sky images taken in the post-sunset period (2140-2234 LT) of 15 February 2002 using 630.0, 557.7 and 777.4 nm, respectively. In the 630.0 and 557.7 nm, dark patches can be seen at the northern end of the FOV in the image taken at 2140 LT. These patches gradually grow equator ward, and extends the entire FOV in the N-S direction by 2304 LT. Since both 630.0 and 557.7 nm show similar features, for further discussion only the 630.0 nm depletions are considered. If the depletions had developed immediately after the sunset and expanded along the geomagnetic field lines, then in Figure 5.16 (where the first image is at 2140 LT), one should see dark bands covering the entire N-S of the FOV. On the contrary, it appears that the irregularities develop equatorward. Out of the 27 nights with depletions in 630.0 nm, about 15 nights having images between 2030-2130 LT showed the appearance of depletions as dark patches from the northern end of the FOV.

In order to confirm the origin of the dark patches in Figure 5.16, the almost simultaneously taken 777.4 nm images are given in Figure 5.18. These images show dark depletion bands that cover the entire N-S FOV from the post-sunset period, unlike the dark patches entering from the northern end in the 630.0 nm. Even though there are marked differences in the appearance of post-sunset depletions in both these emissions, the patterns in general are very similar, and are identical towards the midnight hours. The orientation as well as the eastward drift of the depletions in both the 630.0 and 777.4 nm images, and the fact that spread-F appeared in the ionograms at nearby stations indicate that these depletions are associated with ESF irregularities that generate at the geomagnetic equator. Note that bulk of the 777.4 nm emission comes from the F_2-peak, while that of the 630.0 nm is from the F-region bottom-side. The different behavior of the depletions in these two emissions suggests that the ionosphere altitude plays an important role, by influencing their respective photochemistry.

It should be noted that in Figure 5.16, the first image was taken only after about 2130 LT. This is because in this night the observations could be started only around this time as the moon set was around 2100 LT only. However, to give further evidence for the appearance of dark patches even at earlier local time periods, a few sets of selected 630.0 nm images are given below. The date and time are noted on the top of each case, and separate figure numbers are not provided for these examples.

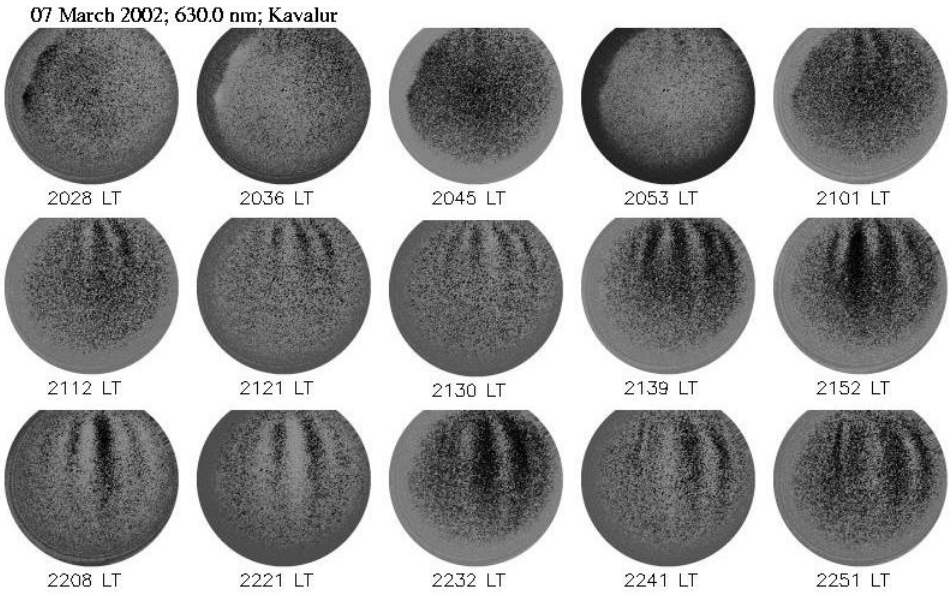

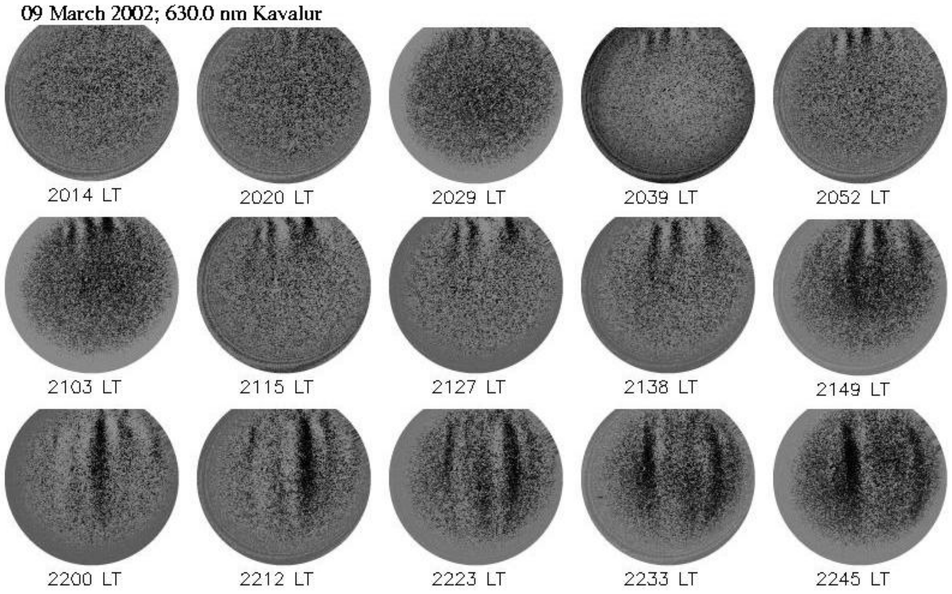

Examples for 630.0 nm depletions appearing as dark patches from the northern end of the image FOV.

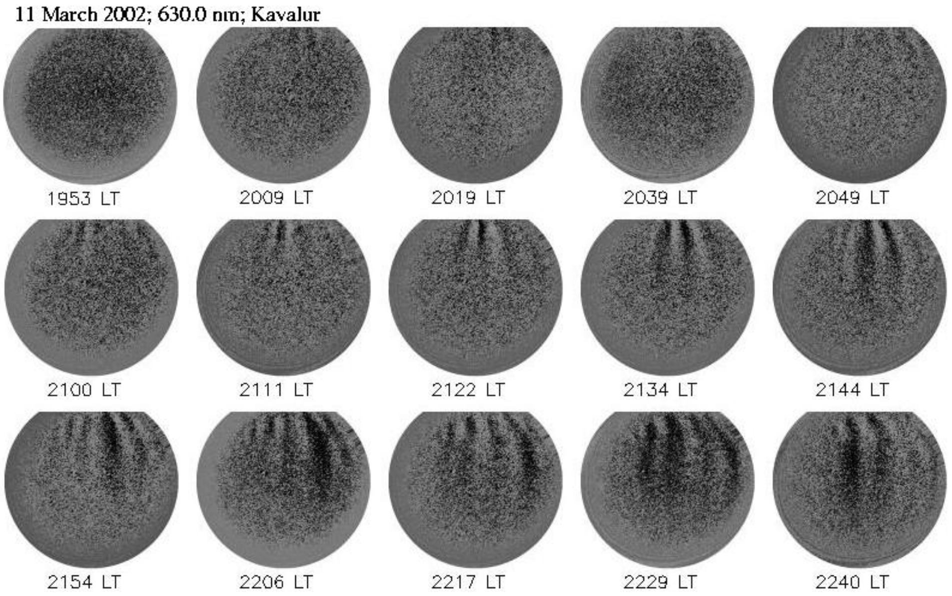

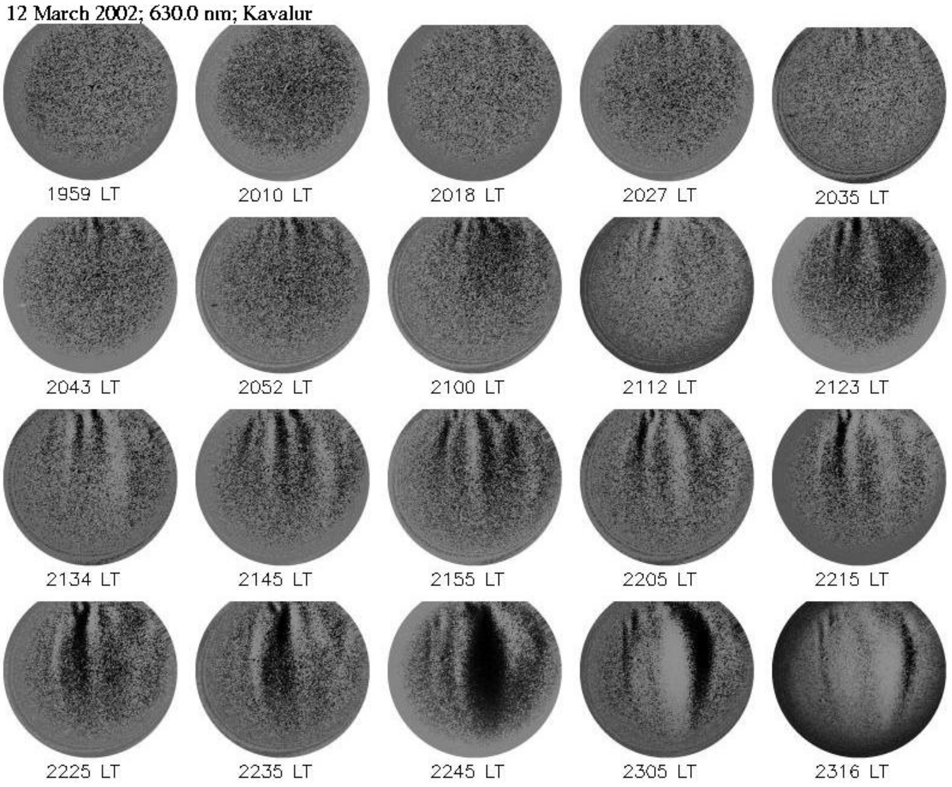

Examples for 630.0 nm depletions appearing as dark patches from the northern end of the image FOV.

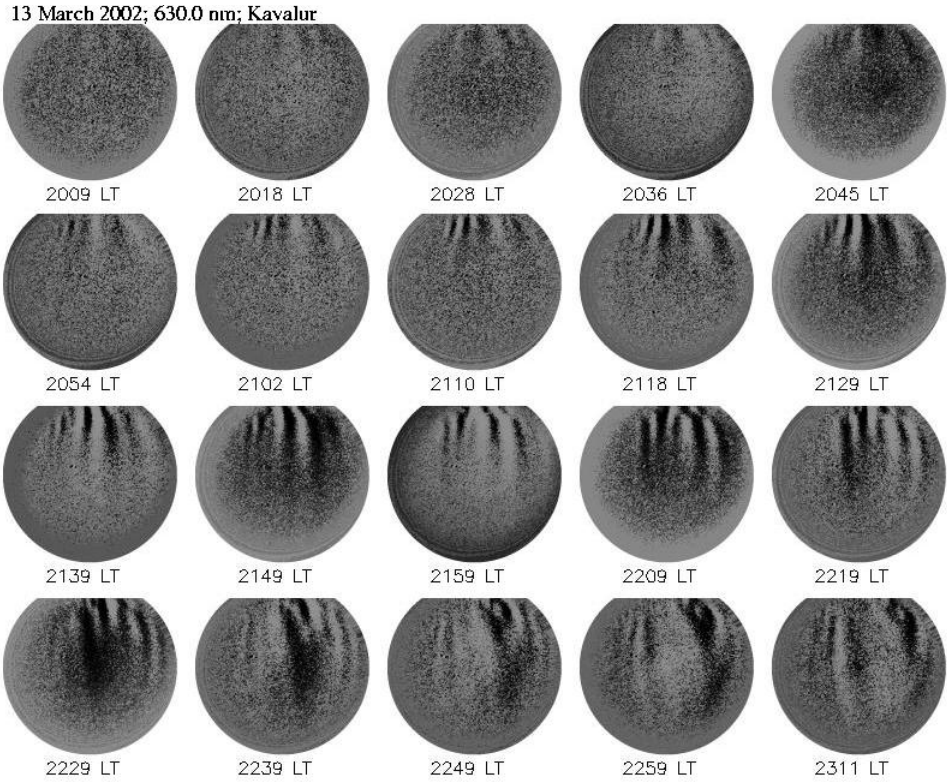

Examples for 630.0 nm depletions appearing as dark patches from the northern end of the image FOV.

In the post-sunset period, the F-layer is usually lifted to higher altitudes due to the pre-reversal enhancement of the eastward electric field [*Kelley*, 1989]. Two ionosondes located at the equatorial station Trivandrum (7.6° N, 76.9° E; 1.2° S geomagnetic), and the off-equatorial station Waltair (17.7° N, 83.3° E; 8.4° N geomagnetic) were operated in some of the nights during the imaging observations. The night-time F-layer base height (h'F) recorded by the two stations, given in Figure 5.19, show that the F-layer at Trivandrum reaches much higher altitudes than that at Waltair does. Also, at Waltair the F-layer moves down to lower altitudes (h'F ≅ 250 km) between 2000-2100 LT, whereas at Trivandrum it remains at higher heights for a further period of about 2 hours, and rapidly lowers to about 250 km altitude by 2200-2300 LT. Thus, when the imaging starts after the post-sunset period, the F-layer is usually at higher altitudes (>300 km) due to the pre-reversal enhancement, resulting in a drastic reduction in the dissociative recombination and the 630.0 nm emission as shown by *Nelson and Cogger* [1971]. Similar to the results of *Abalde et al*. [2001], with the higher F-layer height and reduced airglow intensity, the depletions may not have sufficient contrast to be recognized from the background in the 630.0 nm images immediately after the sunset. Subsequently, the off-equatorial ionosphere descends at earlier local time than the equatorial ionosphere does.

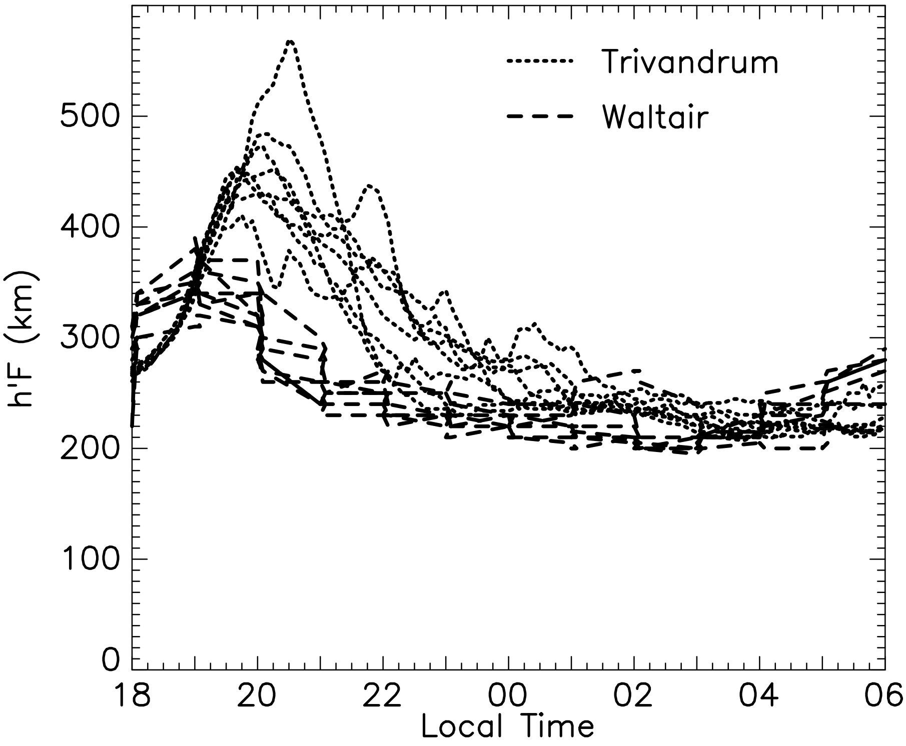

Figure 5.19 *The h'F values derived from the ionograms from Trivandrum (7.6˚N, 76.9˚E, 1.2˚S, geomagnetic), and Waltair (17.7˚N, 83.3˚E, 8.4˚N, geomagnetic) for the nights of 16 February, and 7,8,9,10,12 March 2002.*

Figure 5.20a illustrates this scenario, which shows the latitudinal sketch of the F-layer and the 630.0 nm emission corresponding to the post-sunset observations in Figure 5.16, together with the field-line geometry. In these sketches, the altitude and shape of the F-layer is adapted based on the results from the International Reference

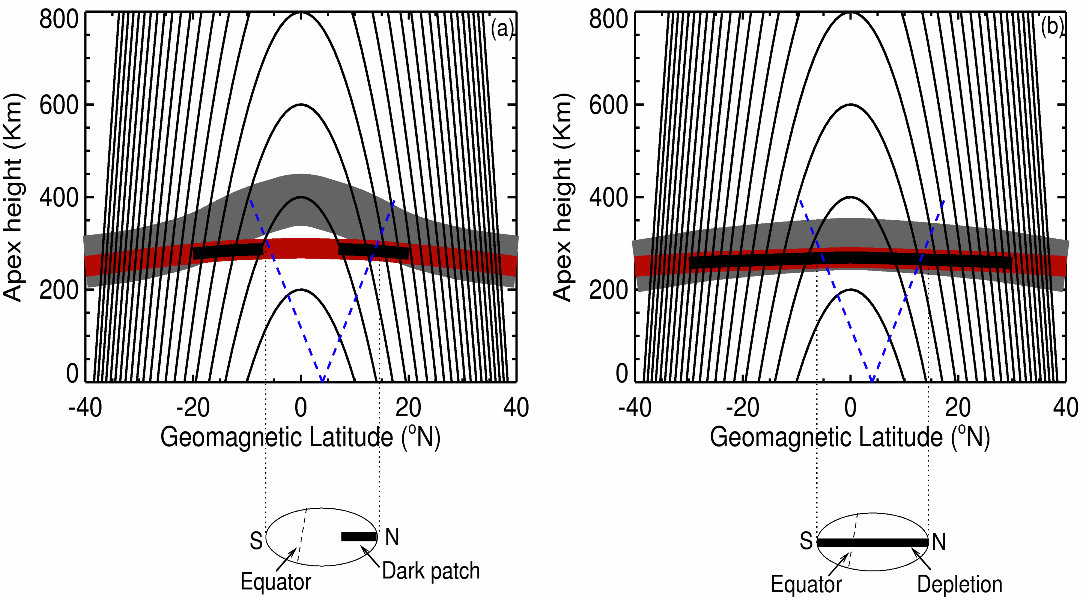

Figure 5.20 *Sketches of the F-layer and the 630.0 nm emission corresponding to the observations in Figure 5.16, together with the field-line geometry for both post-sunset and post-midnight periods. The blue lines denote the 150° FOV of the imager at Kavalur. The portions shaded in gray, red, and black shades stand for the F-layer, the 630.0 nm emission, and the airglow depletion, respectively. Note that the F-layer, the airglow band, and the depletions shown are sketches meant for conceptual understanding and need not necessarily correspond to the exact situation in the ionosphere. (a) The geometry for the post-sunset period, where the F-layer higher at the equator than that at the off-equator. A typical image in this scenario will be similar to the circle with dark patch at the North shown at the bottom. (b) The geometry for the post-midnight case. The F-layer is at lower altitude at all the latitudes encompassed by the FOV, and depletion would appear as dark band extending from North to South as drawn at the bottom.*

Ionosphere (IRI-07) model for the location and period of the imaging observations combined with the h’F values from Trivandrum and Waltair. Similarly, the 630.0 nm emission is based on the simulation results using the Mass Spectrometer Incoherent Scatter (MSISE-00) model and the given F-layer geometry. It can be seen from Figure 20a that at the equatorial latitudes, the F-layer is above the altitude region of the 630.0 nm photochemistry. As a result, the intensity in these regions would be less, and the

ESF irregularities, if generated, might not be detectable in the diminished emission. However, the irregularities that distribute to off-equatorial latitudes along the field lines, where the F-layer is at lower height and hence the emission is stronger, would appear as a dark patch at the northern edge of the FOV as shown in Figure 5.16. As the F-layer height gradually decreases at the latitudes further closer to the equator, the 630.0 nm emission in these regions enhances from the increased recombination, and also carries the signatures of plasma irregularities, producing an apparent equatorward extension of the dark patches as seen in the sequence of images in Figure 5.16. In the post-midnight period the F-layer at both the equatorial and off-equatorial latitudes reaches lower altitudes, and the dark patch would extend over all the latitudes encompassed within the FOV forming an N-S aligned depletion as illustrated in Figure 5.20b.

Figure 5.21 provides supporting evidence for this proposition, where two selected 630.0 nm images (one pre-midnight and one post-midnight), the corresponding h'F values, and the ionospheric geometry for the nights of 16 February 2002 (hereafter referred as case 1), and 10 March 2002 (hereafter referred as case 2) are given. In both the cases, the first image selected is taken at about 2200 LT (at 2204 LT on 16 February and 2159 LT on 10 March, respectively). Note that only two selected example images for each night are given here, and that the observations were conducted in both the nights starting from the post-sunset period till morning hours, depending on sky and moon conditions. For the case 1, the depletions in the first image are confined to the latitudes north of the imaging station, while for the case 2, the depletions more or less fill the FOV along the N-S direction. Now, for case 1, the h’F is about 370 km at 2200 LT, while for case 2, it is about 290 km only. Thus, in case 1, the higher F-layer height results in only those regions far from the equator to have sufficient recombination and hence the 630.0 nm intensity. This produces the dark patches seen at the northern ends

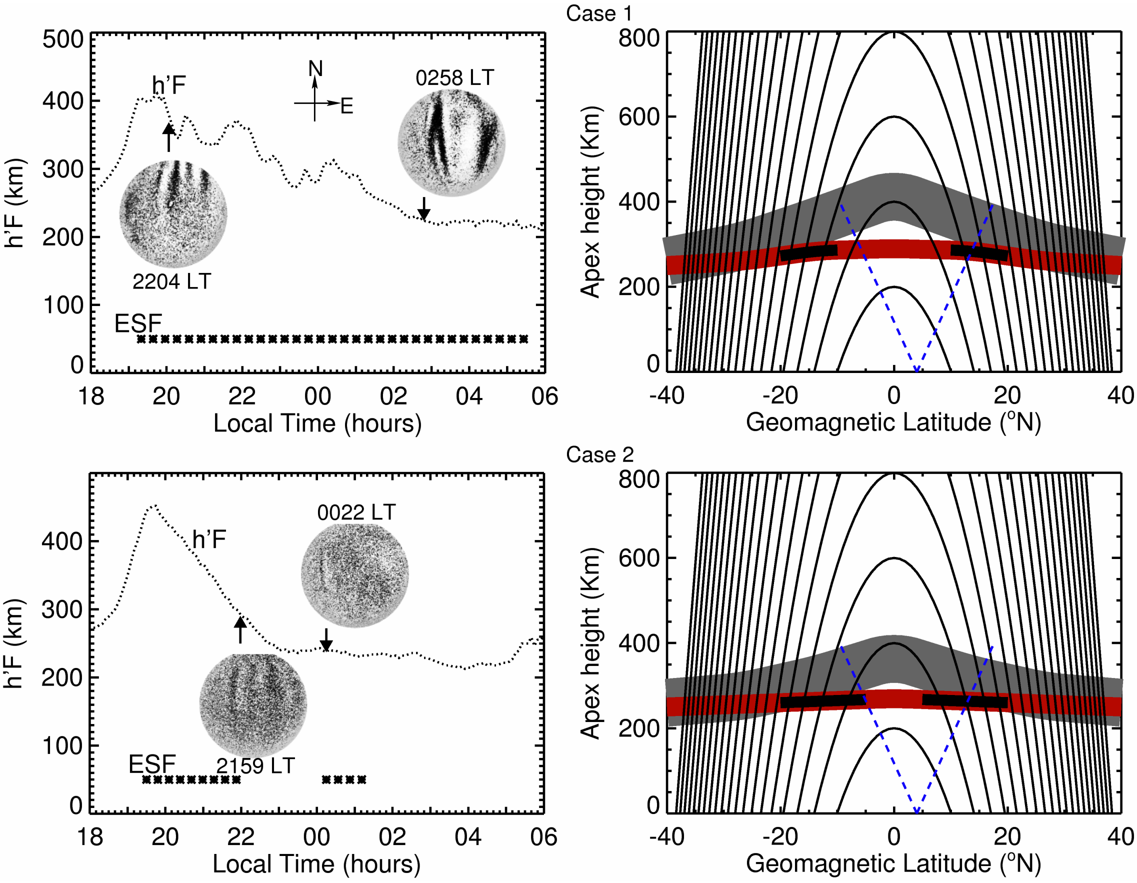

Figure 5.21 *Examples showing the dark patches, appearing as extending equatorward, for two cases for which the F-layer heights are different. The left panels give the h'F values at the equatorial station, Trivandrum, duration of the spread-F as well as sample post-sunset and post-midnight depletions for both case 1 (16 February 2002) and case2 (10 March 2002), respectively. The right panels illustrate the F-layer and airglow geometries for each case in the pre-midnight period.*

of the FOV in the image at 2204 LT. For case 2, as illustrated by the field line geometry and the airglow emission, the depletions in the image at 2159 LT are seen all the way up to the equatorial regions due to the relatively lower F-layer height. Now, consider the images for both the cases where the depletions that develop in the FOV in the post-midnight period are seen. The sample images taken at 0258 LT and 0027 LT for case 1 and case 2 respectively are shown in Figure 5.21. In both the cases it can be seen that the depletions do not begin as dark patches that enter from north, instead they are seen all along the N-S FOV from the time of their development. Note that at the time of the development of these post-midnight depletions in FOV, the h'F is below 250 km for both the cases. The lower F-layer altitude causes the irregularities to be embedded in the enhanced airglow emission producing depletions over all the latitudes to which they extend.

To further confirm the manifestation of 630.0 nm depletions two different F-layer electron density configuration are depicted in the sketches in Figure 5.22. The left and right panels differ in the shape of the F-layer with respect to the equator. In the left panel, there is an N-S asymmetry in the latitudinal distribution of electron density, which could occur, for example, in presence of a meridional wind. Hence, in this case the depletion might not be seen in the 630.0 nm image as illustrated, or could appear as a dark patch at the edge of the FOV, depending on the F-layer height. However, if the F-layer shape is different, as given in the right panel of Figure 5.22, the depletion would be seen throughout the FOV.

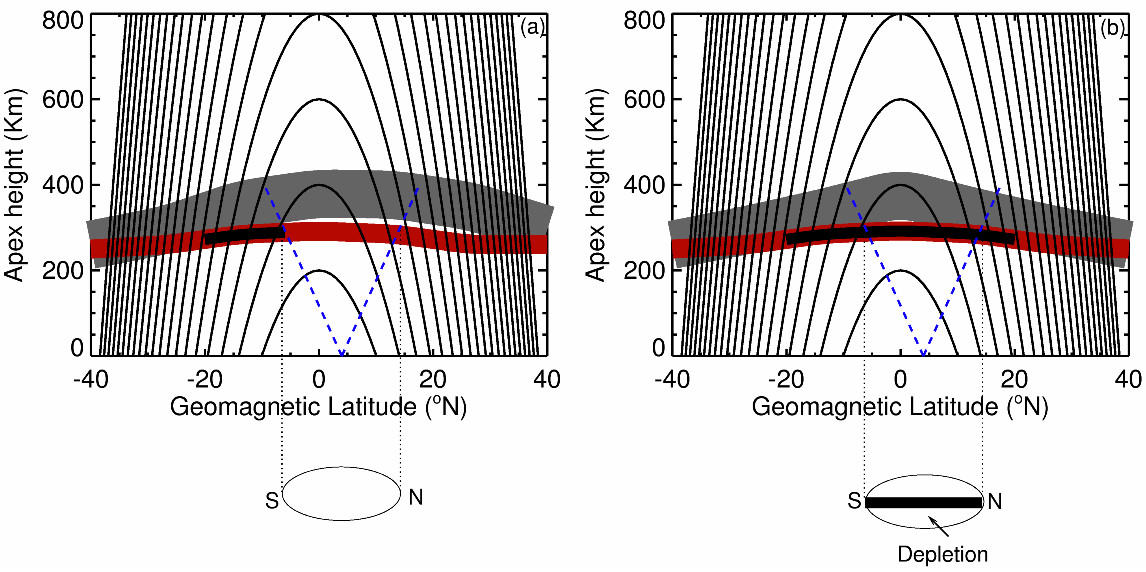

Figure 5.22. *Sketches demonstrating the manifestation of 630.0 nm depletions for different shapes of the F-layer.*

Though the above hypothesis explains the dark patches in the post-sunset 630.0 nm, we need to understand the simultaneous 777.4 nm depletions (Figure 5.18). The fact that the 777.4 nm depletions appear fully extended along the N-S direction, in effect, confirms the idea that the depletions in 630.0 m during the post-sunset period appear to enter the FOV as dark patches from the northern end as a result of the descending F-layer and reduced airglow emission. This is because, the bulk of the 777.4 nm emission comes from the F-peak altitude, and the radiative recombination process responsible for this emission is understood to be height independent [Abalde *et al.,* 2001]. Thus one would see the depletions in 777.4 nm at all latitudes both during the post-sunset and midnight/post-midnight periods as given in Figure 5.18.

The almost simultaneous observations of 630.0 and 777.4 nm intensities are used to further investigate the variation of the F-peak altitude along the meridional direction. It has been shown that the F-region peak altitude could be remotely inferred using atomic oxygen emissions arising from radiative recombination, ion-ion recombination, and dissociative recombination [Tinsley and Bittencourt, 1975; Chandra *et al.,* 1975]. Sahai *et al.,* 1981 demonstrated that the ratio of the square root of the column emission rate of the 777.4 nm (J7774)1/2, to the column emission rate of the 630.0 nm (J6300), shows good correlation with the F-peak altitude from simultaneous ionosonde measurements. Following a similar procedure, the ratio (I7774)1/2 / (I6300), of selected pixel locations from the Northern edge of the FOV towards the geo-magnetic equator at different local times are plotted in Figure 5.23 for the night of 15 Febraury 2002. Here I7774 and I6300 are the average column integrated intensities of the 777.4 and the 630.0 nm emissions within 10x10 pixels around the selected location. Note that the intensities are not calibrated and hence the ratio only indicates the meridional gradient of the F-peak altitude at different local times. Hence, in order to give some confidence to the calculated intensity ratio, the emissions are simulated for the times of the observation period and location. The IRI and MSISE models are used for the simulations. The intensity ratio determined from simulations is given in the top panel in Figure 5.23. It can be seen from the simulations that the ratio of intensities and the corresponding hmF2 show very similar variation at different latitudes. Thus, the ratio of intensities estimated at different pixels in the images should also indicate the F-peak altitude variation.

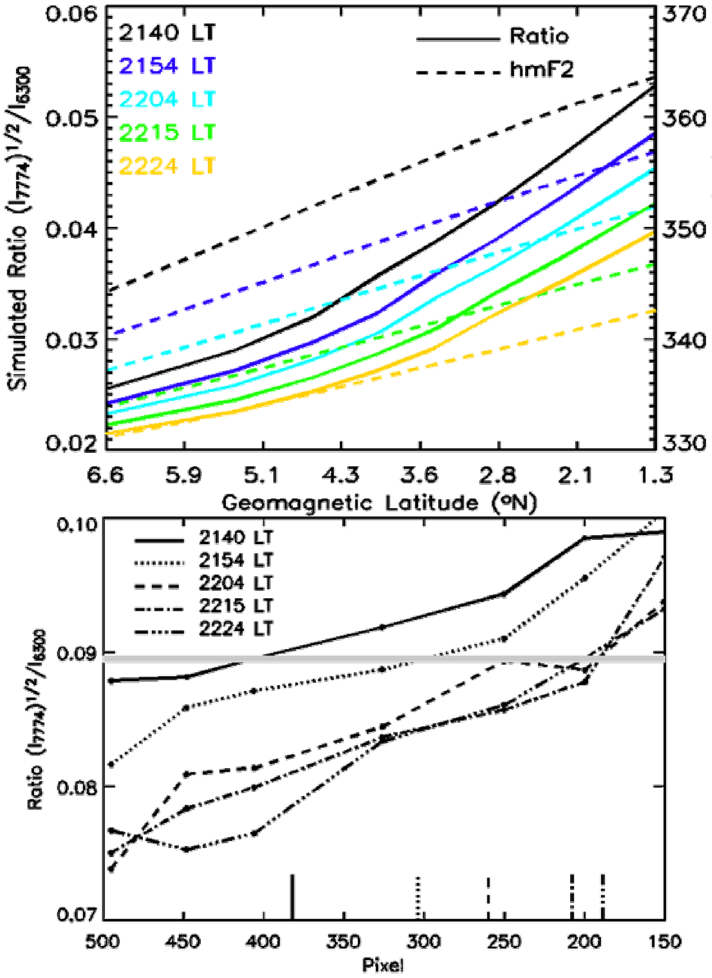

Figure 5.23 *Ratio of the square root of the intensity of 777.4 nm (I7774)1/2, to the intensity of 630.0 nm (I6300); (top): by simulating the emissions and, (bottom): calculated at selected pixels along the meridional direction depicting the variation of F-peak altitude for different local times in the night of 15 February 2002. The pixels are in the decreasing order from the Northward edge of the FOV (500), towards the geo-magnetic equator (150). The vertical lines over the X-axis denote the pixel locations where the equatorward edge of the plasma depletion is seen in the images taken at the corresponding local times, indicated by the different line styles. Each of these vertical lines, if extended, would approximately intersect the respective curve of the intensity ratio at the value shown by the thick horizontal gray line.*

It can be seen from the bottom panel of Figure 5.23 that the ratio or the F-peak altitude increases from the Northern edge of the FOV towards the geo-magnetic equator, confirming that the 630.0 nm emission could be strong enough at the Northern edges and less intense near the equatorial region, to image the depletion as a dark patch as observed. The F-peak altitude tends to lower with time, allowing the depletion to gradually extend towards the equator. At the equatorial regions the F-peak maintains the elevated values resulting from the pre-reversal enhancement even around 2230 LT. This agrees with the general h’F behavior over Trivandrum, given in Figure 5.19. Also, note that the observed Northern edge of the dark patch at different local times (the vertical lines over the X-axis) seems to depend on some particular value of the ratio (here about 0.09), and hence of the F-peak altitude. In other words, the latitudinal extend within which the dark patch would be visible in 630.0 nm depends on whether the F-peak over the corresponding latitudes is above a certain level or not.

In order to explain the poleward extending depletions seen in most of the previous observations, such reports were examined case by case. It is noted that most of these observations have been conducted from locations beyond 10° or more from the geomagnetic equator and those from near equatorial stations have been taken in low solar activity years. When the imager is located at stations far from the equator, most parts of the F-region within the latitudes covered by the FOV would be at sufficiently lower heights for the photochemistry to occur, resulting in poleward extension. This is illustrated in Figure 5.24. The F-layer and the 630.0 nm emission in the figure are based on the simulations using IRI-07 and MSISE-00 for the 45 W longitude sector, and the location of the imager and the time of simulations correspond to the observations of Abalde *et al.*, [2001], which present excellent examples for poleward extension. In the low solar activity period, the evening upward movement of the F-layer is not pronounced [Fejer *et al.*, 1979]. Similar simulations for this case are given in Figure 5.25. It can be seen that at the equatorial and off-equatorial latitudes the F-layer is at low altitudes during both the post-sunset and the post-midnight periods, and hence irregularities, if present, would modify the 630.0 nm emission over the entire latitudes covered by the FOV. Thus, in the case of observations at off-equatorial latitudes as well as in the low solar activity conditions, depletions would be seen extending poleward. Note that the evening vertical motion of the F-layer has significant

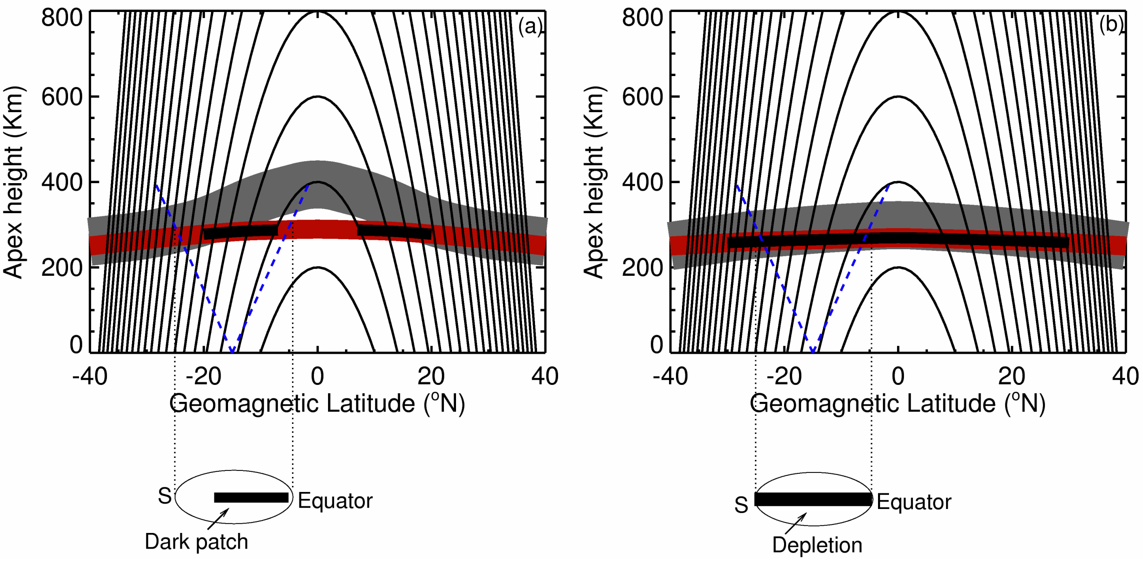

Figure 5.24. *Sketches demonstrating the appearance of poleward extending depletions for an imager located at about 15° away from the equator. The left panel is for the post-sunset case and the right panel is for post-midnight period.*

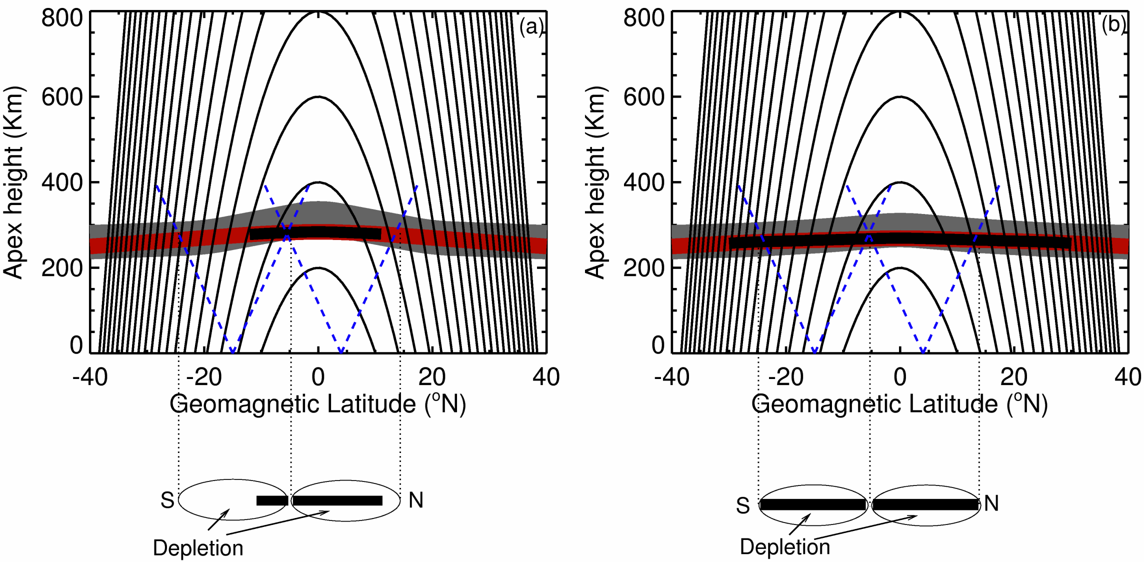

Figure 5.25. *Sketches demonstrating the poleward extensions during solar minimum at both the equatorial and off-equatorial stations. The left panel is for the case immediately after the sunset and the right panel is for the post-midnight period.*

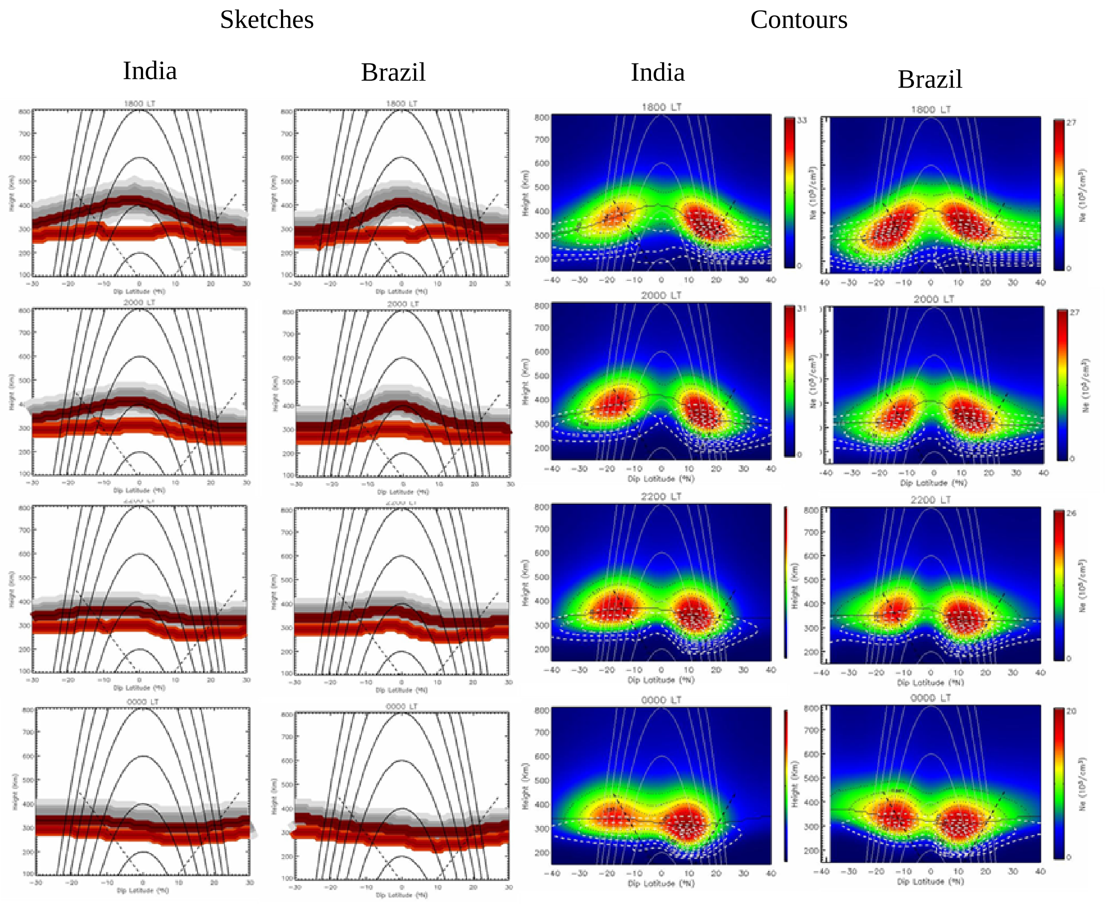

Figure 5.25a *The F-layer electron density distribution and 630.0 nm airglow layer configuration over Indian and Brazilian longitudes on 15 February 2002. The left two panels are the sketches for India and Brazil, and the right two panels the corresponding contours. The filled contour gives the electron density and the overplotted line contour gives the 630.0 nm intensity. From top to bottom, each row are for the local times 1800, 2000, 2200, and 0000 LT, respectively. It can be seen that the in the evening hours, over the equatorial region, the emission is not strong enough because the altitude is higher. However, at off-equatorial latitudes, where there is sufficient electron density even at lower altitudes, the airglow is also strong. However, towards midnight, the F-layer descends over the equatorial region, enhancing the emission.*

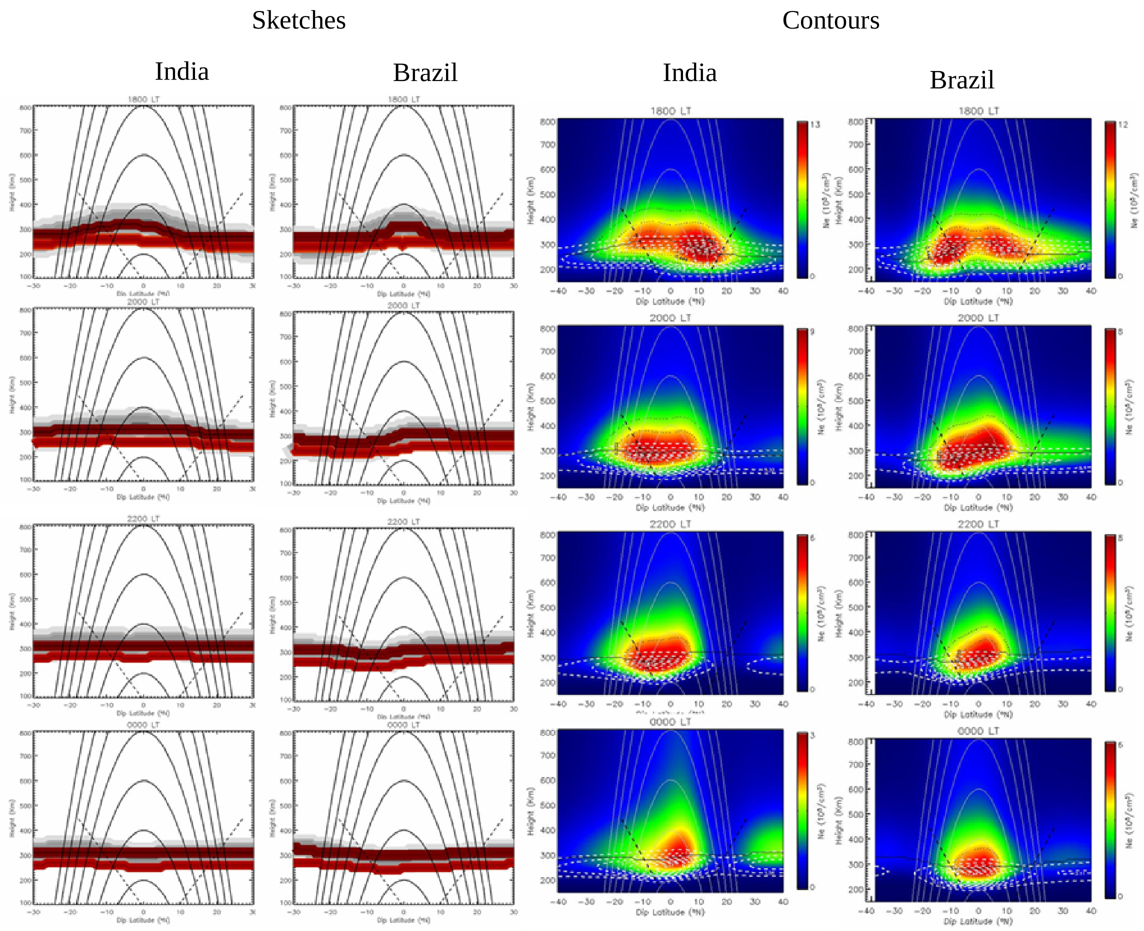

Figure 5.25b *The F-layer electron density distribution and 630.0 nm airglow layer configuration over Indian and Brazilian longitudes on 21 March 1996. The left two panels are the sketches for India and Brazil, and the right two panels the corresponding contours. The filled contour gives the electron density and the over plotted line contour gives the 630.0 nm intensity. From top to bottom, each row are for the local times 1800, 2000, 2200, and 0000 LT, respectively. It can be seen that the in the solar minimum conditions, even in the evening hours the F-layer altitude is not very high over the equatorial region, and the emission is strong at all the latitudes. Towards midnight, the emission continues to be present over all the latitudes. However, the electron density seems to decrease, especially over off-equatorial latitudes, and this might case the airglow intensity also to decrease.*

day-to-day variability, and it also depends on season and longitude [*Fejer et al.*, 1995]. As a result, the latitudinal geometry of the F-layer as well as the 630.0 nm emission could be different in different conditions and could influence the appearance of depletions even if imaged from equatorial stations at different longitudes, seasons, or solar activity periods.

The dark patches in 630.0 nm images in the post-midnight hours, which enter the FOV from northern latitudes and grow towards equator, are in fact the signatures of the field aligned plasma depletions that are seen in the off equatorial latitudes where the depleted flux tubes meet the emission layer owing to the lower F-layer height than that at the magnetic equator. Near the equatorial region, the irregularity layer is above the airglow band, and depletions are limited to northern end of the FOV.

5.3 Bifurcation and joining

The pole ward ends of plasma depletions are sometimes seen bifurcated, especially in the all sky images taken at off-equatorial latitudes [Mendillo and Baumgardner, 1982; Rohrbaugh *et al.,* 1989; Pimenta *et al.,* 2001; Kelley *et al.,* 2002]. Such bifurcations are termed wishbone formation from their *Y* (wishbone) shaped appearance. Numerical simulations show that rising bubbles start bifurcating when contribution of E-region Pedersen conductivity to F-region conductivity is included in the calculations, and the bifurcations occur when the ratio of conductivities inside and outside the bubble becomes less than 10 [McDonald, 1981; Zalesak, 1982]. Anderson and Mendillo, [1983] found that the conductivity ratio inside and outside the bifurcated depletions meet this requirement, but the appearance of linear and bifurcated depletions side-by-side remained unexplained. Huang and Kelley [1996] suggested that bifurcation occurs when the east-west dimension of the bubble is large, and they speculated that this could happen because of the inhomogeneous electric field and upward movement of charged particles within wider bubbles.

Even though several investigators have reported the bifurcation of depletion, there are not many observations of ‘joining’ of two adjacent depletions. Sinha *et al.,* [2003] reported the splitting of depletion into two parts and the joining of one of the parts with a preceding depletion. They speculated that the vertical shear in the zonal plasma drift is responsible for the splitting. The all sky observations reported here show two types of bifurcations. One of the bifurcations is similar to the wishbone structure seen in the previous studies. The second one is a new type of inverted ‘V’ shaped bifurcation. This bifurcation is apparently formed by the joining of an adjacent pair of depletions, which later merge together to become a single depletion.

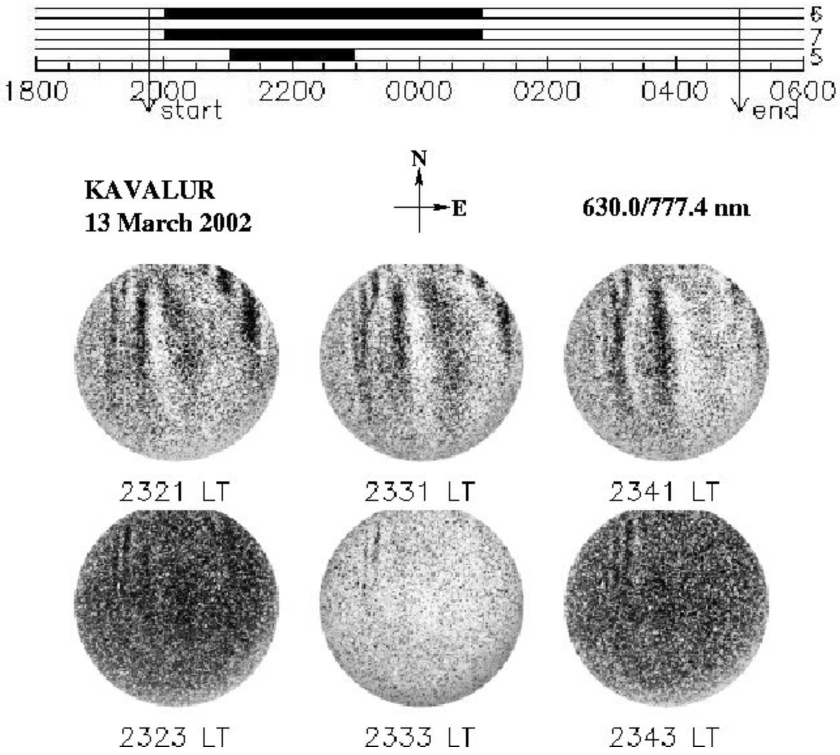

***Figure 5.26**. The top panel shows a series of 630.0 nm images taken on the night of 13 March 2002. The northern end of the depletion at 2331 LT and 2341 LT appear to be bifurcated. The bottom panel shows the series of 777.4 nm images taken in this night during the same time period. The horizontal bar on the top indicates the time history of observations in this night, where the arrows denote the start and end times of observations, and the dark portion gives the duration of depletions.*

The top panel in Figure 5.26 displays a series from the 630.0 nm images taken in the night of 13 March 2002. The northern end of the depletion in the images at 2331 LT and 2341 LT appear bifurcated. The bifurcation is not well defined in at 2321 LT, and in the next image it is seen more or less with a ‘Y’ shape with its west leg linear and the east leg tilted eastward, similar to the wishbone type usually observed. At 2341 LT, the west leg appears to be tilted westward and the east leg is linear. A series from the almost simultaneously taken 777.4 nm images is given in the bottom panel of

Figure 5.26. In this case the depletions are very weak to ascertain if there is any bifurcation. The 557.7 nm images in this night did not show any clear depletion during this period.

Figure 5.27 displays a series of 630.0 nm images taken in the post-midnight period of 16 February 2002. In this night the sky was partially cloudy, and dark cloud patches are seen in some of the images. The gap in the observation between 0211 LT and 0241 LT is due to the bad weather during that interval. In the image at 0241 LT, the depletion appears bifurcated with an ‘inverted V’ shape, where the northern ends of the two legs are joined together. In fact this pair of depletions can be seen as a weak structure in the image at 0202 LT. This is a new type of bifurcation. Interestingly, in the subsequent images the two branches of this bifurcation start merging together, starting from the northern latitudes, and by 0316 LT it becomes single depletion.

An almost simultaneously taken set of 557.7 nm images is given in Figure 5.28. The images during 0239 LT to 0254 LT show very similar ‘V’ shaped bifurcation as seen in the Figure 5.27. Noticeable difference is in the image taken at 0304 LT, where the southern ends of the two legs of the bifurcation cross each other. In fact the eastern leg of the bifurcation remain unchanged in shape apart from its slight westward tilt, while the western leg deformed into ‘C’ shape so that its northern and southern ends join with the adjacent depletion. By 0313 LT, these two depletions completely merge together into a single depletion. The series of 777.4 nm images taken during the same time period in this night are shown in Figure 5.29. The depletions in this case are very weak, and disappear after 0320 LT. No clear signatures of bifurcation or merging of depletions can be seen in these images.

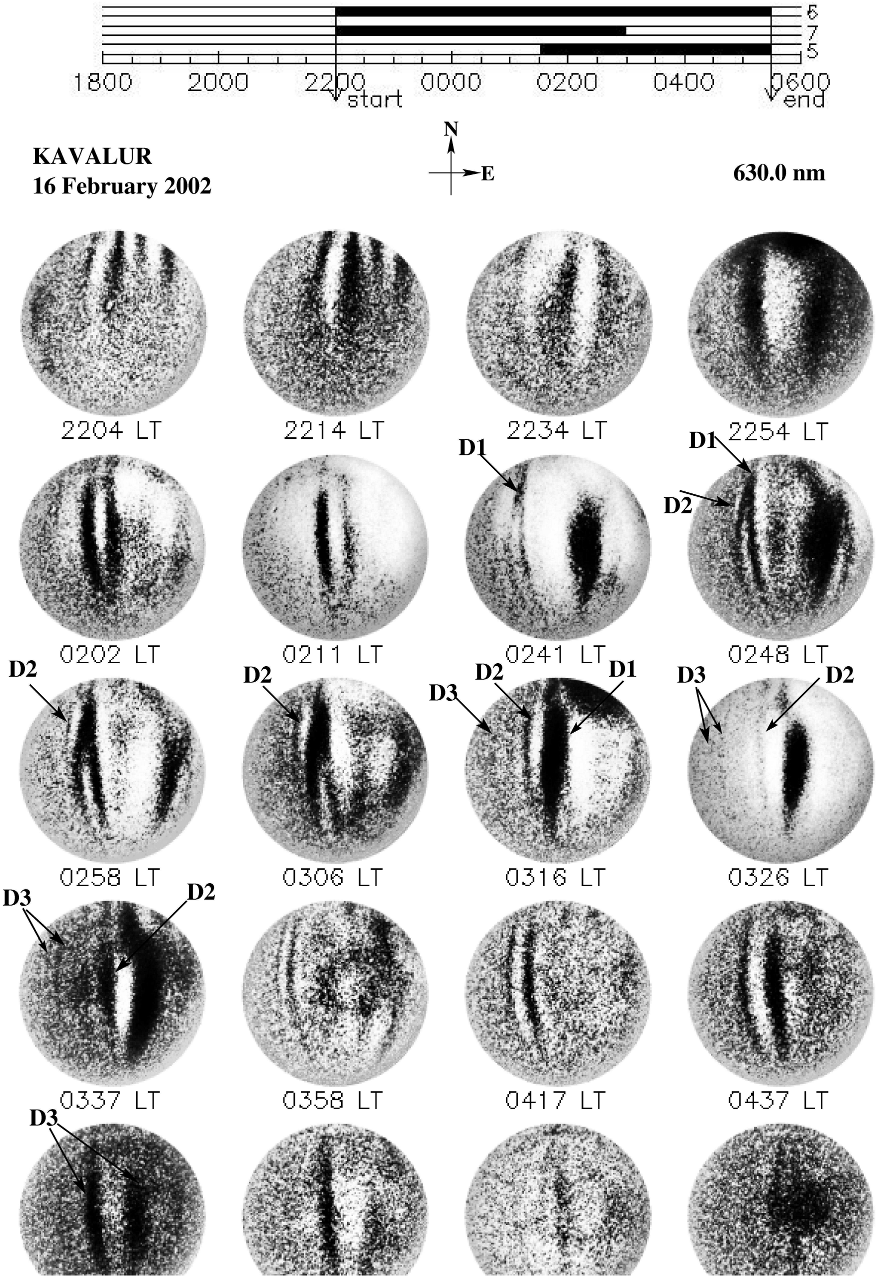

Figure 5.27 *A series from the 630.0 nm images taken in the night of 16 February 2002. The horizontal bar on the top indicates the time history of observations in this night, where the arrows denote the start and end times of observations, and the dark portion gives the duration of depletions. The numbers 6, 7 and 5 in the right stands for 630.0, 777.4 and 557.7 nm, respectively. The letters D1, D2 and D3 indicates the corresponding depletions in different images. The North and East directions are marked using arrows.*

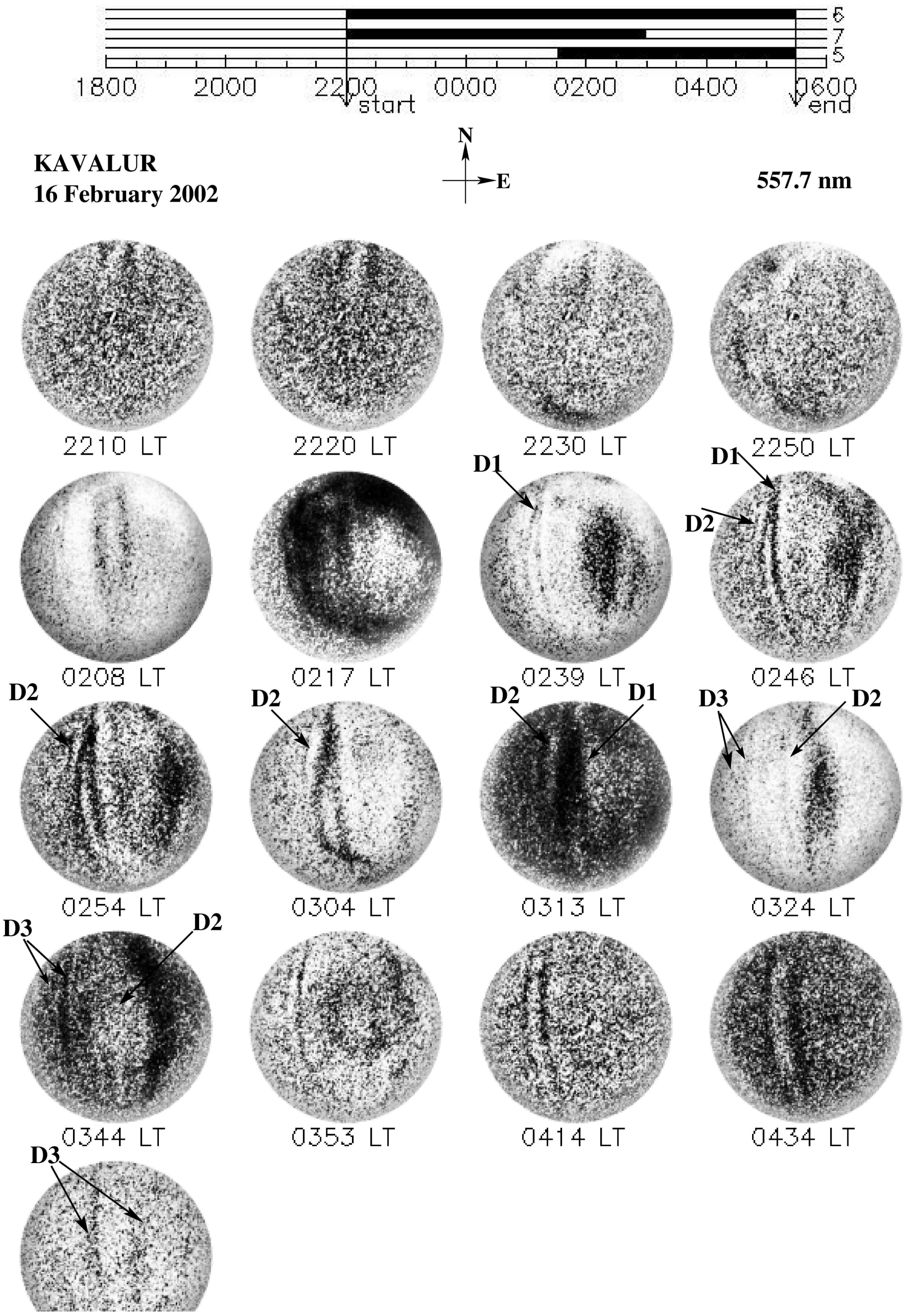

Figure 5.28 *A series from the 557.7 nm images taken in the night of 16 February 2002. The horizontal bar on the top indicates the time history of observations in this night, where the arrows denote the start and end times of observations, and the dark portion gives the duration of depletions. The numbers 6, 7 and 5 in the right stands for 630.0, 777.4 and 557.7 nm, respectively. The letters D1, D2 and D3 indicates the corresponding depletions in different images. The North and East directions are marked using arrows.*

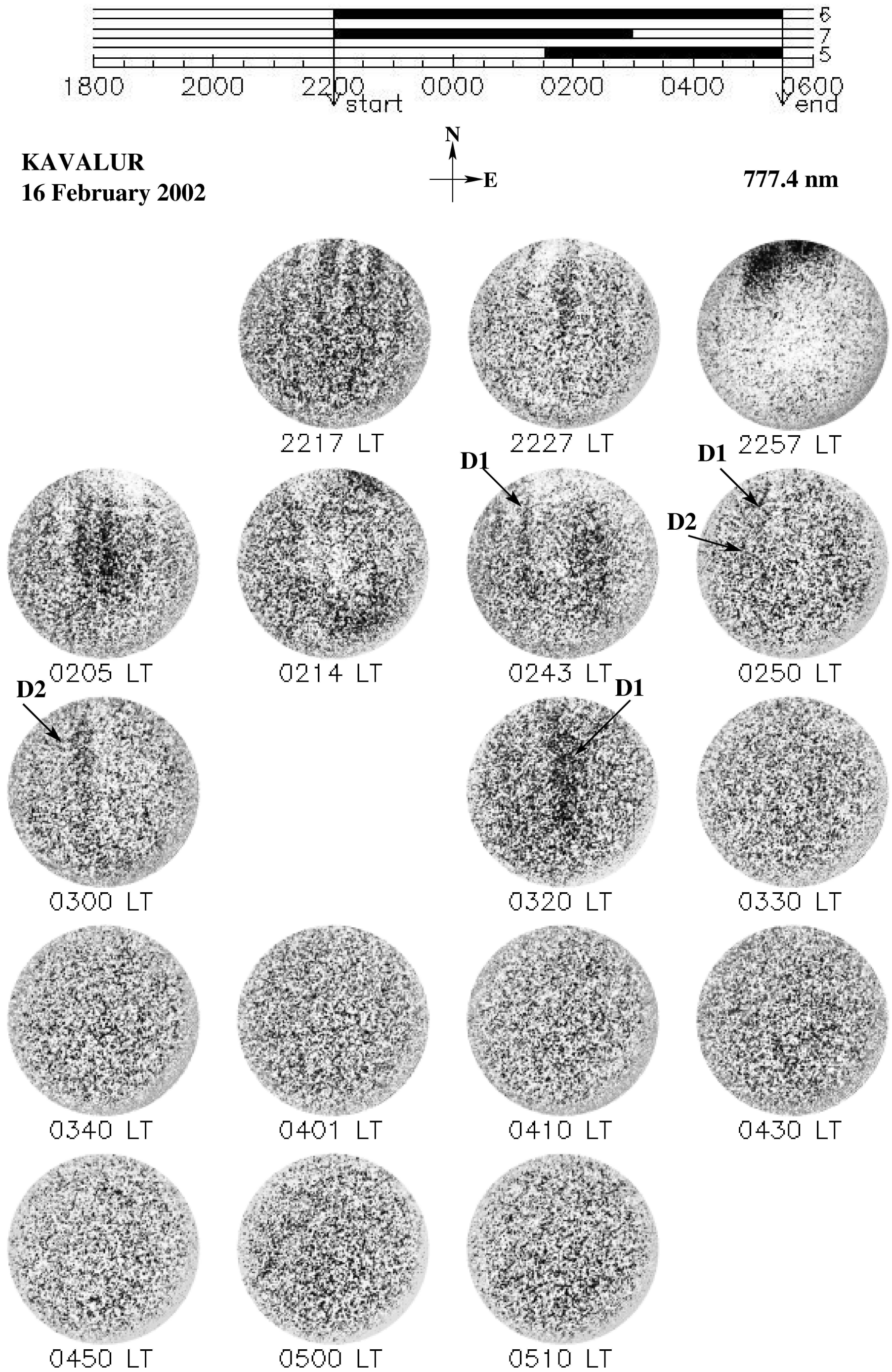

Figure 5.29 *A series from the 777.4 nm images taken in the night of 16 February 2002. The horizontal bar on the top indicates the time history of observations in this night, where the arrows denote the start and end times of observations, and the dark portion gives the duration of depletions. The numbers 6, 7 and 5 in the right stands for 630.0, 777.4 and 557.7 nm, respectively. The letters D1, and, D2 indicates the corresponding depletions in different images. The North and East directions are marked using arrows.*

The bifurcation of the 630.0 nm depletions in Figure 5.26 is similar to the wishbone structures reported by other investigators [Mendillo and Baumgardner, 1982; Rohrbaugh *et al.*, 1989; Pimenta *et al.*, 2001; Kelley *et al.*, 2002]. The westward tilt of the bifurcation (2331 LT and 2341 LT) provides experimental evidence to the suggestion of Mendillo and Tyler [1983] that the bifurcation could be generated with its eastern and western legs symmetrical about the vertical direction, and the westward tilt of the depletions that occur with the passage of time causes the typical appearance with one leg vertical and the other leg tilted to the west.

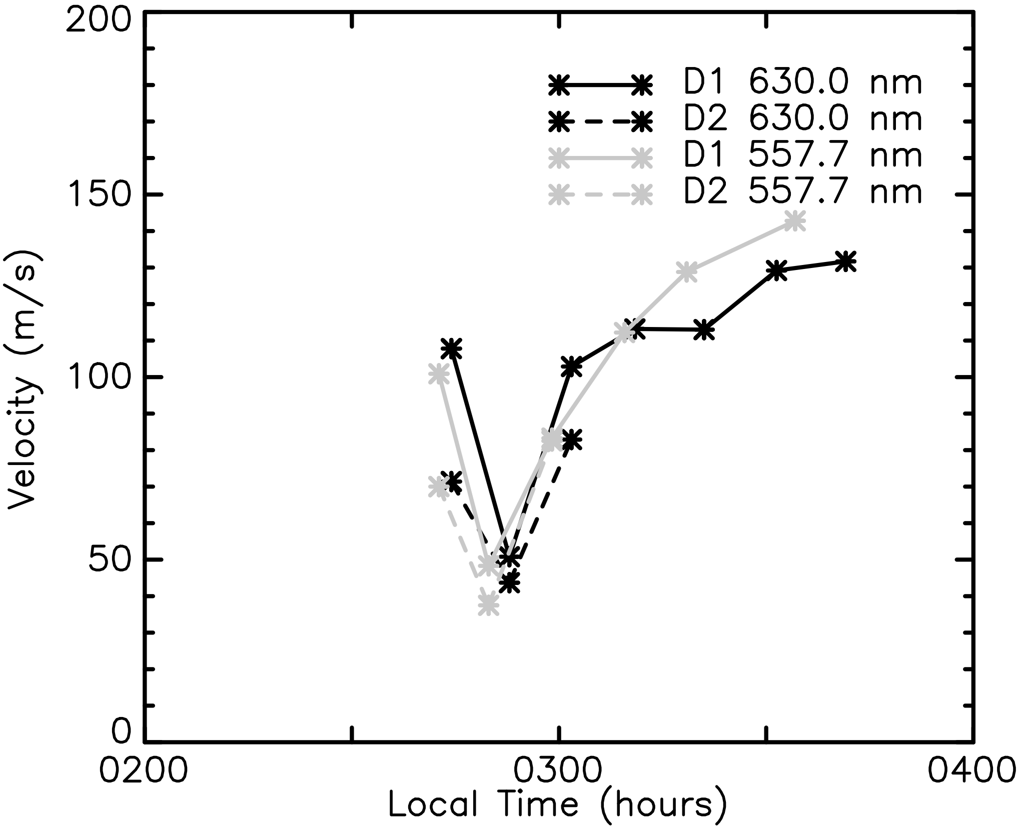

Figure 5.30 *Drift velocities of the depletions in the bifurcated pair seen in the night of 16 February 2002. The solid line corresponds to the eastern leg while the dashed line is for the western leg. The heavy and shaded lines respectively stands for the 630.0 and 557.7 nm depletions.*

The inverted ‘V’ shaped bifurcations in Figures 5.27 and 5.28 are different from the usual bifurcation, and, are formed by the joining of the northern ends of two adjacent depletions as evident from their subsequent merging. This peculiar pair of joined depletions appears developing in the FOV from 0202 LT. The observed joining and merging is possible if the depletion to the west in the pair drifted faster than the one to its east. The eastward drift velocities of both the pairs of the bifurcation for 630.0 as well as 557.7 nm images are plotted in Figure 5.30. These velocities are calculated for a location closer to the center of the image. It can be seen from Figure 30 that there is a tendency for the western depletion to drift slightly faster than its eastern pair.

Depletions usually drift eastwards with velocities equal to the ambient plasma, but in the evolving stage their drift would be influenced by the polarization electric field within the walls of the depletions [Tsunoda *et al.*, 1981a]. Martinis *et al.*, [2003] found that the zonal drift of depletions near the equator is higher than at off equatorial latitude. They suggested that this difference could occur if the depletions in the evolving stage drift at velocities different from that prescribed by F-region dynamo. Recently, Lin *et al.*, [2005] noted that depletions in the early evening hours drifted faster than the background plasma, and they attributed this higher velocity to come from the group velocity of the gravity waves that might have seeded the RT instability. These findings indicate the possibility of depletions drifting with higher eastward velocities when they are in the early stages of their development.

The joined depletions appear developing in the FOV from 0202 LT, and it is possible that the eastern and western depletions of the pair could drift with different velocities if they are at different levels of development. The fact that the pole ward ends of the depletions join before their center regions merge indicates higher eastward velocities at higher altitudes above equator. There is a confirming trend seen in Figure 4.11, which gives the zonal drift velocity of all the depletions observed in different images. The median values of 777.4 nm velocities seem to be larger than that of 630.0nm after 2330 LT, even though it is well within the range of the fluctuation of the velocity values.

The west depletion in the pair at 0304 LT in Figure 5.27 has a pronounced C-shape, while the east depletion appears linear. The C-shape of depletions is different from that of radar plumes, which results from the decrease in the field line integrated conductivity both above and below the F-peak [Zalesak *et al.*, 1982]. In airglow images the C-shape arises due to the mapping of the vertically rising bubbles along the field lines to lower latitudes, where the rising bubbles tilt westwards due to shear in plasma drift. *Kelley et al., [2003]* reported backward C-shape in the airglow images from space, and showed that the ground based airglow depletions match this shape. The C-shape of depletion at 0304 LT in Figure 5.27 is different from the backward C-shape reported by *Kelley et al., [2003]*, as it mainly represent the bubbles that are mapped to northern hemisphere. In the absence of supporting data one can only speculate about the role of a complicated wind and electric field pattern in producing such peculiar depletions.

5.4 Post-midnight depletions

The post-sunset equatorial ionosphere is sometimes characterized by the spectrum of irregularities associated with the phenomenon known as Equatorial Spread-F (ESF), based on their manifestation as diffused traces in ionograms (Booker and Wells, 1938). The Generalized Rayleigh-Taylor (GRT) instability is believed to be the mechanism of generation of ESF, which operates in presence of sharp plasma density gradients anti-parallel to the gravity (Kelley, 1989). The irregularities are generated at the bottom side of the F-region, and evolve non-linearly to the topside (Woodman and La Hoz, 1976; Chaturvedi and Ossakow, 1977). The total growth phase of the irregularities takes about 50 minutes (Tsunoda, 1981). It has been known from ionosonde and radar observations that the pre-reversal enhancement of the eastward electric field and the subsequent vertical motion of the F-layer to very high altitudes are necessary conditions for the generation ESF (Farley *et al.*, 1970; Abdu *et al.*, 1983; Fejer *et al.*, 1999).

A routine vertical sounding ionosonde mainly observes overhead ionospheric parameters, and during ESF one can infer only the base height of the F-layer (h’F) from an ionogram. While, an all sky imager provides a wide range of (180˚) field of view (FOV) (Mendillo and Baumgardner, 1982), and is suitable to study large scale features of ESF such as plasma depletions, which are the manifestations of field aligned irregularities in the airglow images (Abdu *et al.*, 1983a). Following the pioneer work of Weber *et al.* (1978), ground based all sky imagers have been used to study the morphology and dynamics of plasma depletions (Mendillo and Baumgardner, 1982; Sahai *et al.,* 1994; Fagundes *et al.,* 1999; Taylor *et al.,* 1997; Tinsley *et al.,* 1997; Mukherjee *et al.,* 1998; Kelley *et al.,* 2002; Sinha *et al.,* 2003, Martinis *et al.,* 2003; Pimenta *et al.,* 2003, Makela *et al.,* 2004; Mendillo *et al.,* 2005, Rajesh *et al.,* 2007). These investigations have established the all sky imaging as an important diagnostic tool in the study of ionospheric irregularities, even though this technique is limited by the observing conditions such as moon phase, weather, etc. This work report extensive observations of all sky imager from the Indian sector during solar maximum, with concurrent ionosonde measurements.

Depletions in 630.0 and 777.4 nm usually appear in the post-sunset hours in the interval 2000-2200 LT, but there are differences in their duration in different nights. In some nights, depletions are confined to the post-sunset hours and disappear after midnight. However, in several other nights, depletions are present even after the midnight. These post-midnight depletions could be of two types, the ‘fossil’ depletions, which are generated in the early evening hours in other (westward) longitudes that drift into the FOV after midnight, or the fresh depletions that are generated in the post-midnight hours. The ‘fossil’ depletions appear well developed when they are seen in the images, while in the case of generation within the FOV one would be able to see the depletions developing. About 37% (10 out of 27) of the nights with depletions in 630.0 nm showed the development of irregularities within the FOV around midnight or in the post-midnight period.

As described above, Figures 5.27 illustrates the series of 630.0 nm images taken in the night of 16 February 2002, showing examples for pre- and post-midnight depletions as well as overhead developments. The top panel is a series of depletions that appeared in the pre-midnight period. These depletions were seen from the beginning of the observation at 2204 LT till about 2300 LT. At 2204 LT, when the first image was taken, depletions are seen only in the northern half of the FOV. In the subsequent images at 2214 LT and 2234 LT, these depletions extend to southern parts also, and fill the FOV along the North-South direction. During the period 2300-0100 LT, the cloud cover increased, but the observations continued as the depletions could be still seen in the images. By the time the sky became clear these depletions had disappeared, and new depletions started appearing.

The second panel in Figure 5.27 shows the depletions in the post-midnight hours. In the image taken at 0258 LT, a new depletion (D2) is seen to the west of the ‘joined’ depletions. This new depletion is visible as a weak structure (marked as D2) in the image at 0248 LT, which probably indicate the ‘onset’ of the depletion in the imager. The subsequent images depict the development of the depletion. These observations, probably for the first time, show the sequence of post-midnight depletions developing within the FOV. Similar development within the FOV can be seen for the pair of depletions (D3) at 0337 LT. These depletions appeared as a faint structure at 0316 LT. Since they are closer to the western edge of the FOV at 0316 LT, it is difficult to conclude whether they are generated within the FOV or drifted in from western longitudes. Nevertheless, their growth as seen in the subsequent images indicates that they are not fossil depletions. These depletions continued till the pre-sunrise hours up to 0525 LT, and disappeared thereafter. Note that this is the first time the occurrence of depletions extending from the post-sunset period till the pre-sunrise hours is observed at Kavalur.

In this night, the depletions in 557.7 images also showed more or less similar characteristics as can be seen from Figure 5.28. The pre-midnight depletions are seen as faint dark patches in the northern ends of the FOV. As in the 630.0 nm, the post-midnight development of depletion (D2) can be seen from 0246 LT, which become pronounced in the subsequent images. The pair of depletions marked D3 are seen till the pre-sunrise hours. It can be seen that the 630.0 and 557.7 nm depletions are similar in the post-midnight hours, while in the pre-midnight period 557.7 nm depletions are very weak. In Figure 5.29 the examples of 777.4 nm images taken in this night are given. The depletions in these images are very weak compared to the other two filters, and, disappear after 0320 LT. Instead of the pair of joined depletions, only a single depletion (D1) is seen. Very weak signatures of the depletion developing in the FOV (D2) can also be observed.

TRIVANDRUM, 16-17 February, 2002

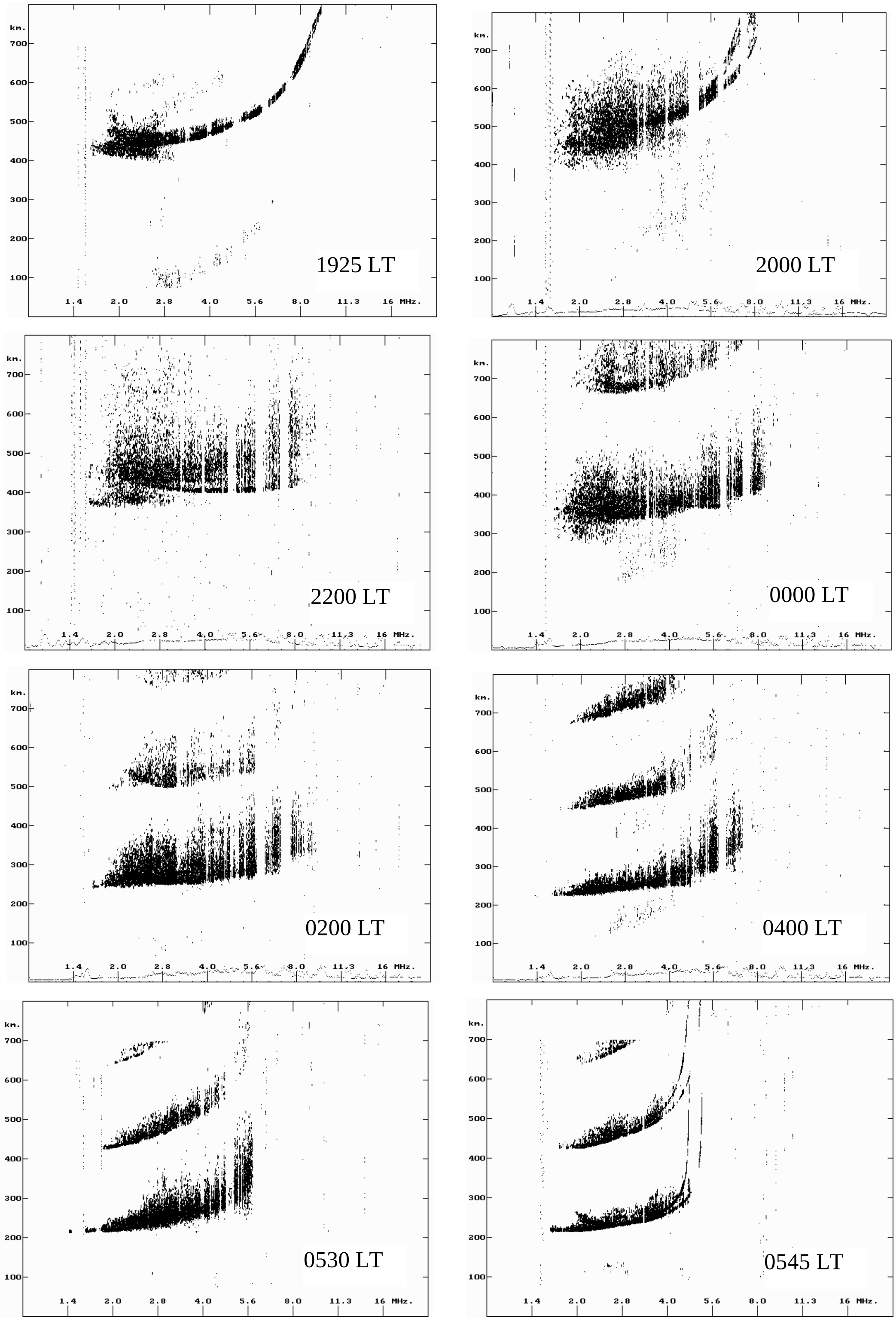

Figure 5.31 *A series of ionograms from the equatorial station Trivandrum (7.6˚N, 76.9˚E; 1.2˚S geomagnetic) recorded in the night of 16 February 2002, showing strong spread-F throughout the night.*

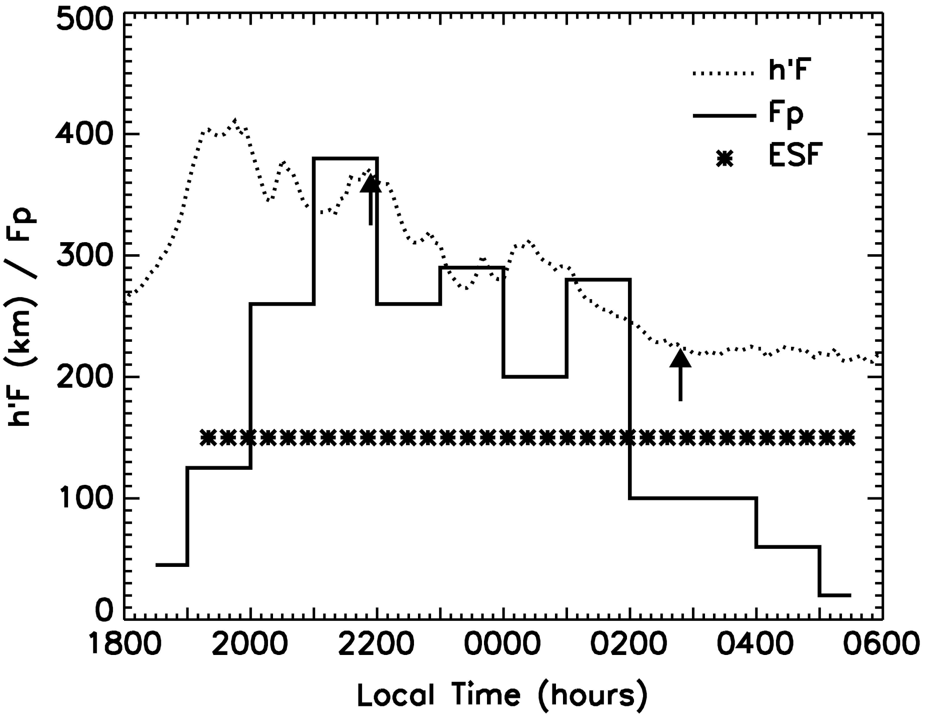

Figure 5.32 *The time variation of h'F at the equatorial station Trivandrum (dotted line) in night of 16 February 2002. The arrows denote the time of appearance of depletions in the 630.0 nm images. The asterisks represent the duration of the spread-F. Mendillo et al. (2000) introduced the GPS phase fluctuation index, Fp, derived from the time variation of the total electron content (TEC), to quantify the strength of plasma irregularities. Fp>200 indicates very strong irregularities, often associated with plasma depletions. Please note that since this work describes only the airglow observations, the Fp index result is not discussed here.*

This remarkable display of depletions in the night of 16 February 2002 is associated with intense spread-F extending throughout the night. The sequence of ionograms showing spread-F is given in Figure 5.31. In this night spread-F started appearing from about 1925 LT, and continued up to about 0545 LT. The variation of the F-region base height (h'F) plotted in Figure 5.32 shows that the F-layer is at higher altitudes when the depletions are seen in the pre-midnight period (in this night, depletions were already developed when the experiment started at 2200 LT), but at the time of appearance of the post-midnight depletions, it is lower than 250 km.

Another example of post-midnight development of depletions is given in Figure 5.33, where a series from the 630.0 nm images recorded on 10 March 2002 are displayed. The first panel displays the series of images taken from the beginning of the observations showing the pre-midnight depletions, which appear very weak. These depletions disappear after 2230 LT, and no depletions are seen in the images till

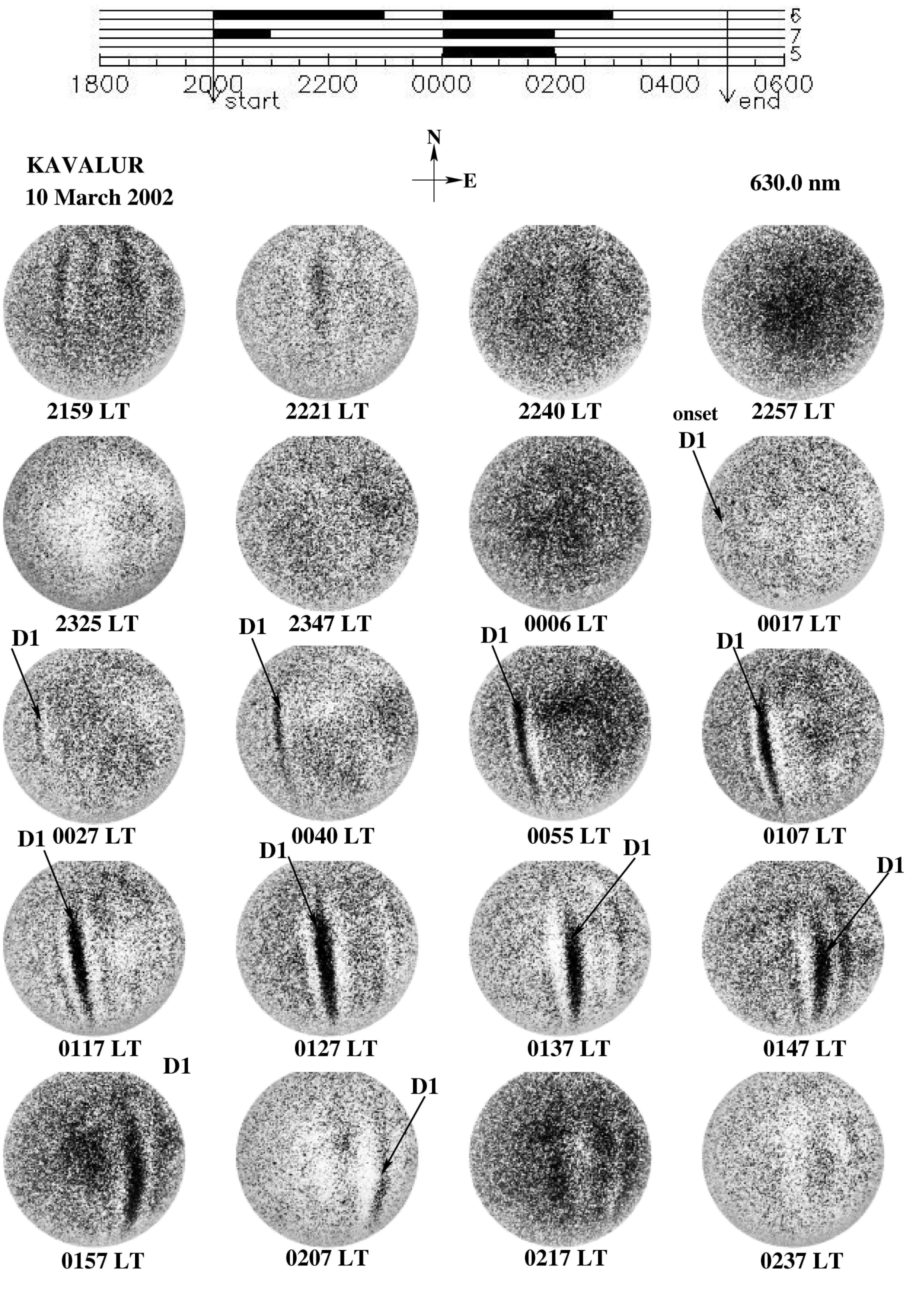

Figure 5.33 *A series from the 630.0 nm images taken in the night of 10 March 2002. The horizontal bar on the top indicates the time history of observations in this night, where the arrows denote the start and end times of observations, and the dark portion gives the duration of depletions. The numbers 6, 7 and 5 in the right stands for 630.0, 777.4 and 557.7 nm, respectively. The letters D1, and, D2 indicates the corresponding depletions in different images. The North and East directions are marked using arrows.*

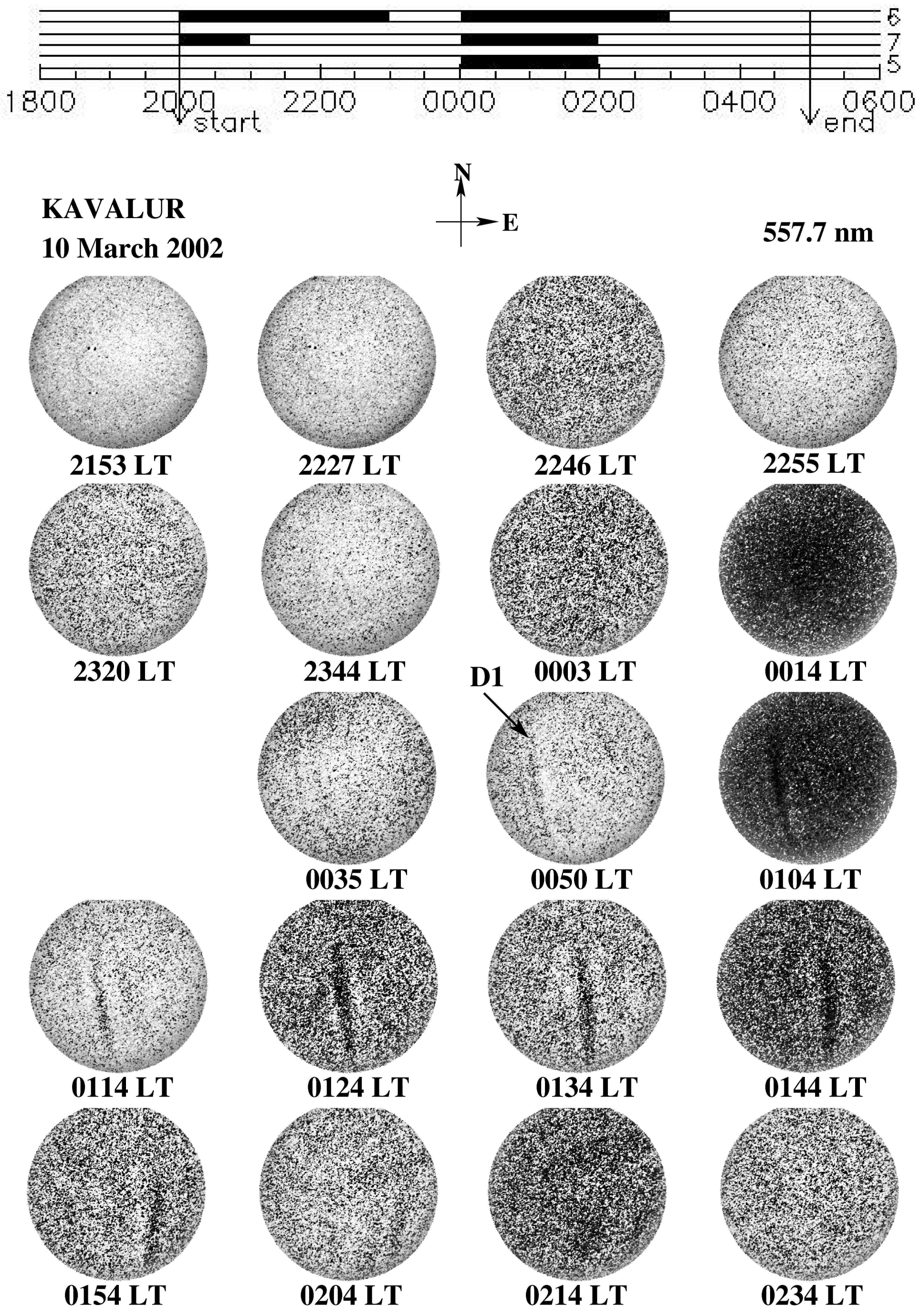

Figure 5.34 *A series from the 557.7 nm images taken in the night of 10 March 2002. The horizontal bar on the top indicates the time history of observations in this night, where the arrows denote the start and end times of observations, and the dark portion gives the duration of depletions. The numbers 6, 7 and 5 in the right stands for 630.0, 777.4 and 557.7 nm, respectively. The North and East directions are marked using arrows.*

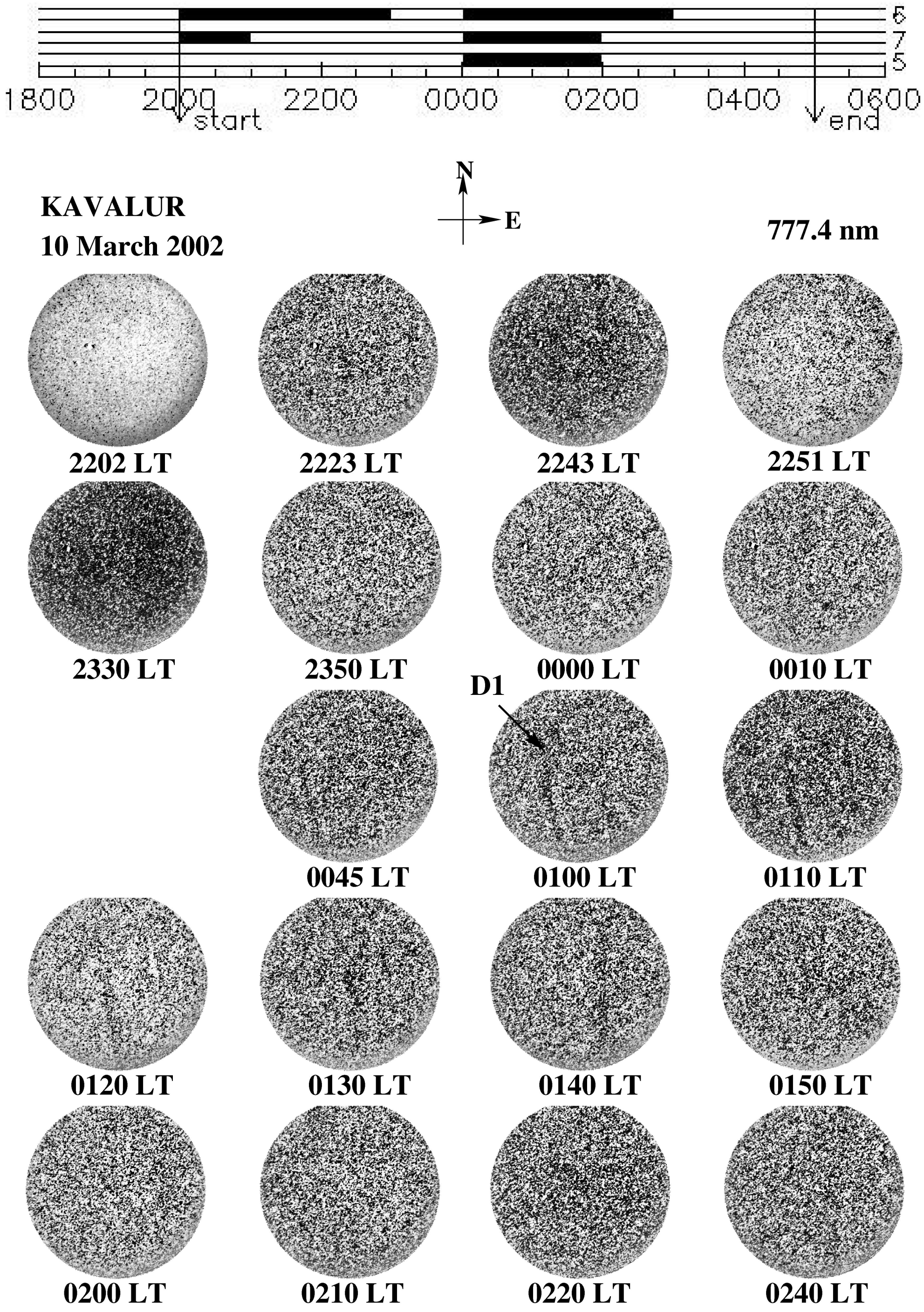

Figure 5.35 *A series from the 777.4 nm images taken in the night of 10 March 2002. The horizontal bar on the top indicates the time history of observations in this night, where the arrows denote the start and end times of observations, and the dark portion gives the duration of depletions. The numbers 6, 7 and 5 in the right stands for 630.0, 777.4 and 557.7 nm, respectively. The North and East directions are marked using arrows.*

midnight (middle panel). At 0017 LT, after a gap of more than 90 minutes of the disappearance of the depletions seen from the pre-midnight hours, the 'onset' of a fresh depletion (D1) is seen in the FOV. The bottom panel depicts the development of this depletion. This post-midnight depletion becomes weak at around 0200 LT, and disappears after 0300 LT. In this night also, the 557.7 nm shows depletions only in the post-midnight period, and as seen in Figure 5.34, these depletions have very similar characteristics to those in the 630.0 nm. In 777.4 nm, the pre-midnight depletions are too weak to identify (Figure 5.35), and the post-midnight depletions are seen during 0045 LT – 0140 LT.

Even though plasma depletions could occur at any hour of the night, depending up on the ionospheric conditions, once generated, they are seen in the images ranging from a few hours to sometimes even the entire night. In the night of 10 March 2002, it is unusual that depletions were found to develop in the FOV in the post-midnight period after more than an hour of the complete disappearance of the pre-midnight depletions. Since it is apparently difficult to see the development of pre-midnight depletions in the FOV, it is not possible to conclude whether irregularities were generated in the imager FOV in the evening hours of 10 March 2002. Thus, the pre-midnight depletions could as well be generated in the longitudes to the west of Kavalur, and later in the midnight hours the ionospheric conditions in the longitude regions within the imager FOV became suitable for irregularity generation. The ionograms show that spread-F in this night was very weak, but exhibit a similar occurrence pattern as that of the depletions, in two phases, each in the pre-midnight (1930 L – 2210 LT) and post-midnight (0015 LT – 0130 LT) hours, as can be seen from Figure 5.36. The h’F values in this night are displayed in Figure 5.37. In this night also the h’F is very high (>400 km) at the time of the pre-midnight depletions, while it is about 250 km at the time of generation of post-midnight depletions.

The probability of occurrence of plasma depletions is found to increase significantly during the periods of high solar activity [Sobral *et al.*, 2002; Sahai *et al.*, 2000]. Sobral *et al.*, [2002] reported about 80% increase in the bubble occurrence in high solar activity period than the low activity period in the equinoctial months. The results presented here indicate a similar higher bubble occurrence over the Indian sector in solar maximum period.

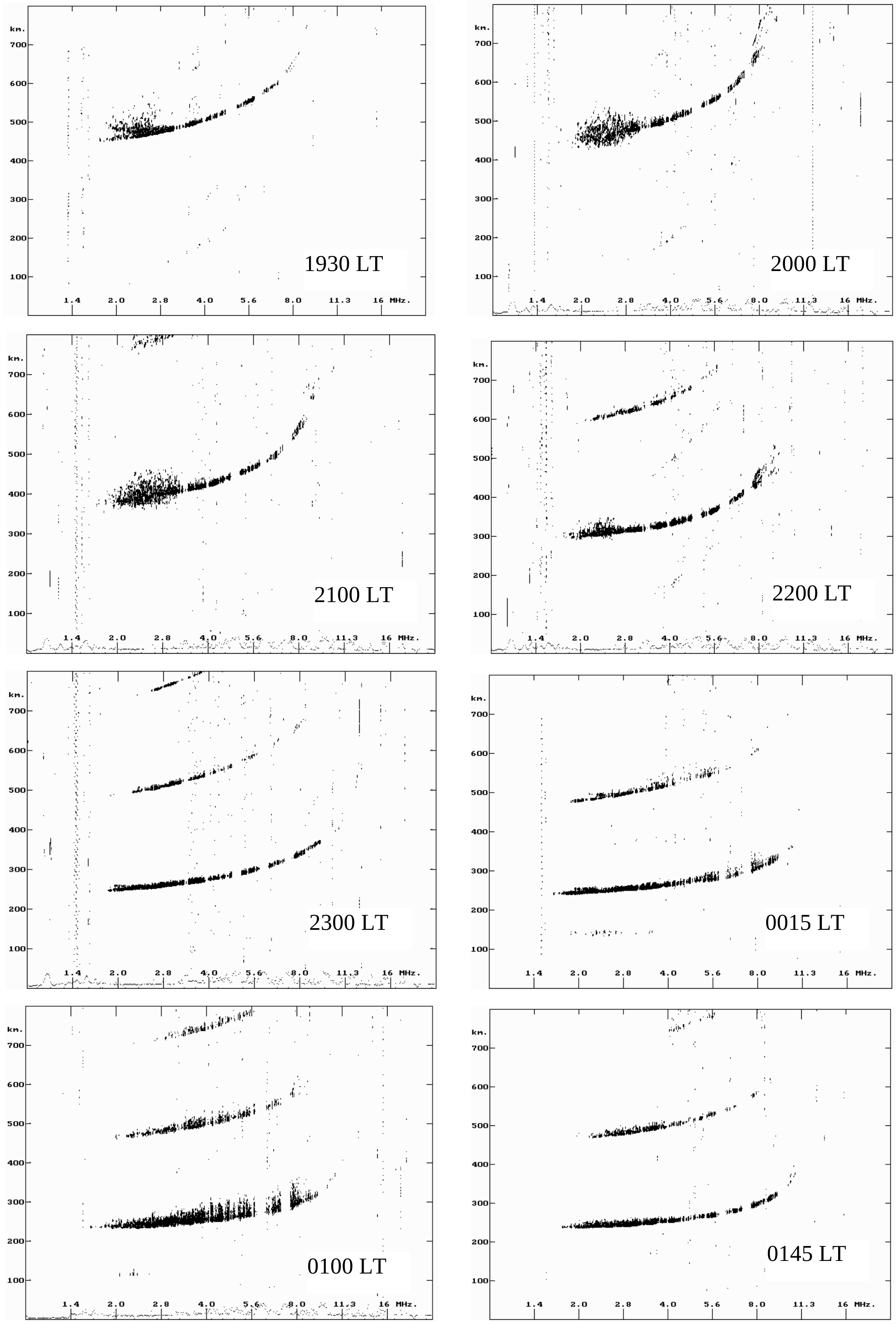

Figure 5.36 *A series of ionograms from the equatorial station Trivandrum (7.6˚N, 76.9˚E; 1.2˚S geomagnetic) recorded in the night of 10 March 2002. The spread-F disappears about 2000 LT, but reappears again about 0015 LT.*

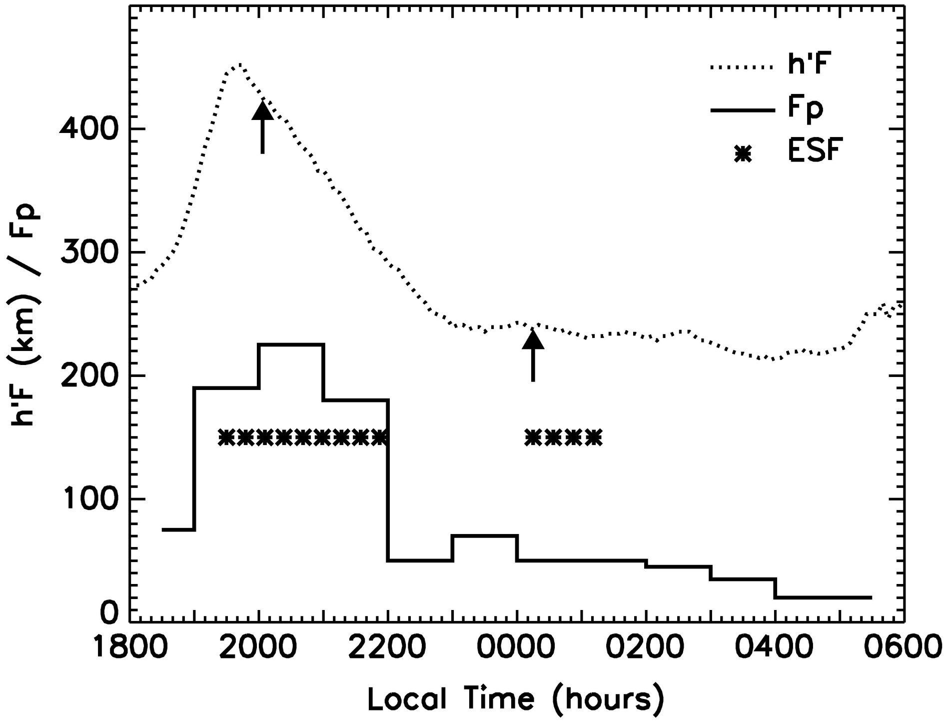

Figure 5.37 *The time variation of h'F at the equatorial station Trivandrum (dotted line) and that of the Fp values (solid line) in night of 10 March 2002. The arrows denote the time of appearance of depletions in the 630.0 nm images. The asterisks represent the duration of the spread-F. (Fp is explained in figure caption of fig.5.36)*

One of the basic requirements for the development of spread-F is the rapid uplifting of the F-layer to very high altitudes by the pre-reversal enhancement of electric field in the post-sunset hours [Farely *et al.*, 1970]. The zonal electric field, which itself is destabilizing, contributes to the instability growth rate by ensuring higher F-layer altitudes (lower ion-neutral collision frequency) [Kelley, 1989]. The evening vertical drift, or the pre-reversal electric field, increases with solar flux [Fejer *et al.*, 1999] during equinoctial months. The vertical rise velocity of the F-layer was calculated using the time rate of change of h'F for some of the nights in this observation period, for which, ionograms were available. The velocities were in the range 30-70 m/s with average value of 41 m/s, which are much greater than the threshold vertical velocity (17 m/s) suggested by Abdu *et al.*, [1983b], for the generation of spread-F. This indicates that the large evening vertical rise velocities are thus one of the factors responsible for the observed intense and continuous occurrence of plasma depletions in the solar maximum of 2002.

This rapid uplifting of the F-layer was mainly observed in the post-sunset hours, and as evident from Figures 5.32, h'F did not exhibit any upward motion prior to the development of the post-midnight depletions. The previous reports of post-midnight spread-F generation were caused by magnetic storm time electric field lifting equatorial F layer again in the post mid night period irrespective of solar activity.[Subba Rao and Krishna Murthy, 1994; Abdu *et al.,* 1998; MacDougall *et al.,* 1998; Niranjan *et al.,* 2003]. The present observations give examples of post-midnight development of spread-F depletions during solar maximum in the Indian region when the F-layer was at relatively low altitudes. Shiokawa *et al.,* [2004] reported the generation of depletions at midnight on 4 April 2002, from conjugate observations at the mid-latitude stations, Sata, Japan (31.0˚N, 130.7˚E; 21˚N, geomagnetic), and Darwin, Australia (12.4˚S, 131.0˚E; 22˚S, geomagnetic). Note that the observations of Shiokawa *et al.,* [2004] are conducted within the period of the current experiment.

Plasma depletions, which are the manifestations of ESF bubbles in the all sky imagers, evolve to the top side when the non-linear processes takes over after the linear growth phase of the Rayleigh-Taylor (RT) instability [Woodman and La Hoz, 1976; Chaturvedi and Ossakow, 1977]. The ‘onset’ of depletions in the images will occur when the irregularities develop to a level so that they are within the sensitivity range of the imager, and do not indicate the time of generation of the ESF irregularities. Tsunoda [1981b] have shown that the total growth phase of the irregularities takes about 50 minutes. In other words, prior to the appearance of the post-midnight depletions the instability would be already in process, generating irregularities of different scales that might not be detected by the all sky imager but could manifest as spread-F or cause scintillations. Thus, even though the h’F is not high enough when depletions appear in the images in the post-midnight time, at the time of onset of the instability process the conditions could be suitable to provide sufficient growth rate.

Chapter 6 **Conclusions**

The all sky observations conducted from Kavalur during the months of February-April, in the year 2002 reveals the occurrence of plasma depletions in several nights. The observations were remarkable in that there were several nights with intense depletions. Moreover, depletions appeared in all the three wavelengths in some of the nights. There were total 33 nights of observations possible, with 10 days of observations in February (6-16), and 12 days in March (4-17), and 11 days in April (5-15). The 630.0 nm images showed depletions in 27 nights, which is about 80% of the total observations. Similarly depletions were seen in the 777.4 nm in about 25 (~75%) nights. Also, about 19 (~57%) nights there were depletions in the 557.7 images. It is rather unusual that depletions were observed in 630.0 nm in 11 consecutive nights of March (4-14), and April (5-15). About 70% (19/27) of the nights with depletions in 630.0 nm also had depletions in 557.7 nm images. There is no significant geomagnetic activity during the observation period.

The east-west extensions (or width) of the observed depletions were in the range of 50-350 km. For the case of 557.7 and 630.0 nm images, the east-west extent is very similar. However, the depletions seem to be a bit wider in the 777.4 nm. In the pre-midnight the width of the depletions were mostly in the range 100-300 km. In the post-midnight period, in some of the cases, depletions of narrower width (less than 100 km) were also observed. However, in some of the nights during the observations there were cases when depletions seemed to develop overhead in the post-midnight period. Such developing depletions could have smaller widths. Width of the depletions appears to decrease with time, with a rate of about 3.1-3.6 km/minute. However, for the depletion in the post-midnight period, the rate of decrease is about 2.3-2.5 km/minute. The density gradient associated with the depletions that are seen in the post-midnight period could be different from that in the earlier hours, and hence their rate of decay also could be different.

The observations were used to estimate the drift velocity of the depletions in three different wavelengths. The median values who about 100-120 m/s in the evening period, which gradually decreases with time in the night, and becomes about 50 m/s in the post-midnight period. The 777.4 velocities are slightly less than that of the 630.0

nm values in the evening period. However, in the post-midnight period, the 777.4 nm velocities are a bit larger. The 630.0 and 777.4 nm velocities are estimated for different altitudes, and the observed difference in their values could thus indicate altitude difference in the zonal plasma drift. In the mid-night and early post-midnight period, the 557.7 nm velocities are slightly less than that in the 630.0 nm, probably because of the much less number of depletions in 557.7 nm images in this period compared to that in the 630.0 nm. In the later part of the night, both the velocities are very similar. There is an increasing trend in the 557.7 and 630.0 nm velocities in the post-midnight period, which could be influenced by newly developing depletions imaged in that period.

Several new features of plasma depletions are observed in this study such as the new type of ‘joined’ pair of depletions where the northern (and later the southern) ends join together, producing an inverted ‘V’ shape bifurcation, which later merge together, sequences of depletions developing in the field of view of the all sky imager in the post-midnight period, depletions in 630.0 nm images entering the field of view (FOV) as dark patches from the north end in the post-midnight period, and the frequent observations of plasma depletions in 557.7 nm images.

The joining and merging of depletions and the post-midnight development provide information about the ionospheric conditions and that could result in such features. The joined depletions appear developing in the FOV, and it is possible that the eastern and western depletions of the pair could drift with different velocities if they are at different levels of development. The fact that the pole ward ends of the depletions join before their center regions merge indicates higher eastward velocities at higher altitudes above equator. Similar influence of shear in the zonal plasma drift is evident in the spitting and joining of depletions observed from Mt. Abu, indicating the complex turbulent nature of the irregularities. The westward tilt and bifurcation of depletion are more frequent when imaged from low latitude stations such as Mt. Abu, or Mt. Lulin, while at the locations such as Kavalur, which is more close to the equator, depletions tend to appear as dark bands with minimum structures. This indicates that bifurcation occurs as the bubble rise over certain altitude, and it is unlikely that it is produced when irregularity is generated.

Sequences of depletions that develop within the FOV are imaged in these observations, and when these depletions appear the h’F values are about 250 km. Since the instability growth requires higher F-layer altitudes, it is possible that small scale irregularities are generated several minutes earlier when the h’F was higher, and by the time they grow to a sufficient level to be captured by the imager the F-layer moves down to lower altitudes.

The field aligned mapping of irregularities together with the altitude dependence of the 630.0 nm emission is proposed to be responsible for the depletions to appear as dark patches at the northern ends of the FOV. The dark patches in 630.0 nm images in the post-midnight hours, which enter the FOV from northern latitudes and grow towards equator, are in fact the signatures of the field aligned plasma depletions that are seen in the off equatorial latitudes where the depleted flux tubes meet the emission layer owing to the lower F-layer height than that at the magnetic equator. Near the equatorial region, the irregularity layer is above the airglow band, and depletions are limited to northern end of the FOV.

Detailed analysis is carried out to understand the important physical parameters that influence the emissions of the 557.7 nm in various local times and solar activities, and result in the appearance of depletions in the ground based images. The results indicate that due to the enhancement of the thermospheric component of the 557.7 nm emission and/or the less efficient masking effect, the occurrence of depletions becomes pronounced in the post-midnight period of the solar maximum. By contrast, the significant mask results in the 557.7 nm depletions of the thermosphere being unlikely observed during years of the solar minimum.

REFERENCES

Abdu, M. A., J. H. A. Sobral, I. S. Batista, V. H. Rios, and C. Medina (1998), Equatorial spread-F occurrence statistics in the American longitudes: diurnal, seasonal and solar cycle variations, *Adv. Space Res*., *27*, 851-854.

Abdu, M. A., R. T. Medeiros, J. A. Bittencourt, and I. S. Batista (1983b), Vertical ionization drift velocities and range spread F in the evening equatorial ionosphere, *J. Geophys. Res*., *88*, 399-402.

Ablade, J. R., P. R. Fagundes, J. A. Bittencourt, and Y. Sahai (2001), Observations of equatorial F region plasma bubbles using simultaneous OI 777.4 nm and OI 630.0 nm imaging: new results, *J. Geophys. Res*., *106*, 30,331-30,336.

Ablade, J. R., P. R. Fagundes, Y. Sahai, V. G. Pillat, A. A. Pimenta, and J. A. Bittencourt (2004), Height-resolved ionospheric drifts at low latitudes from simultaneous OI 777.4 and OI 630.0 nm imaging observations, *J. Geophys. Res*., *109*, A11308, doi:10.1029/2004JJA010560.

Anderson, D.N., and M. Mendillo (1983), Ionospheric conditions affecting the evolution of equatorial plasma depletions, *Geophys. Res. Lett., 10,* 541-544.

AARONS. J., M. MENDILLO, B. LIN and M. COLERICO, EQUATORIAL F REGION IRREGULARITY MORPHOLOGY DURING AN EQUINOCTIAL MONTH AT SOLAR MINIMUM, *Space Science Reviews* 87: 357–386, 1999.

Baluja, K. L., and C. J. Zeippen (1988), M1 and E2 transition probabilities for states within $2p^4$ configuration of the O I isoelectronic sequence, *J. Phys. B: At. Mol. Opt. Phys., 21*, 1455-1471.

Basu, Su., S. Basu, J. Aarons, J. P. McClure, and M. D. Cousins (1978), On the co-existence of kilometer and meter scale irregularities in the nighttime equatorial F region, *J. Geophys. Res., 83*, 4219.

Bates, D. R. (1981), The green light of the night sky, *Planet. Space Sci*., *29*(10), 1061–1067.

Bilitza, D. (2001), International Reference Ionosphere 2000, *Radio Sci*., *36*, 261-275.

Bittencourt, J. A., and Y. Sahai, (1979), Behavior of the [OI] 6300 Å emission at the magnetic equator and its reaction to the vertical ExB drift velocity, *J. Atmos. and Terr. Phys., 41*, 1233-1239.

Bittencourt, J. A., Y. Sahai, P. R. Fagundes, and H. Takahashi (1997), Simultaneous observations of equatorial F-region plasma depletions and thermospheric winds, *J. Atmos. Solar-Terr. Phys*., *59*, 9, 1049-1059.

Booker, H. G., and H. W. Wells (1938), Scatter of radio waves by the F-region of the ionosphere, *Terr. Mag. and Atmos. Elec*., *43,* 249-256.

Burke, W. J., M. C. Kelley, R. C. Sagalyn, M. Smiddy, and S. T. Lai (1979), Polar cap electric field structures with a northward interplanetary magnetic field, *Geophys. Res. Lett*., *6*, 21-24.

Chakrabarti, S. (1998), Ground based spectroscopic studies of sunlit airglow and aurora, *J. Atmos. and Solar-Terr. Phys., 60,* 1403-1423.

Chatruvedi, P. K., S. L. Ossakow (1977), Nonlinear theory of the collisional Rayleigh-

Taylor instability in equatorial spread-F, *Geophys. Res. Lett., 4*, 558-560.

Colerico, M., Mendillo, M., Nottingham, D., Baumgardner, J., Meriwether, J., Mirick, J., Reinisch, B. W., Scali, J. L., Fesen, C. G., and Biondi, M. A. (1996), Coordinated measurements of F-region dynamics related to the thermospheric midnight temperature maximum, *J. Geophys. Res., 101*, 26,783-26,793.

Fagundes, P. R., Y. Sahai, and H. Takahashi (1995), Investigation of OI 557.7 nm and OI 630.0 nm nightglow intensity ratios during the occurrence of equatorial F-region plsama bubbles, *J. Atmos. and Terr. Phys., 57*(8), 929-932.

Fagundes, P. R., Y. Sahai, I. S. Batista, M. A. Abdu, J. A. Bittencourt, H. Takahashi (1999), Observations of day-to-day variability in precursor signatures to equatorial F-region plasma depletions *Ann. Geophysicae, 17*, 1053-1063.

Farely, D. T., B. B. Balsley, R. F. Woodman, and J. P. McClure (1970), Equatorial spread-F, implications of VHF radar observations, *J. Geophys. Res., 7*5, 7199-7216.

Fejer, B. G., L. Scherliess, and E. R. de Paula (1999), Effects of the vertical plasma drift velocity on the generation and evolution of equatorial spread F, *J. Geophys. Res., 104*, 19,859-19,869.

Garcia, F. J., M. C. Kelley, J. J. Makela, and C.-S. Huang (2000), Airglow observations of mesoscale low-velocity traveling ionospheric disturbances at midlatitudes, *Geophys. Res., 105*(A8), 18,407-18,415.

Greenspan, J. A. (1966), Synoptic description of the 6300 Å nightglow near 78° west longitude, *J. Atmos. Terr. Phys., 28*, 739-745.

Hanson, W. B. (1970), A comparison of the oxygen ion-ion neutralization and radiative recombination mechanisms for producing the ultraviolet nightglow, *J. Geophys. Res., 75*, 4343-4349.

Hanson, W. B., and S. Sanatani (1973), Large N_i gradients below the equatorial F peak, *J. Geophys. Res., 78*, 1167-1173.

Hargreaves, J. K. (1992), The Solar-Terrestrial Environment, Cambridge University Press.

Hedin, A. E. (1991), Extension of the MSIS thermosphere model into the middle and lower atmosphere, *J. Geophs. Res., 96*, 1159-1172.

Herrero, F. A., and J. W. Meriwether (1980), 6300 Å airglow meridional intensity gradients, J. Geophys. Res., 85, 4194-4204.

Hines, C. O., (1960), Internal gravity waves at ionospheric heights, *Can. J. Phys., 38*, 1441-1481.

Huang, C. S., and M. C. Kelley (1996), Nonlinear evolution of equatorial spread F 2. Gravity wave seeding of Rayleigh-Taylor instability, *J. Geophys. Res., 101*(A1), 293-302.

Immel, T. J., E. Sagawa, S. L. England, S. B. Henderson, M. E. Hagan, S. B. Mende, H. U. Frey, C. M. Swenson, and L. J. Paxton (2006), Control of equatorial ionospheric morphology by atmospheric tides, *Geophys. Res. Lett., 33*, L15108, doi:10.1029/2006GL026161.

Kelley, M. C. (1989), The Earth's ionosphere: plasma physics and electrodynamics, *International Geophys. Series, 43,* Academic Press.

Kelley, M. C., J. J. Makela, B. M. Ledvina, and P. M. Kintner (2002), Observations of equatorial spread-F from Haleakala, Hawaii, *Geophys. Res. Lett., 29,* (20), 2003, doi:10.1029/2002GL015509.

Kelley, M. C., J. J. Makela, L. J. Paxton, F. Kamalabadi, J. M. Comberiate, and H. Kil (2003), The first coordinated ground- and space-based optical observations of equatorial plasma bubbles, *Geophys. Res. Lett., 30*(14), 1766, doi:10.1029/2003GL017301.

Kelley, M. C., M. F. Larsen, C. Lahoz, J. P. McClure (1981), Gravity wave initiation of equatorial spread-F, a case study, *J. Geophys. Res. 86*, 9087-9100.

Keskinen, M. J., S. L. Ossakow, and B. G. Fejer (2003), Three-dimensional nonlinear evolution of equatorial ionospheric spread-F bubbles, *Geophys. Res. Lett.,30(16),* 1855, doi:1029/2003GL017418, 2003.

Knudsen, W. C. (1970)**,** Tropical ultraviolet nightglow from oxygen ion-ion neutralization, *J. Geophys. Res., 75,* 3862-3868.

Lin, C. S., T. J. Immel, H.-C. Yeh, S. B. Mende, and J. L. Burch (2005), Simultaneous observations of equatorial plasma depletions by IMAGE and ROCSAT-1 satellites, *J. Geophys. Res., 110,* A06304, doi:10.1029/2004JA010774.

Link, R. (1992), N(^{2}D) + O_2: A source of thermospheric 6300 Å emission?, *Planet. Space Sci., 40,* 699–705.

Link, R., and L. L. Cogger (1988), A reexamination of the OI 6300 Å nightglow, *J. Geophys. Res., 93*(A9), 9883-9892.

MacDougall, J. W., M. A. Abdu, P. T. Jayachandran, J.-F Cecile, and I. S. Batista (1998), Presunrise spread F at Fortaleza, *J. Geophys. Res., 103,* 23,415-23,425.

Makela, J. J., B. M. Ledvina, M. C. Kelley, and P. M. Kintner (2004), Analysis of the seasonal variations of equatorial plasma bubble occurrence observed from Haleakala Hawaii, *Ann. Geophysicae, 22,* 3109-3129.

Martinis, C., J. V. Eccles, J. Baumgardner, J. Manzano, and M. Mendillo (2003), Latitude dependence of zonal plasma drifts obtained from dual-site airglow observations, *J. Geophys. Res., 108*(A3), 1129, doi:10.1029/2002JA009462.

Maruyama, T. (1988), Diagnostic model for equatorial spread F. 1. Model description and application to electric field and neutral wind effects, *J. Geophys. Res., 93*(A12), 14,611-14,622.

McClure, J. P., W.B. Hanson, and J. F. Hoffman (1977), Plasma depletions and irregularities in the equatorial ionosphere, *J. Geophys. Res., 82,* 2650-2656.

McDade, I. C., D. P. Murtagh, R. G. H. Greer, P. H. G. Dickinson, G. Witt, J. Stegman, E. J. Llewllyn, L. Thomas, and D. B. Jenkins (1986), ETON 2: quenching parameters for the proposed precursors of $O_2b^1\Sigma_g^+$) and O(^{1}S) 557.7 nm in the terrestrial nightglow, *Planet. Space Sci., 34,* 789-800.

McDonald, B. E., S. L. Ossakow, S. T. Zalesak, and N. J. Zabusky (1981), Scale sizes and lifetimes of F region plasma cloud straitions as determined by the condition of marginal stability, *J. Geophys. Res., 86,* 5775-5784.

Mende, S. B., and E. H. Eather (1976), Monochromatic all-sky observations and auroral precipitation patterns, *J. Geophys. Res., 81, 22*, 3771-3780.

Mendillo, M., and A. Tyler (1983), Geometry of depleted plasma regions in the equatorial ionosphere, *J. Geophys. Res., 88*, 5778-5782.

Mendillo, M., and J. Baumgardner (1982), Airglow characteristics of equatorial plasma depletions, *J. Geophys. Res*., *87*, 7641-7652.

Mendillo, M., J. Baumgardner, M. Colerico, and D. Nottingham (1997), Imaging science contributions to equatorial aeronomy: initial results from the MISETA program, *J. Atmos. and Solar-Terr. Phys.*, *59*, 1587-1599.

Mendillo, M., J. Baumgardner, X. Pi, P. J. Sultan, and R. Tsunoda (1992), Onset conditions for equatorial spread F, *J. Geophys. Res*., *97*(A9), 13,865-13,876.

Moore, J. G., and E. J. Weber (1981), OI 6300 A and 7774 A airglow measurements of equatorial plasma depletions, *J. Atmos. Terr. Phys.*, *43*, 8, 851-858.

Mukherjee G.K., (2003) The signature of short-period gravity waves imaged in the OI 557:7 nm and near infrared OH nightglow emissions over Panhala, J.*Atmo. and Solar-Terrestrial Physics* 65 1329– 1335

Mukherjee, G. K. (2003), Studies of the equatorial F-region depletions and dynamics using multiple wavelength nightglow imaging, *J. Atmos. and Solar-Terr. Phys.*, *65*, 379-390.

Nelson, G. J., and L. L. Cogger (1971), Dynamical behavior of the nighttime ionosphere at Arecibo, *J. Atmos. Terr. Phys.*, *33*, 1711-1726.

Niranjan, K., P. S. Brahmanandam, P. R. Ramakrishna Rao, G. Uma, D. S. V. V. D. Prasad, and P. V. S. Rama Rao (2003), Post midnight spread-F occurrence over Waltair (17.7° N, 83.3° E) during low and ascending phases of solar activity, *Ann. Geophysicae*, *21*, 745-750.

Ogawa, T., N. Balan, Y. Otsuka, K. Shiokawa, C. Ihara, T. Shimomai, and A. Saito (2002), Obserevations and modeling of 630 nm airglow and total electron content associated with traveling ionospheric disturbances over Shigaraki, Japan, *Earth Planets Space*, *54*, 45-56.

Ossakow, S. L. (1981), Spread-F theories -A review, *J. Atmos. and Terr. Phys.*, *43*(5-6), 437-452.

Otsuka, Y., T. Kadota, K. Shiokawa, T. Ogawa, S. Kawamura, S. Fukao, and S.-R. Zhang (2003), Optical and radio measurements of a 630-nm airglow enhancement over Japan on 9 September 1999, *J. Geophys. Res*., *108*, (A6) 1251, doi:10.1029/2002JA009594.

Peterson, V. L., T. E. Van Zandt (1969), *Planet Space Sci*, *17*, 1725.

Peterson, V. L., T. E. Van Zandt, and R. B. Norton (1966), F-region nightglow emissions of atomic oxygen, 1. Theory, *J. Geophys. Res.*, *71*, 2255-2265.

Peverall, R., S. Rosen, M. Larsson, J. Peterson, R. Bobbenkamp, S. L. Guberman, H. Danared, M. af Uggals, A. Al- Khalili, A. N. Maurellis, and W. J. van der Zande (2000), The ionospheric oxygen green airglow: electron temperature dependence and aeronomical implications, *Geophys. Res. Lett.*, *27* (4), 481-484.

Pimenta, A. A., J. A. Bittencourt, P. R. Fagundes, Y. Sahai, R. A. Buriti, H. Takahashi, and M. J. Taylor (2003b), Ionospheric plasma bubble zonal drifts over the tropical region: a study using OI 630.0 nm emission all-sky images, *J. Atmos. Solar-Terr. Phys*., *65*, 1117-1126.

Pimenta, A. A., P. R. Fagundes, J. A. Bittencourt, and Y. Sahai (2001), Relevant aspects of equatorial plasma bubbles under different solar activity conditions, *Adv. Space Res*., *27*(6-7), 1213-1218.

Pimenta, A. A., P. R. Fagundes, Y. Sahai, J. A. Bittencourt, J. R. Abalde (2003a), Equatorial F-region plasma depletion drifts: latitudinal and seasonal variations, *Ann. Geophysicae*, *21*, 2315-322.

Prölss, G. W., (1987), Storm-induced changes in the thermospheric composition at middle latitudes, *Planetary Space Sci*. *35*, 807–811.

Rajesh, P. K., J. Y. Liu, H. S. S. Sinha, S. B. Banerjee, R. N. Misra, N. Dutt, and M. B. Dadhania (2007), Observations of plasma depletions in 557.7 nm over Kavalur, *J. Geophys. Res*. (in press).

Raizada Shika, (1998) Ph.D thesis July 1998. Ionospheric irregularities in the F-region at low latitude.

Rees, M. H. (1989), Physics and chemistry of the upper atmosphere, *Cambridge Atmospheric and Space Science Series*, Cambridge University Press.

Rishbeth, H., and O. K. Garriott (1969), Introduction to Ionospheric Physics, Academic Press.

Rishbeth, H., T. J. Fuller-Rowell, and D. Rees (1987), Diffusive equilibrium and vertical motion in the thermosphere during a severe magnetic storm: a computational study', *Planetary Space Sci. 35*, 1157–1165.

Roble, R. G., A. D. Richmond, W. L. Oliver, and R. M. Harper (1978), Ionospheric effects of the gravity wave launched by the september 18, 1974, sudden commencement', *J. Geophys. Res., 83*, 999–1009.

Rohrbaugh, R. P., W. B. Hanson, B. A. Tinsley, B. L. Cragin, J. P. McClure, and A. L. Broadfoot (1989), Images of transequatorial bubbles based on field-aligned airglow observations from Haleakala in 1984-1986, *J. Geophys. Res*., *94*(A6), 6763-6770.

Sahai, Y., J. Aarons, M. Mendillo, J. Baumgardener, J. A. Bittencourt, and H. Takahashi (1994), OI 630 nm imaging observations of equatorial plasma depletions at 16^{o} dip latitude, *J. Atmos. Terr. Phys*., *56*, 11, 1461-1475.

Sahai, Y., P. R. Fagundes, and J. A. Bittencourt (2000), Transequatorial F-region ionospheric plasma bubbles: solar cycle effects, *J. Atmos. and Solar-Terr. Phys.*, *62*, 1377-1383.

Sahai, Y., P. R. Fagundes, J. A. Bittencourt, and M. A. Abdu (1988), Occurrence of large scale equatorial F-region plasma depletions during geo-magnetic disturbances, *J. Atmos. Solar-Terr. Phys*., *60*, 16, 1593-1604.

Saito, A., M. Nishimura, M. Yamamoto, S. Fukao, M. Kubota, K. Shiokawa, Y. Otsuka, T. Tsugawa, T. Ogawa, M. Ishii, T. Sakanoi, and S. Miyazaki (2001), Travelling ionospheric disturbances detected in the FRONT campaign, *Geophys. Res. Lett.*, *28*(4), 689-692.

Sales,G. S., B. W. Reinisch, J. L. Scali, C. Dozois, T. W. Bullett, E. J. Weber, and P. Ning (1996), Spread F and the structure of equatorial ionization depletions in the southern anomaly region, *J. Geophys. Res.*, *101*(A12), 26,819-26,828.

Sheeshan, C. H., and J.-P. St.-Maurice (2004), Dissociative recombination of N_2^+, O_2^+, and NO^+: rate coefficients for ground state and vibrationally excited ions, *J. Geophys. Res.*, *109,* A03302, doi:10.1029/2003JA010132.

Shepherd, G. G., R. G. Roble, C. McLandress, and W. E. Ward (1997), WINDII observations of the 558 nm emission in the lower thermosphere: the influence of dynamics on composition, *J. Atmos. and Solar-Terr. Phys*., *59*(6), 655-667.

Shepherd, G. G.., C. McLandress, and B. H. Solheim (1995), tidal influence on $O(^1S)$ airglow emission rate distributions at the geographic equator as observed by WINDII, *Geophys. Res. Lett., 22,* 275-278.

Shiokawa, K., C. Ihara, Y. Otsuka, and T. Ogawa (2003), Statistical study of nighttime medium-scale traveling ionospheric disturbances using midlatitude airglow images, *J. Geophys. Res*., *108,* (A1) 1052, doi:10.1029/2002JA009491.

Shiokawa, K., Y. Otsuka, M. K. Ejiri, Y. Sahai, T. Kadota, C. Ihara, T. Ogawa, K. Igarashi, S. Miyazaki, and A. Saito (2002), Imaging observations of the equatorward limit of midlatitude traveling ionospheric disturbances, *Earth Planets Space, 54,* 57-62.

Shiokawa, K., Y. Otsuka, T. Ogawa, and P. Wilkinson (2004), Time evolution of high-altitude plasma bubbles imaged at geomagnetic conjugate points, *Ann. Geophysicae, 22,* 3137-3143.

Singh, V., I. C. McDade, G. G. Shepherd, B. H. Solheim, and W. E. Ward (1995), The $O(^1S)$ day glow emission as observed by the WIND Imaging Interferometer on UARS, *Ann. Geophysicae, 14,* 637-646.

Sinha, H. S. S., and S. Raizada (2000), Some new features of ionospheric plasma depletions over the Indian zone using all sky optical imaging, *Earth Planets Space*, *52,* 549-559.

Sinha, H. S. S., P. K. Rajesh, R. N. Misra, and N. Dutt (2001), Multi-wavelength imaging observations of plasma depletions over Kavalur, India, *Ann. Geophysicae*, *19,* 1119-1131.

Sinha, H. S. S., P. K. Rajesh, R. N. Misra, R. Pandey, N. Dutt, M. B. Dadhania, and S. B. Banerjee (2003), Imagenes opticas de las disminuciones de plasma en la cresta de la anomalia ecuatorial, *Revista Boliviana de Fisic*, *9*, 52-59.

Sinha et al., 1996, Multi-wavelength optical imaging of ionospheric depletioms, *Ind. J. Rad. and Space Phy*. 25, 44-52, 1996.

Sobral, J. H. A., H. Takahashi, M. A. Abdu, P. Muralikrishna, Y. Sahai, C. J. Zalmutti, E. R. de Paula, and P. P. Batista (1993), Determination of the quenching rate of the $O(^1D)$ by $O(^3P)$ from rocket-borne optical (630 nm) and electron density data, *J. Geophys. Res.*, *98*(A5), 7791-7798.

Sobral, J. H. A., H. Takahashi, M. A. Abdu, P. Muralikrishna, Y. Sahai, and C. J. Zalmutti (1992), $O(^1S)$ and $O(^1D)$ quantum yields from rocket measurements of electron densities and 557.7 and 630.0 nm emissions in the nocturnal F-region, *Planet. Space Sci., 40,* 607-619.

Sobral, J. H. A., M. A. Abdu, H. Takahashi, M. J. Taylor, E. R. de Paula, C. J. Zamlutti, M. G. de Aquino, and G. L. Borba (2002), Ionospheric plasma bubble climatology over Brazil based on 22 years (1977-1988) of 630 nm airglow observations, *J. Atmos. and Solar-Terr. Phys., 64,* 1517-1524.

Sobral, J. H. A., M. A. Abdu, P. Muralikrishna, H. Takahashi, H. S. Sawant, C. J. Zamlutti, and M. G. de Aquino (1997), Horizontal gradients of the nocturnal OI 557.7 nm and OI 630.0 nm photoemission rates in the equatorial ionosphere based on rocket electron density data, *Adv. Space Res., 20* (6), 1317-1320.

St.-Maurice, J. P., and D. G. Torr (1978), Nonthermal rate coefficients in the ionosphere: The reactions of O^+ with N_2, O_2, and NO, *J. Geophs. Res., 83,* 969-977.

Subbarao, K. S. V., and B. V. Krishnamurthy (1994), Seasonal variations of equatorial spread-F, *Ann. Geophysicae, 12,* 33-39.

Takahashi, H., B. R. Clemesha, P. P. Batista, Y. Sahai, M. A. Abdu, and P. Muralikrishna (1990), Equatorial F-region 6300Å and OI 5577 Å emission profiles observed by rocket-borne airglow photometers *Planet. Space Sci., 38*(4), 547-554.

Takahashi, H., M. J. Taylor, J. H. A. Sobral, A. F. Medeiros, D. Gobbi, and D. C. Sanrana (2001), Fine structure of the ionospheric plasma bubbles observed by the OI 6300 and 5577 airglow images, *Adv. Space Res., 27,* 1189-1194.

Taylor, M. J., J. V. Eccles, J. Labelle, and J. H. A. Sobral (1997), High-resolution OI (630 nm) image measurements of F-region depletion drifts during the Guara campaign, *Geophys. Res. Lett., 24,* 1699-1702.

Tinsley, B. A., A. B. Christensen, J. Bittencourt, H. Gouveia, P. D. Angerji, and H. Takahashi (1973), Excitation of oxygen permitted line emissions in the tropical nightglow, *J. Geophys. Res., 78*(7), 1174-1184.

Tsunoda, R. T. (1981b), Time evolution and dymanics of equatorial backscatter plumes 1. Growth phase, *J. Geophys. Res., 86,* 139-149.

Tsunoda, R. T., (1980), Magnetic-field-aligned characteristics of plasma bubbles in the nighttime equatorial ionosphere, *J. Atmos. and Terr. Phys., 42,* 743-752.

Tsunoda, R. T., R. C. Livingston, and C. L. Rino (1981a), Evidence of a velocity shear in bulk plasma motion associated with the post sunset rise of the F layer, *Geophys. Res. Lett., 86,* 807-810.

Vlasov M N. , Modeling of airglow and ionospheric parameters at Arecibo during quiet and disturbed periods in October 2002, JOURNAL OF GEOPHYSICAL RESEARCH, VOL. 110, A07303, doi:10.1029/2005JA011074, 2005

Vlasov, M. N., M. J. Nicolls, M. C. Kelley, S. M. Smith, N. Aponte, and S. A. Gonzalez (2005), Modeling of airglow and ionospheric parameters at Arecibo during quiet and disturbed periods in October 2002, *J. Geophs. Res., 110,* A07303, doi:10.1029/2005JA011074.

Weber, E. J., H. C. Brinton, J. Buchau, and J. G. Moore (1982), Coordinated airborne and satellite measurements of equatorial plasma depletions, *J. Geophys. Res.,* *87*(A7), 10,503-10,513.

Weber, E. J., J. Buchau, and J. G. Moore (1980), Airborne studies of equatorial F layer ionospheric irregulrities, *J. Geophys. Res.*, *85*(A9), 4631-4641.

Weber, E. J., J. Buchau, R. H. Eather, and S. B. Mende (1978), North-south aligned equatorial depletions, *J. Geophys. Res.*, *83*, 712-716.

Weber, E. J., S. Basu, T. W. Bullett, C. Valladares, G. Bishop, K. Groves, H. Kuenzler, P. Ning, P. J. Sultan, R. E. Sheehan, and J. Araya (1996), Equatorial plasma depletion precursor signatures and onset observed at 11° south of the magnetic equator, *J. Geophys. Res.*, *101*(A12), 26,829-26,838.

Woodman R. F., and C. La Hoz (1976), Radar observations of F-region equatorial irregularities, *J. Geophys. Res.*, *81*, 5447-5466.

Zalesak, S. T., and S. L.Ossakow, and P. K. Chaturvedi (1982), Nonlinear Equatorial spread F: The effects of neutral winds and background Pederson conductivity, *J. Geophys. Res.*, *87*, 151-166.

Zhang, S. P., and G. G. Shepherd (1999), The influence of the diurnal tide on the O(^{1}S) and OH emission rates observed by WINDII on UARS, *Geophys. Res. Lett.*, *26*, 529-532.

Zhang, S. P., R. G. Roble, and G. G. Shepherd (2001), Tidal influence on the oxygen and hydroxyl nightglows: Wind Imaging Interferometer observations and thermosphere/ionosphere/mesosphere electrodynamics general circulation model, *J. Geophs. Res.*, *106*, 21, 381-21, 393.

List of publications of the author

H.S.S. Sinha, P. K. Rajesh, R. N. Misra, R. Pandey, N. Dutt, M. B. Dadhania and **S. B. Banerjee,** "All sky optical imaging of plasma depletions from the crest of the equatorial anomaly", *Bolivian J. of Physics* 2003.

P. K. Rajesh, J. Y. Liu, H. S. S. Sinha, **S. B. Banerjee**, R. N. Misra, N. Dutt, and M. B. Dadhania, "*Observations of plasma depletions in 557.7-nm images over Kavalur*", **JGR**, 112, A07307, 2007

P. K. Rajesh, J. Y. Liu1, H. S. S. Sinha, and, **S. B. Banerjee**, 'Appearance and Extension of Airglow Depletions', **JGR-Space Physics**, 2009/12/30 RE:2009JA014952RR

Post-midnight depletions, spread-F, and GPS phase fluctuations, P. K. Rajesh, J. Y. Liu, H. S. S. Sinha, W. S. Chen, **S. B. Banerjee**, R. N. Misra, N. Dutt, M. B. Dadhania, and F. D. Chu, JASTP, (Under Review).

Bifurcation, joining and merging of plasama depletions, P. K. Rajesh, J. Y. Liu, H. S S. Sinha, and **S. B. Banerjee**, (To be communicated).

P. K. Rajesh, J. Y. Liu, H. S. S., Sinha, and **S. B. Banerjee**, "Manifestation of the latitude expansion of plasma depletions in airglow images", Western Pacific Geophysics Meeting (WPGM), Taipei, Taiwan, 22-25 June, 2010.

P. K. Rajesh, J. Y. Liu, H. S. S., Sinha, and **S. B. Banerjee**, "Altitude latitude mapping of plasma depletions", AGU Fall meeting, 10-14 December, 2007.

P. K. Rajesh, J. Y. Liu, H. S. S., Sinha, W. S. Chen, and **S. B. Banerjee**, "Characteristics of equatorial plasma depletions over Indian zone during solar maximum", AOGS, Bangkok, Thailand, 30 July – 3 August, 2007.

P. K. Rajesh, J. Y. Liu, H. S. S., Sinha, and **S. B. Banerjee**, "Observations of plasma depletions in 557.7, 630.0, and 777.4 nm all sky images in solar maximum", AGU Fall meeting, 11-15 December, 2006.

P. K. Rajesh, J. Y. Liu, H. S. S., Sinha, **S. B. Banerjee**, R. N. Misra, N. Dutt, and M. B. Dadhania, "Characteristics of Plasma Depletions during Solar Maximum over India: Pronounced Appearance in 557.7 nm Images", AGU Fall meeting, San Francisco, USA, 5-9 December, 2005.

P. K. Rajesh, H. S. S., Sinha, J. Y. Liu, R. N. Misra, **S. B. Banerjee**, N. Dutt, and M. B. Dadhania, "Observations of Plasma Depletions during Solar Maximum", AOGS, Singapore, 20-24 June, 2005.

P. K. Rajesh, H. S. S., Sinha, J. Y. Liu, and **S. B. Banerjee** "Plasma depletions in 557.7 nm images", ISEA-11, Taipei, Taiwan, 9-14 May, 2005.

H. S. S., Sinha, P. K. Rajesh, J. Y. Liu, R. N. Misra, **S. B. Banerjee**, N. Dutt, M. B. Dadhania, and Uma Kota, "All sky imaging of plasma depletions over Indian zone during solar maxima", ISEA-11, Taipei, Taiwan, 9-14 May, 2005.

H.S.S. Sinha, Uma Das, R.N. Misra, M.B. Dadhania, **Swaroop Banerjee** and N. Dutt"Study of Mesospheric Turbulence using Rocket-borne Electron Density Measurements" Poster presented at 12th International Symposium on Equatorial Aeronomy from May 18-24, 2008, Crete, Greece.

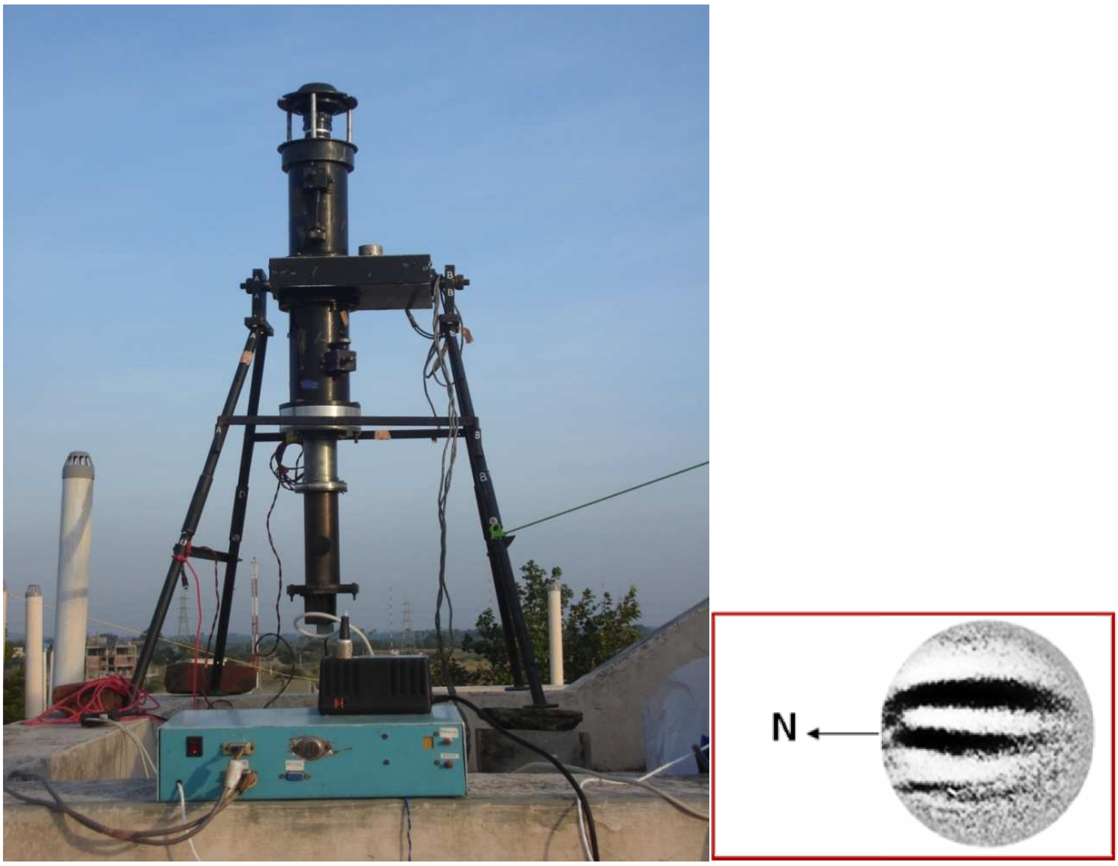

The All Sky Imager with a typical plasma depletion image taken with 630 nm optical filter, with north south aligned structure.

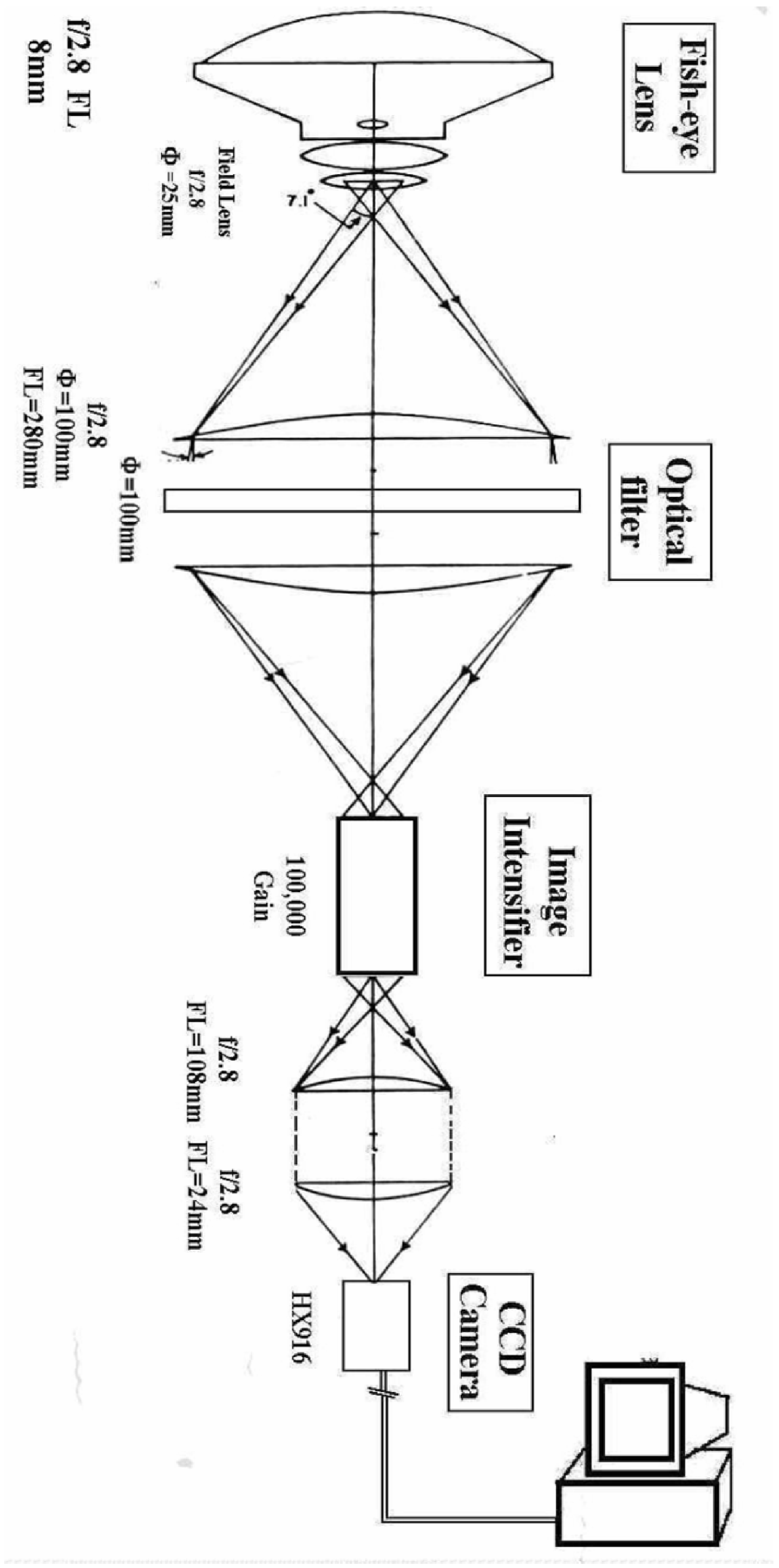

The ray diagram of the All sky imager